

1. Report No. FHWA/TX-90+365-3F	2. Government Accession No.	3. Recipient's Catalog No.	
4. Title and Subtitle STRENGTH AND DUCTILITY OF A THREE-SPAN EXTERNALLY POST-TENSIONED SEGMENTAL BOX GIRDER BRIDGE MODEL		5. Report Date January 1989	6. Performing Organization Code
7. Author(s) R. J. G. MacGregor, M. E. Kreger, and J. E. Breen		8. Performing Organization Report No. Research Report 365-3F	
9. Performing Organization Name and Address Center for Transportation Research The University of Texas at Austin Austin, Texas 78712-1075		10. Work Unit No.	11. Contract or Grant No. Research Study 3-5-85/8-365
12. Sponsoring Agency Name and Address Texas State Department of Highways and Public Transportation; Transportation Planning Division P. O. Box 5051 Austin, Texas 78763-5051		13. Type of Report and Period Covered Final	
15. Supplementary Notes Study conducted in cooperation with the U. S. Department of Transportation, Federal Highway Administration. Research Study Title: "Evaluation of Strength and Ductility of Precast Segmental Box Girder Construction with External Tendons"		14. Sponsoring Agency Code	
16. Abstract <p>This report is the third and final report in a series outlining a major study of the behavior of post-tensioned concrete box girder bridges with post-tensioning tendons external to the concrete section. It summarizes the design, construction, testing and interpretation of a very comprehensive three-span externally-post-tensioned box girder bridge model. The model was constructed from precast segments using the span-by-span construction procedure. Careful measurements were made during construction to document the actual stresses and prestress losses occurring. One span of the model had dry joints while the other two spans had epoxy joints.</p> <p>Loading was applied at design service load levels, design factored load levels, and ultimate load cycles for both maximum flexure and maximum shear loading configurations. Careful observations were made of deformations, tendon stress changes, joint openings and reaction changes. Companion analysis was performed to assist in development of the model and in the interpretation of the test data.</p> <p>The model bridge was very stiff at service load conditions and exhibited linear behavior to loads higher than the factored design load. The cracking load for epoxy-jointed spans was approximately twice the load required to decompress the flexural tension fiber and begin to open a previously cracked joint. This suggests that epoxied joints can provide a reasonable factor of safety against joint opening and that this same factor of safety can be provided in dry-jointed spans only by applying additional prestress force. Both the dry and epoxy-jointed spans displayed considerable ductility during flexural strength tests.</p>			
17. Key Words strength, ductility, concrete box girder bridge, segmental, tendons, post-tensioning, precast, stresses, prestress, load levels, joints, cracks		18. Distribution Statement No restrictions. This document is available to the public through the National Technical Information Service, Springfield, Virginia 22161.	
19. Security Classif. (of this report) Unclassified	20. Security Classif. (of this page) Unclassified	21. No. of Pages 324	22. Price

**STRENGTH AND DUCTILITY OF A THREE-SPAN
EXTERNALLY POST-TENSIONED SEGMENTAL BOX GIRDER BRIDGE MODEL**

R.J.G. MacGregor, M.E. Kreger and J.E. Breen

Research Report No. 365-3F

Research Project 3-5-85/8-365

**“Evaluation of Strength and Ductility of Precast Segmental
Box Girder Construction with External Tendons”**

Conducted for

Texas

State Department of Highway and Public Transportation

**In Cooperation with the
U.S. Department of Transportation
Federal Highway Administration**

by

**CENTER FOR TRANSPORTATION RESEARCH
BUREAU OF ENGINEERING RESEARCH
THE UNIVERSITY OF TEXAS AT AUSTIN**

January 1989

The contents of this report reflect the views of the authors, who are responsible for the facts and the accuracy of the data presented herein. The contents do not necessarily reflect the official views or policies of the Federal Highway Administration. This report does not constitute a standard, specification, or regulation.

There was no invention or discovery conceived or first actually reduced to practice in the course of or under this contract, including any art, method, process, machine, manufacture, design or composition of matter, or any new and useful improvement thereof, or any variety of plant which is or may be patentable under the patent laws of the United States of America or any foreign country.

PREFACE

This report is the third and final report in a series which summarizes an investigation of the behavior of precast segmental box girder bridges with external tendons. This report summarizes the design, construction and testing of a comprehensive scale model of a three span segmental box girder bridge constructed by the span-by-span method. Loading was applied typical of construction loads, design service loads, design factored loads, and ultimate loads.

This work is part of Research Project 3-5-85-365 entitled "Evaluation of Strength and Ductility of Precast Segmental Box Girder Construction with External Tendons." The research was conducted by the Phil M. Ferguson Structural Engineering Laboratory as part of the overall research programs of the Center for Transportation Research of The University of Texas at Austin. The work was sponsored jointly by the Texas State Department of Highways and Public Transportation and the Federal Highway Administration under an agreement with The University of Texas at Austin and the State Department of Highways and Public Transportation. Important financial support to augment the main program and in particular to develop the complex testing rig utilized for the companion deviator tests was provided by the National Science Foundation through Grant ECE-8419430, "Seismic Behavior of Prestressed Concrete Segmental Box Girders with External Tendons."

Liaison with the State Department of Highways and Public Transportation was maintained through the contact representative, Mr. Alan Matejowsky. The authors would like to particularly acknowledge the contributions from Mr. Alan Matejowsky of the TSDHPT who provided valuable suggestions and practical insight throughout all phases of the research project. In addition, the authors would like to acknowledge the guidance and assistance provided by local industry in development and construction of the model bridge structure. In particular, the assistance and cooperation of Prescon Corporation of San Antonio and Ivy Wire and Steel of Houston were especially appreciated. Finally, the hard work and personal contributions by student laboratory assistant Elie Homsy (now employed by Prescon Corporation) were greatly appreciated. Mr. Peter Chang was the contact representative for the Federal Highway Administration.

This portion of the overall study was directed by Michael E. Kreger, Assistant Professor of Civil Engineering. He was assisted by John E. Breen, who holds the Nasser I. Al-Rashid Chair in Civil Engineering, who was co-investigator on the overall TSDHPT and NSF projects. The design, construction and testing was the direct responsibility of Robert J.G. MacGregor, Assistant Research Engineer.

This page replaces an intentionally blank page in the original.

-- CTR Library Digitization Team

SUMMARY

This report is the third and final report in a series outlining a major study of the behavior of post-tensioned concrete box girder bridges with post-tensioning tendons external to the concrete section. It summarizes the design, construction, testing and interpretation of a very comprehensive three-span externally-post-tensioned box girder bridge model. The model was constructed from precast segments using the span-by-span construction procedure. Careful measurements were made during construction to document the actual stresses and prestress losses occurring. One span of the model had dry joints while the other two spans had epoxy joints.

Loading was applied at design service load levels, design factored load levels, and ultimate load cycles for both maximum flexure and maximum shear loading configurations. Careful observations were made of deformations, tendon stress changes, joint openings and reaction changes. Companion analysis was performed to assist in development of the model and in the interpretation of the test data.

The model bridge was very stiff at service load conditions and exhibited linear behavior to loads higher than the factored design load. The cracking load for epoxy-jointed spans was approximately twice the load required to decompress the flexural tension fiber and begin to open a previously cracked joint. This suggests that epoxied joints can provide a reasonable factor of safety against joint opening and that this same factor of safety can be provided in dry-jointed spans only by applying additional prestress force. Both the dry and epoxy-jointed spans displayed considerable ductility during flexural strength tests.

This page replaces an intentionally blank page in the original.

-- CTR Library Digitization Team

IMPLEMENTATION

The successful conclusion of this project resulted in specific guidance to designers and constructors regarding design and construction details to provide safer, more serviceable and more easily constructed external tendon bridges. The benefit of the epoxy jointing were already indicated as well as the ability of the construction system to develop full plastic mechanisms before failure. Specific recommendations regarding design and specification approaches based on this project have been made to AASHTO through another NCHRP study which helped in the development of design and construction specifications for externally post-tensioned segmental bridges.

A number of precast segmental box-girder bridges have been constructed with the prestressing tendons removed from the webs and flanges and placed in the void area of the box section. In addition, techniques have been used which eliminate epoxy in joints between segments. Substantial economic savings have been claimed for this type of construction; for example, the rapid rate of erection associated with the span-by-span method used can result in direct savings to the constructor, in greatly reduced detour and fuel costs, and in time savings to the motoring public.

However, questions have recently been raised as to how these bridges will behave when they are subjected to loads greater than service level loads, and, moreover, during the life of these bridges it will be necessary to know the proper criteria for assessing their responses to overloads. Thus, the objectives of this study for the Texas SDHPT, which is currently using this type of construction in several miles of overhead freeway in San Antonio, were to (1) determine the level of strength and ductility that may be expected for precast segmental bridges with external tendons, current tendon anchorages and joint details, and alternate joint details; (2) investigate the strength and ductility of typical tendon deviator details; (3) recommend changes in joint details, deviator details, and tendon locations where changes will improve the behavior of the system without significantly reducing construction efficiency; (4) develop suitable analysis methods; and (5) recommend methods for design and load rating criteria.

This page replaces an intentionally blank page in the original.

-- CTR Library Digitization Team

TABLE OF CONTENTS

CHAPTER ONE	INTRODUCTION	1
1.1	Background	1
1.1.1	Literature Review	3
1.1.2	Historical Development and Construction Methods	3
1.1.3	Rehabilitation of Existing Structures	4
1.1.4	Advantages and Disadvantages of External Post-Tensioning	4
1.2	Flexural Behavior of Girders with External Tendons	6
1.2.1	Before Cracking	6
1.2.1.1	Comparison between Bonded and Unbonded Systems	6
1.2.2	After Cracking	6
1.2.2.1	Ideal Rigid Body Mechanism	6
1.2.2.2	Plastic Hinges in Concrete Structures	9
1.3	Previous Studies on Externally Post-Tensioned Girders	15
1.3.1	Experimental	15
1.3.1.1	St. Remy Laboratory	15
1.3.1.2	Construction Technology Laboratory	15
1.3.2	Analytical	19
1.4	Object and Scope of Study	21
1.5	Summary	21
CHAPTER 2	DESIGN AND CONSTRUCTION OF BRIDGE MODEL	23
2.1	Development of Bridge Model	23
2.1.1	Dimensional Analysis	23
2.1.2	Scale Selection	23
2.1.3	Design Criteria	24
2.1.4	Description of Model Bridge Structure	31
2.2	Material Properties	44
2.2.1	Concrete	44
2.2.2	Prestressing Strands	44
2.2.3	Steel Reinforcement	44
2.3	Bridge Model Details	47
2.3.1	Typical Segment Details	47
2.3.1.1	Reinforcement	47
2.3.1.2	Fabrication of Typical Segments	48

2.3.1.3	Deviators	50
2.3.1.4	Shear Keys	51
2.3.1.5	Fabrication Tolerances for Typical Segments	51
2.3.1.6	Segment Repair Procedures	51
2.3.2	Pier Segment Details	53
2.3.2.1	Reinforcement	53
2.3.2.2	Anchorage Zone Pretest	54
2.3.2.3	Fabrication of Pier Segments	59
2.3.3	Bearings and Piers	61
2.4	Erection Procedures and Details	64
2.4.1	Span-by-Span Erection Method	64
2.4.2	Geometry Control	64
2.4.3	Temporary Post-Tensioning	64
2.4.4	Erection Falsework	66
2.4.5	Segment Joints	67
2.4.6	Cast-in-Place Closure Strips	68
2.4.7	Post-Tensioning Methods	69
2.4.8	Tendon Ducts and Grouting Details	70
 CHAPTER 3 - INSTRUMENTATION AND DATA ACQUISITION		73
3.1	General Requirements	73
3.2	Data Acquisition	73
3.3	Instrumentation Identification Code	73
3.4	Instrument Locations	75
3.5	Support Reactions	75
3.6	Measurement of Applied Loads	75
3.7	Deflection Measurements	75
3.8	Strand Strain Measurement	79
3.9	Joint-Opening Measurement	80
 CHAPTER 4 - BEHAVIOR OF STRUCTURE DURING CONSTRUCTION		83
4.1	Stressing Observations	83
4.2	Tendon Stress History	89
4.3	Deflections	89
4.4	Support Reactions	96
4.5	Summary of Observations Made During Erection	100

CHAPTER 5 - ANALYSIS OF ERECTION STRESSES	103
5.1 Nonlinear Finite Element Analysis	103
5.2 Plastic Mechanism Analysis	103
5.3 Plane Frame Analysis	104
5.4 Estimate of Conditions in the Structure Before Testing	113
CHAPTER 6 - LOAD TESTS OPERATIONS	131
6.1 Loading Program	131
6.2 Description of Loading System	133
6.2.1 Reduced Scale Truck Loads	133
6.2.1.1 Location of Loads	133
6.2.1.2 Load Application Equipment	134
6.2.2 Equivalent Live Load with Impact	135
6.2.3 Factored Dead Load	136
6.3 General Test Procedure	136
6.4 Presentation of Test Data	137
6.5 Center-span Service Load Tests	138
6.5.1 Live Load Cycles for Center-Span	139
6.5.2 Cracking Cycle for Center-Span	139
6.5.3 Decompression Load Test of Center-Span	143
6.6 North-span Load Tests (Dry Jointed)	148
6.6.1 Service Load Tests of North-Span	148
6.6.1.1 Live Load Cycles of North-Span	148
6.6.1.2 Decompression Load Cycles for North-Span	149
6.6.1.3 Torsional Load Cycles	152
6.6.2 Factored Load Cycles for North Span	152
6.6.3 Flexural Strength Tests of North Span	155
6.6.3.1 Joint Opening Cycles for North Span	155
6.6.3.2 Flexural Strength Cycles for North Span	163
6.6.4 Shear Strength Test of North Span	178
6.7 South-span Load Tests (Epoxyed Joints)	187
6.7.1 Service Load Tests of South-Span	187
6.7.1.1 Live Load Cycles for South-Span	187
6.7.1.2 Cracking Cycle for South-Span	188
6.7.1.3 Decompression Load Cycles for South-Span	193
6.7.2 Factored Load Cycles for South-Span	195

6.7.3	Flexural Strength Tests Of South-Span	202
6.7.3.1	Crack Opening Cycles for South-Span	202
6.7.3.2	Flexural Strength Cycle for South-Span	209
6.7.4	Shear Strength Cycle for South-Span	217
7.	INTERPRETATION OF TEST DATA	229
7.1	Observations from Load Tests	229
7.1.1	Service Load Behavior	229
7.1.1.1	Live Load Response	229
7.1.1.2	Comparison with Elastic Analysis	229
7.1.1.3	Torsional Response	230
7.1.1.4	Fretting Fatigue at Deviators	230
7.1.2	Factored Load Behavior	232
7.1.3	Ultimate Flexural Behavior	234
7.1.4	Shear Behavior	235
7.1.5	Ductility	238
7.2	Estimation of Insitu Forces	242
7.2.1	Insitu Dead Load Forces	242
7.2.2	Effective Prestress Forces at Critical Joints	242
7.2.3	Service Load Tendon Stresses	246
7.3	Effect of Epoxy on Model Behavior	249
7.3.1	Effect of Epoxy on Construction	249
7.3.2	Effect on Service Load Behavior	249
7.3.3	Effect on Factored Load Behavior	250
7.3.4	Effect on Flexural Strength	251
7.3.5	Effect on Shear Strength	251
7.3.6	Effect on Ductility	251
7.4	Flexural Strength Model	252
7.4.1	Observations from Load Tests	253
7.4.2	Factors Affecting the Unbonded Tendon Stress at Nominal Flexural Capacity	255
7.4.2.1	Effective Prestress Force	255
7.4.2.2	Ratio of Prestress Depth to Tendon Free Length	258
7.4.2.3	Neutral Axis Depth	258
7.4.2.4	Rotation Capacity at Precast Joints	258
7.4.2.5	Tendon Slip at Deviators	260
7.4.3	Prediction Equations for Tendon Stress in Unbonded Tendons	

Corresponding to Nominal Capacity	261
7.4.3.1 ACI	261
7.4.3.2 AASHTO	261
7.4.3.3 Tam and Pannell	261
7.4.3.4 Canadian Standards Association (CSA)	264
7.4.3.5 Virlogeux	264
7.4.3.6 Comparison of Prediction Equations with Test Data	265
7.4.4 Recommendation for Calculation of Flexural Strength	268
7.5 Load Rating Existing Structures	271
7.6 Secondary Prestress Forces at Ultimate Load Levels	273
7.6.1 Background Information	273
7.6.2 Secondary Prestress Forces from Construction	275
7.6.3 Redistribution of Secondary Prestress Forces	278
8. CONCLUSIONS AND RECOMMENDATIONS	287
8.1 Fabrication Conclusions and Recommendations	287
8.2 Erection Process	288
8.3 Analysis	289
8.4 Behavior	290
8.5 Research Needs	295
REFERENCES	297

This page replaces an intentionally blank page in the original.

-- CTR Library Digitization Team

LIST OF FIGURES

Figure	Page
1.1 External Post-tensioning in Long Key Bridge	2
1.2 General Layout of Simple-Span Structure with Straight Tendons	7
1.3 Applied Moment vs. Deflection	7
1.4 Tendon Stress vs. Deflection	7
1.5 Calculation of Tendon Elongation	8
1.6 Moment-Deflection Response for Bonded Tendons	10
1.7 Moment-Deflection Response for Unbonded Tendons	11
1.8 Tendon Elongation in the Plastic Hinge Region	13
1.9 Saint-Remy Test Girders	16
1.10 Moment-Deflection Behavior	17
1.10 Moment-Deflection Behavior – Continued	18
1.11 PCA Test Girders	20
2.1 Possible Model Cross-Sections	25
2.2 (1/4) Scale Truck Load	27
2.3 Design Loads	29
2.4 Scale Model of Externally Post Tensioned Box Girder	35
2.5 Test Set-up	36
2.6 Model Cross-Sections	37
2.7 Schematic Post-Tensioning Layout	39
2.8 Theoretical Tendon Locations	40
2.8 Theoretical Tendon Locations – Continued	41
2.8 Theoretical Tendon Locations – Continued	42
2.8 Internal and Auxiliary Tendons – Continued	43
2.9 Typical Segment Reinforcing	49
2.10 Deviator Force Components	50
2.11 Shear Key Details	52
2.12 South Interior Pier Segment	54
2.13 Pier Segment Reinforcement	55
2.13 Anchorage Zone Reinforcement – Continued	56
2.13 Pier Segment Reinforcement Schedule – Continued	57
2.14 Pier Segment Reinforcement	58
2.15 Post-Tensioning Anchorage Pretest	60
2.16 Bearing Schematics	62

2.17	Pier Details	63
2.18	Span-by-Span Erection System	65
3.1	Instrumentation Identification Code	74
3.2	Instrumentation Layout During Testing	76
3.3	Joint-Distortion Instrumentation	77
3.4	Locations of Deflection Instrumentation During Construction	78
3.5	Joint Opening Instrumentation	81
3.6	Joint Opening Instrumentation	82
4.1	Strain Gage Calibration Results (Ref. 18)	84
4.2	Case with Parallel Data Lines	85
4.3	Measured Data Corrections	86
4.4	Tendon Stress Profiles During Stressing	88
4.5	Tendon Stress History	90
4.6	Deflection Profiles	92
4.6	Deflection Profiles - continued	93
4.6	Deflection Profiles - continued	94
4.7	Resultant Deflected Shape after Construction	95
4.8	Measurement of North Exterior Reactions	97
4.9	Lift-Off Force Determination	98
4.10	Equalization of North Exterior Reactions	99
4.11	Equalization of South Interior Reactions	100
5.1	Plastic Mechanism Analysis	105
5.1	Plastic Mechanism Analysis(continued)	106
5.1	Plastic Mechanism Analysis(continued)	107
5.2	Possible Complex Mechanism in Dry Jointed Span	108
5.3	Plate Frame Elastic Analysis Models	109
5.4	One Span Configuration	114
5.4	One Span Configuration - Continued	114
5.5	Two Span Configuration	116
5.5	Two Span Configuration - Continued	117
5.6	Three Span Configuration	118
5.6	Three Span Configuration - Continued	119
5.7	Theoretical Three Span Structure	121
5.7	Theoretical Three Span Structure - Continued	122
5.8	Comparison of Extreme Fiber Stresses for As-Built and Theoretical Structures	123
5.9	Extreme Fiber Live Load Stresses	125

5.10	Service Stress Range	126
5.11	Test Load Forces	128
5.11	Test Load Forces – Continued	129
6.1	Test Load Configurations	134
6.2	Load Frame	135
6.3	Center Span Service Load Test Deflection Profile	138
6.4	Center Span Cracking Cycle Applied Load vs. Deflection	140
6.5	Center Span Cracking Cycle Reactions and Joint Moments	141
6.6	Center Span Cracking Cycle - Change in Tendon Stress vs. Applied Load	142
6.7	Center Span Decomposition Cycles Applied Load vs. Deflection	144
6.8	Center Span Decompression Cycles Reactions and Joint Moments	145
6.9	Center Span Decompression Cycles Change in Tendon Stress vs. Applied Load	146
6.10	Change in Tendon Stress vs. Applied Load Comparison Between First and Second Cycles	147
6.11	North Span Service Load Tests Deflection Profile	149
6.12	North Span Decompression Cycles Applied Load vs. Deflection	150
6.13	North Span Decompression Cycles Reactions and Joints Moments	151
6.14	North Span Factored Load Cycles Applied Load vs. Deflection	153
6.15	North Span Factored Load Cycles Reactions and Joint Moments	154
6.16	North Span Joint Opening Cycles Applied Load vs. Deflection	156
6.17	North Span Joint Opening Cycles Reactions and Joint Moments	157
6.18	North Span Joint Opening Cycles - Change in Tendon Stress vs. Applied Load	158
6.19	North Span Joint Opening Cycles Joint Opening Potentiometer vs. Applied Load	159
6.20	North Span Joint Opening Cycles Comparison of Tendon Stresses for Cycles 1 & 2	162
6.21	North Span Joint Opening Cycles - Tension Stress Profile	163
6.22	North Span Joint Opening Cycles Comparison of Joint Moments for Cycles 1 & 2	164
6.23	North Span Flexural Strength Test Applied Load vs. Deflection	165
6.24	North Span Flexural Strength Tests Applied Load vs. Deflection	166
6.25	North Span Flexural Strength Tests Reactions and Joint Moments	167
6.26	North Span Flexural Strength Tests Change in Tendon Stress vs. Applied Load (North-Span Tendons)	168

6.27	North Span Flexural Strength Tests Change in Tendon Stress vs. Applied Load (Center-Span Tendons)	169
6.28	South Span Flexural Strength Tests Joint Opening Behavior	170
6.29	North Span Flexural Strength Test Crushing on Top of Key at Joint (5, 6)	171
6.30	North Span Flexural Test - Deflection Profile	176
6.31	Plastic Mechanism Rotations for Propped Cantilever	177
6.32	North Span Flexural Test - Cracking Summary	179
6.33	North Span Shear Strength Test Applied Load vs. Deflection	180
6.34	North Span Shear Strength Test Reactions and Joint Moments	181
6.35	North Span Shear Strength Test Change in Tendon Stress vs. Applied Load (North Span)	182
6.36	North Span Shear Strength Test Change in Tendon Stress vs. Applied Load (Center Span)	183
6.37	North Span Shear Strength Test Joint Opening Behavior	184
6.38	North Span Shear Test - Deflection Profiles	185
6.39	North Span Shear Test - Cracking Summary	186
6.40	South Span Service Load Tests Deflection Profile	187
6.41	South Span Cracking Cycle Applied Load vs. Deflection	188
6.42	South Span Cracking Cycle Reactions and Joint Moments	189
6.43	South Span Cracking Cycle Change in Tendon Stress vs. Applied Load	191
6.44	South Span Cracking Cycle Joint Opening Potentiometer vs. Applied Load	192
6.45	South Span Decompression Cycles - Applied Load vs. Deflection	193
6.46	South Span Decompression Cycles - Reactions and Joint Moments	194
6.47	Comparison of South Span Cracking Cycle and Decompression - Load Cycle Response for Tendon 4a	196
6.48	South Span - Tendon 4a Stress Profile	197
6.49	Comparison of South - Span Cracking Cycle and Decompression - Load Cycle Response for Tendon 5	198
6.50	Tendon Slip After Cracking Cycle	199
6.51	South Span Factored Load Cycles - Applied Load vs. Deflection	199
6.52	South Span Factored Load Cycles - Reactions and Joint Moments	200
6.53	South Span Crack Opening Cycles - Applied Load vs. Deflection	202
6.54	South Span Crack Opening Cycles - Reactions and Joint Moments	203
6.55	South Span Crack Opening Cycles - Joint Opening Potentiometer vs. Applied Load	205
6.56	South Span Cracking Cycle - Joint Opening Potentiometer vs. Applied Load	207
6.57	South Span Crack Opening Cycles - Tendon 4a Stress Profile Before Cycles 1 & 2	208

6.58	South Span Flexural Strength Test - Applied Load vs. Deflection	208
6.59	South Span Flexural Strength Test - Reactions and Joint Moments	210
6.60	South Span Flexural Strength Test - Change in Tendon Stress vs. Applied Load - South Span Tendons	211
6.61	South Span Flexural Strength Test - Change in Tendon Stress vs. Applied Load - South Span Tendons	212
6.62	South Span Flexural Strength Test - Crack Opening Behavior	213
6.63	South Span Flexural Strength Test - Deflection Profiles	216
6.64	South Span Flexural Strength Test - Cracking Summary	218
6.65	South Span Shear Test - Applied Load vs. Deflection	219
6.66	South Span Shear Test - Reactions and Joint Moments	220
6.67	South Span Shear Test - Change in Tendon Stress vs. Applied Load - South Span Tendons	221
6.68	South Span Shear Test - Change in Tendon Stress vs. Applied Load - Center Span Tendons	222
6.69	South Span Shear Test - Crack Opening Behavior	223
6.70	South Span Shear Test - Deflection Profile	224
6.71	South Span Shear Test - Cracking Summary	227
7.1	Beam and Suspension Systems	231
7.2	Deviator Force Components	232
7.3	Stress Condition for Strand in Contact with Deviator	233
7.4	Stages of Flexural Behavior	235
7.5	Ultimate Deflection Profile	236
7.6	Shear Mechanisms at Opening Joints	237
7.7	Bridge Collapse During Construction	240
7.8	Service Load Tendon Stresses	247
7.8	Service Load Tendon Stresses – continued	248
7.9	Flexural Model	253
7.10	Tendon Stress Response to Applied Load	254
7.11	Typical Tendon Stress Response	256
7.12	Comparison of Ultimate Flexural Behavior of Exterior Spans	257
7.13	Tendon Profile Slenderness Ratio	259
7.14	Methods for Calculating f_{ps}	262
7.14	Methods for Calculating f_{ps} – continued	263
7.15	Recommended Design Equation	269
7.16	Neutral Axis Depth, c_y	270
7.17	Free Tendon Length	272

7.18	Primary and Secondary Prestress Forces	274
7.19	Secondary Prestress Forces from the Construction Method	276
7.20	Staged Construction to Relieve Secondary Forces	277
7.21	Reactions and Joint Moments	279
7.22	Rotational Stiffness at an Opening Joint	281
7.23	Rotational Joint Stiffness vs. Moment	281
7.24	Applied Load vs. Bending Moment	284

LIST OF TABLES

<u>Table</u>	<u>Page</u>
2.1 AASHTO-83 Stress Limits	32
2.2 PTI Proposed Stress Limits for Segmental Construction	33
2.3 Load Combinations	34
2.4 Concrete Mix Types	45
2.5 Segment Concrete Properties	46
2.6 Reinforcement Properties	47
4.1 Summary of Tendon-Stress Losses	91
4.2 Exterior Reaction Corrections	98
5.1 Member Properties for Elastic Analysis	111
5.2 Dead Loads for Elastic Analysis	112
5.3 Concrete Stress Limits for Model Structure	124
5.4 Multiple of Line Plus Impact Loads Required for Joint Decompression	130
6.1 Loading Program	131
6.2 Center-Span Cracking Cycle - Maximum Response Values	140
6.3 Center-Span Cracking Cycle - Change in Tendon Stress (ksi)	143
6.4 Summary of Center-Span Cracking Cycle	143
6.5 Center-Span Decompression Cycles - Maximum Response Values	144
6.6 Center-Span Decompression Cycles - Change in Tendon Stress	148
6.7 Summary of Center-Span Decompression Cycles	148
6.8 North-Span Decompression Cycles - Maximum Response Values	150
6.9 North-Span Decompression Cycles - Change in Tendon Stress (ksi)	152
6.10 Summary of North-Span Decompression Cycles	152
6.11 North Span Factored Load Cycle - Maximum Response Values at Factored Load = 2.9(LL+I)	155
6.12 North Span Factored Load Cycle - Change in Tendon Stress at Factored Load = 2.9(LL+I)	155
6.13 Summary of North Span Factored Load Cycles	155
6.14 North-Span Joint Opening Cycles - Maximum Response Values at Load = 4.7(LL+I)	160

6.15	North Span Joint Opening Cycles - Change in Tendon Stress at Load = 4.7(LL+I)	160
6.16	Summary of North Span Joint Opening Cycles	161
6.17	Instantaneous Stiness During North-Span Tests (measured in (LL+I)/inch)	171
6.18	North Span Flexural Strength Cycles - Maximum Response Values - Flexural Strength Load = 6.8(LL+I)	172
6.19	North Span Flexural Strength Cycles Change in Tendon Stress (ksi) - Flexural Strength Load = 6.8(LL+I)	172
6.20	Summary of North Span Flexural Strength Cycle	173
6.21	North Span Shear Test - Maximum Response Values - Shear Strength Load = 7.2(LL+I)	174
6.22	North Span Shear Test - Change in Tendon Stress - Shear Strength Load = 7.2(LL+I)	174
6.23	Summary of North-Span Shear Test	175
6.24	South-Span Cracking Cycle - Maximum Response Values	190
6.25	South-Span Cracking Cycle - Change in Tendon Stress	192
6.26	Summary of South-Span Cracking Cycle	192
6.27	South-Span Decompression Cycles - Maximum Response Values	195
6.28	South-Span Decompression Cycles - Change in Tendon Stress (ksi)	195
6.29	Summary of South-Span Decompression Cycles	195
6.30	South-Span Factored Load Cycles - Maximum Response Values at Factored Load = 2.9(LL+I)	201
6.31	South-Span Factored Load Cycles - Change in Tendon Stress (ksi) at Factored Load = 2.9(LL+I)	201
6.32	Summary of South-Span Factored Load Cycles	201
6.33	South-Span Crack Opening Cycles - Maximum Response Values at Load = 4.8(LL+I)	204
6.34	South-Span Crack Opening Cycles - Change in Tendon Stress (ksi) at Load = 4.7(LL+I) Cycle 1	204
6.35	Summary of South-Span Crack Opening Cycles	206
6.36	Tangent stiness During South-span Tests (measured in (LL+I)/inch)	214
6.37	South-span Flexural Test - Maximum Response Values Flexural Strength Load = 7.7(LL+I)	214

6.38	South-span Flexural Test - Change in Tendon Stress (ksi) Flexural Strength Load = 7.8(LL+I)	215
6.39	Summary of South-span Flexural Strength Cycle	215
6.40	South-span Shear Test - Maximum Response Values - Shear Strength Load = 8.0(LL+I)	219
6.41	South-span Shear Test - Change in Tendon Stress (ksi) Shear Strength Load = 8.0(LL+I)	224
6.42	Summary of South-Span Shear Strength Cycle	225
7.1	Service Load Deflections	230
7.2	Factor of Safety and Safety Margin	241
7.3	Insitu Dead Load Forces	243
7.4	Calculation of Effective Prestress Force	245
7.5	Cracking and Decompression Loads	250
7.6	Comparison Between Measured and Calculated Tendon Stress Response	266

CHAPTER ONE INTRODUCTION

1.1 Background

The development of post-tensioned concrete box girder bridges in the U.S. has progressed at a remarkable rate. The introduction of segmental technology, with its time-saving and economic advantages, has resulted in widespread use of segmental prestressed box girder construction for medium to moderately long span bridges. An important recent development in U.S. box girder bridge construction is the use of external post-tensioning tendons (tendons external to the concrete cross section), as opposed to traditional internal tendons which are contained in ducts within the webs or flanges. The United States' first externally post-tensioned concrete box girder structure, the Long Key bridge was completed in 1980. Long Key was one of four externally post-tensioned bridges linking the Florida Keys. Since 1980, a significant number of these bridges have been built and many more are in design and planning stages. At the present time, the Texas Department of Highways and Public Transportation is involved in a four-part project to construct several miles of elevated highway through San Antonio. Segmental precast box girders with external tendons were the lower cost alternates bid by the contractors and are being used throughout that project.

"Internal post-tensioning" refers to the practice of embedding tendon ducts, in straight or draped patterns as required by design, within the webs and flanges of the box girder section. This practice requires time-consuming placing and securing of the ducts inside the box girder reinforcing cage. The presence of multiple ducts often results in congestion and interference with the reinforcing cage. After the concrete is placed and cured, or after precast segments are assembled, the tendons are pulled through the embedded ducts and then stressed. After post-tensioning, the ducts are normally cement grouted. The grout bonds the tendon to the duct and the concrete along the full length of the tendon, and, if the ducts are completely filled with a dense grout, should improve corrosion protection for the tendon.

"External post-tensioning" implies that the tendons are removed from the webs and flanges of the concrete section, and are relocated inside the void of the box girder, or between the webs of non-box girders. The draped profile is maintained by passing the tendons through deviation devices cast monolithically with the webs and/or flanges at discrete points along the span. These "deviators" vary in shape and size, though the most common form is a small block or saddle located at the junction of the web and flange of the box girder section. Anchorages for the external tendons are usually placed in thick diaphragms situated over the piers, although blister anchorages are sometimes used at intermediate points within a span. Tendons typically overlap at diaphragm anchorages for continuity. The cut-away view of the Long Key bridge in Fig. 1.1 clearly illustrates the concept of external post-tensioning. The only positive connection of the external tendon

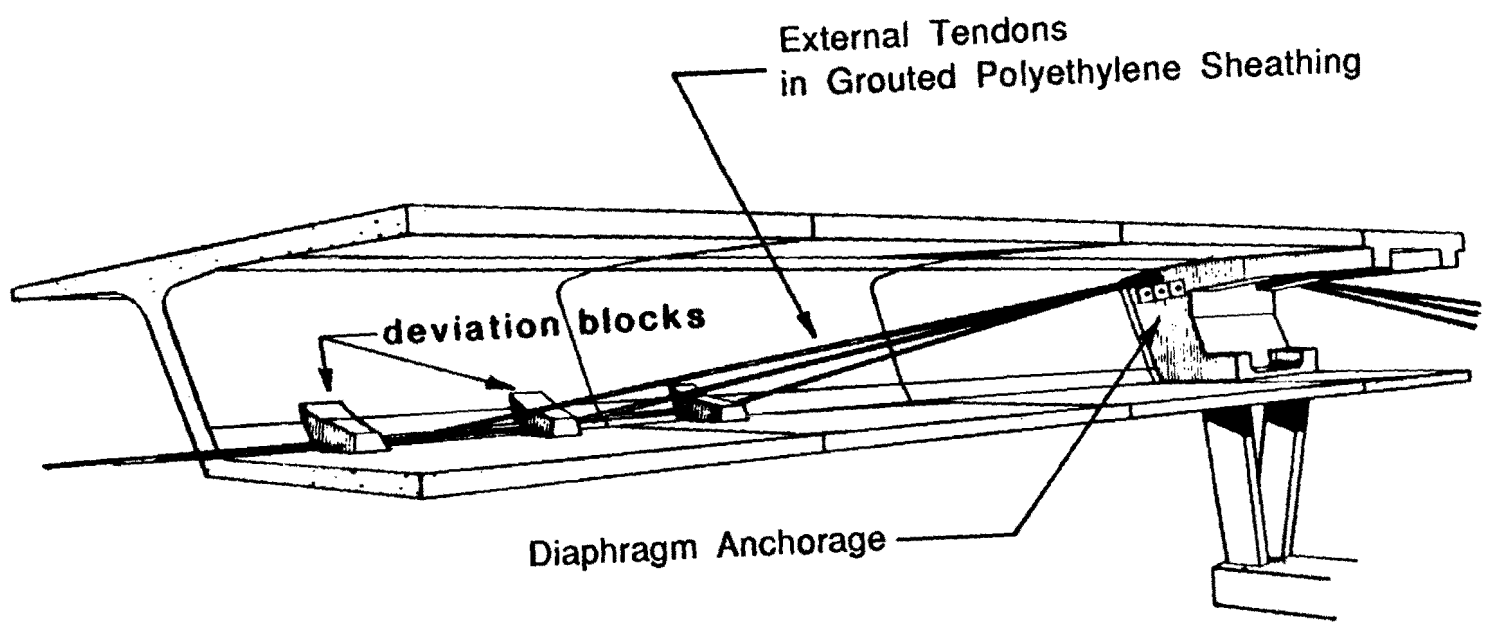


Fig. 1.1 External post-tensioning in Long Key Bridge

to the concrete section occurs at anchorages and deviators. Between attachment points, the exposed tendon is enclosed in sheathing, typically polyethylene tubing. The tendon is usually grouted along its entire length for protection against corrosion. External tendons are considered unbounded since the majority of the tendon is not bonded to the concrete section and the strains in the tendon are independent of the strains in the adjacent concrete sections.

The behavior of bridges constructed using external tendons and subjected to overload has not been thoroughly documented. Uncertainty also exists concerning the proper design criteria and methodology for deviation details. This study has been conducted in the Ferguson Laboratory to explore these topics. The first report in this series [1] summarizes in detail the history and some of the advantages and disadvantages of externally prestressed bridges [2]. The second report in this series [3] documents a comprehensive investigation of the deviator details [4]. This report summarizes the design, construction, and testing of a scale model of a three-span externally post-tensioned precast segmental box girder bridge with emphasis on determining the ductility of current details and evaluating the efficiency of epoxy joints. This report is based on the dissertation of the senior author [5].

1.1.1 Literature Review. Experimental research in the area of external post-tensioning for bridges is just beginning in this country, although research efforts in Europe, especially in France and Belgium, have been underway for some time. In fact, although external post-tensioning is a very recent development in the United States, the concept has been incorporated in a number of European structures over the last several decades. Report 365-1 [1] presented a detailed literature review to trace the development of the use of external tendons, citing both successes and problems that have been experienced from inception to the present. Such information provides insight to the current state of the art and points to uncertainties that could benefit from experimental investigation. Only a brief review of important and directly pertinent factors will be repeated in this report.

1.1.2 Historical Development and Construction Methods. Report 365-1 [1] provides details on a large number of externally prestressed bridges. It becomes clear on studying that report that the external tendon bridges have developed as an evolution of the construction process. Very early structures were often cast-in-situ with external tendons provided for ease of fabrication and to reduce web congestion. Relatively little consideration was given to the basic differences between bonded and unbonded tendons and in a number of cases corrosion protection of the tendon was a problem. With further development of cast-in-situ bridges the trend moved to internal, grouted, and hence fully bonded tendons, which could develop most of the tendon strength at ultimate. With the advent of precast box girder construction, the internal tendons caused severe congestion problems in the webs and external tendons were seen as a way of reducing such congestion. Similarly for shorter span bridges, the span-by-span process speeded construction and was very well suited to external tendons. Since service level conditions rather than ultimate conditions

tended to govern design, the relative inefficiency at ultimate of unbonded external tendons (which cannot develop very much higher prestress tendon strength than the initial prestress levels) was more acceptable.

The rapid developments in this area indicate that the ideal systems are still evolving. There has been an impressive use of external tendon concrete truss bridges fabricated from precast prestressed web elements. There is a growing use of mixed systems (blends of concrete and structural or tubular steel shapes) for long spans constructed in cantilever. A most logical development is mixed systems of internal and external tendons with some continuous bonded reinforcement crossing segment joints (either rebar cast in concrete topping or internal grouted tendons).

1.1.3 Rehabilitation of Existing Structures. In addition to new construction, there has been a wide use [1] of external tendons for rehabilitating existing structures. A wide number of examples have been reported in both bridges and in parking structures.

1.1.4 Advantages and Disadvantages of External Post-Tensioning. Report 365-1 [1] has reported in some detail the main pro's and con's for external prestressing of bridges. These can be briefly summarized as:

Advantages

- (1) Concrete cross-section is free of ducts.
 - (a) Thinner web sections can be used.
 - (b) There is no interference with passive reinforcement which reduces the time required to assemble the segment cage. The segment cages can be assembled without worry of interference with the post-tensioning ducts, thus leading to "assembly line" efficiency.
 - (c) There is appreciably reduced congestion in the concrete cross-section which leads to significantly better consolidation.
- (2) Accessibility of tendons is greatly improved. This eases the installation and grouting procedures and allows for possible tendon replacement.
- (3) The overall loss of prestress due to friction is reduced. Angular friction is approximately the same as with internal tendons, but the amount of horizontal angle change tends to be reduced. Wobble effects are almost non-existent.
- (4) Conventional fatigue problems are substantially eliminated because of the relatively low service load stress range in unbonded external tendons.
- (5) The corrosion protection in a continuous external tendon duct can be made more certain than in an internal duct. Tendons are protected by continuous sheathing instead of epoxied joints where tendons pass between segments.

- (6) Misalignment of internal tendon ducts are not a problem.
- (7) Very rapid construction is possible with the span-by-span erection system.

Disadvantages

- (1) Potential alignment problem of deviation hardware can lead to concentrated stress points in the external tendons and possibly decrease life due to fretting.
- (2) Vibrations of unrestrained lengths of external tendons have been noticed on several structures.
- (3) The external tendons are removed from the concrete section and extend through the inside of the girder void box. The range of possible eccentricities is limited since the tendons must be below the bottom of the top flange at the pier segment and above the top of the bottom flange near midspan. This reduces the efficiency of the post-tensioning in two ways. First, the smaller eccentricities require larger tendon forces to achieve the desired service load stresses in the concrete section. Second, the smaller effective depth, from the extreme compression fiber to the tendon center-line, requires increased tendon forces to achieve the desired ultimate strength.
- (4) The external tendons are attached to the concrete section only at a few discrete locations along the span. Since the tendon strains are not compatible with the adjacent concrete strains, as in bonded construction, large tendon elongations must occur to achieve the increased tendon strains required to develop the full tendon capacity for ultimate load conditions. This results in failure being governed by a mechanism behavior with large concentrated rotations occurring at critical cracks or joints along the span. The ultimate tendon stress is a function of the effective tendon stress and develops considerably less stress than a similar bonded tendon.
- (5) The shear behavior of the system is changed because of this mechanism behavior. At opening cracks or joints, the force is transferred across the joint by a local plastic truss mechanism. At regions between critical mechanism joints, the shear behavior may be expected to be similar to monolithic construction. However, the shear strength at opening joints is limited by the tensile capacity of the web reinforcement crossing the joint and is therefore expected to be less than that of monolithic construction.
- (6) As shown in Report 365-1 [1], the use of external tendons may result in reduced ductility since failure is governed by the rotation capacity at the joint. In addition the tendon stress is highly dependent on the end anchorage devices and zones. There could be possible catastrophic results if the tendons or the diffusion elements are damaged.

- (7) Post-tensioning forces are applied to the structure at discrete locations inducing local diffusion forces to the structure. Failure of any of the diffusion mechanisms could have serious consequences. Design of the deviators is covered in Report 365-2 [3] and throughout this study is assumed as fully adequate.

1.2 Flexural Behavior of Girders with External Tendons

As outlined below, external tendon girders have two distinct ranges of behavior, before and after cracking. There is linear behavior until cracking or joint opening occurs. After joint opening, the structure behaves as a mechanism with hinges forming at critical joints. The flexural strength occurs when the rotation capacity is reached at the segment joints.

1.2.1 Before Cracking.

1.2.1.1 Comparison between Bonded and Unbonded Systems. In a fully bonded system where the tendon is completely encased in the concrete sections and effectively grouted, the tendon strains are assumed to be the same as the concrete section at the level of the tendon. In an unbonded system (as typical of external tendons), the tendon strains are not compatible with the adjacent concrete strains. Assuming no friction with the surrounding duct, the tendon strain is constant for the full length between the anchorages. The change in tendon strain due to applied loads is calculated from the total change in length of the tendon over its entire length. This is equal to the average accumulation of concrete strains at the level of the tendon between the ends of the tendon. This leads to relatively low increases in tendon stress due to live load, even under ultimate test conditions.

1.2.2 After Cracking. In an externally prestressed continuous girder, when the section cracks or a dry joint opens, the girder begins to "hinge" at that location. This locally increases the curvatures at that location causing increased tendon stresses.

1.2.2.1 Ideal Rigid Body Mechanism. The behavior of a multiple span external tendon bridge can be simply modeled as a series of rigid members connected by hinges at the extreme compression fiber and containing draped or straight tendons. One can conduct a plastic mechanism analysis on the structure to determine the critical mechanism joint locations. While one generally thinks of mechanism analysis in terms of continuous structures, in this hybrid system it is very interesting to examine first the rigid body mechanism for a simple span structure with straight tendons. The general layout of the structure is shown in Fig. 1.2 and the load-deformation response and the tendon stress response are shown in Figs. 1.3 and 1.4, respectively. In developing these figures, load is applied to the mechanism and moment is plotted at the hinge location with respect to deflection. Because

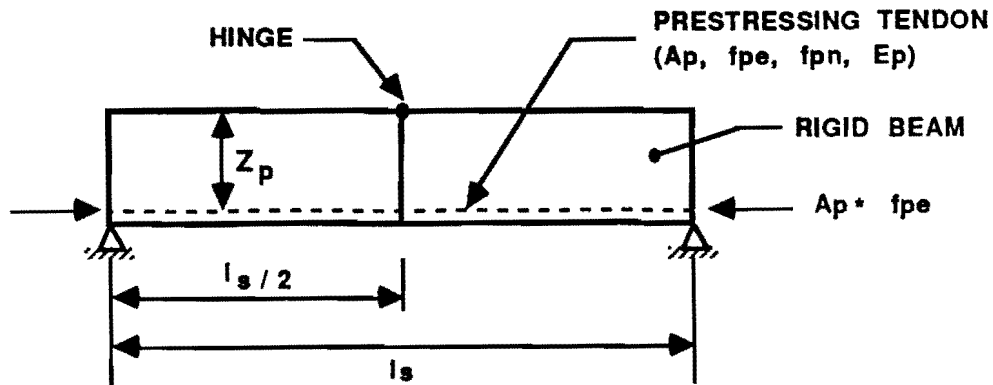


Fig. 1.2 General Layout of Simple-Span Structure with Straight Tendons

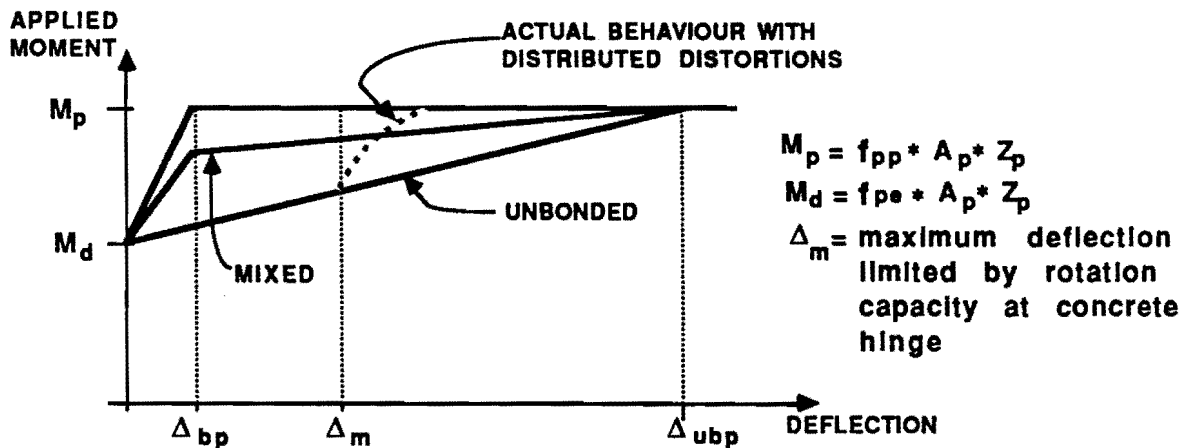


Fig. 1.3 Applied Moment vs. Deflection

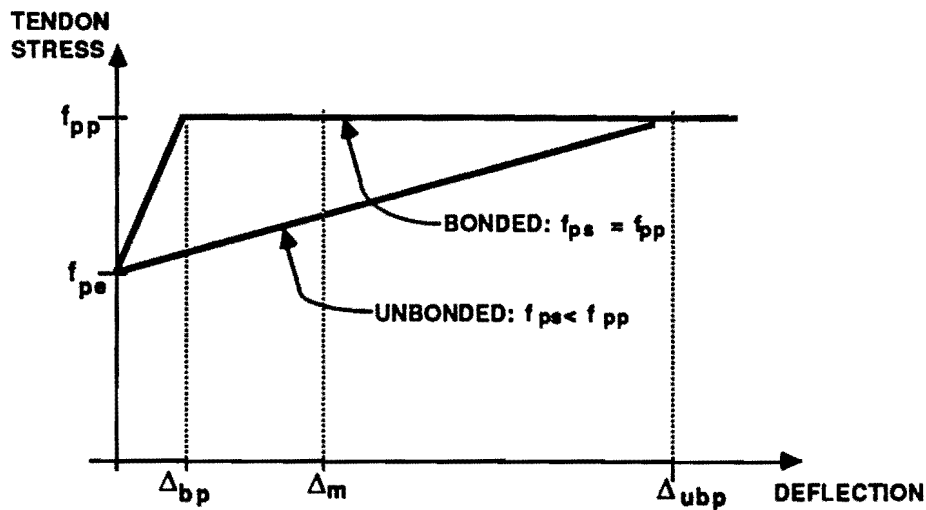
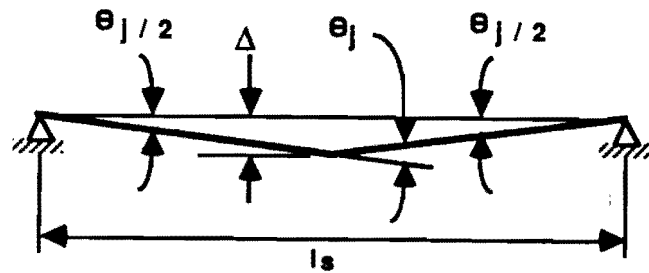


Fig. 1.4 Tendon Stress vs. Deflection

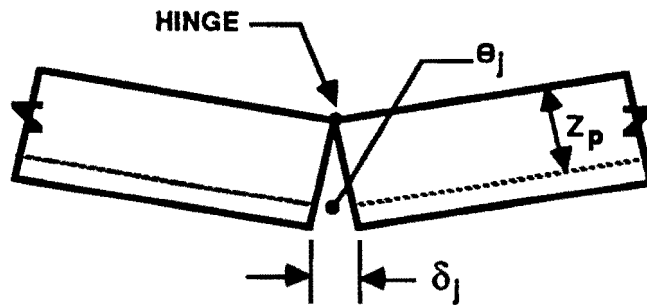
the structure consists of rigid bodies, no deflection occurs until the moment exceeds the initial clamping moment due to the prestressing. Similarly, no elongations occur in the tendon until the hinge or joint starts to open. When the joint begins to open there is a geometric relationship between the midspan deflection and the elongation of the tendon. With rigid bodies, the tendon elongations occur entirely at the opening joint. The magnitude of the elongation is calculated as shown in Fig. 1.5.



MECHANISM GEOMETRY

$$\frac{\theta_j}{2} = \frac{\Delta}{l_s/2}$$

$$\therefore \theta_j = \frac{4\Delta}{l_s}$$



JOINT GEOMETRY

$$\delta_j = \theta_j \cdot z_p$$

$$\delta_j = \frac{4\Delta \cdot z_p}{l_s}$$

Fig. 1.5 Calculation of Tendon Elongation

The corresponding tendon strains can be calculated from the calculated tendon elongation at the opening joint and the characteristic "free" length of tendon. Two cases must be considered:

(a) With bonded tendons:

The increase in tendon force occurs linearly over a development length, $1d$. The total elongation can therefore be calculated as the area under the tendon-force curve as shown in Fig. 1.6. From moment equilibrium the change in tendon force is equal to the moment above the decompression moment divided by the distance, Z_p , between the resultant compressive force and the center of the tendon. Therefore equating the two expressions for elongation yields an expression relating applied moment and midspan deflection for a bonded tendon girder.

(b) With unbonded tendons:

In a similar manner an expression can be developed for unbonded tendons. In this case the strains are calculated from the elongations that occur at the opening joint and averaged over the free length of the tendon-segment, l_i . The resultant expression in terms of the tendon-segment length, l_i , and the span length, l_s , is shown in Fig. 1.7. In this case with anchorages at the end of the span, $l_i=l_s$, which leads to a very simplified equation.

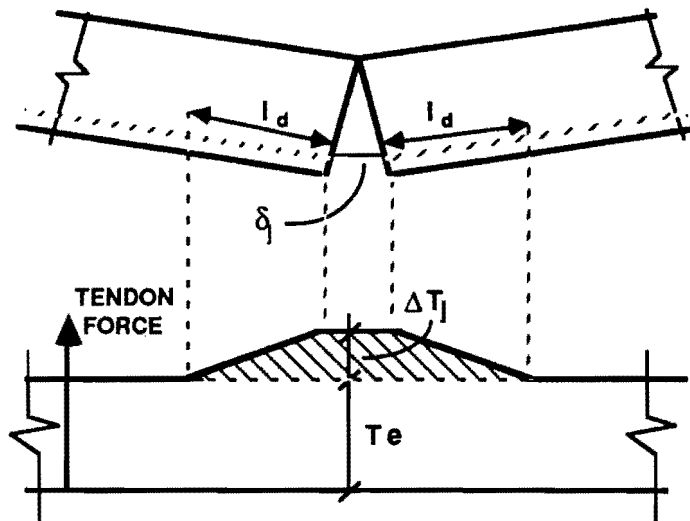
Assuming the tendons behave in an elastic-plastic manner, the maximum plastic-moment capacity is calculated as:

$$M_u = A_{ps} * f_{pp} * Z_p$$

The deflections corresponding to plastification of the tendons can therefore be calculated and are shown on Fig. 1.3. Note that the deflection required to plastify the unbonded tendons is much greater than the deflection required to plastify the bonded tendons. With mixed systems, in which bonded and unbonded tendons are used, care must be taken to ensure that the bonded tendons do not rupture before the unbonded tendons plastify.

The simple model outlined describes the upper limit to behavior of prestressed systems and illustrates important considerations. A similar articulated rigid member system can be developed for any arrangement of prestressed system. Slab systems as well as draped externally prestressed systems can all be analyzed using this method. As perfect plastic behavior is assumed, this method represents an upper bound to the true strength.

1.2.2.2 Plastic Hinges in Concrete Structures. In order to extrapolate this simple plastic model to a real structure, the plastic hinge behavior must be included in the formulation. Instead of allowing unlimited rotation at an ideal hinge, the concentrated



l_d = development length of bonded tendon

$$\Delta T_j = \frac{(M - M_d)}{Z_p}$$

$$T_e = A_p * f_{pe}$$

With Rigid Members: δ_j = Tendon Elongation

$$\therefore \delta_j = \frac{\text{Shaded Area above } T_e}{A_p E_p}$$

$$\delta_j = \frac{(\Delta T_j) * l_d}{A_p E_p} \quad (\text{assumes } l_d \gg \delta_j)$$

From Mechanism and Joint Geometries

$$\delta_j = \frac{4 * \Delta * Z_p}{l_s} = \frac{(\Delta T_j) * l_d}{A_p E_p}$$

$$\therefore \Delta = \frac{l_d l_s}{4 A_p E_p Z_p^2} (M - M_d)$$

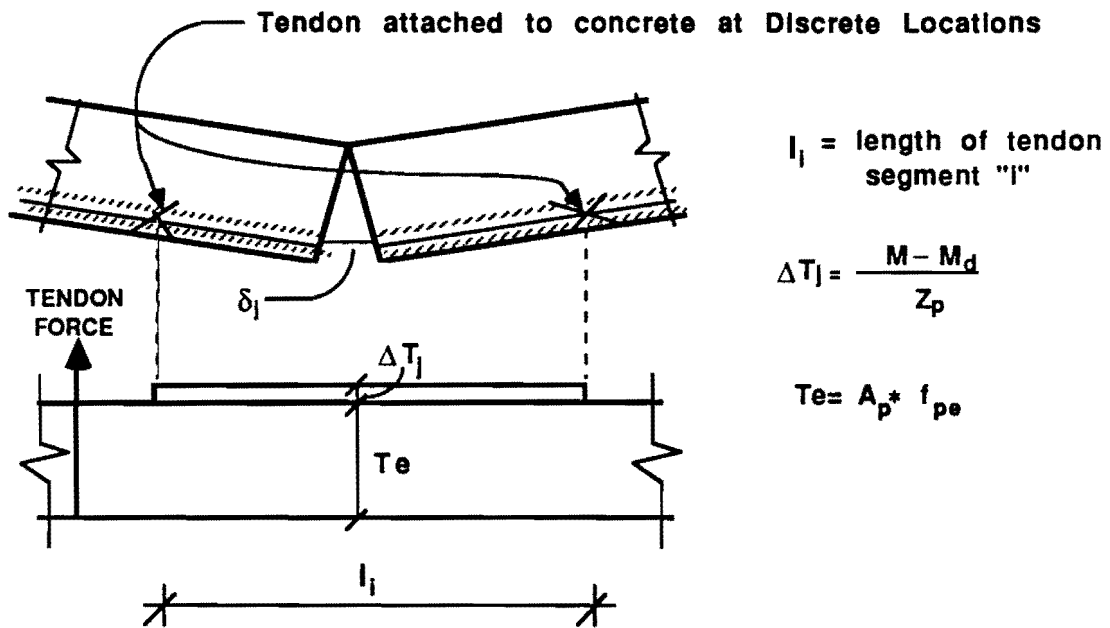
Deflection Causing Plastification of Bonded Tendons, Δ_{bp}

$$M = M_p = f_{pp} * A_p * Z_p$$

$$M_d = f_{pe} * A_p * Z_p$$

$$\therefore \Delta_{bp} = \frac{l_d l_s}{4 A_p E_p Z_p^2} (f_{pp} - f_{pe})$$

Fig. 1.6 Moment-Deflection Response for Bonded Tendons



With Rigid Members: $\delta_l =$ Tendon Elongation

$$\delta_l = \frac{\Delta T_j + l_i}{A_p E_p} \quad (\text{assumes } l_i \gg \delta_l)$$

From Mechanism and Joint Geometries

$$\Delta = \frac{l_i l_s}{4 A_p E_p Z_p^2} (M - M_d)$$

Deflection Causing Plastification of Unbonded Tendons, Δ_{ubp}

$$\Delta_{ubp} = \frac{l_i l_s}{4 A_p E_p Z_p^2} (f_{pp} - f_{pe})$$

Fig. 1.7 Moment-Deflection Response for Unbonded Tendons

rotations must occur in the concrete adjacent to the critical opening joints. The plastic hinge occurs over some finite length and the maximum rotation is limited by the curvature capacity of the reinforced segments. Several recommendations have been made for calculating the rotation capacity and the resultant tendon elongations at plastic hinges. Various methods are described below.

1.2.2.2.1 Rotation Capacity and Tendon Elongations. Virlogeux [6] assumed that the concentrated rotations were distributed over a plastic hinge length equal to $2*Z_s$, (Z_s on either side of the critical crack or joint) where Z_s is the distance from the resultant concrete compressive force to the center of the passive reinforcement in the tension side of the segment. This corresponds to a force diffusion angle of 45 degrees.

The curvature, ϕ_h , was assumed to be constant over the hinge length and was determined by limiting strains in the concrete compression zone and the passive segment reinforcement. The concrete compressive strains are ultimately limited by the crushing strain of the concrete, i.e., ϵ_{cu} or conservatively for design by ϵ_{cd} (recommended to be 0.002 by Virlogeux). The tensile strain in the segment is limited by the maximum acceptable tensile strain in the passive segment reinforcement, ϵ_{sd} and possibly depends on the anchorage characteristics of the tension-side reinforcement of the segment. Virlogeux suggested using a value of 0.010 for design.

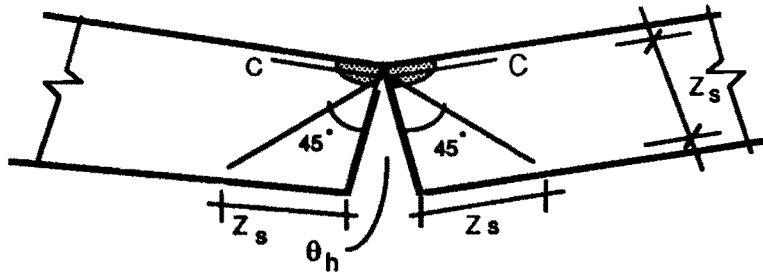
If rotation is assumed to be centered about the resultant compressive force, and the curvature is constant over the hinge region then the tendon elongation in the concrete plastic hinge, Δ_h , (shown in Figure 1.8) can be written in terms of the maximum curvature, ϕ_m , the distance from the compressive force resultant to the prestressing tendon, Z_p , and the distance to the passive segment reinforcement, Z_s . $Z_p(x)$ is Z_p as a function of x and will be approximately constant over the short hinge length region. Therefore for constant eccentricity, the tendon elongation in the hinge region can be written as:

$$\Delta_h = \phi_m * Z_p * Z_s$$

In order to calculate the change in tendon-stress that occurs at the hinge, the tendon hinge elongation must be divided by the free length of the tendon-segment under consideration. With bonded tendons the increase in tendon stress occurs over a free length equal to the development length, l_d . The maximum stress is also limited by the capacity of the tendon. Therefore the change in bonded tendon stress caused by the elongations at a plastic hinge is:

Bonded Tendons

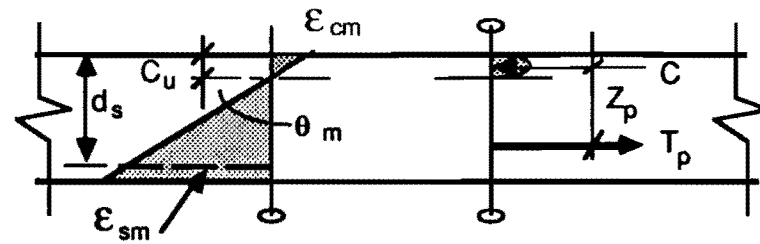
$$\Delta_{pb} = \frac{\Delta_h}{l_d} < f_{pp} - f_{pe}$$



Opening Joint

Z_s = distance from resultant compressive force to the segment reinforcement on the tension side

Concrete Hinge Length = $2 * Z_s$



Strains

Forces

ϵ_{cm} = maximum concrete strain = .002 for design (Virlogeux)

ϵ_{sm} = Maximum strain in segment reinforcement = .010 for design (Virlogeux)

$\phi_m = \frac{\epsilon_{cm} + \epsilon_{sm}}{d_s}$ = maximum allowable currative

Assume Curvature is Constant over Hinge Length

δ_h = Tendon Elongation occuring in Concrete Hinge region

$$\delta_h = \int_{-Z_s}^{Z_s} \left[\phi_m * Z_p(x) * \left(\frac{x}{Z_s} \right) \right] dx$$

with Constant eccentricity: $Z_p(x) = \text{Constant} = Z_p$

$$\delta_h = \frac{2\phi_m Z_p}{Z_s} \int_0^{Z_s} x dx \Rightarrow \underline{\delta_h = \phi_m Z_p Z_s}$$

Fig. 1.8 Tendon Elongation in the Plastic Hinge Region

With unbonded tendons the increase in tendon stress occurs over the entire free length of the tendon-segment. The tendon-segment length, l_i , can range from the length between the anchorages for friction free systems to the length between deviators for slip free systems. Therefore the change in unbonded tendon stress that occurs because of hinging is calculated as:

Unbonded Tendons

$$\Delta f_{pu} = \frac{\Delta h}{l_i}$$

The rotation capacity at a hinge limits the plastic behavior of the system. Using the simple rigid-body plastic-mechanism described above the following limiting midspan deflection results.

$$\Theta = \frac{4 * \Delta}{l_s}$$

$$\Theta_m = \frac{\delta_h}{Z_p = \Phi_m * Z_s}$$

Therefore:

$$\Delta_m = \frac{(1}{4}) * (\Phi_m * Z_s * l_s)$$

This maximum deflection is shown schematically in the applied - moment / deflection curve for the rigid body mechanism in Fig. 1.3. This illustrates how the rotation capacity at a plastic hinge limits the maximum attainable strength. The true situation is probably even worse than this since bonded tendons will allow more distributed distortions and possibly higher total rotation. The true gradation of strengths may be more closely represented by the dotted line shown in Fig. 1.3.

Ritz [7] used a similar mechanism analysis method but made a slightly different assumption for calculating the ultimate rotation capacity at a hinge. Ritz pointed out the importance of considering the deflection-to-span ratio limits in developing the dependable tendon stress that can be mobilized in unbonded tendons. He has indicated that the values for attainable tendon stress used in the ACI Building Code are probably unrealistically high for longer span members found in bridges.

One of the major unknowns in this area is the effect of friction between tendon and duct, particularly at the deviators. The general mechanism analysis assumes a frictionless connection and a tendon free to slip as necessary. A major interest in the experimental

program is the amount of slip that might actually occur in the model between tendon and deviator during the various load cycles. Instrumentation was provided to verify tendon strains and hence forces along the span.

1.3 Previous Studies on Externally Post-Tensioned Girders

1.3.1 Experimental

1.3.1.1 **St. Remy Laboratory.** Under the combined auspices of the French organizations SETRA (Service d'Etude Technique des Routes et Autoroutes) and CEBTP (Centre Experimentale de Recherche et D'Etudes du Bâtiment et des Travaux Publics), engineers at the laboratory at Saint-Rémy conducted tests of four externally post-tensioned segmental box girders. The primary objective of the study was to examine the ultimate behavior of girders with external tendons in order to furnish or justify the assumed criteria used for ultimate strength calculations [6].

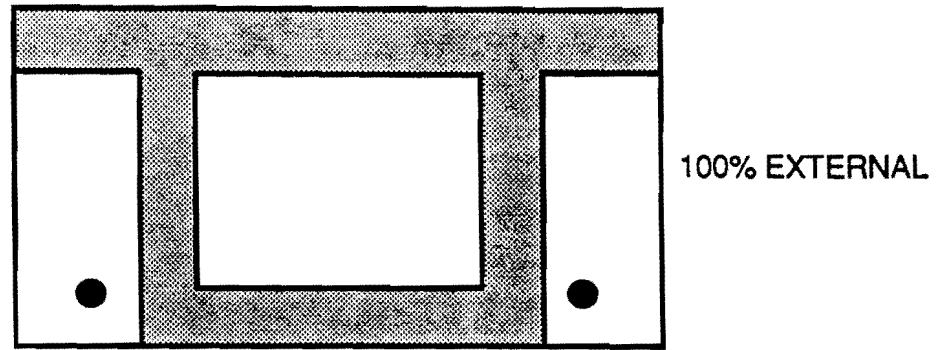
The test girders were match cast and erected with dry joints. The reduced-scale cross section used for all four tests was a simple, compact prismatic box girder (Fig. 1.9). The girders differed in tendon profile and type of tendon protection (grouted, hot wax injected). The fourth test girder also included some internal tendons. The behavior of the deviators, and their effect on overall behavior, was not a parameter in this study.

The simply supported girders were loaded symmetrically with point loads at outer quarter points. All girders experienced the same failure mode, independent of tendon profile or protection. First, the central joints opened and continued to open up to the level of the bottom surface of the top flange. At the same time, diagonal cracks propagated upward from the shear keys in the compressed region. The stress in the tendons did not rise significantly until the applied load was within approximately 10 to 15 top flange in the presence of concentrated strains.

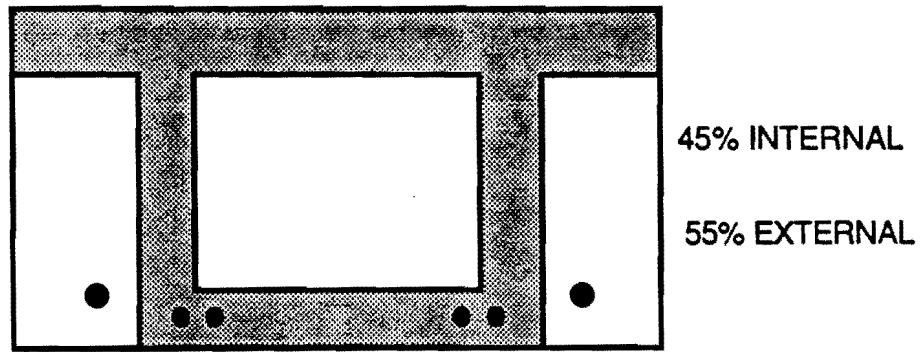
The experimental results agreed reasonably well with calculations performed according to methods presented previously by M. Virlogeux [6,8].

Fig. 1.10a shows a theoretical moment-deflection curve for a simple beam model, similar to the St. Remy tests, analyzed assuming monolithic construction with internal bonded tendons. It also shows test results for the same member with a mixture of internal bonded tendons and external bonded tendons, as well as test results with external bonded tendons alone. This comparison illustrates the loss of tendon strength development and possible reduction in ductility for the external tendon case.

1.3.1.2 **Construction Technology Laboratory.** At the request of Figg and Muller Engineers, Inc., Construction Technology Laboratories conducted tests of three simply supported segmental girders with differing post-tensioning systems. One girder had

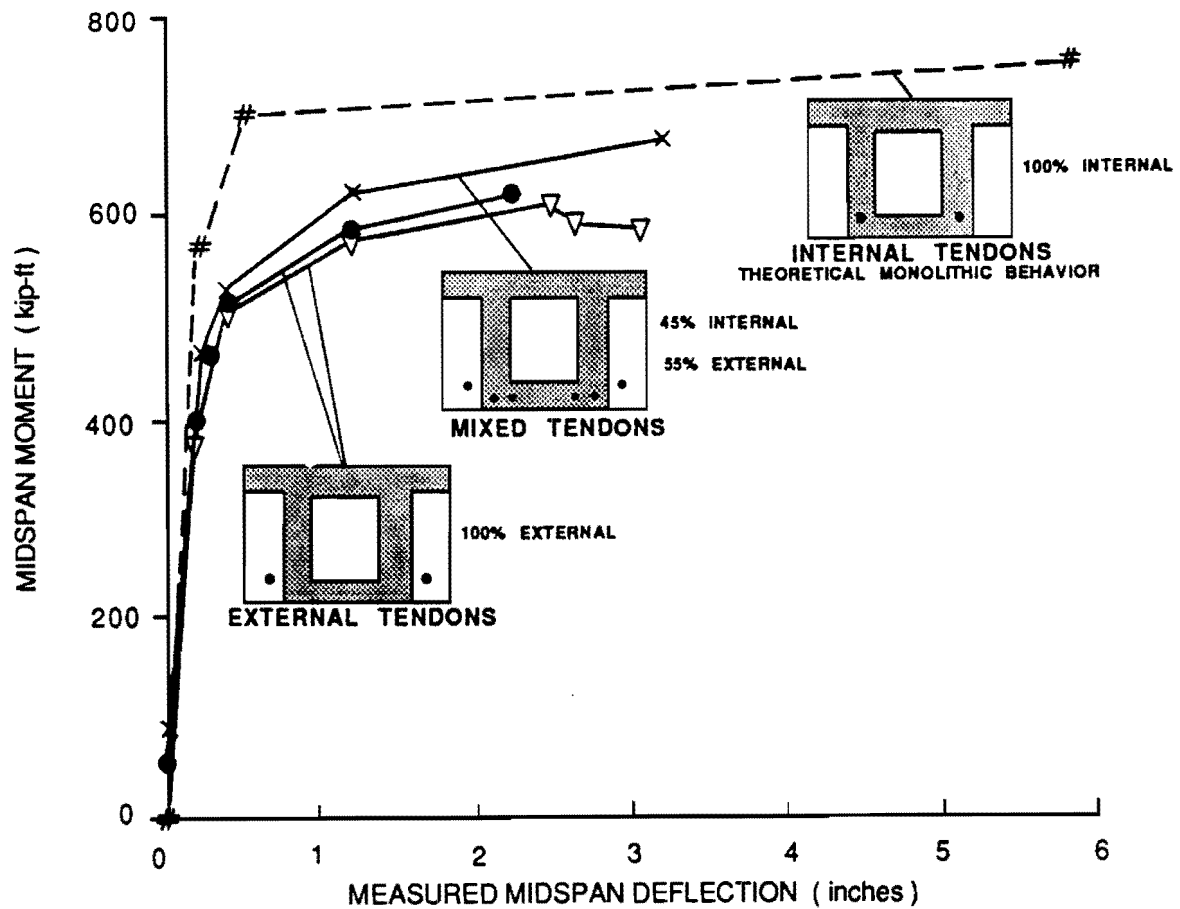


EXTERNAL TENDONS



MIXED TENDONS

Fig. 1.9 Saint-Remy Test Girders



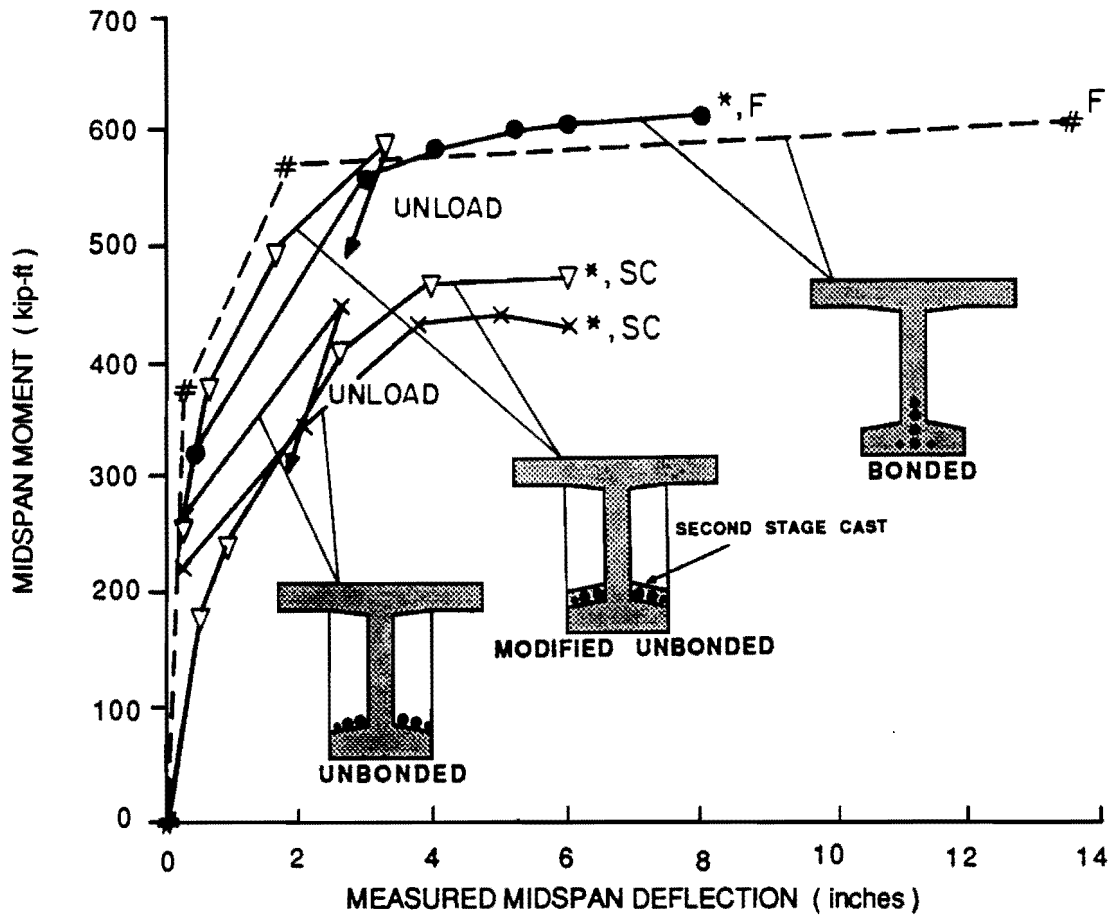
Notes:

Midspan Moment = dead load moment + applied load moment

Measured midspan deflection = deflection due to applied load only

- #-- Monolithic, bonded internal tendons (theoretical)
- Segmental, external tendons, dry joints, cement grouted ducts
- ∇— Segmental, external tendons, dry joints, grease-injected ducts
- x— Segmental, mixed tendons, dry joints, cement grouted ducts

Fig. 1.10(a) Moment-Deflection Behavior



Notes:

Midspan Moment = dead load moment + applied load moment
 Measured midspan deflection = deflection due to applied load only

- # -- Monolithic with bonded tendons (theoretical)
- Segmental with bonded tendons and dry joints
- ×— Segmental with unbonded tendons and dry joints
- ▽— Segmental with modified unbonded tendons and dry joints

Failure modes: *F* = Flexural failure

SC = Shear compression failure

* Some anchorages burned before reloading.

Fig. 1.10(b) Moment-Deflection Behavior

conventional bonded internal tendons, a second had unbonded external tendons, and a third included external tendons enclosed with a secondary cast, making them modified unbonded. The primary objectives were to verify the theoretical analyses and to compare the behavior of the three types of post-tensioning system [9].

Figure 1.11 shows the I-shaped cross section used for each girder. Deviator behavior was not of interest in this test series, so deviators were conservatively designed. The match-cast segments were assembled with dry joints and the ducts containing all tendons were cement-grouted.

The girders were statically loaded in two cycles. The first cycle loading increased incrementally until the girder reached a midspan deflection of about 3 inches. The girders were subsequently unloaded and, in an attempt to simulate an anchorage loss in the case of an earthquake, the wedges for some of the strands were burned and removed. The girders were then reloaded incrementally to failure.

The failure mode for the bonded tendon girder was flexural; concrete in the compression zone crushed simultaneously with the fracturing of strands in the tensile zone. The unbonded and modified bonded tendon girders both experienced a shear-compression failure in the top flange. Joints opened and shear keys progressively broke, concentrating strain in the top flange.

When the CTL test results are compared with a theoretical moment-deflection curve for a monolithic, fully bonded girder as shown in Fig. 1.10b, the reduced capacity of unbonded systems in both strength and deformation capacity is evident. Because of the test procedures used in these tests, it is difficult to determine the insitu condition of the structure. Having the anchors burnt at their ends, the tendons tend to unstress in the end region. Depending on whether the tendon slips in the anchorage or deviator, the effective tendon area in the midspan region is unknown.

Because of the test procedures used in these tests, it is difficult to determine the insitu condition of the structure. Having the anchors burnt at their end, the tendons tend to unstress in the end region. Depending on whether the tendon slips in the anchorage or deviator, the effective tendon area in the midspan region is unknown.

1.3.2 Analytical. Several programs have been developed to analyze externally post-tensioned box girders. Most of these programs are based on finite element formations with generalized assumptions regarding the behavior near opening joints. Working in parallel with this project at The University of Texas at Austin, El Habir [10] coded and tested a program based on fibrous strip beam elements, joint elements which differentiate between dry joint and epoxy joints, and external tendon elements attached to the concrete beam by rigid links. The method needs improvement to allow for slip at deviators and a more convenient way to tackle construction process constraints.

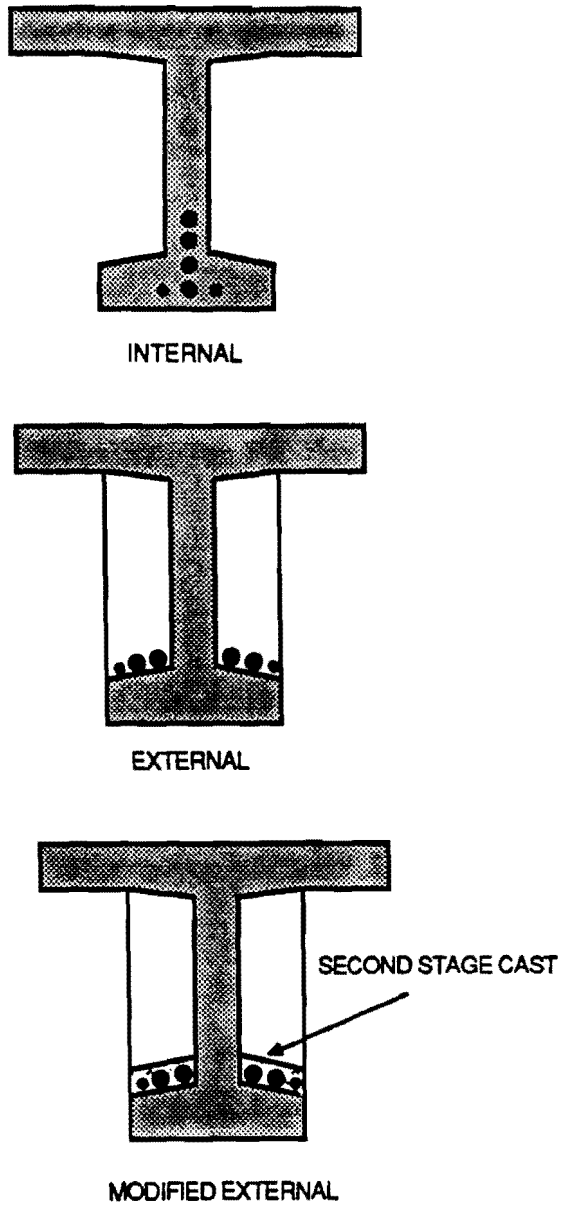


Fig. 1.11 PCA Test Girders

Virlogeux [6] has shown promising comparisons with French tests using an analytical model developed in France by SETRA. At the recent International Symposium on Externally Post-Tensioned Bridges held in Houston, Texas in October 1988, Muller and Gauthier [11] reported on a computer program DEFLECT which showed very good agreement in modelling the CEBTP-SETRA and CTL test data.

1.4 Object and Scope of Study

The objectives of this portion of the study for the Texas SDHPT, which is currently using this type of construction in several miles of overhead freeway in San Antonio, were to (1) determine the level of strength and ductility that may be expected for precast segmental bridges with external tendons, current tendon anchorages and joint details, and alternate joint details; (2) recommend changes in joint details and tendon patterns where changes will improve the behavior of the system without significantly reducing construction efficiency; (3) develop suitable analysis methods; and (4) recommend methods for design and load rating criteria.

This phase of the study was restricted to the behavior of multi-span segmental box girder bridges with external tendons and focused on the results of the major model test.

Another study, now currently underway at the Ferguson Laboratory, will continue testing of this same model but will improve tendon bonding by physically connecting the tendons to each segment. This should improve the ability to increase tendon stresses under overload. In addition, the current tests will study the effect of mixed external and internal tendons. Both of these subjects are outside the scope of the study reported herein.

One of the significant variables in the model test was the presence or absence of epoxy joints. One span of the model was constructed with dry joints, while the other two spans had epoxy joints.

1.5 Summary

The body of this report is organized as follows:

Chapter 2 contains a summary of the design and construction of the bridge model. Chapter 3 gives technical details of the Instrumentation and Data Acquisition. Chapter 4 presents the observations made on the structure during the construction process, and Chapter 5 furnishes an analysis and interpretation of the erection stresses. Chapter 6 outlines and discusses the service level, factored design level, and ultimate load tests. Chapter 7 evaluates the major findings of the study based on all test results, while Chapter 8 summarizes the conclusions and recommendations developed from the model test.

This page replaces an intentionally blank page in the original.

-- CTR Library Digitization Team

CHAPTER 2 DESIGN AND CONSTRUCTION OF BRIDGE MODEL

2.1 Development of Bridge Model

This chapter summarizes the design and construction of the scale model bridge. Model similitude requirements are determined and dimensionless behavioral parameters are formed. Design criteria are scaled from the prototype structure. Material, structural components, and erection procedures and details of the model are described in detail.

2.1.1 Dimensional Analysis. The purpose for building a scale model is to conveniently simulate the behavior of a prototype structure. To construct a true structural model, from which behavioral observations can be directly extrapolated to the prototype structure, geometric, material, and loading conditions must be properly scaled. A detailed dimensionless analysis was performed and is documented in Ref. 5. Considerable insight, as well as specific model requirements, are gained through examination of the dimensional analysis parameters. A few of the more important results are included herein.

For correct deflection modelling, the dimensions and loading of the model structure must be geometrically similar to prototype construction. There is an inherent problem in reduced-scale prestressed concrete models. Section forces, and therefore tendon forces, vary with the square of the scale factor. However, the tendons are anchored in the pier segments which have a volume that decreases by the cube of the scale factor. This means that a proportionally larger amount of force must be transferred per unit volume of pier segment. This causes severe congestion in the anchorage regions of reduced scale models of post-tensioned systems. The model must be constructed with materials having similar properties as those used in the prototype structure. The stress-strain relationships for the concrete, prestressing strand, and mild steel reinforcement must be similar to those used in prototype construction.

To achieve similar self-weight stresses in the model and in the prototype, the model must be constructed with a material having a density that scales inversely with the scale factor. Since it is not practical to construct the model with an increased density and still maintain material similitude requirements, dead load compensating weights must be suspended from the structure. To achieve the same stresses in the model and in the prototype, a uniformly distributed load must be scaled linearly with the scale factor, and a concentrated load must be scaled by the square of the scale factor.

2.1.2 Scale Selection. The selection of scale for a particular model involves the consideration of many interrelated factors. The availability of materials and model components, such as small-scale reinforcing bars, will often dictate a range of minimum and maximum scales. If conventional post-tensioning strands and anchorages are to be

used, then minimum strand diameters and stressing hardware may dictate a minimum scale. Budget limitations and the availability of test space may dictate a maximum scale.

Externally post-tensioned box-girder bridges are usually constructed continuous over several spans. The Phase 1a Development of the San Antonio Y project consists of four- to eight-span continuous box girders ranging in length between 390 and 720 feet. A multi-span model was therefore chosen, and it was decided that a three-span structure would be appropriate with the interior span providing a realistic amount of restraint for the end spans. The continuity of the structure over the interior supports allows for investigation of negative- moment flexure and shear at an opening joint. The two similar end spans were planned to be identical except that one would have dry joints while the other would have epoxy joints to allow for direct comparison of the effects of epoxy joints on service and ultimate load behavior.

The detailed layout of precast segments was determined using the San Antonio Y structure as a guide. A large portion of the Phase 1 development consists of 100 ft spans with ten 9' segments per span, 9' pier segments, and 6-inch cast-in-place closure strips between the pier segments and the span segments. A 1/4 scale was eventually chosen to allow the use of multiple strands and conventional anchorage hardware for the tendons and of locally available ready-mixed concrete. The model structure has essentially the same segment layout as the prototype structure, except proportionately larger closure strips were used in the model to ensure proper concrete consolidation.

2.1.3 Design Criteria. For the model structure to be a good representative of prototype construction, the design must follow the same general procedures and criteria. Cross-sectional requirements, loading and load combinations, and design allowable stress limits used in the model were appropriately scaled from prototype design requirements.

Podolny and Muller [12] suggest the use of an "efficiency factor" for comparing similar cross-sections. This factor, E , uses the radius of gyration, r^2 , and the distances from the neutral axis to the top and bottom fibers (y_t and y_b).

$$E = \frac{r^2}{y_t y_b} = \frac{I}{A y_t y_b}$$

An efficiency factor of approximately 60% is considered optimum for box-girder construction.

Several types of cross-sections were considered for use in the model. A box-section, shown in Fig. 2.1a, is geometrically similar to prototype construction and would provide the best representation. Difficulties in fabrication and instrumentation of the external tendons within the reduced-scale box forced the use of another type section. An open box, with torsional bracing in the top flange, shown in Fig. 2.1b, was briefly considered

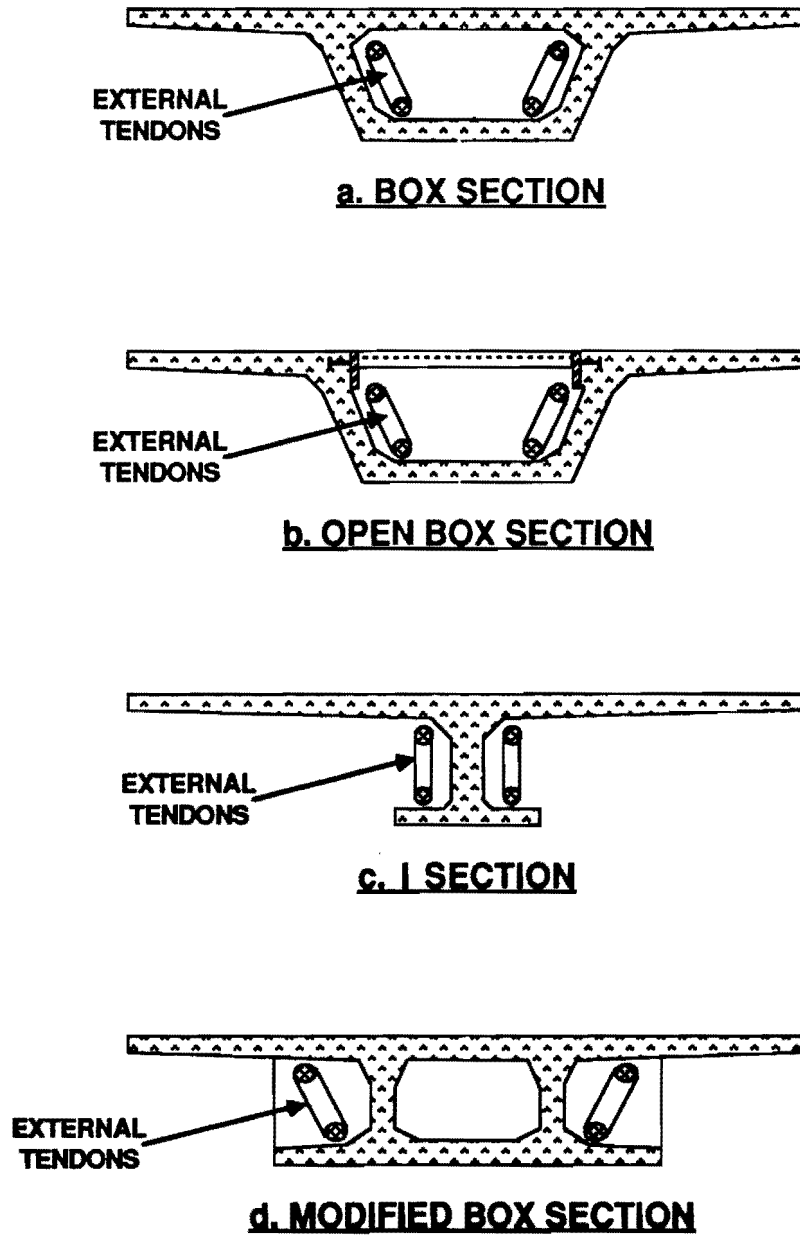


Fig. 2.1 Possible Model Cross-Sections

because of its true tendon profile and open access for fabrication and instrumentation. This section was considered to be too different from actual construction to be a representative model. An "I" section (Fig. 2.1c) was also considered for its ease of construction but was also regarded as not representative of box-girder bridge construction. Finally a modified box-section (shown in Fig. 2.1d) was developed. The webs were shifted towards the center to provide space for the draped external tendons on the outside of the box. This section maintains a good representation of conventional box-girders as well as provides access to the primary external tendons. Differences in tendon deviation reinforcement and torsional response of the cross-section did not affect the overall behavior of the system.

To obtain the same dead load stresses in the model as in the prototype structure, the model should have been constructed with a material having four times the density of the prototype structure. Because this was not practical, dead load compensating weights, equalling three times the structural weight, were suspended from the model structure.

Model Dead Load Calculations:

$$\text{Model Section Weight} = 433 \text{ in}^2 \times 0.150 \text{ kcf} \times 1/144 = 0.451 \text{ klf}$$

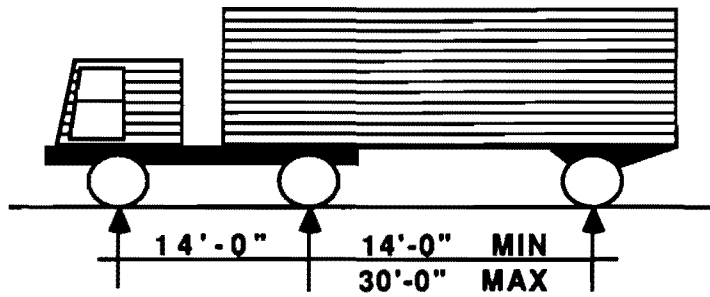
$$\text{Dead Load Compensating Weights} = 3 \times 0.451 \text{ klf} = 1.353 \text{ klf}$$

$$\text{Total Dead Load} = 0.451 \text{ klf} + 1.353 \text{ klf} = 1.804 \text{ klf}$$

The model structure was designed to carry its own dead weight plus superimposed live loads in conformance with the AASHTO Bridge Design Specification [13]. Since the primary objective of this research was to investigate in-plane flexural and shear behavior, and because the structure was constructed in a protected and controlled environment, only vertical traffic loads were considered during design. A_k HS-20 Truck load, shown in Fig. 2.2, was adopted as the traffic loading for design of the model structure. The AASHTO specification requires design to be based on the maximum effect caused by either a uniformly distributed lane load or a set of concentrated truck axle loads. For a prototype structure with 100 foot spans the concentrated truck axle loads govern the design. Similarly, the impact factor was calculated using a prototype span length of 100 feet.

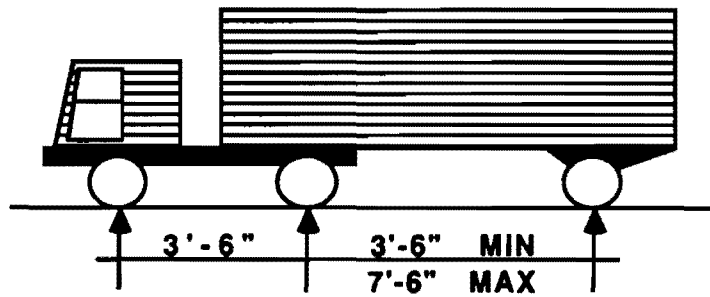
$$I = \frac{50}{(L + 125)} = \frac{50}{(100 + 125)} = 0.22$$

The width of the top flange of the model structure was dictated by the 4' spacing of the bolt clusters in the test floor. A 7' top flange width was selected to fit within a load frame tied down to the test floor at 8'. With a scale of 1/4, the corresponding prototype width would be 28 feet, and two lanes of traffic would be possible. Therefore, the loading on the model structure was appropriately scaled from two lanes of AASHTO HS-20 truck load with impact.



HS20 TRUCK	=	8 KIPS	32 KIPS	32 KIPS
IMPACT (22%)	=	1.8 KIPS	7.0 KIPS	7.0 KIPS
HS20 W/ IMPACT	=	9.8 KIPS	39 KIPS	39 KIPS
2 LANES OF HS20 W/ IMPACT	=	20 KIPS	78 KIPS	78 KIPS

a. AASHTO HS20 Truck Load



1/4 SCALE

HS20 TRUCK	=	0.5 KIPS	2.0 KIPS	2.0 KIPS
IMPACT (22%)	=	0.11 KIPS	0.44 KIPS	0.44 KIPS
HS20 W/ IMPACT	=	0.61 KIPS	2.4 KIPS	2.4 KIPS
2 LANES OF HS20 W/ IMPACT	=	1.2 KIPS	4.9 KIPS	4.9 KIPS

b. Reduced Scale HS20 Truck Load

Fig. 2.2 1/4-Scale Truck Load

The structure was built in a sequential "Span-by-Span" manner similar to prototype construction (see section 2.4.1). In the prototype, the completed spans are often used to support erection equipment or for delivery of segments, materials, and equipment. Each intermediate structural configuration must therefore carry the weight imposed during erection. Construction live loads can vary from small traffic loads to the governing live load case depending on the specific method of construction.

The tendon layout is affected by the magnitude of the erection loads. The structure is typically erected by stressing single-span tendons to support each erected span and then further stressing multispan "continuity" tendons to provide additional service load capacity. If continuity tendons are to be used then the erection loads must be less than the service loads to provide sufficient strength with only a portion of the tendons stressed. For the model structure, this erection load deficit was achieved by using two lanes of HS-20 truck load plus impact for service loads and two lanes of HS-20 truck load without impact for construction loads. Lower ultimate load factors were also used on construction live loads to increase this load difference.

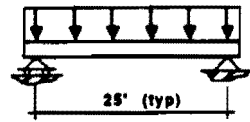
The design loading for two lanes of the AASHTO HS20 Truck Load, including impact is shown in Fig. 2.2a. To satisfy similitude requirements, the concentrated truck axle loads are reduced by the square of the scale factor (1/16) for application to the model structure. The axle spacing is a geometric property and scales directly with the scale factor (1/4). The reduced scale "HS20" truck load is shown in Fig. 2.2b.

The load cases considered during design of the model structure are shown in Fig. 2.3. As the structure evolved during construction, three structural configurations were apparent. In the one- and two-span configurations, shown in Fig. 2.3a and 2.3b, dead load and construction live loads were considered. In the three-span configuration, shown in Fig. 2.3c, dead load and service live loads were considered. All live load cases were chosen to produce maximum midspan and support moments. Shear and torsional load cases were also considered in determining the required web shear capacity.

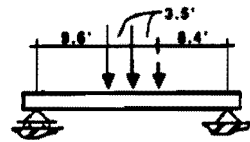
The structure was erected on falsework in a sequential span-by-span manner. After stressing of the falsework supported first span, the falsework is advanced to the second span. The second span is erected on the falsework and is matched with the first span with a cast-in-place closure strip (see section 2.4.6). This erection procedure "locks in" the stresses and curvatures which exist in the structure due to the stressing of the previous span. When the second span is stressed onto the first span (using continuity tendons), the weight of the second span is carried by the current two-span structure. The dead loads, live loads, and prestress forces must act on the current two-span structure. The loads for the second and third span are shown schematically in Figs. 2.3b and 2.3c, respectively.

To ensure adequate behavior of a post-tensioned concrete structure it is necessary to consider two levels of behavior. The structure must meet serviceability requirements with

LOAD CASE DESIGNATION



DL1

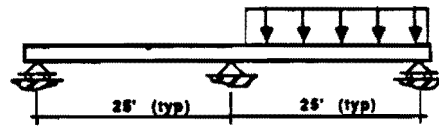


LC1-M1

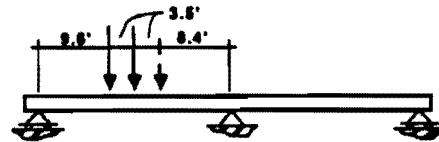


LC1-V

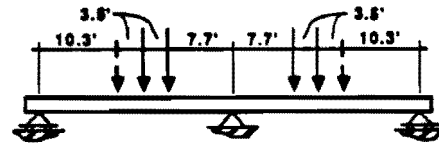
II) ONE SPAN CONFIGURATION



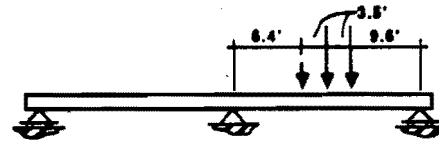
DL2



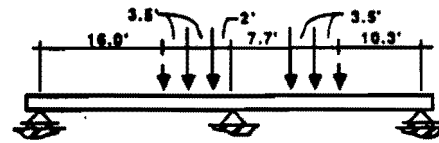
LC2-M1



LC2-M2



LC2-M3

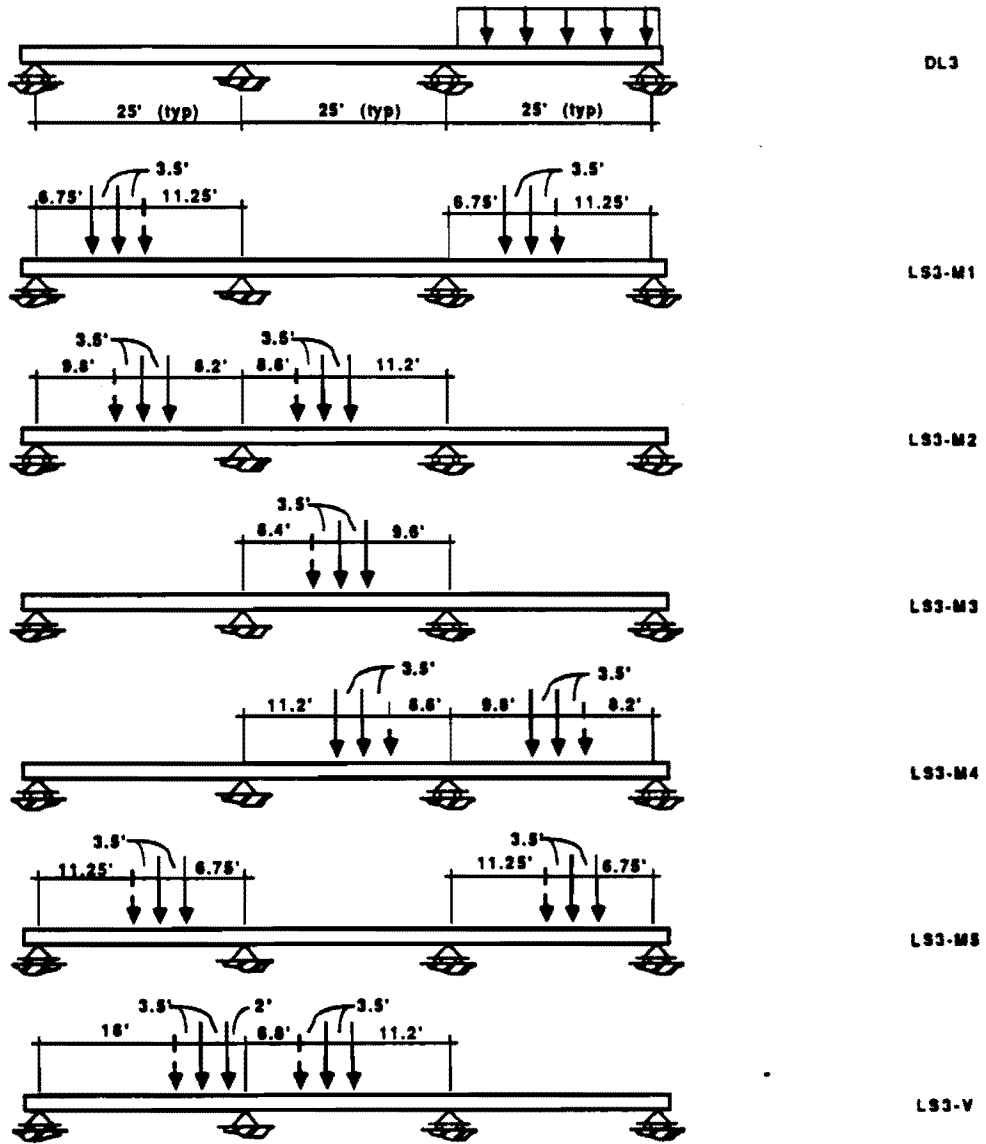


LC2-V

III) TWO - SPAN CONFIGURATION

Fig. 2.3 Design Loads

LOAD CASE DESIGNATION



g) THREE - SPAN CONFIGURATION

Fig. 2.3 Design Loads - continued

respect to service level stresses and deflections, and also must have sufficient strength to resist forces caused by factored ultimate loads. For each structural configuration of the evolving structure, service load stresses and deflections must be within prescribed limits and ultimate strength must be ensured.

The model structure was designed to meet the stress limits outlined in the 1983 AASHTO Bridge Design Specification [13]. Table 2.1 summarizes the stress limits for concrete and prestressing steel, as outlined in the 1983 specification. This specification is intended for design of conventional prestressed and post-tensioned structures and does not specifically address the problems of segmental box-girders with external tendons. Recently, PTI [14] has proposed design requirements to AASHTO which are specifically for segmental box girder construction. These requirements are outlined in Table 2.2 and provide specific stress limits for various types of segmental construction. An earlier draft proposal [20] was used in some of the design of the model. The concrete compressive stress limits have remained the same as in the current AASHTO specification, while the tensile stress limits have been adjusted to reflect differences in segmental construction.

If the structure is segmentally cast in place, or segmentally precast with glued joints, and has a minimum of 50% bonded tendons, then the tensile stress limit depends on whether nonprestressed reinforcement is provided across segment joints. If less than 50% of total tendon area is bonded then a residual compressive stress is required in the tensile zone. The amount of reserve compressive stress depends on whether the segment joints are epoxied or dry.

The model structure was designed for the service and ultimate load combinations outlined in the 1983 AASHTO specification. As described previously, only vertical self weight and traffic loads were considered for design. Table 2.3 summarizes the design load combinations considered at various stages of construction. At each stage of construction, service load combinations were considered with respect to stress limits and deflections, and ultimate load combinations were considered for strength requirements.

As discussed previously, the magnitude of the erection loads must be minimized so that additional strength does not have to be provided for temporary conditions. For this reason impact factors were not included for construction live loads. The construction live-load multipliers were also decreased to reduce the temporary structural requirements. Slightly higher risk was accepted for the short term, controlled construction period. A load factor of 1.5 was chosen for the construction live loads. This load factor combined with the load combination factor of 1.3 provides an ultimate load factor of 1.95 on construction live loads.

2.1.4 Description of Model Bridge Structure. The model structure was constructed in the Ferguson Structural Engineering Laboratory at the Balcones Research Center of the University of Texas at Austin. The model bridge, shown in Fig. 2.4, was a

Table 2.1 AASHTO-83 Stress Limits

ALLOWABLE STRESSES AASHTO-83

Material	Force Type	Specific	Limiting Stresses		
			Monolithic	Segmental Epoxy Jointed	Segmental Dry Jointed
Temporary Stresses Before Long Term Losses					
Concrete	Compression Tension	Post-Tensioned Members	.55*f'ci	.55*f'ci	.55*f'ci
		Precompressed Tensile Zone:	Not Spec.	Not Spec.	Not Spec.
		Other Areas:			
		with Bonded Reinf.*Crossing Joint	$7.5*\sqrt{f'_c}$	$7.5*\sqrt{f'_c}$	$7.5*\sqrt{f'_c}$
		without Bonded Reinf. Crossing Joint	200 psi or $3*\sqrt{f'_c}$	200 psi or $3*\sqrt{f'_c}$	Assume = 0 psi Not Spec.
		*reinforcement designed to resist total tension force in concrete computed with uncracked section			
Prestressing Steel	Tension	During Stressing	.80*fpu	.80*fpu	.80*fpu
		After Transfer	.70*fpu	.70*fpu	.70*fpu
Stress at Service Load After Losses Have Occurred					
Concrete	Compression Tension	All Members	.40*f'c	.40*f'c	.40*f'c
		Precompressed Tensile Zone:			
		With Bonded Reinf. Crossing Joint			
		Normal Environments	$6*\sqrt{f'_c}$	$6*\sqrt{f'_c}$	$6*\sqrt{f'_c}$
		Corrosive Environments	$3*\sqrt{f'_c}$	$3*\sqrt{f'_c}$	$3*\sqrt{f'_c}$
		Without Bonded Reinf. Crossing Joint	0 psi	0 psi	0 psi
		Other Areas:			
		With Bonded Reinf. * Crossing Joint	$7.5*\sqrt{f'_c}$	$7.5*\sqrt{f'_c}$	$7.5*\sqrt{f'_c}$
		Without Bonded Reinf. Crossing Joint	200 psi or $3*\sqrt{f'_c}$	200 psi or $3*\sqrt{f'_c}$	200 psi or Not Spec.
		*reinforcement designed to resist total tension force in concrete computed with uncracked section			
Prestressing Steel	Tension	At Service Load	.80*fpv	.80*fpv	.80*fpv

Table 2.2 PTI Proposed Stress Limits for Segmental Construction

Material	Force Type	Specific	Monolithic	Limiting Stresses Segmental Epoxy Jointed	Segmental Dry Jointed
Temporary Stresses Before Long Term Losses					
Concrete	Compression Tension	Post-Tensioned Members	$0.55 \cdot f'_c$	$0.55 \cdot f'_c$	Not Spec.
		Precompressed Tensile Zone:			
		With Min. 50% Bonded P.T. Tendons			
		With bonded mild reinf. crossing joint	$3 \cdot \sqrt{f'_c}$	$3 \cdot \sqrt{f'_c}$	Not Spec.
		Without bonded mild reinf. crossing joint	0 psi	0 psi	Not Spec.
		Less Than 50% Bonded P.T. Tendons			
With bonded mild reinf. crossing joint	Not Spec.	Not Spec.	Not Spec.		
Without bonded mild reinf. crossing joint	N.A.	$3 \cdot \sqrt{f'_c}$	$6 \cdot \sqrt{f'_c}$		
Transverse Tension in Precompressed Tensile Zone	$3 \cdot \sqrt{f'_c}$	$3 \cdot \sqrt{f'_c}$	$3 \cdot \sqrt{f'_c}$		
Other Areas:					
With bonded reinf. * crossing joint	$7.5 \cdot \sqrt{f'_c}$	$7.5 \cdot \sqrt{f'_c}$	$7.5 \cdot \sqrt{f'_c}$		
Without bonded reinf. crossing joint	200 psi or $3 \cdot \sqrt{f'_c}$	200 psi or $3 \cdot \sqrt{f'_c}$	Assume = 0 psi Not Spec.		
Prestressing Steel	Tension	*reinforcement designed to resist total tension force in concrete computed with uncracked section			
		During Stressing	.80* f_{pu}	.80 f_{pu}	.80 f_{pu}
		After Transfer	.70* f_{pu}	.70* f_{pu}	.70* f_{pu}
Stress at Service Load After Losses Have Occurred					
Concrete	Compression Tension	All Members	$.40 \cdot f'_c$	$.40 \cdot f'_c$	$.40 \cdot f'_c$
		Precompressed Tensile Zone:			
		With Min. 50% Bonded P.T. Tendons			
		With bonded mild reinf. crossing joint	$3 \cdot \sqrt{f'_c}$	$3 \cdot \sqrt{f'_c}$	Not Spec.
		without bonded mild reinf. crossing joint	0 psi	0 psi	Not Spec.
		Less Than 50% Bonded P.T. Tendons			
With bonded mild reinf. crossing joint	Not Spec.	Not Spec.	Not Spec.		
Without bonded mild reinf. crossing joint	N.A.	$3 \cdot \sqrt{f'_c}$	$6 \cdot \sqrt{f'_c}$		
Transverse Tension in Precompressed Tensile Zone	$3 \cdot \sqrt{f'_c}$	$3 \cdot \sqrt{f'_c}$	$3 \cdot \sqrt{f'_c}$		
Other Areas:					
With Bonded Reinf.*Crossing Joint	$7.5 \cdot \sqrt{f'_c}$	$7.5 \cdot \sqrt{f'_c}$	$7.5 \cdot \sqrt{f'_c}$		
Without Bonded Reinf. Crossing Joint	200 psi or $3 \cdot \sqrt{f'_c}$	200 psi or $3 \cdot \sqrt{f'_c}$	Assume = 0 psi Not Spec.		
Prestressing Steel	Tension	At Service Load	.82* f_{py} (.74* f_{pu})	.82* f_{py} (.74* f_{pu})	.82* f_{py} (.74* f_{pu})

Table 2.3 Load Combinations

A. Construction Load Combinations

One Scan Configuration

Load Case	DL1	P51A P	2	P51B P	2	LC1 M1	LC1 V1
Service Load Cases							
SUM1	1	1	1	1	1		
CS1, M1	1	1	1	1	1	1	
CS1, V1	1	1	1	1	1		1
Ultimate Load Cases							
SU1, M1	1.3		1*		1*	1.95	
SU1, V1	1.3		1*		1*		1.95

Two Scan Configuration

Load Case	SUM1	DL1	DL2	P52 P	2	P53 P	2	LC2 M1	LC2 M2	LC2 M3	LC2 V1
Service Load Cases											
SUM2	1		1	1	1	1	1				
CS3, M1	1		1	1	1	1	1	1			
CS2, M2	1		1	1	1	1	1		1		
CS2, M3	1		1	1	1	1	1			1	
CS2, V1	1		1	1	1	1	1				1
Ultimate Load Cases											
CU2-M1		1.3	1.3		1*		1*	1.95			
CU2-M2		1.3	1.3		1*		1*		1.95		
CU2-M3		1.3	1.3		1*		1*			1.95	
CU2-V1		1.3	1.3		1*		1*				1.95

B. Service Load Combinations

Three Span Configuration

Load Case	SUM2	DL1	DL2	DL3	PS4a P	2	PS4b P	2	PS5 P	2	PSi P	2	LS3 M1	LS3 M2
Service Load Cases														
SUM3	1			1	1	1	1	1	1	1	1	1		
SS-M1	1			1	1	1	1	1	1	1	1	1	1	
SS-M2	1			1	1	1	1	1	1	1	1	1	1	1
SS-M3	1			1	1	1	1	1	1	1	1	1		1
SS-M4	1			1	1	1	1	1	1	1	1	1		
SS-M5	1			1	1	1	1	1	1	1	1	1		
SS-V	1			1	1	1	1	1	1	1	1	1		
Ultimate Load Cases														
SU-M1		1.3	1.3	1.3		1*		1*		1*		1*	2.86	
SU-M2		1.3	1.3	1.3		1*		1*		1*		1*		2.86
SU-M3		1.3	1.3	1.3		1*		1*		1*		1*		
SU-M4		1.3	1.3	1.3		1*		1*		1*		1*		
SU-M5		1.3	1.3	1.3		1*		1*		1*		1*		
SU-V		1.3	1.3	1.3		1*		1*		1*		1*		

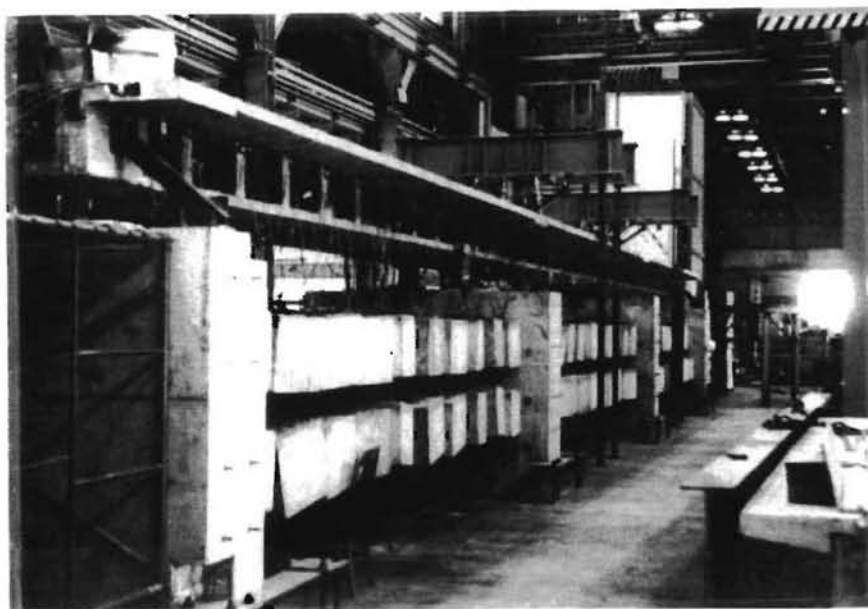


Fig. 2.4 Scale Model of Externally Post-Tensioned Box Girder

three-span structure geometrically symmetrical about the center line. Fig. 2.5 shows a plan and elevation of the structure. Each span consists of ten typical segments. Over each support is a pier segment which contains the anchorages for all post-tensioning tendons. Since the typical segments were precast separately from the pier segments, a cast-in-place closure strip was provided at each end of the pier segments.

The model cross-sections are shown in Fig. 2.6. As described in Sec. 2.1.1, the typical segment shape, shown in Fig. 2.6a, was chosen to give a span/depth ratio and efficiency rating typical of contemporary construction. At midlength of each typical segment was a full-height diaphragm through which the external tendons were deviated. Flanges tapered towards the ends and had form chamfers at each flange/web junction. The calculated section properties of the gross concrete section are also given in Fig. 2.6a.

The shape of the pier segment, shown in Fig. 2.6b evolved from several requirements and considerations. The top and bottom flange widths, and the overall structural depth, were chosen to match the typical segments. The top flange thickness was increased to a constant 3.5" to meet cover and spacing requirements for larger-size reinforcement. The external tendon anchorages were contained in the solid portion outside the web interface. A stiff diaphragm beam was then added to concentrate torsional shear flow from the span to the reactions. The remainder of the box section was filled in to ease forming, congestion,

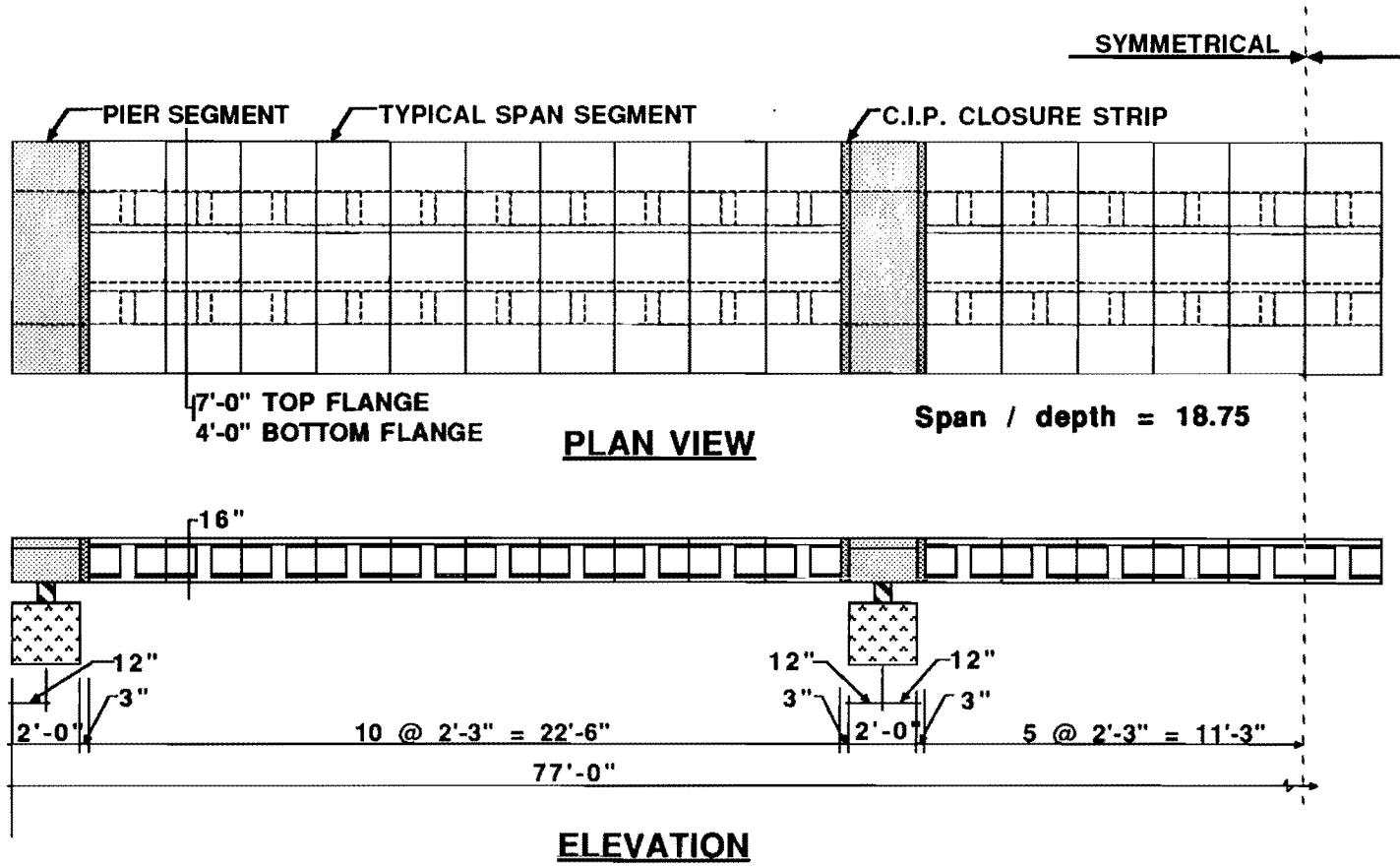
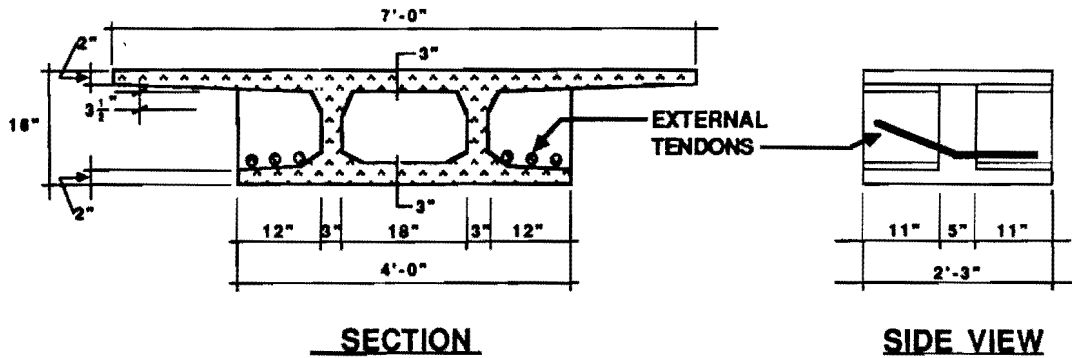


Fig. 2.5 Test Set-Up

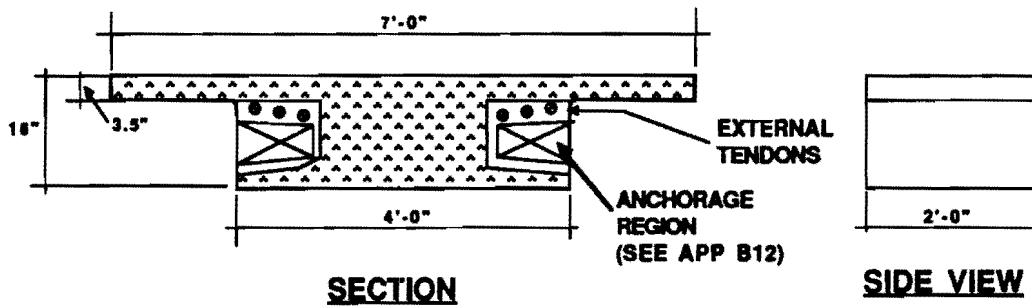


NOTES:

SPAN to DEPTH RATIO = 18.75
 EFFICIENCY FACTOR = .60

$A^* = 450 \text{ in}^2$
 $I^* = 16540 \text{ in}^4$

a. TYPICAL SPAN SEGMENT



$A^* = 894 \text{ in}^2$

$I^* = 20741 \text{ in}^4$

b. PIER SEGMENT

* Transformed Section Properties

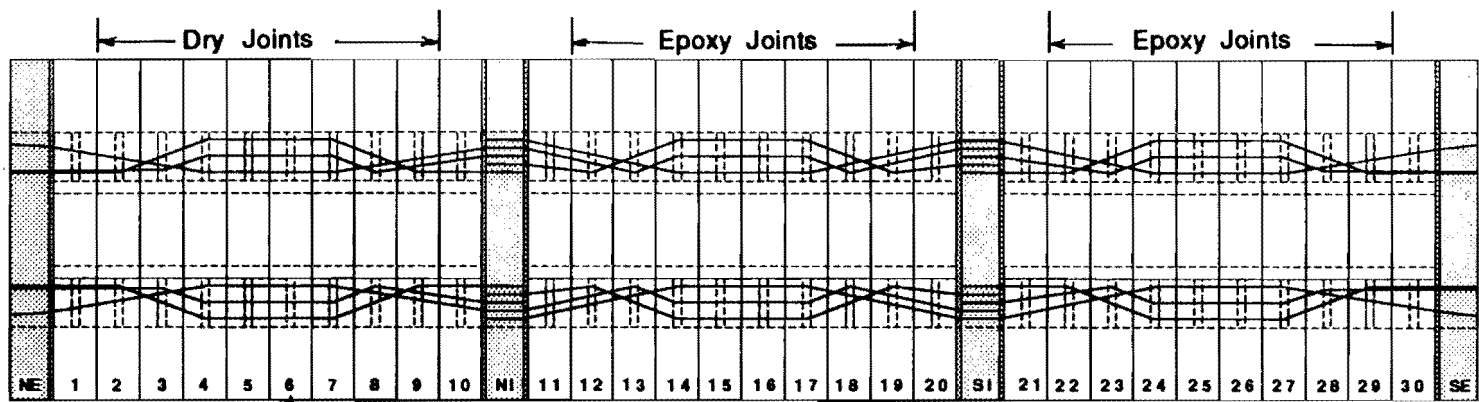
Fig. 2.6 Model Cross Sections

and consolidation problems. The calculated section properties of the gross concrete section are also shown in Fig. 2.6b.

A schematic of the post-tensioning tendons is shown in Fig. 2.7. The tendons were draped down from high points over the supports to low points near midspan. Theoretical tendon locations are shown for sections at the exterior support, midspan, and interior supports. At the exterior support, the tendon locations were chosen to give approximately zero eccentricity of the resultant tendon forces. At midspan, the tendons were located to allow the external tendon ducts to be placed flush with the bottom flange. So that the primary vertical deviation forces were transmitted directly into the box webs, the tendons were draped down to the duct location closest to the web and then deviated vertically and horizontally away from the web. This allowed the next tendon to be vertically deviated close to the web also. This crossing tendon pattern can be seen in the plan view of Fig. 2.7. The theoretical tendon locations at the interior support were chosen so that the external tendon ducts would penetrate the pier segment below the bottom of the top flange of the typical segments.

As previously described, the structure was constructed with single-span "erection" tendons and then additionally stressed with multispan continuity tendons. Tendon 1A, 1B, 2, 4A, and 4B all contained 10-3/8" diameter strands (5 each side) and were stressed as each span was erected. Tendons 3 and 5 contained 4-3/8" diameter strands (2 each side) and were stressed after erecting span 2 and span 3 respectively. Fig. 2.8 gives the theoretical tendon locations for Tendons 1A, 1B, 2, 3, 4A, 4B, and 5. In addition to the external tendons, tendons were also provided within the concrete section. The internal tendons (Fig. 2.8d) were provided at the corners of the box to augment the flexural and torsional capacity, as well as at the ends of the thin top flange to control shear lag. All internal tendons had a straight profile and were anchored at the extreme ends of the structure. Two 3/8" diameter strands were provided at each corner of the box and in each top flange overhang [5]. Only the top internal tendons were stressed for this test series. The internal tendons will also be grouted in a future test to investigate the effect of having bonded prestressed reinforcement crossing the joints.

The new PTI specification for segmental box-girder construction [14] requires that provisions be made to add future post-tensioning if needed. This provides the ability to add additional prestress to the system for unexpected prestress losses or for serviceability considerations such as deflection adjustment or deteriorated external tendon replacement. Four 3/8" dia. straight strands were provided for such contingencies within the box void and anchorages were provided at the exterior pier segments. These strands were not stressed in this test program.

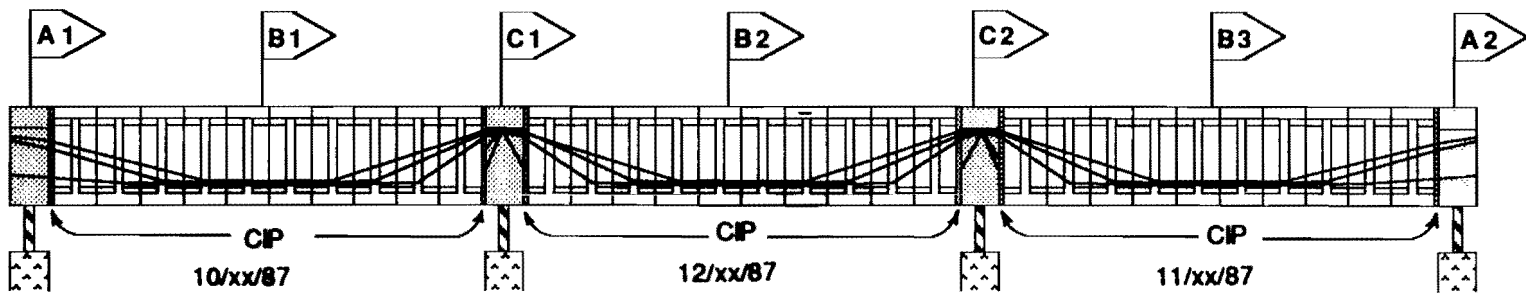


NORTH

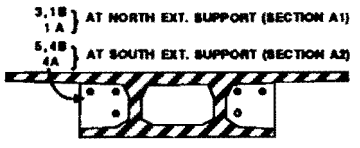
SEGMENT NUMBER

PLAN VIEW

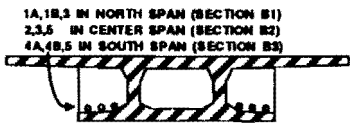
SOUTH



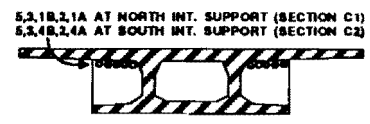
ELEVATION



SECTION A

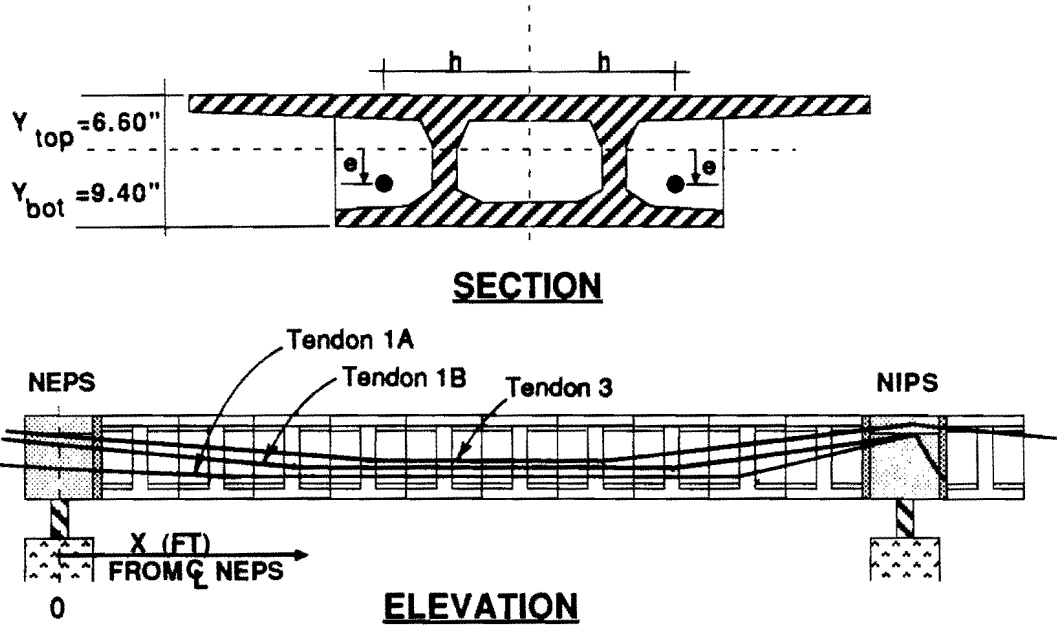


SECTION B



SECTION C

Fig. 2.7 Schematic Post-Tensioning Layout



TENDON 1A : 2 x (5-3/8" dia. Grade 270 Strands)

x (ft)	-1	0	4.625	9.125	15.875	20.375	25	26
e (in)	2.9	3.4	5.65	6.23	6.23	5.65	-2.67	3.15
h (in)	15	15	15	22	22	15	14	15.25

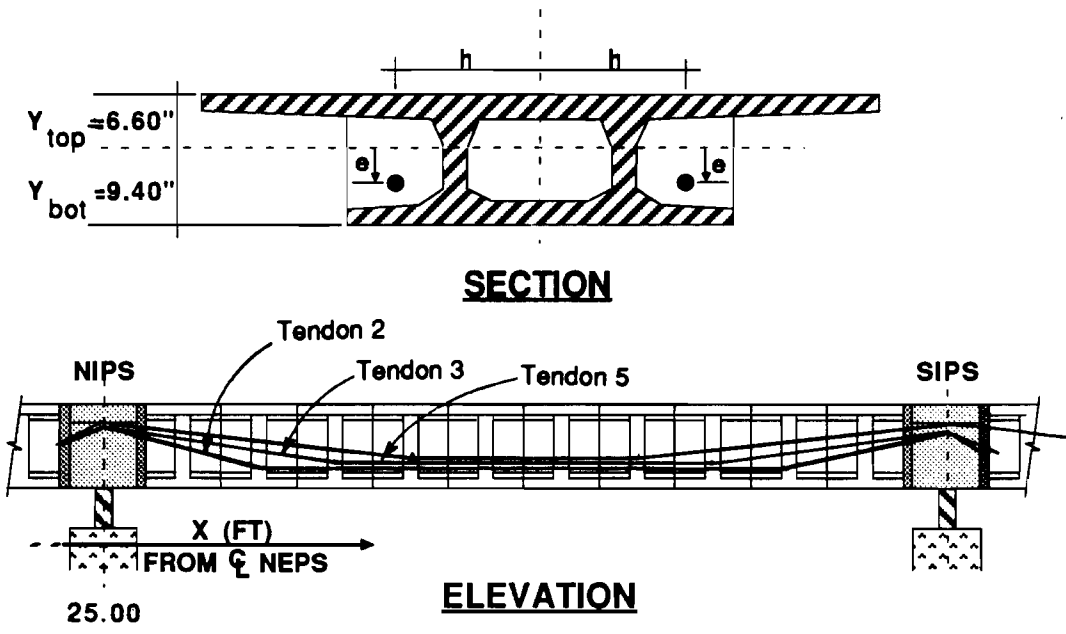
TENDON 1B : 2 x (5-3/8" dia. Grade 270 Strands)

x (ft)	-1	0	6.875	9.125	15.875	18.125	25	26
e (in)	-2.48	-2.1	5.65	5.94	5.94	5.65	-2.81	3.15
h (in)	15	15	15	18.5	18.5	15	18.25	20.75

TENDON 3 : 2 x (2-3/8" dia. Grade 270 Strands)

x (ft)	-1	0	9.125	15.875	25	31.875	Continues in Center Span	
e (in)	-2.6	-2.1	5.65	5.65	-2.88	5.65		
h (in)	21.5	21.5	15	15	20.38	15		

Fig. 2.8a Theoretical Tendon Locations



TENDON 2 : 2 x (5-3/8" dia. Grade 270 Strands)

x (ft)	24	25	29.625	34.125	40.875	45.375	50	51
e (In)	2.65	-2.74	5.65	6.23	6.23	5.65	-2.74	2.65
h (In)	16	16.13	15	22	22	15	16.13	16

TENDON 3 : 2 x (2-3/8" dia Grade 270 Strands)

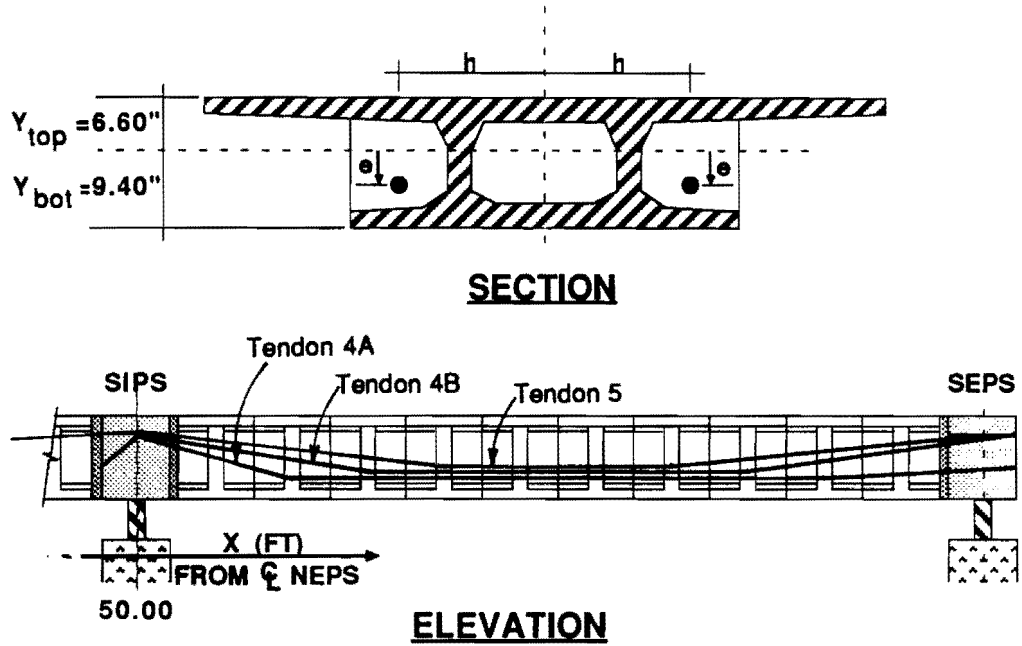
x (ft)*	15.875	25	31.875	34.125	40.875	43.125	50	51
e (In)	5.65	-2.88	5.65	5.94	5.94	5.65	-2.88	2.4
h (In)	15	20.38	15	18.5	18.5	15	20.38	22

*continues in North Span

TENDON 5 : 2 x (2-3/8" dia. Grade 270 Strands)

x (ft)	24	25	34.125	40.875	50	59.125	Continues
e (In)	1.4	-2.95	5.65	5.65	-2.95	5.65	In South Span
h (In)	22	22.5	15	15	22.5	15	

Fig. 2.8b Theoretical Tendon Locations



TENDON 4A : 2 x (5-3/8" dia. Grade 270 Strands)

x (ft)	49	50	54.625	59.125	65.875	70.375	75	76
e (in)	3.15	-2.67	5.65	6.23	6.23	5.65	3.4	2.9
h (in)	15.25	14	15	22	22	15	15	15

TENDON 4B : 2 x (5-3/8" dia. Grade 270 Strands)

x (ft)	49	50	56.875	59.125	65.875	68.125	75	76
e (in)	3.15	-2.81	5.65	5.94	5.94	5.65	-2.1	-2.48
h (in)	20.75	18.25	15	18.5	18.5	15	15	15

TENDON 5 : 2 x (2-3/8" dia. Grade 270 Strands)

x (ft)	Continues	40.875	50	59.125	65.875	75	76
e (in)	In Center Span	5.65	-2.95	5.65	5.65	-2.1	-2.6
h (in)		15	22.5	15	15	21.5	21.5

Fig. 2.8c Theoretical Tendon Locations

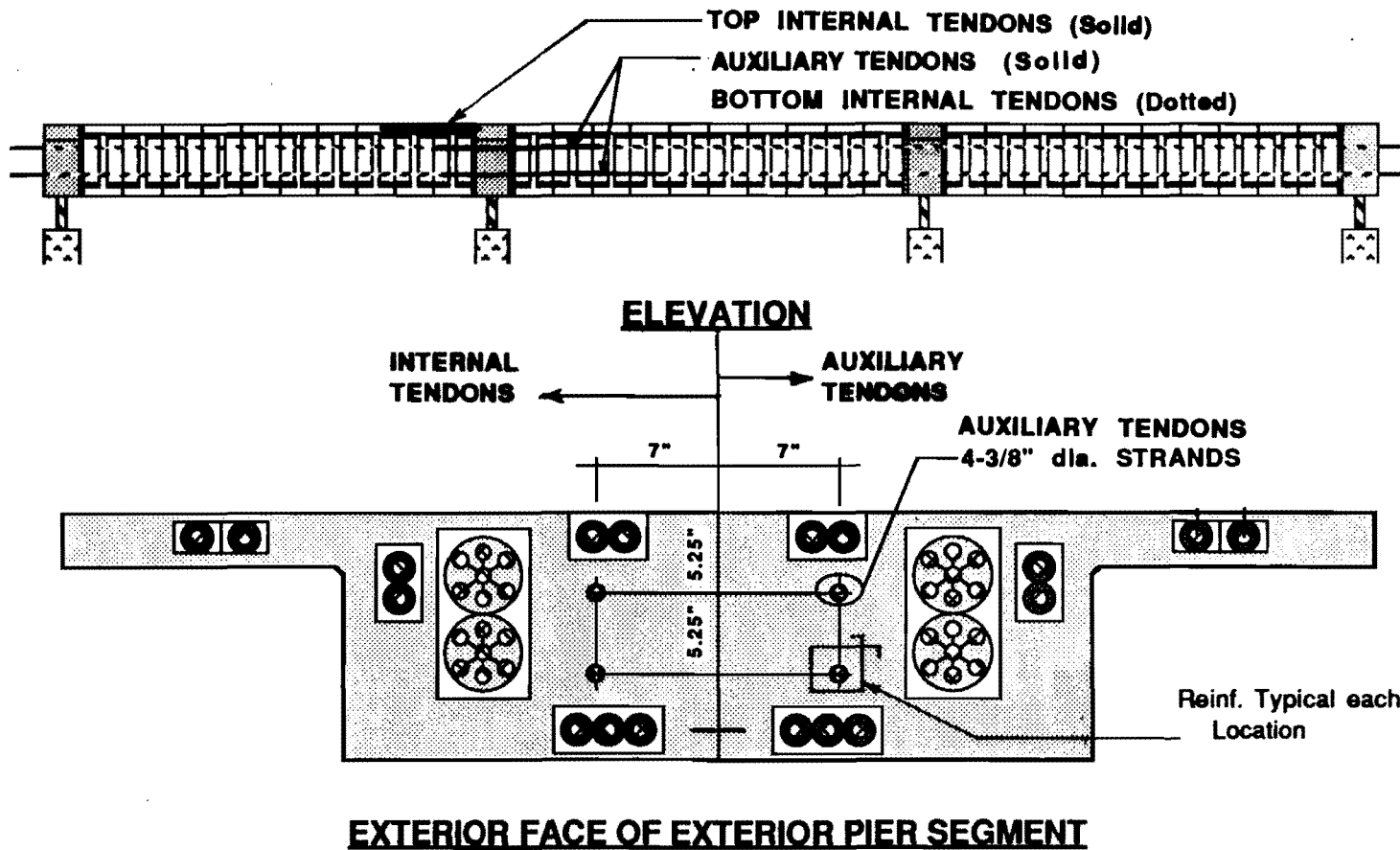


Fig. 28d Internal and Auxiliary Tendons

2.2 Material Properties

2.2.1 Concrete. In order to match prototype construction, the minimum 28 day concrete compressive strength was chosen as 6000 psi. The reduced scale dictated a minimum concrete cover of 1/2", so a maximum aggregate size of 3/8-inches was required. To ensure that the webs and bottom flanges would be properly consolidated, the tops of the bottom flanges were left open during casting. This dictated a maximum slump of approximately 4.5-inches to keep the concrete from slumping out of the webs. A slump of 2-inches was chosen as a minimum, based on placement considerations. The concrete mix was also required to remain workable, with high ambient air temperatures, for a minimum of one hour after it arrived on site. Additional retarding admixture was used during the hot summer months to provide the required workability period. A final consideration was the ease with which the exposed flanges could be finished. The fine-to-coarse aggregate ratio was increased to facilitate finishing.

Four general types of ready mix concrete were used in the model structure. Table 2.4 summarizes the four mixes used. The concrete strength and elastic modulus data are presented in Table 2.5. Preliminary trial batches indicated that the 6 sack mix, shown as Type 1, would yield concrete with the necessary characteristics. Several segments were cast using this mix until 28-day cylinder tests revealed low strengths. The cement content was then increased to 6.5 sacks to achieve the desired strength. This basic mix, designated Types 2 and 3, was used for all remaining typical segments.

Batch control problems at the first ready-mix company forced a change to a second company for 9 segments of the last span. The basic mix design, Type 3, is the same as Type 2. The piers were also cast using the Type 2b mix with larger 3/4" aggregate replacing the 3/8" crushed stone.

To allow for higher bearing stresses behind the post-tensioning anchorages, high-strength concrete was used for the pier segments. This mix, Type 4, was batched by a third ready-mix supplier so that fly ash could be substituted for some of the cementitious material.

2.2.2 Prestressing Strands. All prestressing steel used in the model structure was 3/8" diameter 270 Grade low relaxation strand. The strand has an area of 0.085 square inches, an ultimate strength of 279 ksi at 5.47% elongation, and an elastic modulus of 28,400 ksi.

2.2.3 Steel Reinforcement. Several types of mild steel reinforcement were used in the model structure. Welded wire fabric formed the skeleton of the typical segment cages. Web mats were annealed to improve ductility. Small diameter micro-reinforcing bars were used in the typical segments in the diaphragms and to tie together the welded wire mats. Normal size Grade 60 reinforcement was used in the typical segments for the

Table 2.4 Concrete Mix Types

CONCRETE MIX PROPORTIONS (per cubic yard)				
	Type 1	Type 2	Type 3	Type 4
Water (gal)	35	35	35	35
Cement (lbs)	564	611	611	691
Fly Ash (lbs)	-	-	-	298
Sacks	6	6.5	6.5	10.5
W/C	.52	.48	.48	.29 ^a
Sand (lbs) ^b	1355	1355	1355	1039
Rock ^b	1700	1700	1680	1821 ^c
Retarder (oz)	24	39	24	30
Superplasticizer (oz)	-	<i>d</i>	-	160 ^e
Ready Mix Co.	1	1	2	3
Segment	(3-8)	(1, 2, 9-20, 25)	(21-24, 26-30)	(Pier Segments)

Notes

- W/C includes total cementitious material
- Aggregate weights are for saturated surface dry condition
- 3/8" crushed Burnet Limestone
- Low dosages of superplasticizer were occasionally used to increase slump. Approximate dosage rate: 12 oz per yd. per inch of slump increase.
- Half of superplasticizer was added at the batch plant and half at the laboratory.

primary tendon deviator reinforcement. The pier segment and pier cages were fabricated almost entirely from Grade 60 reinforcement.

All wires that were not heat treated exhibited high strengths and low ductility. The annealing process for the web reinforcing wires reduced the yield strength and reestablished the mild steel behavior. The yield and ultimate strengths for the welded wire is summarized in Table 2.6.

In addition to the welded wire reinforcement, small diameter micro-reinforcing bars were used in the typical segments. These bars exhibited erratic yield and ultimate strengths with very brittle behavior. After inspection of the small reinforcing bars it appeared that they were probably cold-drawn steel wire with deformations stamped into the sides. These bars were also process annealed to restore their mild steel behavior. The strength characteristics of this reinforcement are also shown in Table 2.6.

Table 2.5 Segment Concrete Properties

Segment Information							
Segment No.	Mix No.	Date Cast	f'_{c28} (psi)	$f'_{c_{cast}}$ Cylindr. (psi)	$f'_{c_{cast}}$ Calc. (psi)	E_{c28} Cylindr. (ksi)	E_{c28} Calc. (ksi)
NEPS	4	5/26/87	12746 ^a		12282		6594
1	2	7/31/86	5855		6558		3986
2	2	7/28/86	5094		5705		3718
3	1	6/30/86	4343		4864		3592
4	1	6/12/86	5355	6022		3997	
5	1	5/28/86	6006	6839			4260
6	1	6/12/86	5355	6022		3997	
7	1	6/30/86	4343		4864		3592
8	1	7/14/86	4744		5313		3755
9	2	7/28/86	5094		5705		3718
10	2	7/31/86	5855		6558		3986
NIPS	4	7/28/87	9652 ^b		10135		5738
11	2	9/10/86	6707		7512		4266
12	2	8/27/86	5930		6642		4012
13	2	8/21/86	5630		6306		3909
14	2	8/18/86	6429	7187			4173
15	2	8/15/86	6429	7187			4173
16	2	8/18/86	6429	7187			4173
17	2	8/21/86	5630		6306		3909
18	2	8/27/86	5930		6642		4012
19	2	0/10/86	6707		7512		4266
20	2	9/16/86	6954		7788		4342
SIPS	4	3/12/87	12805 ^c		13445		6609
21	3	10/16/86	6498		7148		4495
22	3	10/10/86	6780		7458		4591
23	3	10/8/86	6709	7348			4557
24	3	10/6/86	7351	7409		4576	
25	2	9/25/86	7744	8769			4610
26	3	10/6/86	7351	7409			4576
27	3	10/8/86	6709	7348			4557
28	3	10/10/86	6780		7458		4591
29	3	10/16/86	6498		7148		4495
30	3	10/24/86	7848		8633		4940
SEPS	4	6/8/87	13270 ^d		13934		6728

^a 94-day strength^b 31-day strength^b 35-day strength^b 81-day strength

Table 2.6 Reinforcement Properties

	f_y	f_{ult}
Welded Wire Fabric (W5.5)		
Non-heat treated	82	88
Heat treated	75	79
Micro Reinforcing Bars		
#1.25 (non-heat treated)	83.0	92.5
#1.5 (heat treated)	42.5	61.3
#2 (heat treated)	44.5	65.7
Standard Reinforcing Bars		
#3	67.3	110
#4	85.3	128
#5	78.7	117

The pier segment and pier cages were fabricated from conventional Grade 60 reinforcing bars, #3, #4 and #5 in the pier segments and #3 and #8 in the piers. The strength characteristics of the segment reinforcement are also shown in Table 2.6.

2.3 Bridge Model Details

2.3.1 Typical Segment Details

2.3.1.1 Reinforcement. A typical span segment of a precast segmental box-girder structure must resist several types of forces. Longitudinal bending stress, caused by self weight and applied load, must be transmitted through the segment. Shear flow in the webs and flanges, resulting from shear and torsion, must be resisted by the segment. Bending in the transverse direction is also necessary to transfer eccentric loads to the load-carrying box. Finally, an individual segment must be properly detailed to resist local forces within the segment.

In addition to the force components mentioned above, the local forces at tendon deviation points must be superimposed. The reinforcement for typical span segment consists of a basic cage that is a typical for all segments, plus special local reinforcement to transfer the tendon deviation forces to the box girder. The general design requirements for

the typical reinforcing cage, and the special reinforcement required for tendon deviation is discussed and comprehensive details presented in Ref. 5.

The basic cage of a typical span segment is shown in Fig. 2.9. The cage consists of six specially fabricated mats of welded wire reinforcement tied together with micro reinforcing bars. The tendon deviation diaphragm is reinforced with basic wall reinforcement which was adjusted to mesh with the particular tendon duct configuration.

Superimposed on the basic reinforcement of a typical segment is the special reinforcement required to deviate the primary external tendons. Figure 2.10 shows the force components that are caused by deviating a tendon. The tendons are draped down from the ends of the span and are vertically and horizontally bent at the deviator. This results in vertical and horizontal force components applied to the segment at the deviator as shown in Fig. 2.10. The horizontal deviation forces are resisted by transverse bars which confine the bottom of the diaphragm region. The vertical deviation forces are resisted by "link" bars which are bent down and under the transverse confining bars. Additional confinement was also provided around the tendon ducts using bent #2 bars.

2.3.1.2 Fabrication of Typical Segments. Two general methods are available for match-cast precasting of box-girder segments [12]. The short line method uses a single stationary set of forms to match-cast segments. After casting a particular segment it is slid forward and used to match-cast the next segment. Complex horizontal, vertical, and rotational alignments are possible by adjusting the position of the matching segment. The position of the matching segment must be set very accurately since a check of the alignment of a span is not made until final erection. Several stationary casting machines are commonly setup in the casting yard providing high segment production with small space requirements.

The long-line method uses one or more traveling forms to match-cast a series of segments. After casting a particular segment, the formwork is advanced to cast the next segment with the previous segment left in position for match casting. Complex geometries are also possible with the long-line method by using an adjustable soffit form. A final check of the span alignment is made in the casting yard with casting errors being corrected rather than accumulated. A major problem with the long-line casting method is the space required to set up the long casting beds. Also, foundation conditions for the casting bed must be firm at all locations to minimize settlement under the weight of the segments.

Since the model bridge structure had neither horizontal or vertical curvature the simpler long-line casting method was used. A long planar casting bed, 4'-6" wide by 30 feet long, was fabricated using a liquid Acrylic Polymer grout formed with carefully leveled side rails. The plan locations of the ten segments of one span were laid out on the casting bed with a transit and tape. Segments were cast directly on the casting bed with the top elevations set using a surveying level and rod. The ten typical segments of one span were

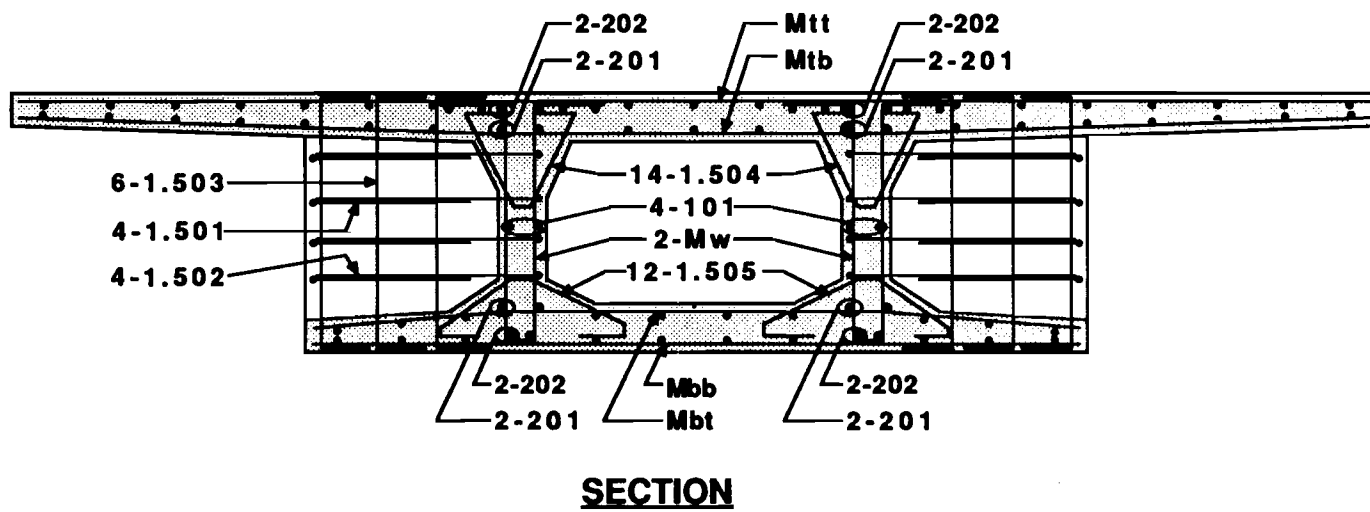


Fig. 2.9 Typical segment Reinforcing

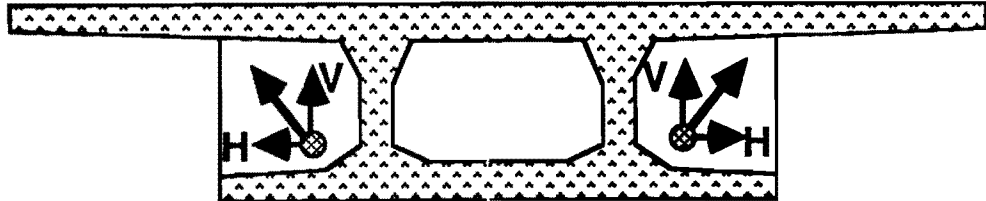


Fig. 2.10 Deviator Force Components

precast by starting at a central segment and match casting outward in both directions towards the ends of the span.

A debonding agent consisting of flax soap and talc (6:1 by volume) was applied to all match-cast faces and to the casting bed prior to concrete placement. This mixture was also used as a form release agent.

After the segment was completely consolidated the flange surfaces were screened and finished. Once the concrete had achieved its initial set, wet burlap was applied to all exposed surfaces and the entire segment was shrouded with polyethylene sheets. The forms were removed after one day so that preparations could begin for the next segment. After removal of the forms, the segments were then recovered with burlap and plastic for an additional two days.

2.3.1.3 Deviators. With externally post-tensioned box-girders, the tendons are draped down from the ends of the span and are horizontally and vertically redirected through the deviators. The deviator region is very important since it provides the only attachment between the concrete girder and the post-tensioning tendons. Since the model bridge was to be used to investigate the global behavior of the structural system, the action of the local deviator regions was studied separately by Carter and Beaupre [1,2,3,4]. In the model bridge structure, the tendons were deviated through an oversized 5" thick diaphragm element to ensure that local effects at the deviator would not limit the global behavior.

In the prototype structure the external tendons are commonly deviated through a bent steel pipe that is cast into the concrete section. In the model structure, the tendons were deviated through an 8-inch length of 1-1/2-inch diameter thin walled electrical conduit. The conduit was bent to an angle equaling the calculated angle change plus 2 degrees. This was done to ensure that the tendon would not bear on the edge of the deviator pipe. The deviator conduit was bent using a hydraulically assisted electrician's conduit bender. Since the conduit bender had a fixed radius of curvature that was smaller than required, the total angle change was divided into three equal concentrated bends. These concentrated bends were spaced at the center of the diaphragm and at 1-1/2-inches on either side of center to produce the proper overall angle change.

2.3.1.4 Shear Keys. Shear keys are used on segment faces to transfer shear across segment joints and to provide an interlock between match-cast segments. Exploratory studies by Koseki and Breen [15] indicated that a multiple-key pattern provided the most uniform shear transfer across the joint between segments. A study of contemporary segmental structures provided approximate ranges of key dimensions. Keys are also provided in the flange regions.

The shear keys were laid out on the end of the segment as shown in Fig. 2.13.

2.3.1.5 Fabrication Tolerances for Typical Segments. After casting and separating all the segments, they were systematically measured at critical locations [5]. In most cases the match-cast face of a segment was wider than the new end. At the new end the formwork was adjusted to the proper position and held with turnbuckles. At the match-cast end of the segment the formwork overlapped the previous segment by 6-inches for closure. This distance and small irregularities in the concrete did not allow the forms to close completely against the previous segment.

2.3.1.6 Segment Repair Procedures. As would be expected with an inexperienced contractor, some problems developed during precasting the model bridge segments. The hydraulic pressure exerted by the concrete on the web forms was not properly restrained and resulted in the outside web form in segment 4 to shift out during the casting operation taking the diaphragm form with it. This caused the duct hole in the diaphragm to also shift to the outside. The forces exerted on the structure by this misalignment were insignificant, but the outer duct hole was too close to the outside edge of the bottom flange. The diaphragm and bottom flange were chipped out, the reinforcing and outer duct hole were realigned, and the diaphragm and bottom flange were recast.

In segment 2 the interface between the webs and top flange were not consolidated and a layer of honeycombing occurred. This was caused by incomplete mixing of the two lifts of concrete. Segment 2 was recast and care was taken to ensure proper consolidation at this critical joint.

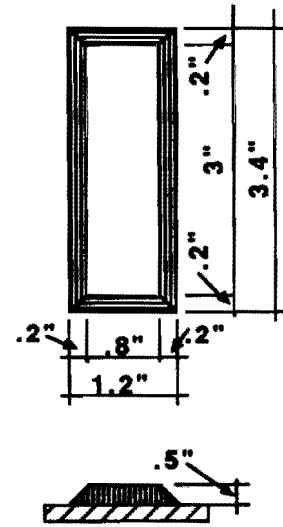
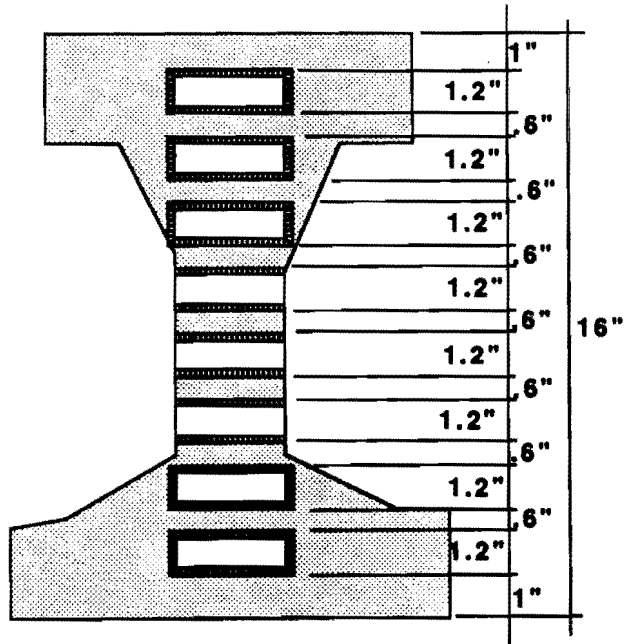
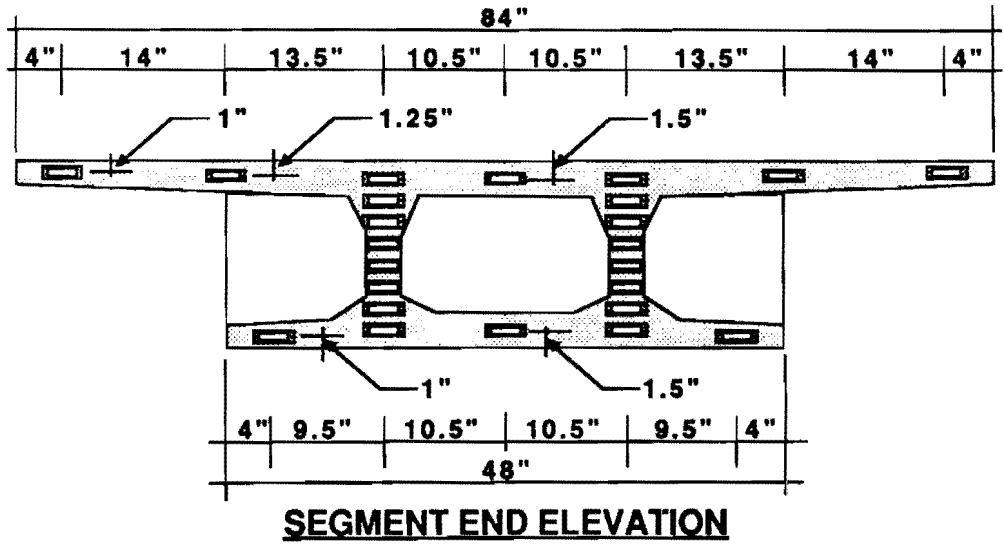


Fig. 2.11 Shear Key Details

The top flange thickness was too thin to be properly vibrated using immersion type vibrators. Therefore to consolidate the top flange, the vibrator was hooked into the reinforcement so that the vibratory energy was transmitted to the concrete through the reinforcement. In segment 7, the vibrator was inadvertently hooked onto one of the internal tendon ducts and dislodged it from its support system. The concrete was chipped back approximately 2" on each side of the proper alignment and the duct was repositioned and cast in place. To ensure proper alignment, the adjacent segments (6 and 8) were matched and a nominal stress of 50 psi was applied to the matching faces.

Another problem that was encountered during the casting operation was damage to the shear keys while separating the segments. Shear key damage was caused by two general problems. In some segments, the debonding agent was not completely applied to all surfaces causing the match-cast concrete to partially bond together. This caused generally minor damage local to the bonded area. A more serious problem was caused by overlapping lips in the match-cast keys which engaged when the segments were separated. These lips were caused by fresh concrete filling air voids and irregularities in the match-cast face. Depending on the size and location of the overlapping lips, the key damage ranged from small corners breaking off to complete removal of a key. This problem can be minimized by carefully sealing around the edges of the forms and filling any air voids and irregularities with sealant prior to match casting.

To ensure that the match-cast segments will fit back together, repair of damaged keys must be done after the segments have been stressed together. Since key damage did not occur at critical joints they were not repaired for this test series.

2.3.2 Pier Segment Details. The pier segments for externally post-tensioned box-girders are the critical segments in the structure. They contain most, if not all, of the anchorages for the post-tensioning tendons. The pier anchorage details were pretested to ensure adequacy. For interior pier segments, anchorages are required on both faces with tendons crossing within the segment. In addition to the anchorage requirements, the bearing hardware is also required in the pier segments. A photograph of the south interior pier segment for the model structure is shown on the casting bed in Fig. 2.12.

2.3.2.1 Reinforcement. As was mentioned previously, severe congestion problems can be expected in the anchorage regions of reduced-scale models of post-tensioned systems.

The basic cage of the pier segment shown in Fig. 2.13 was designed to resist several types of forces. In line with the span webs, the shear forces must be transferred to the bearings. Each web was reinforced with the welded-wire mats used in the webs of the typical segments. The external tendons were draped up from the span and deviated and anchored in the pier segments. The anchorage region was enclosed with stirrups to confine the entire region and resist the high shears from the anchorages and curvatures. With the

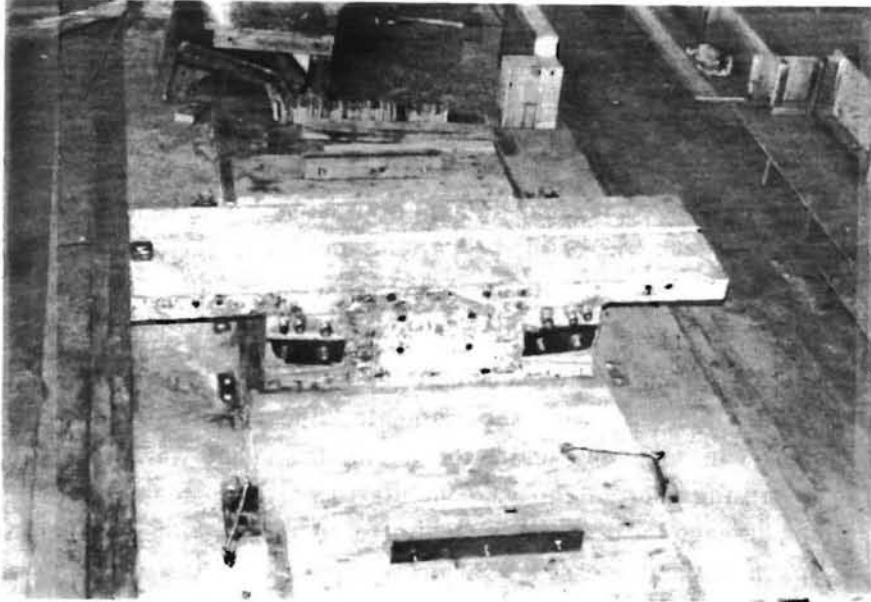


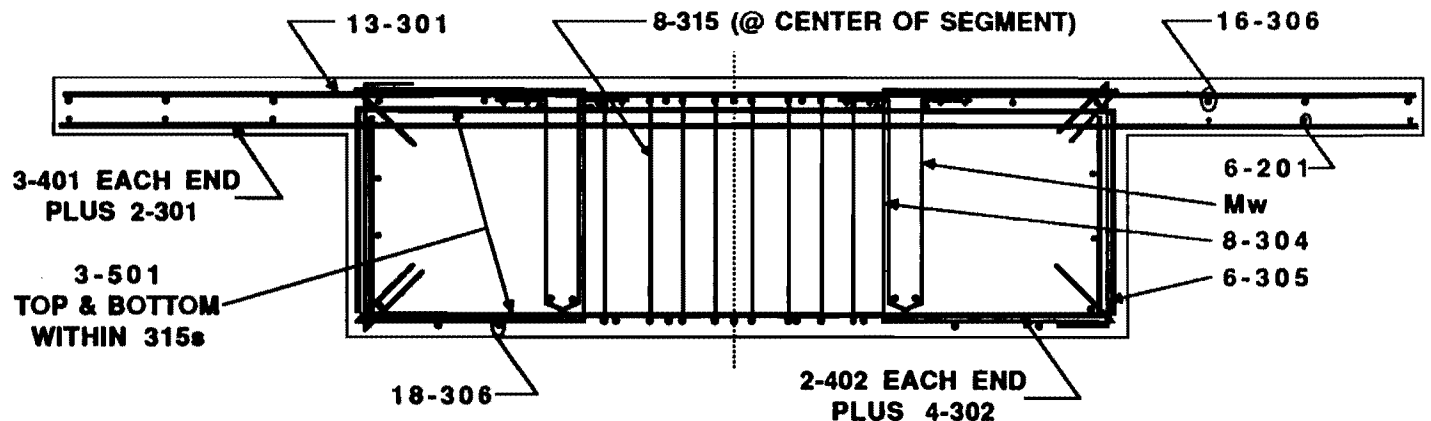
Fig. 2.12 South Interior Pier Segment

anchorage outside the line of the webs, transverse reinforcement was required to direct the forces to the webs. The transverse flange reinforcement was therefore bundled near the edges. Longitudinal reinforcement was designed to resist the longitudinal moments over the bearing. Finally a stiff shear diaphragm was provided over the bearings to resist torsional shear flow from the span.

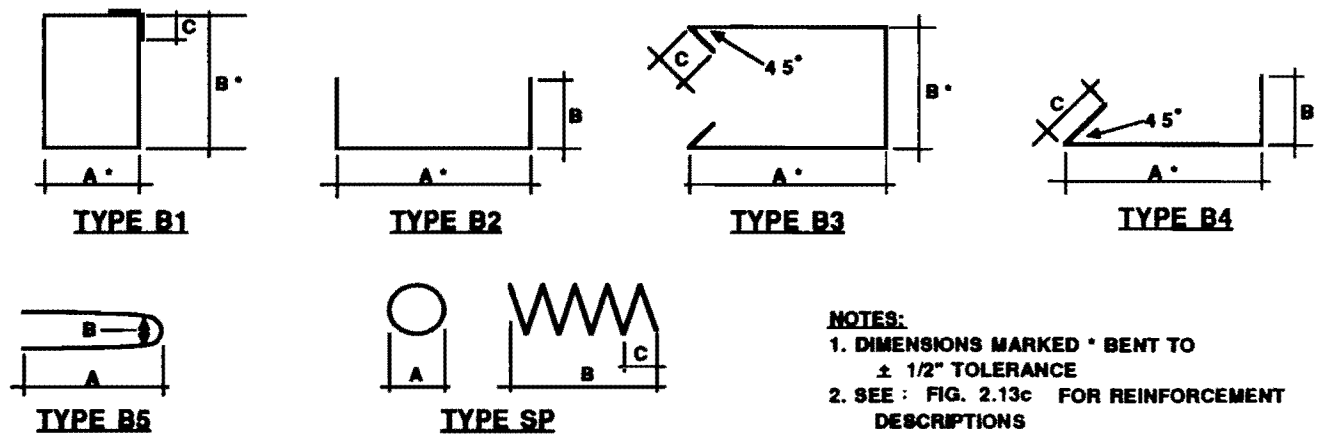
The reinforcement for the anchorage regions was designed to resist the bursting stresses that occur behind the anchorage [5]. An equivalent triangular stress prism was calculated and reinforcement was provided at 20 ksi to resist the maximum of the vertical or horizontal force requirements. A spiral was then added behind the bearing plate for confinement [16]. Spirals were also provided at locations of high tendon curvature to resist the multi-strand tendon splitting forces [16]. A photograph of the completed cage for an interior pier segment is shown in Fig. 2.14a. The extreme congestion of the anchorage region, as viewed from under the top flange after partial form assembly, is shown in Fig. 2.14b.

Bearing stresses behind the anchorage bearing plates were limited to those recommended by the ACI 318-83 Building Code [17] with a loaded area-to-total area ratio of 1.0. High strength concrete, with a minimum 28 day compressive stress of 10 ksi, was used to reduce overall plate dimensions.

2.3.2.2 Anchorage Zone Pretest. Before casting the pier segments it was prudent to pretest the anchorage zone configurations. This can be done by testing each

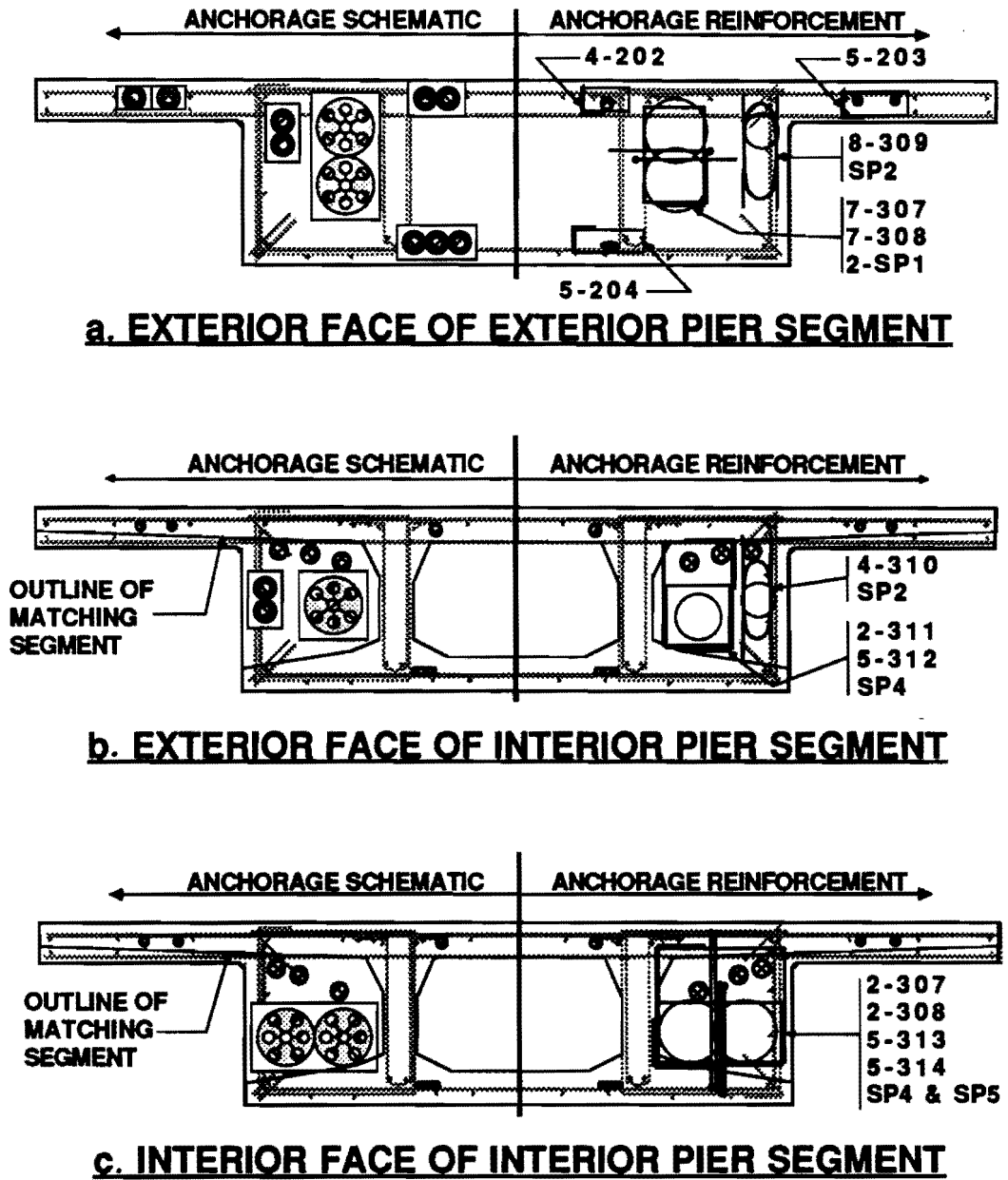


SECTION



- NOTES:**
1. DIMENSIONS MARKED * BENT TO $\pm 1/2"$ TOLERANCE
 2. SEE : FIG. 2.13c FOR REINFORCEMENT DESCRIPTIONS

Fig. 2.13a Pier Segment Reinforcement



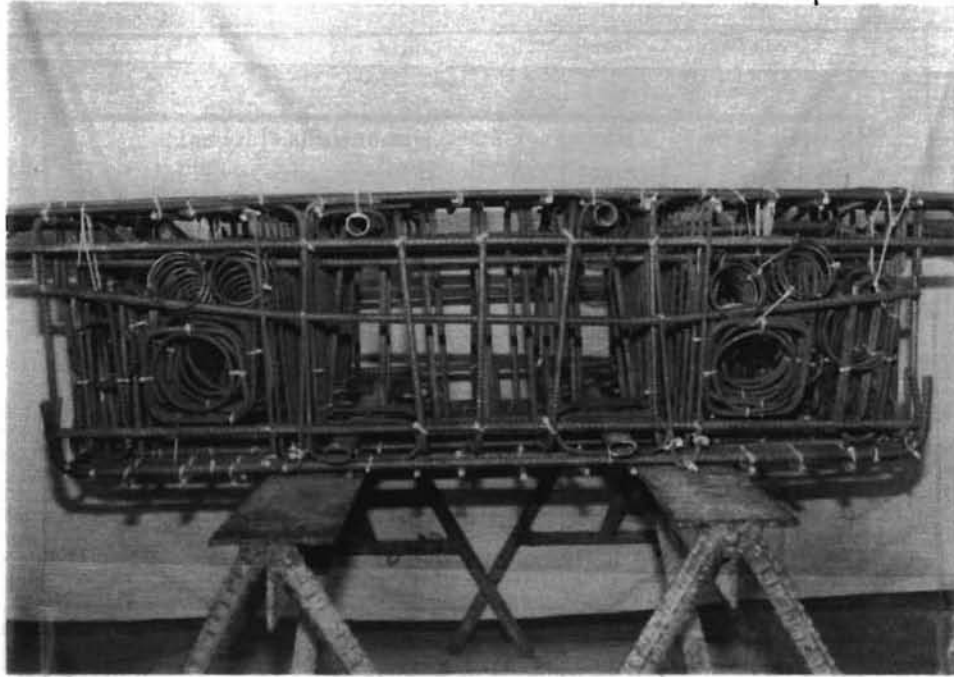
SEE Fig. 2.13c FOR REINFORCEMENT DESCRIPTION

Fig. 2.13b Anchorage Zone Reinforcement

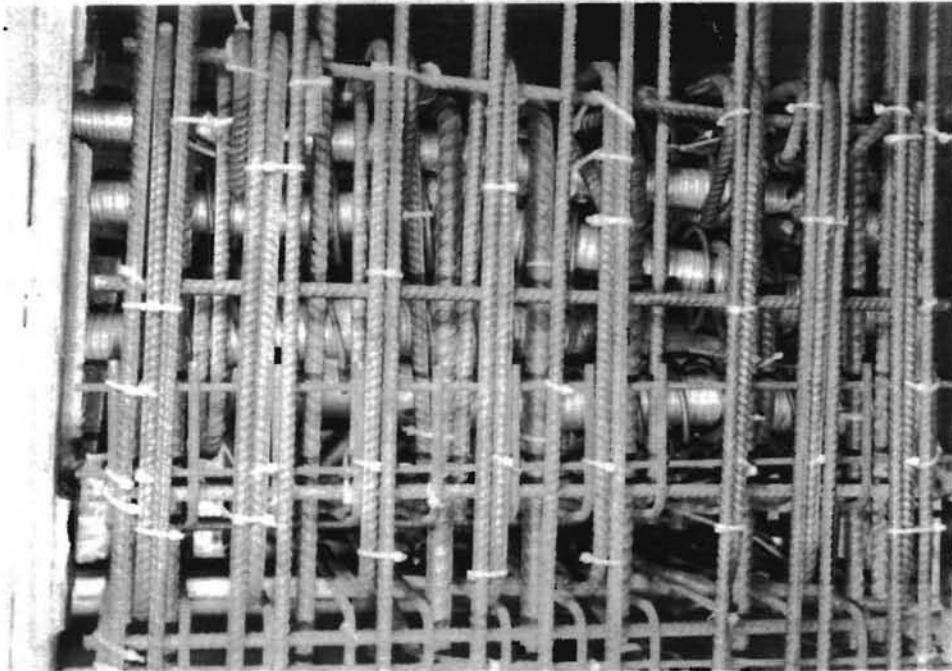
Bar No.	Type	Bar Size	Dimensions (inches)		
			A	B	C
201	Straight	2	23		
202	B1	2	2	4	2
203	B1	2	2	5.5	2
204	B1	2	2	6	2
301	Straight	3	83		
302	B2	3	47	4	
303	Straight	3	47		
304	B3	3	14	14.5	4
305	B4	3	14.5	2.5	4
306	Straight	3	23		
307	B1	3	5.5	11	4
308	B5	3	1.75	10	
309	B5	3	2.25	9	
310	B5	3	1.75	9	
311	B1	3	5.5	5.5	4
312	B1	3	6	9	4
313	B1	3	10	11	4
314	B5	3	1.75	14	
315	B1	3	6.5	14.5	4
401	Straight	4	83		
402	B2	4	47	4.5	
403	Straight	4	47		
501	B2	5	47	12	
SP1	SP	1/4"	5	11	1
SP2	SP	1/4"	3	6	1
SP3	SP	1/4"	1.5	4.5	.75
SP4	SP	1/4"	4	4	.75
SP5	SP	1/4"	2.5	18	1
SP6	SP	1/4"	4	6	.75
SP7	SP	1/4"	2.5	20	1

a. Used at location of high tendon curvature to resist splitting

Fig. 2.13c Pier Segment Reinforcement Schedule



a. Reinforcement for south interior pier segment.



b. Congestion in anchorage region.

Fig. 2.14 Pier Segment Reinforcement

pier segment for a proof load greater than the expected anchorage load. This does not give any indication of the ultimate safety factor and involves considerable wasted effort if found to be deficient since the entire pier segment would be rejected. A better method of investigating the strength of the anchorage zone region is to construct a simplified mock-up that includes the critical bearings, reinforcement, and tendon inclinations and curvatures. The mock-up can then be loaded to higher loads providing design information for cracking and possibly ultimate strength.

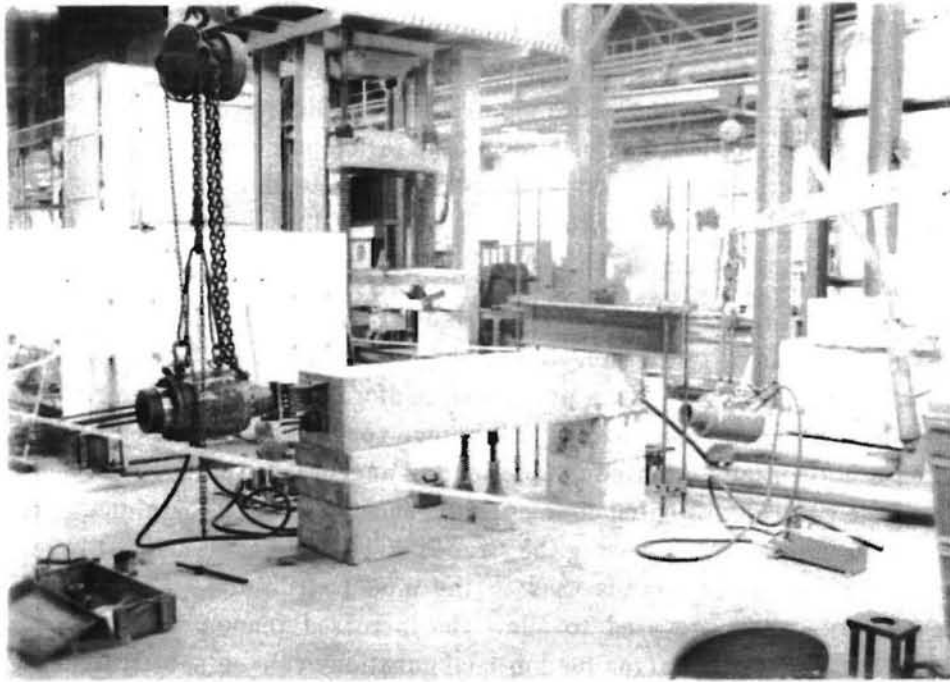
An anchorage zone pretest was designed with a critical anchorage assembly at each end of a rectangular prism. The layout of the test is shown in Fig. 2.15a with reinforcing details shown in Fig. 2.18b. The prism was reinforced with the same reinforcement that was used to confine the pier segment anchorage zone regions. The east end of the prism contained a horizontally oriented double-tendon anchorage, and the west end of the prism contained the vertically-oriented double tendon anchorage. To allow higher anchorage forces to be reached without overstressing the strands, 7-1/2" diameter strands were used instead of the 5- 3/8" diameter strands used in the model structures ($A_{mockup}/A_{model} = 2.5$). Larger tendon ducts were used to allow the increased tendon area. For a similar test for prototype structures, larger tendon configurations can be substituted with the same reinforcement scheme.

The mock-up was tested by alternately stressing tendons from each end of the concrete prism. Tendons were stressed in equal increments to a maximum load level of approximately 200% of the load that the model structure was subjected to, (i.e., $2.0 * 0.8 * f_{pu} * (A_{ps-model})$). No external cracking was evident, although cracking sounds at approximately 188% of the maximum model load indicated some internal cracking probably occurred. The test was discontinued before surface cracking or ultimate anchorage strength was reached, when the increased tendon area reached approximately 70% of ultimate strength.

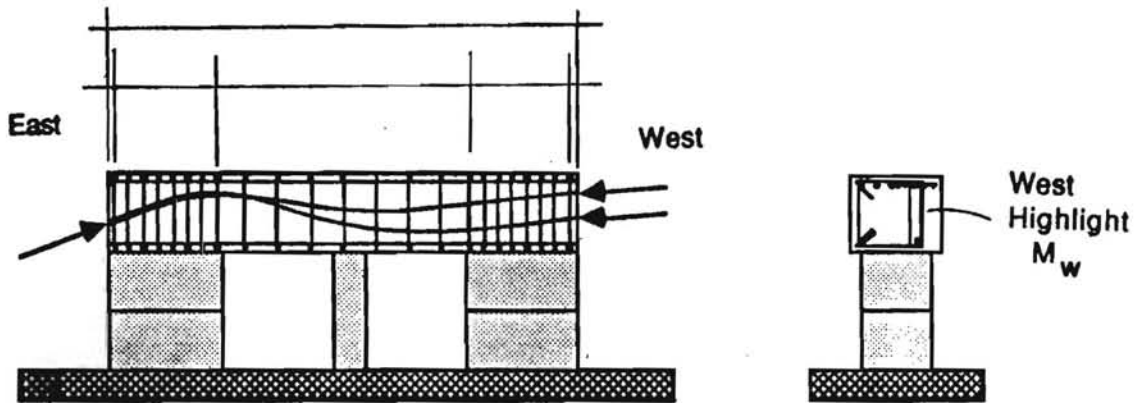
2.3.2.3 Fabrication of Pier Segments. Because of the complexity of the pier segments they were precast separately from the typical span segments and joined with a cast-in-place closure strip at each end. This was similar to the Phase 1a portion of the San Antonio project in which the pier segments were set independently or incorporated into the face of the straddle bents.

The pier segments were cast on the long-line casting bed using the end forms from the typical span segments plus a new top flange and end-face form. The end form contains the shear key blockouts and internal tendon support systems. The forms were modified by cutting holes to accept the anchorage bearing assemblies and external tendon extensions.

To ensure external tendon ducts did not have concentrated curvatures at the face of the pier segments, they had to extend from the segment face at the proper inclination. This was accomplished by extending dowels from tendon ducts at the segment face at the



a. Anchorage zone pretest set-up



b. Reinforcing details

Fig. 2.15 Post-Tensioning Anchorage Pretest

correct inclination, and attaching them to a plywood jig located 36-inches from the face of the segment.

2.3.3 Bearings and Piers. The arrangement of lateral and longitudinal restraint used in the model structure is shown schematically in Fig. 2.16. To satisfy erection and testing requirements the translationally fixed bearing was located on the north interior pier. With the span-by-span construction method each intermediate structural configuration must be fully restrained. This required lateral restraint at both ends of the first span erected, the north span. In addition, longitudinal restraint was also required at one of these two supports. The longitudinal restraint was located at the north interior pier to reduce longitudinal movements at the far end and to provide the same exterior support condition for the two end spans.

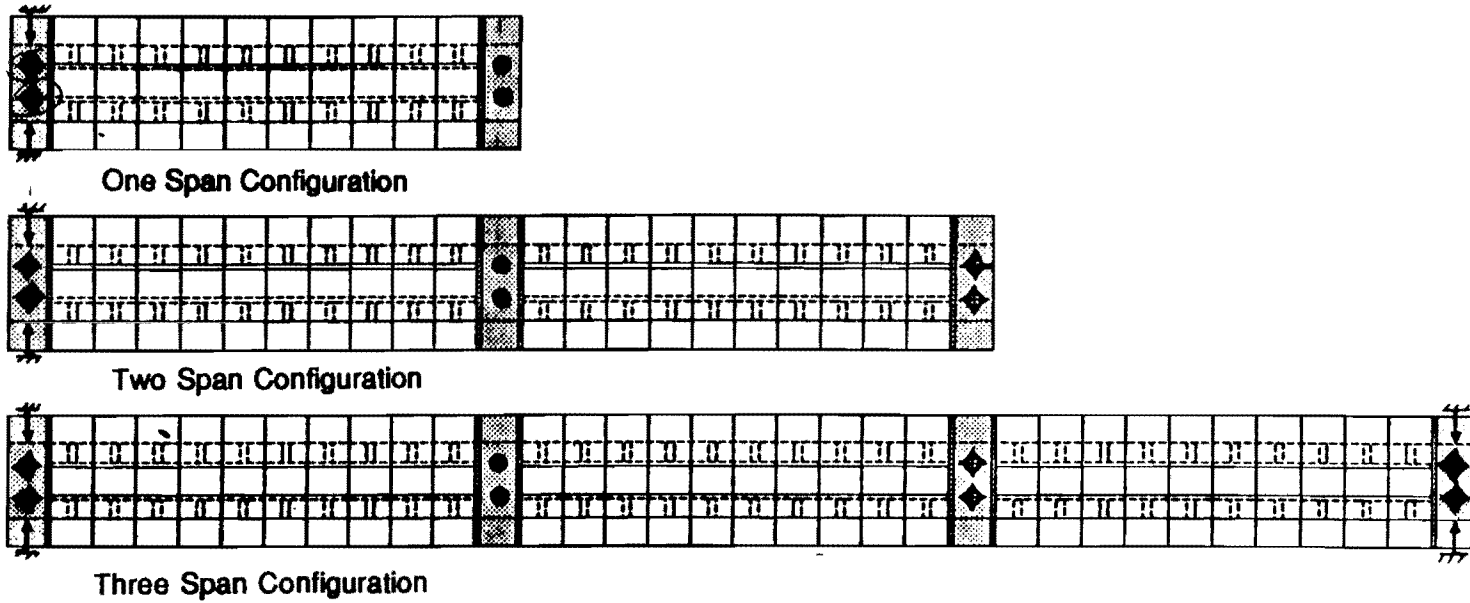
Both exterior support reactions were measured with load cells. A third reaction at the south interior pier, was also measured to provide a statistical check. The exterior pier support reactions were measured under each web with a 100-kip capacity load cell. Rotational and longitudinal movements were allowed for by using neoprene bearing pads on top of each load cell. So that the measured reactions would not be affected, the lateral restraint at the exterior piers was provided with angle bracing which beared against the side of the pier segment.

The support reaction at the south interior pier was measured with a 200-kip capacity load cell under each web. Neoprene bearing pads were used to allow unrestrained movement at this support. Lateral restraint was not provided at this location.

So that reactions could be equalized under each web at a particular support, provisions were made for jacking and setting all the measured reactions. After completing erection, each support was individually lifted from its bearing, the load cell was zeroed, and then the structure lowered onto the bearings. The structure was again lifted and shims were placed under the web of the lowest reaction. Several layers of aluminum foil shims were used to provide a fine adjustment capability. This process was continued until the reactions under each web were measured to be within 10% of each other.

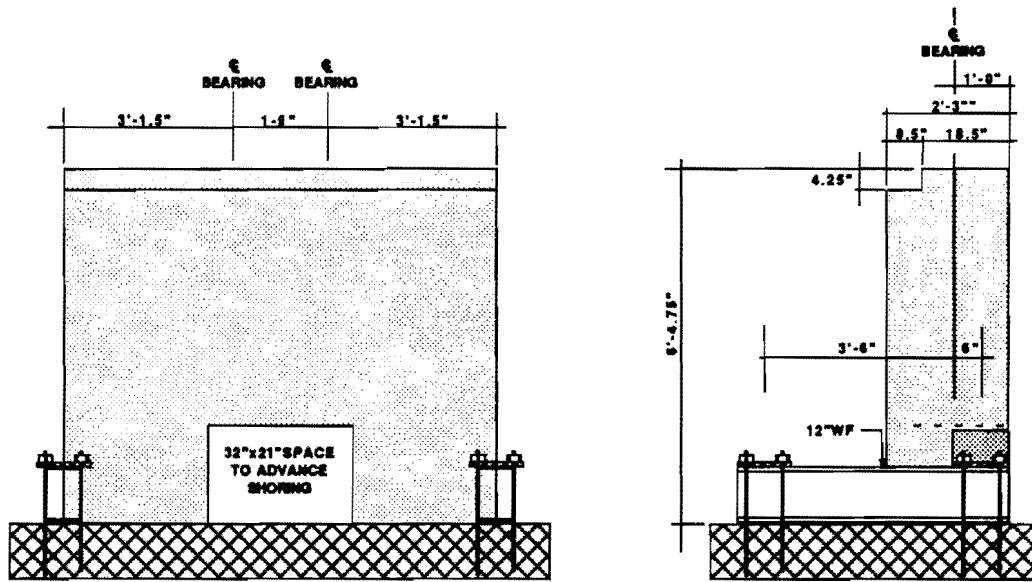
These structural bearings at the north interior pier were fabricated from a spherical machine bearing set into a heavy steel plate. The pier segment was adjusted to its final elevation by tightening nuts on rod anchors set in the top of the pier. Finally, the space between the top of the pier and the bottom of the steel bearing plate was filled with a liquid gout.

The piers were proportioned conservatively as shown in Fig. 2.17. All the piers were tied down to the test floor with 12-in. steel wide flanges on each side, and were cast in their final position. A 32-in. by 21-in. opening was provided in each pier to allow movement of the erection girder to the next span to be erected. Both exterior piers were identical and had a stepped top to provide additional space for jacking (adjustment of end

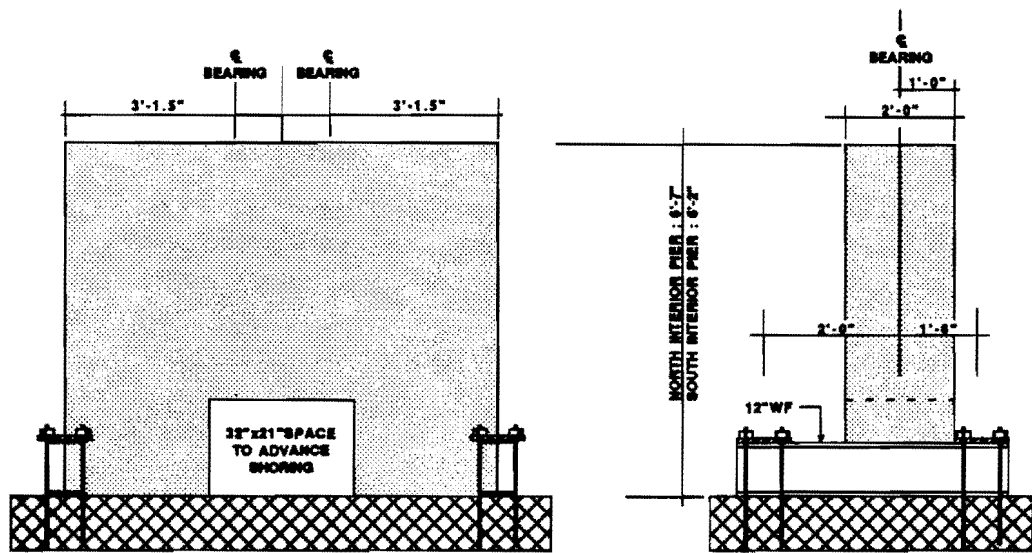


- LEGEND:**
- ◆ - 100 kip Load Cell Assembly
-Allows translational and rotational movements
 - ◆ - 200 kip Load Cell Assembly
-Allows translational and rotational movements
 - - Fixed Bearing Assembly
-Restrains Translational movement; Allows rotational movements
 - ↑
- External Lateral Restraint to pier

Fig. 2.16 Bearing Schematics



EXTERIOR PIER



INTERIOR PIER

Fig. 2.17 Pier Details

reactions). The interior piers had different top elevations to correspond to the two types of interior bearings used. Sufficient space was provided within the bearing height to jack up the structure.

2.4 Erection Procedures and Details

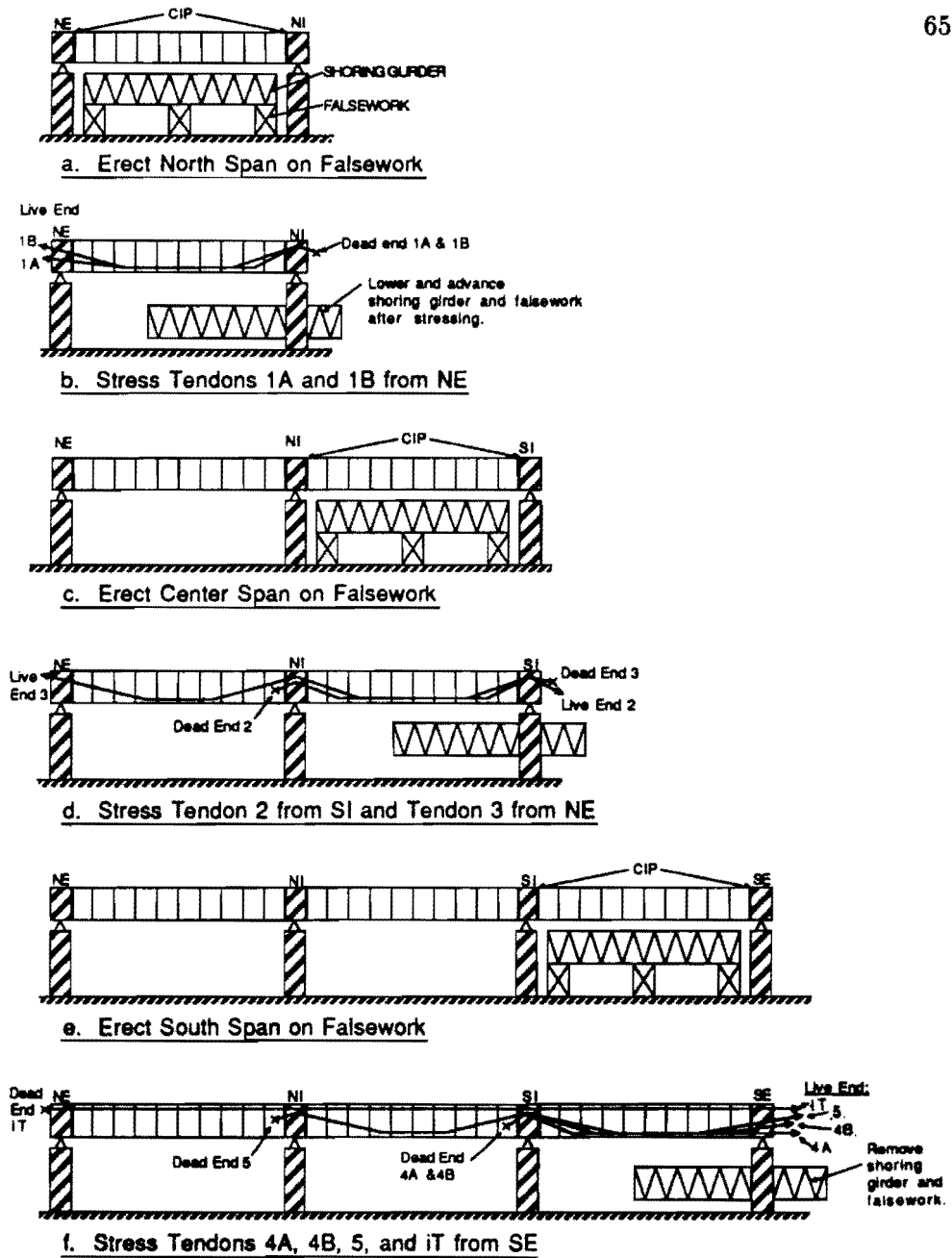
2.4.1 Span-by-Span Erection Method. Although other methods of construction can be used with external post-tensioning, the majority of existing structures have been built using the sequential span-by-span method. For medium-span elevated highway viaducts with approximately equal spans, the repetitive nature of this method leads to good economy. Erection equipment is fabricated once and used to erect many similar spans.

The model was therefore erected in a sequential span-by-span manner similar to prototype construction. The sequence of erection is shown schematically in Fig. 2.18. Erection began at the north exterior span and progressed towards the south. Falsework was erected in the north span to support all the segments for the entire span. The span segments were erected onto the falsework and drawn together with temporary post-tensioning. The pier segments were then erected and matched with the span segments with a cast-in-place closure strip. The dead-load compensating blocks were suspended and the entire span was prestressed to make it self-supporting. The falsework was then lowered and moved under the pier to the center span.

The center span was erected in the same manner as the north span. The span segments and pier segment were erected and then matched with the north span with a cast-in-place closure strip. After suspending the dead load blocks, the second-span tendons and continuity tendons were stressed to make the structure continuous over two-spans. The falsework was then moved to the south span which was erected in a similar manner.

2.4.2 Geometry Control. An instrument stand, fabricated from a hollow structural tube, was erected on top of the south exterior pier. A theodolite was attached to the top of this stand and was positioned directly over the longitudinal bench-mark at Station 75'. A target, at the same elevation as the instrument and in line with the centerline of the structure, was marked on the wall to the north of the structure. Initial sightings were taken on this target to set zeros on the instrument. Vertical elevations were surveyed using a surveying rod with the theodolite in the level position. Longitudinal alignment was sighted directly. The instrument stand remained in position until just prior to erecting the south exterior pier segment. Alignment of the south exterior pier segment was achieved using a temporary instrument setup on the bridge structure.

2.4.3 Temporary Post-Tensioning. During erection, the segments were positioned on the falsework, carefully drawn together, and if epoxy was used, stressed together. To pull the segments into their match-cast position, and to provide a contact pressure for



- STEPS:**
- Erect North Span Segments on Falsework
 - Stress Tendons 1A, 1B
 - Erect Center Span Segments on Falsework
 - Stress Tendons 2 & 3
 - Erect South Span Segments on Falsework
 - Stress Tendons 4A, 4B, 5 and Top Internal Tendon

Fig. 2.18 Span-by-Span Erection System

the epoxy to cure, temporary post-tensioning was required. This stress had to be maintained until the permanent tendons were stressed.

To ensure that joints will not open before the permanent tendons have been stressed, a residual compressive stress is desirable. Minimum specified residual compressive stresses range between 50 and 75 psi [14] and are dependent on the segment weight, and exposure condition. A value of 50 psi was used for design of the temporary post-tensioning and supporting falsework.

The temporary post-tensioning is applied to the segments in two stages. After applying the epoxy to the segment joints the segments must be drawn back into their original match-cast position. This first stressing stage requires side-to-side adjustment so that segment joints can be closed evenly. After full contact is achieved, the second stage of stressing is applied to induce a minimum residual compressive stress at all epoxied joints. To achieve the desired stress distribution in the segments, it was also necessary to have top-to-bottom adjustment. The total time period available for stressing (stage 1 and 2) is limited by the pot-life of the epoxy. A complex valve assembly was used to change quickly from horizontal to vertical adjustment.

The temporary stress was applied to the concrete segments through heavy steel brackets. These brackets were clamped to the top and bottom of the segments by vertically stressing 2-5/8" diameter DYWIDAG bars. To increase the frictional force between the steel bracket and the concrete segment a hydrastone layer was cast at the interface. The brackets were clamped to segments at four locations along the span. With nine joints between ten segments, three joints were closed in each stressing operation. This was considered to be the maximum number of joints that could be epoxy coated, closed, and stressed within the usable life of the epoxy.

The longitudinal stress was applied by stressing 4-5/8" diameter DYWIDAG bars between the brackets. The segment at the north end was held in position on the shoring and segments were added and temporarily prestressed, three at a time. DYWIDAG rod couplers were used to extend the rods for the full span length.

2.4.4 Erection Falsework. As described above, a stiff shoring girder consisting of two 18-inch steel wide flange sections supported at approximately 5 feet on center, was chosen in conjunction with the temporary post-tensioning system. The two 18-inch steel beams were centered under the webs of the concrete box section and were braced together to act as a single shoring girder. The heavy shoring girder was supported on light-gauge rented shoring and was continuous between faces of adjacent piers.

The concrete segments were erected on wooden blocks resting on variable-height steel spacers which were bolted to the heavy shoring girder. The steel spacers were necessary to allow the temporary post-tensioning hardware to slide forward during closing of the segments. The concrete segments were also laterally restrained.

2.4.5 Segment Joints. A primary interest of this test program was to investigate the effect epoxy jointing material had on ultimate load behavior. Its use has been prescribed in bridge structures to provide a reserve against joint openings caused by unusual load cases or calculation inaccuracies. The possible benefit to ultimate load behavior is unknown and will be examined herein.

To study the effects of epoxy on service, moderate overload, and ultimate load behavior, one exterior span was constructed with dry joints and the other with epoxy joints. This provided two otherwise identical spans in which behavior could be compared directly. The interior span was constructed with epoxy joints to provide the possibility for additional testing of epoxy jointed segments. The layout of epoxy and dry joints is shown in Fig. 2.7.

The epoxy jointing material must meet three general requirements: adequate tensile and compressive strength, minimum usable time, and viscosity [15]. The epoxy must transmit compressive stresses across the joint plus provide a tensile capacity between match-cast segments. Ideally, the epoxy should develop a tensile capacity higher than the adjacent concrete. This forces the segmental girder to behave more as a monolithic beam. The second requirement of the epoxy involves the method of segment erection and epoxy application. The epoxy must remain workable for a minimum time period for a certain range of ambient air temperature to enable organized assembly of the segments. The epoxy must be applied to all matching surfaces and the joints must be closed and temporarily stressed, all within the working life of the epoxy. The epoxy application process was practiced using water on the dry north span to ensure time limits could be met. Finally, the epoxy must have the proper consistency to be properly applied, and the necessary viscosity to not drip onto the area below the bridge.

Several brands of segmental application epoxies were investigated prior to use in the model structure. The epoxy was tested by comparing modulus of rupture tests for monolithic and match-cast specimens. A 6 x 6 x 20 in. concrete prism was match-cast in two halves. Characteristic monolithic prisms were cast from the concrete used for each beam half. The debonding agent used on the typical segment faces was used on the match-cast face. A central duct was cast in the specimens to enable stress to be applied during closing. The matching faces of the specimens were cleaned and prepared in the same way as the segment faces, and epoxy was applied to both matching faces. A uniform stress of 50 psi was applied to the joined face and remained in place for a minimum of four days to ensure the epoxy had fully cured. A standard modulus of rupture test was conducted on all specimens. A third-point loading system was used to minimize shear forces across the joint and to provide a constant moment region so that specimens could break away from the joint. For approval, the modulus of rupture of the joined specimen was required to be greater than 90% of the modulus of rupture for monolithic prisms. Pot-life and workability characteristics were also assessed. The epoxy was delivered to the laboratory in two components (resin and hardener) with mix proportions labeled on the container. Two

types of epoxies were approved for use depending on the ambient air temperature. The mix proportions were preweighed and mixed in a large bowl using a T shaped extension on an electric hand drill. After mixing for a minimum of 3 minutes the epoxy was applied to both matching faces of a segment joint using rubber gloves. After closing the joints, the internal tendons were cleaned of epoxy by inserting a rod with an attached cloth into the internal tendon ducts. The cloths were replaced several times until they came out of the duct clean.

To ensure proper bonding of the epoxy with the underlying concrete, matching surfaces were lightly sandblasted prior to joining the segments. This cleaned off all the residue left from the casting operation, such as bond-breaker, cement laitance, and form deterioration debris, as well as removing loose or soft concrete resulting from consolidation or form sealant problems.

A light duty sandblaster was purchased from a local retailer and was used to sandblast all the segments. All matching faces of the typical span segments and pier segments were sandblasted prior to erection. All segments were sandblasted whether they were to be epoxied or not. Preliminary trials revealed that the severity of sandblasting was related to the air pressure, the size of blasting sand used, and the distance from the nozzle to the treatment surface. Proper blasting provided a clean porous surface without removing an excessive amount of the fine concrete aggregate.

2.4.6 Cast-in-Place Closure Strips. At the end of each span between the pier segment and the first span segment, a 3-inch thick cast-in-place (CIP) strip was provided. This CIP closure strip joined the separately precast pier and span segments, and corrected fabrication and erection errors.

In the prototype structure, the closure strip is an unreinforced strip ranging in width between 6 and 10-inches. The web reinforcement was sized and spaced so that the closure strip width was contained approximately within one spacing of the web reinforcement. In this way, web reinforcement was not required in the CIP closure strips. In the model structure, a 3-inch CIP width was chosen as a practical minimum for proper consolidation of this critical joint. The web reinforcement of the typical span segments was spaced at 2-inches to reduce bar sizes and allow for the tight bar-bend diameters required in the 3-inch thick webs. A layer of reinforcement was therefore required in the CIP strip to maintain a constant web reinforcement spacing. A wire was cut from each of the mats of welded wire reinforcement used for the typical segments. These wires were tied together to form a layer of reinforcement within the 3-inch CIP closure strip.

The closure strips were fabricated using plywood forms which closed the space between the span segments and the pier segments. The end of the box void of the last span segment was filled with an expansive polyurethane foam to act as a blockout during

casting. The tops of the bottom flanges outside the web interface were left open to ensure proper consolidation of the critical bottom flange regions.

The internal tendon ducts were supported during casting using threaded pipe nipples. These pipe nipples were welded to the side of the internal tendon ducts and bolted to the plywood for support. The pipe nipples extended from the face of the finished concrete segment and can also be used for grout injection (see section 2.4.8). The strands of the internal tendon ducts were fed through prior to casting the CIP closure strip. The auxiliary tendons were sheathed through the CIP region to prevent bonding.

The concrete was mixed in a 9 cubic foot mixer using a mix similar to the Type 3 mix shown in Table 2.4. A small dosage of super-plasticizer was used to increase the slump to approximately 8-inches. With the high surface-to-volume ratio in the pour strips it was important to moisten the forms and matching segment faces to reduce water loss due to absorption. The super-plasticizer was beneficial in providing a concrete with a high workability that was independent of water loss to absorption.

The concrete was consolidated with a 1-inch diameter immersion vibrator from the top and also from the sides in the bottom flange regions. After initial set was achieved, all exposed surfaces were covered with burlap and a plastic sheet. The burlap was kept continuously moist for a minimum of 4 days and then the forms were removed.

2.4.7 Post-Tensioning Methods. Three general types of post-tensioning tendons exist in the model bridge structure. The external tendons consist of single span 5-strand tendons used for erecting each span, and double span 2-strand continuity tendons used to increase service load strength. The final type of tendons used in the model are the internal tendons which were stressed from the extreme ends after the structure was fully constructed.

The jacking force was controlled for all stressing operations by using a visual pressure gauge and an electronic pressure transducer. Approximate force changes during stress increments were controlled visually by reading the pressure gauge. Exact jacking forces were measured with the pressure transducer connected to a strain indicator box. Each hydraulic setup (rams, hoses, pumps, pressure gauges and transducers) used during construction of the model was calibrated prior to applying force to the tendons. This is recommended since it acts as a pressure check of the hydraulic system as well as providing a condition check of the pressure gauges and transducers.

Two basic setups were used for stressing the 5-strand external tendons. For tendons 1a and 1b of the north span, the tendons were stressed using two 200-ton rams that were pressurized by the same pump in parallel. This is not a recommended setup since the hydraulic oil went to the location of least resistance. The piston movement on both rams was erratic with the pistons stopping and starting as resistances in the rams and

tendons changed. Also, ram travel was exceeded on one of the rams while stressing tendon 1a and was not immediately noticed because oil continued to be pumped to the other ram.

For stressing the remaining 5-strand tendons (2, 4a, and 4b) a 100-ton ram and a 200-ton ram were operated simultaneously. Each ram was operated separately with its own pump and pressure control system. Far better control was achieved by using the two separate setups. Differences between the two sides were noticed immediately by the pump operator and jacking forces were known at all times for both rams. Side to side control of jacking force was achieved automatically.

To reduce the prestress losses due to wedge set in the anchor head, a special chair was designed to incorporate a hydraulic seating device. A small 25-kip hydraulic ram was used to apply force to a lever bar. The lever bar was tied to the chair at the back and pressed against the anchor wedges at the front. A force of 4.5-kips was applied to each wedge prior to releasing the tendons. This hydraulic seating device was tested prior to use in the structure, and the anchorage set after hydraulically seating the wedges was measured to be approximately 1/8-inch.

For the first tendon stressed, the wedges were hydraulically seated and the tendons released. In an attempt to reduce anchorage set even more, the tendons were restressed to the jacking force and the "power seating" device was applied again. This applied a local surface shear to the previously seated strands which caused a wire to break in one of the strands. Because it was not possible to distress the anchored system, the tendons had to be cut. The tendons were cut in a controlled manner using a 1/8-inch thick cutting wheel on a small hand grinder. Four wires were cut alternately on each side of the structure until all 5 strands (35 wires) had been cut.

The 2-strand external tendons were stressed using a monostrand ram with internal seating device. During the seating process, the internal seating cone extends forward until the ram force bears against the wedges. This forces the wedges into the anchor barrel and reduces the subsequent seating loss.

The two-strand external tendons were stressed by alternately stressing each strand in small increments. This was done to ensure that a stressed strand would not bear against and bind an unstressed strand.

The top interior tendons were also stressed using the monostrand equipment described previously. Because crossing and binding of these strands was not possible they were stressed in one operation to the full jacking force.

2.4.8 Tendon Ducts and Grouting Details. Considerable effort was spent in locating suitable ducting for tendons in the model bridge structure. Since standard post-tensioning ducts were not locally available in the small sizes required it was necessary to examine other avenues of supply. The ducting consisted of two basic types. The locations

where tendons were within the concrete section (internal tendons) ideally required a duct with a ribbed profile for interlock, water-tightness for casting, and rigid enough to maintain its alignment during casting. In the locations where tendons were external to the concrete section, the duct was required to withstand an internal pressure of approximately 100 psi to avoid splitting during grouting.

There were two types of tendons that were internal to the concrete section. At the corners of the box and at the ends of the flanges were internal tendons with a straight profile between the ends of the structure. To facilitate feeding of the strands through these long continuous tendons it was critical to have a rigid duct that would hold its alignment in the forms. A profiled duct with sufficient rigidity was not located so a smooth thin walled electrical conduit was used. The bottom internal-tendon ducts were flattened to fit through the layering of reinforcement in the bottom flange.

The second location where tendons were internal to the concrete section was where the external tendons passed through and were anchored in the pier segments. In these locations, the tendons had sharp curvatures, and a ribbed profile was desirable to improve the stress transfer from the strands to the concrete section. In these locations a water-tight flexible electrical conduit was used as ducting. This ducting had a coiled metal profile similar to conventional post-tensioning ducts, except with a relatively larger rib profile.

The external tendon ducts consisted of two basic types. In the inclined portions of the draped tendons a polyethylene pipe was used. This pipe was similar to the pipe used in prototype construction. In the midspan regions, where the external tendons were parallel to the bottom flange, a flexible electrical conduit was used as ducting. This profiled ducting was used to facilitate the possibility of bonding the external tendons to the midspan regions of the bottom flange in future tests.

At the locations where the external tendons pass through the segment diaphragms, a short length of thin-walled electrical conduit was used. This conduit was spliced with the external tendon duct and was provided to allow for the possibility of bonding the tendons to intermediate diaphragms. This could possibly reduce the free length of the external tendon and perhaps improve ductility of the system.

All tendons were provided with injection nozzles for filling the ducts with grout. Grouting is done to bond the internal tendons to the concrete section and to provide protection against corrosion for the exposed external tendons. So that instrumentation could be attached to the external tendons, the tendon duct was made discontinuous at three locations on each side of each span. This provided a short length of exposed tendon to which strain gages could be attached. Grout nozzles were provided on both sides of this instrumentation blockout. The open ends of the ducts were sealed for grouting by injecting

an expansive foam into the end. Grout ports for the internal tendon ducts were provided at the cast-in-place closure strips at the end of each span.

The grout mixture used was the standard Texas State Department of Highways and Public Transportation grout mixture used for post-tensioning ducts. It consists of 1 part cement to 1/2 parts water (by weight) with 1 oz per hundred pounds of cement expansive admixture. The grout was mixed in a large grout mixer and then dispensed into a 10 gallon pressure canister. Compressed air was pumped into the pressure canister which forced the grout into the tendon ducts. This compressed air system was used so that excessive pressures would not build up within the tendon ducts.

The external tendons were grouted after the entire structure was erected. The top internal tendon ducts were left ungrouted so that unbonded behavior of internal tendons could be investigated.

CHAPTER 3 INSTRUMENTATION AND DATA ACQUISITION

3.1 General Requirements

The reduced-scale bridge model was instrumented to measure the structural response to applied loads ranging from service level to ultimate strength. Several types of measurements were made to monitor the behavior of the structure during construction and load tests. Applied loads were monitored and reactions were measured to provide a check of static equilibrium as well as to provide information regarding load distribution in the continuous structure. Deflections were measured at key locations and when combined with the applied loads provided important load-deflection information. Local deformations, such as external tendon strains and joint openings, were also measured to determine internal forces and local joint distortions at all levels of loading.

3.2 Data Acquisition

Since a large number of measurements were required to record the behavior of the model, the majority of the data was measured with an electronic data acquisition system. Reactions, applied loads, deflections, and joint-opening behavior were all recorded with the electronic system. Manual readings for deflections and joint distortions were also made to verify and augment electronically recorded data.

3.3 Instrumentation Identification Code

To avoid confusion during testing and data reduction a systematic data identification method was employed. The instrumentation identification code is illustrated in Fig. 3.1. The general form of the code is TYPE-LOCATION-SPECIFIC.

The reactions are designated as Type RX and are located at each of the supporting piers (NE, NI, SI, SE) on either the west or east side. The deflections were measured with either potentiometers, designated as Type DP, or with dial gauges, designated as Type DG, and were located under a particular segment, either on the longitudinal centerline or symmetrically located on the west and east side. The external tendon strains are designated as Type T and are located at a particular segment joint where the tendon strains are measured in a specific tendon on either the west or east side. Joint distortions were measured with either linear potentiometers, designated as Type JP, or with a grid crack monitor, designated as Type JC. Type JP measurements were made at a particular segment joint on either the west or east side. Type JC measurements were made at a specific depth of a particular joint on the west side only.

Basic Form: TYPE - LOCATION - SPECIFIC

TYPE -

RX Reaction Load Cell
 DP Vertical Deflection Measured with Potentiometer
 DG Vertical Deflection Measured with Dial Gauge
 T Tendon Strain Gauge
 JP Joint Opening Potentiometer
 JC Joint Opening Crack Monitor

LOCATION -

SUPPORT DESIGNATION Particular Support
 e.g. NE = North Exterior
 SEGMENT DESIGNATION Particular Segment
 e.g. 5 = Segment 5
 JOINT DESIGNATION Particular Joint Specified
 e.g. (N. Seg., S. Seg.) where N. Seg. and S. Seg. are the segments on the North and South sides of the joint, respectively

SPECIFIC -

Reactions Form: RX - SUPPORT DESIGNATION - SIDE
 Side = West or East
 Deflections Form: D? - SEGMENT DESIGNATION - SIDE
 Side = West, Center or East
 Tendon Strains Form: T - JOINT DESIGNATION - TENDON
 Tendon = Tendon #, West or East, #1 or 2
 e.g. T - (5,6) - (1A.W1)
 Joint Opening Form: JP - JOINT - SIDE
 Side = West or East
 JC - JOINT - DEPTH
 Depth = TF, TW, BW, BF
 TF = Top Flange
 TW = Top Web
 BW = Bottom Web
 BF = Bottom Flange

Figure 3.1 Instrumentation Identification Code

3.4 Instrument Locations

The layout of the permanent instrumentation used during testing of the structure is shown in Fig. 3.2. This instrumentation was the same for all tests and included the instrumentation for reactions, tendon strains, and deflections. The joint distortion instrumentation, shown in Fig. 3.3, was assembled differently for each test. During construction, deflections were measured at the temporary locations shown in Fig. 3.4. The choice of instrumentation type and location is described in detail in the following sections.

3.5 Support Reactions

Reactions were measured at three of the four supporting piers. Web reactions were measured at the two exterior supports as well as at the south interior support (See Fig. 3.2). At each location, two calibrated load cells were used to measure the reaction in each of the segment webs. At the exterior supports, two 100-kip load cells were used, and at the south interior support, two 200-kip load cells were used. The complete bearing assembly was compressed in the testing machine during calibration and the overall compressive deformations were measured. This measured stiffness of the load cell bearing assembly was used for analytical modeling of the supports, (see section 5.3).

3.6 Measurement of Applied Loads

The loads were applied to the structure with two 60-kip capacity hydraulic rams. Hydraulic line pressure was measured using two 10 ksi pressure transducers which were used to control hydraulic line pressure during testing.

3.7 Deflection Measurements

The location of the vertical deflection instrumentation during all load tests is shown in Fig. 3.2. Vertical deflections were measured at each support plus three locations in each span. The center measurements in each span were situated at approximately the location of maximum deflection. The other measurement locations were approximately equidistant from the maximum deflection location and the bearing.

All vertical deflections during testing were measured under the bottom flange, either along the centerline or at two points equidistant from the centerline. At the maximum deflection location, vertical deflections were measured under both of the box-girder webs. At the quarter points, vertical deflections were measured under the centerline of the structure. The vertical deflections of the pier segments were measured at locations 22 in. each side of the centerline, in line with the bearings.

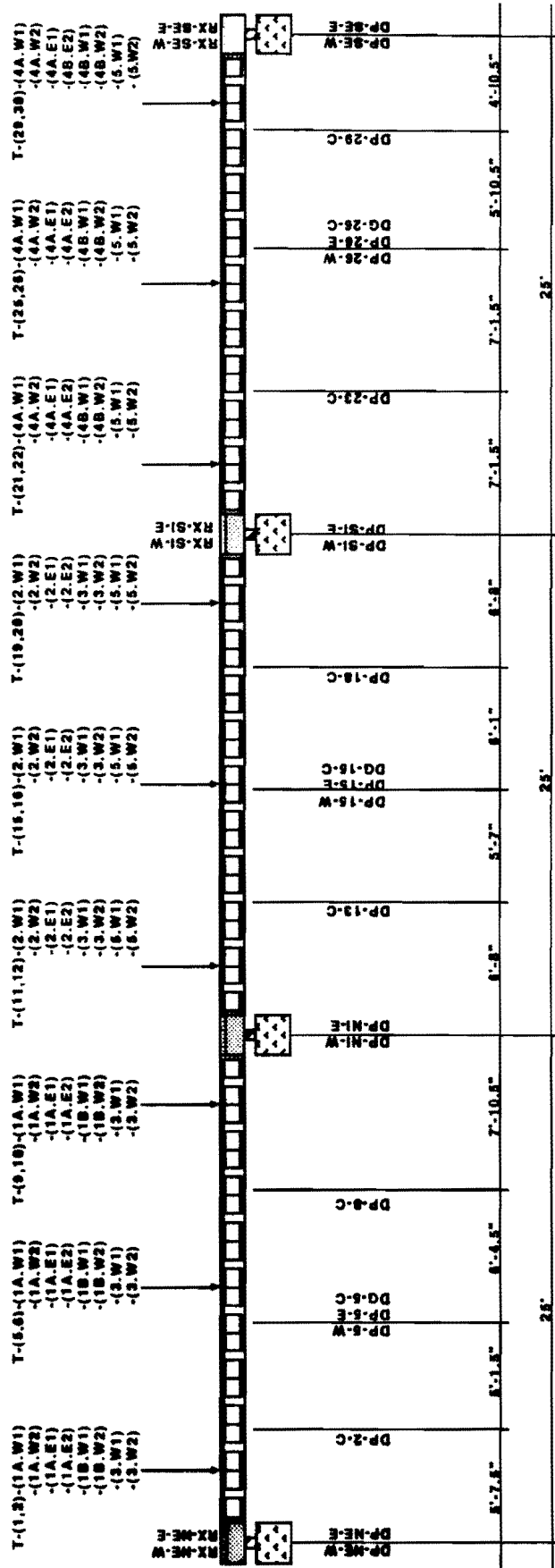
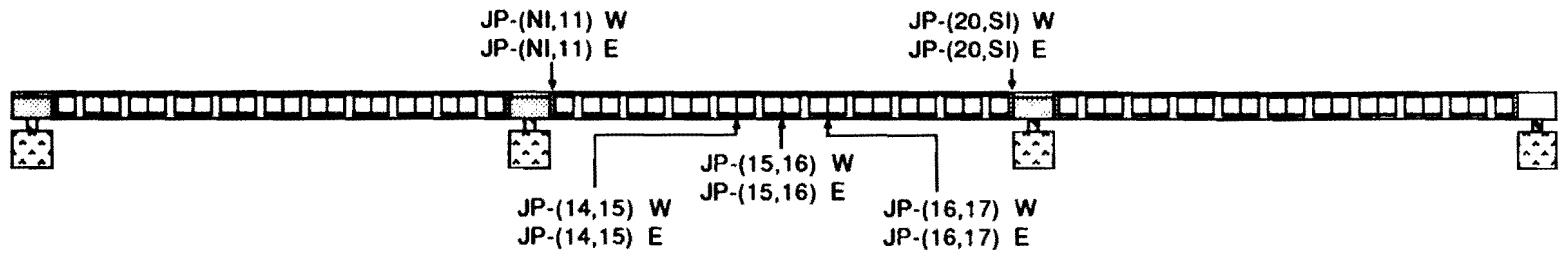
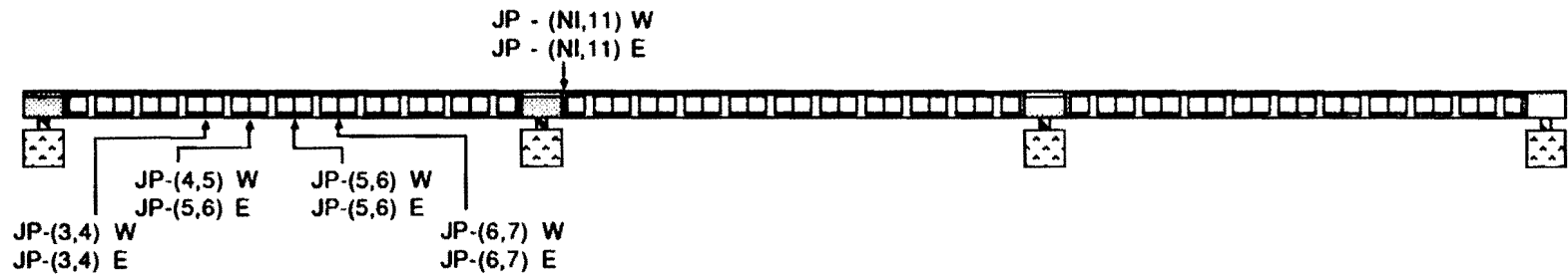


Fig. 3.2 Instrumentation Layout During Testing

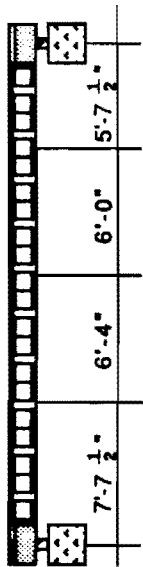


a. CENTER - SPAN TESTS

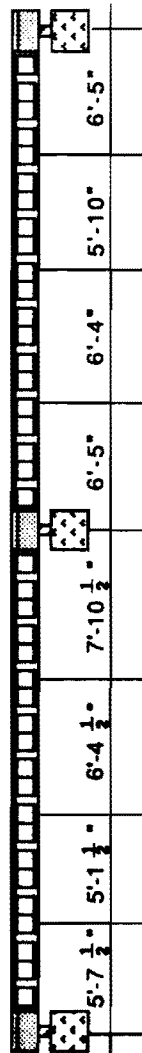


b. NORTH - SPAN TEST (SOUTH- SPAN TEST SIMILIAR)

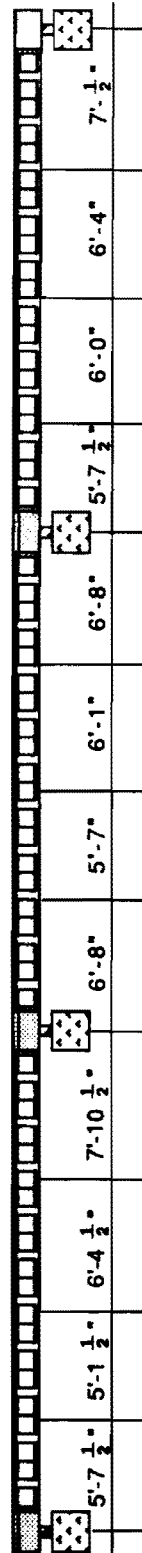
Fig. 3.3 Joint-Distortion Instrumentation



a. DURING CONSTRUCTION OF NORTH SPAN



b. DURING CONSTRUCTION OF CENTER SPAN



c. DURING CONSTRUCTION OF SOUTH SPAN

Fig. 3.4 Locations of Deflection Instrumentation During Construction

During the three stages of construction, vertical deflections were measured at the temporary locations shown in Figure 3.4. Measurements were taken at each support and at three locations along each span. In the span under construction, the longitudinal locations of the measurements were dictated by the instrumentation-stand configuration and the location of the tie-down rods in the test floor. Vertical deflections were measured approximately 6 in. from the edges of the top flange. In the completed north span of the two-span configuration, vertical deflections were measured under the bottom flange along the centerline of the structure at longitudinal locations corresponding to the test locations described above. Vertical deflections of the pier segment were measured as described earlier. To provide additional information related to the torsional response of the structure during erection of the third span, deflections of the completed north and center spans were measured at midspan under the box-girder webs.

Vertical movements of the model were monitored using linear voltage displacement transducers (LVDT, also called potentiometers) and dial gauges which were also used to verify electronic data. The vertical deflection instrumentation was mounted on frames set in a hydrastone bed to ensure firm support.

Horizontal displacements were also monitored during construction and load testing. During construction, the horizontal deflections were measured using dial gauges at each pier segment. A theodolite was also used with a measuring tape to record movements from the theoretical alignment. Horizontal movements were monitored during load tests at the supports and at the center of the span being tested. At the supports, dial gauges measured the horizontal displacement of one side face of the pier segments. At the center of the span being tested, horizontal movements were monitored by hanging a plumb-line from the edge of the top flange to a steel measuring-tape epoxied to the test floor.

3.8 Strand Strain Measurement

The external tendon strains were measured at nine locations on each side of the three-span structure. The tendon layout is described in detail in Section 2.1.4. In general terms, the tendons drape down from high points over the supports and are horizontal in the midspan regions. Strains were measured in each tendon in the inclined portions near the supports and also in the horizontal region at midspan. Since knowledge of tendon stresses is critical for determination of internal forces, two strain gages were attached to each tendon at each location. To reduce the total number of strain gages, all three tendons were instrumented at each location on the west side while only one tendon was instrumental at each location on the east side.

The strain in the post-tensioning strand was measured by attaching a small 0.16 in. by 0.24 in. resistance-type strain gauge to a single wire of a strand in a multistrand tendon. The strain gauge was chosen to fit cleanly on a single wire of a 3/8 in. diameter,

7-wire post-tensioning strand. The strain gages were mounted on the strands after the multistrand tendon had been pulled through the duct, and before the tendons were stressed. At a particular location, strain gages were attached to two randomly selected, accessible wires from different strands of a particular multistrand tendon. Strain gages were not necessarily attached to the same wire (or strand) along the length of the tendon.

3.9 Joint-Opening Measurement

Distortions along the height of segment joints were measured during load tests. Critical joints were determined for each test-load case using both an elastic analysis and a plastic mechanism analysis, as described in Chapter 5. The critical joints for center-span tests, shown in Fig. 3.3a, include three joints in the midspan region and two joints in the support regions. The critical joints for the north exterior-span tests, shown in Fig. 3.3b, include four midspan joints and one joint near the support. The critical joint in the support region is on the interior side of the north interior pier-segment, as discussed in section 5.2. The critical joints for south exterior-span tests appear as the mirror image to the north span.

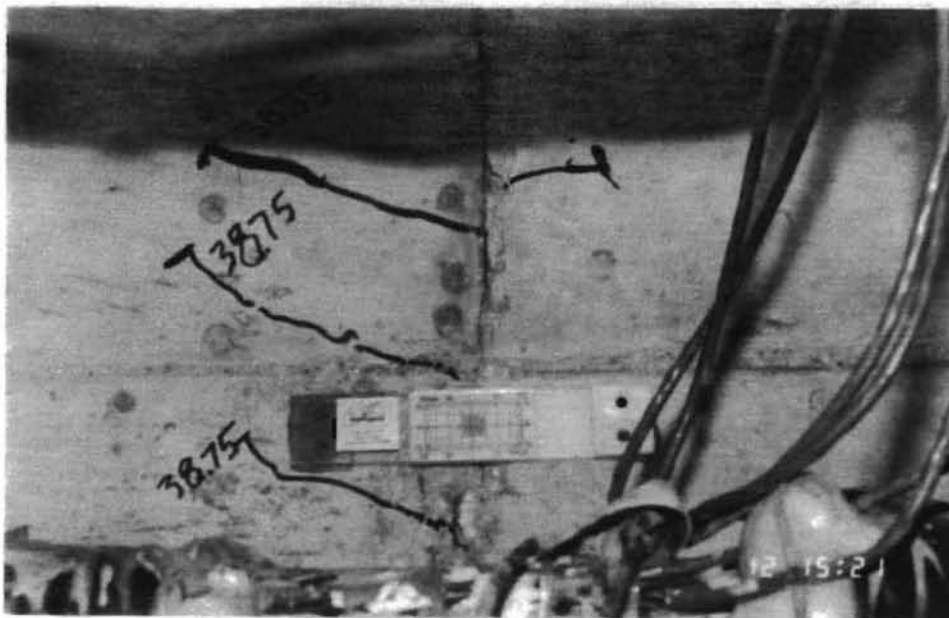
Two types of instrumentation were used to measure the behavior of joint regions at higher load levels. Linear voltage displacement transducers were mounted on the flange of the tension side of critical joints using a plexiglass bracket. The bracket, shown in Fig. 3.5a, was epoxied to the concrete segment, and held the potentiometer parallel to the concrete surface. The potentiometer extended across the joint to a light-gauge steel angle epoxied to the adjacent segment.

To measure distortions at various depths of the joint, a grid-type crack monitor was used. This device, shown in Fig. 3.5b, consists of overlapping planes of plexiglass, each with a matching grid. Relative displacement of the centers matching grids reflected the amount of joint opening at the level of the crack monitor. Close upviews were obtained by sighting through a telescopic instrument. Very small movements could be recorded by averaging the relative movements of the grids at the extreme edges of the crack monitor. Approximate joint rotations were also calculated from the relative grid movements.

The crack monitors were attached at several locations along each joint. For bottom-opening joints, crack monitors were provided at the top and bottom of the vertical portion of a web as well as on the end of the bottom flange, as shown in Fig. 3.6a. The locations of each of the crack monitors, and bottom- flange potentiometers, for critical joints are tabulated in Fig. 3.6a. For top- opening joints, the inclined tendons did not allow access to the web regions, so a single crack monitor was used on an end of the top flange, as shown in Fig 3.6b.

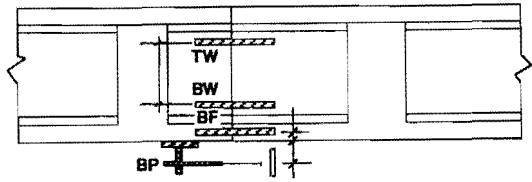


a) Joint Opening Potentiometers

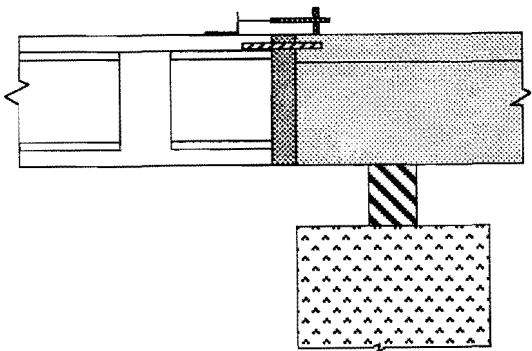


b) Crack Monitor

Fig. 3.5 Joint Opening Instrumentation



a. BOTTOM OPENING JOINT



b. TOP OPENING JOINT

Distance from Top (inches) *

LOCATION	JOINT				
	(3,4)	(4,5)	(5,6)	(25,26)	(26,27)
Top Web	6.95	7.00	7.05	7.11	7.12
Bottom of Web	11.01	11.06	11.11	11.17	11.18
Bottom of Flange	15.12	15.18	15.19	15.10	15.15
Bottom Potentiometer	17.65	17.71	17.72	17.63	17.68

*Calculated from measured segment dimensions

Fig. 3.6 Joint Opening Instrumentation

CHAPTER 4

BEHAVIOR OF STRUCTURE DURING CONSTRUCTION

The model structure was instrumented during construction, and measurements were taken during the erection process. This construction data provided vital erection control information and a history of behavior of the structure for determination of the final in-situ condition. The construction data also provided important practical information regarding construction of segmental structures of this type.

This chapter summarizes observations made during the construction process. Tendon stresses were determined from strand strain measurements, and observations were made regarding friction losses. Model deflections were monitored throughout erection, and observations were made concerning the interaction of the shoring system with the bearings. Finally, web reactions were measured at the end of construction, and unequal web reactions are discussed.

4.1 Stressing Observations

The tendons were stressed using the methods and equipment described in Chapter 2. The tendon designation, eg. Tendon 1a, refers to a pair of multistrand tendons located symmetrically on each side of the structure. The two tendons were stressed simultaneously so that lateral bending stresses would not be excessive. Stress was applied slowly to the tendons while constantly advancing the wedge anchors. The tendons were stressed to a jacking force, P_j , of approximately 75 to 80 percent of the nominal tendon capacity. Data was recorded at the following ram force increments: 0, $0.1 * P_j$, $0.25 * P_j$, $0.40 * P_j$, $0.60 * P_j$, $0.80 * P_j$, and P_j . Ram travel was also measured at each of these load stages.

In spite of the careful stressing procedures and the use of strain gages on some strands, two problems exist that make the estimation of average tendon stress difficult. The first problem was investigated by Yates [18], who found that in a stressed 7-wire prestressing strand the individual wires have appreciably different stresses. In Fig. 4.1, nominal strand stress is plotted against measured strain in the 6 exterior wires of a 7-wire strand. Initially, as the strand gripping system engaged wires of the strand, each wire picked up load at a slightly different rate. Once all wires were fully anchored, all wires strained at an equal rate. The average of the six measured strains was linear and passed through the origin. However, results from a single gage could give a misleading value of tendon stress.

A second problem in estimating the average tendon stress is similar to the above, since each strand within a multistrand tendon could have slightly different stress. The temporary anchorage system of the stressing ram fully engages each strand at a slightly different force level. After all the strands are fully engaged, they should exhibit similar

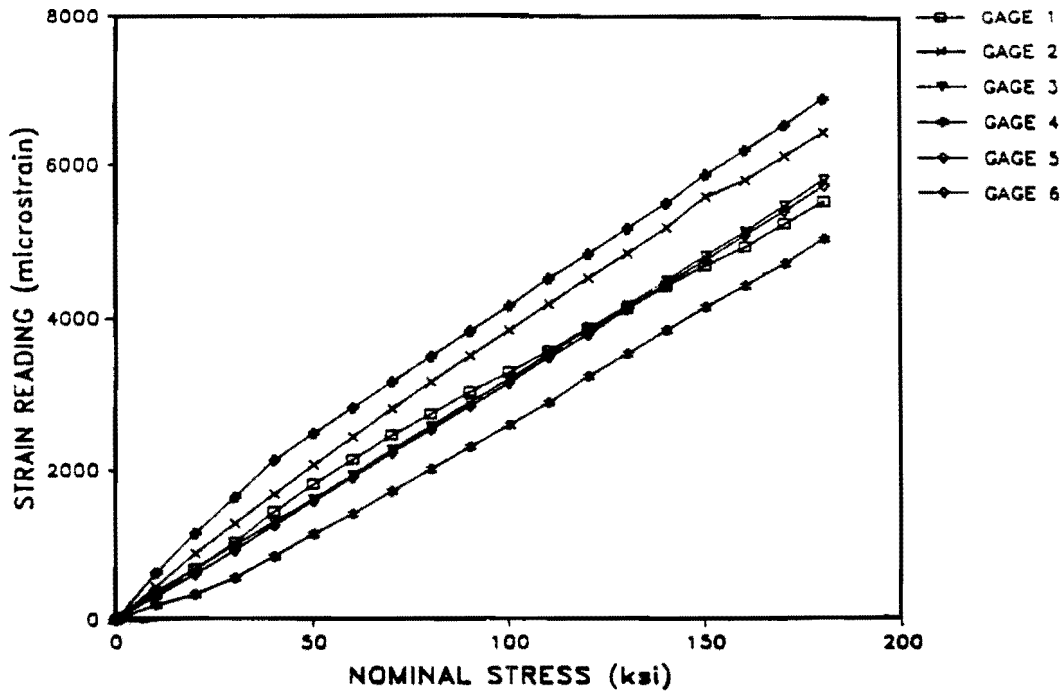


Fig. 4.1 Strain Gage Calibration Results (Ref. 18)

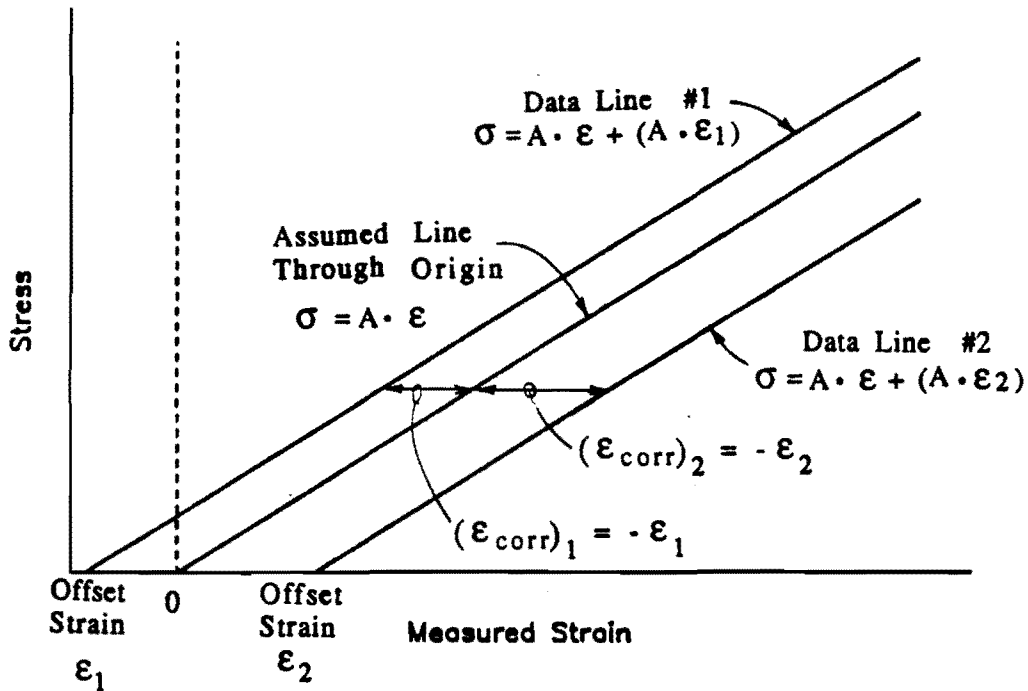
stress strain behavior, with the average of all the strands providing the average tendon stress that lies on a line passing through the origin.

The correction of both of these problems is achieved by applying a linear transformation to each data line. This process transforms each data line to a line passing through the origin, with each line having a slope equal to the average of all data-line slopes. Ideally all lines are parallel, so the linear transformation reverts to the addition of an offset, as shown in Fig. 4.2a. If the data lines are not exactly parallel, then the linear transformation also includes a slope correction, as shown in Fig. 4.2b.

The method used to estimate the average tendon stress from the measured strand strains follows this general procedure. A comparison was made between the jacking force at the live end of the tendon and the measured strains from two gages attached to wires in a tendon at a particular location. In most cases, this yielded two approximately parallel lines, as shown in Fig. 4.3a, with the lines offset from the origin by some initial strain. The corrected average tendon strain was assumed to lie on a line passing through the origin and having a slope equal to the average slope of the two data lines. A linear transformation algorithm was then developed to transform each data line to the assumed average line. The average tendon stress was then calculated using the apparent elastic modulus of 30,300 ksi determined during calibration and described in Chapter 2.

NOMINAL TENDON STRESS vs MEASURED STRAIN

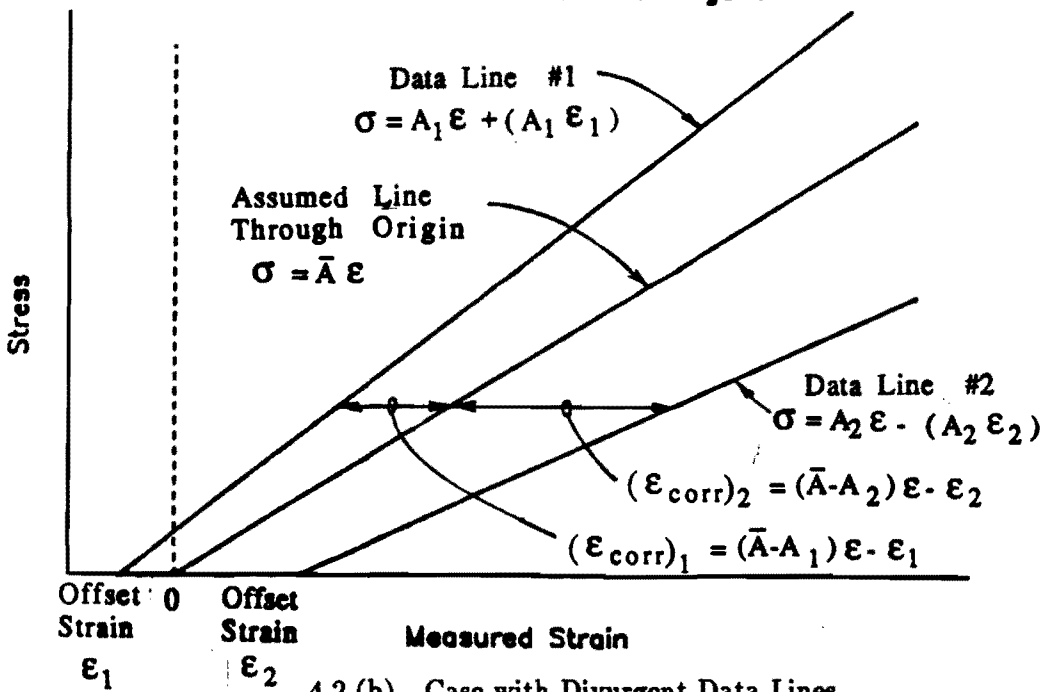
Parallel Data Lines



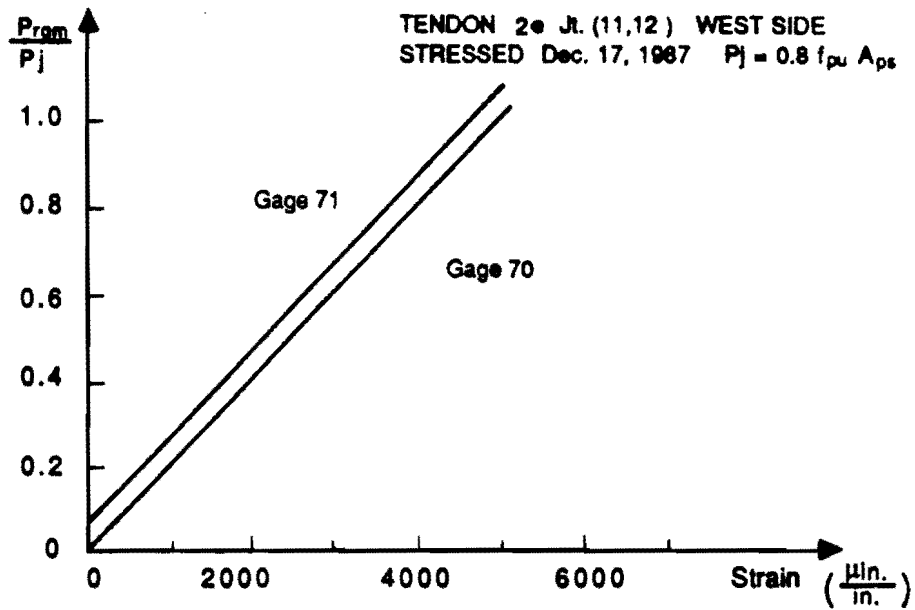
4.2 (a) Case with Parallel Data Lines

NOMINAL TENDON STRESS vs MEASURED STRAIN

Data Lines Divergent



4.2 (b) Case with Divergent Data Lines



a. Typical Case with Approximately Parallel Data

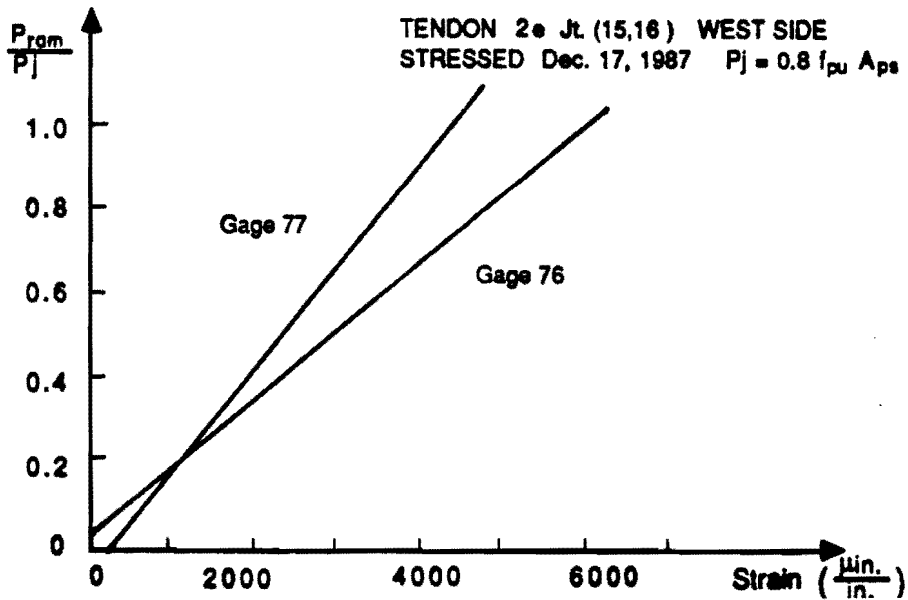


Fig. 4.3 Measured Data Corrections

In a few cases the two data lines were divergent. The worst case is shown in Fig. 4.3b. It is unknown why this happened, but may have partially been caused by incorrect application of the gages to the strands. The average tendon stresses for these strands were calculated using the same procedure as above.

Tendon elongations were measured during stressing by recording the travel of the prestressing ram. The measured elongations ranged from 95 to 108 percent of the calculated elongations (using an apparent elastic modulus of 27500 ksi).

Typical tendon stress profiles (here during stressing of Tendons 4a and 1a) are shown in Fig. 4.4. Similar plots for the remainder of the tendons are contained in Ref. 5. In these plots the tendon stress is plotted at locations along the span. The solid lines represent the theoretical tendon stresses for a jacking load, P_j , at the live end. These lines were determined from the tendon angle changes, α , and an angular friction coefficient, μ , using the exponential reduction equation in the AASHTO Bridge Specification [13]. The upper and lower lines represent the calculated tendon stresses with angular friction coefficients of 0.20 and 0.40, respectively. Because the majority of the tendons are external to the concrete, wobble effects were assumed as zero during calculation of frictional losses.

The measured tendon stresses are also plotted for jacking forces of $0.40 \cdot P_j$, $0.80 \cdot P_j$, P_j , and after releasing the tendon. Several observations can be made from the tendon stress profiles. First, there appears to be a reduction in stress at the live end of the tendons. In all but one case the measured stress closest to the live end was lower than calculated considering friction. This reduction could be caused by a number of factors including high friction in the pier-segment ducting, friction at the tendon-duct/anchorage transition, or friction between strands and wedges, or strand and the anchor-head at the live-end anchor. These problems were possibly aggravated by model details, but similar reductions were also noticed by Quade [19] using standard industry hardware. Research is needed to quantify friction losses within standard industry anchorage hardware as well as at locations of high duct curvature.

A second observation that can be made from the tendon stress profiles is the apparently low friction between the tendons and deviators. In most cases, after the initial loss at the live-end anchorage, tendons exhibited small losses along the remainder of the span. The angular friction losses through the deviators in most cases were less than predicted using $\mu = 0.20$. Additional research is needed to quantify friction losses through concentrated angle changes at deviators.

Tendon 1a was stressed by simultaneously pressurizing two rams with one pump. After the tendons were stressed to their full jacking force, the load was held while the anchor wedges were hydraulically seated. This process took almost an hour, during which time the stress in the west side tendon, shown in Fig. 4.4b, reduced to approximately 93 percent of the original stress. Even though the hydraulic line pressure was maintained, the

ram force did not remain constant. The reason for this drop in stress is unknown, but may likely be attributed to the interaction of hydraulically-linked rams and the friction in the individual rams. All subsequent tendons were stressed using an independent system for stressing each of the two multistrand tendons.

4.2 Tendon Stress History

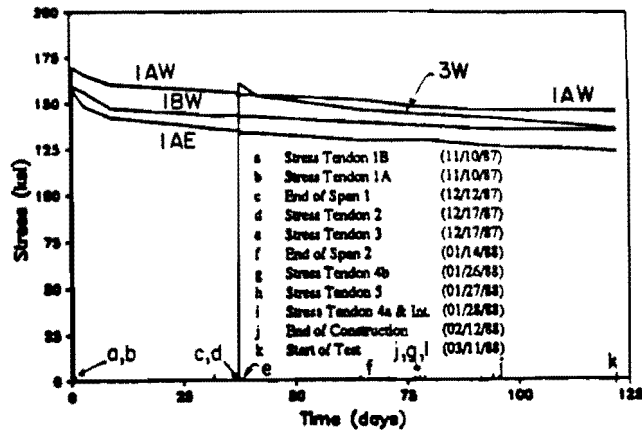
The measured tendon stresses at the center joint of each span during the three stages of construction are shown in Fig. 4.5. The time scale was chosen to correspond with the construction time of 122 days between stressing the first tendon, Tendon 1b on November 10, 1987, and starting the load tests, on March 11, 1988. Key times during the erection process are shown on the time scale and are described in the figure notes. The measured prestress losses at 3 days, 7 days, 28 days, and before initiation of testing, are shown in Table 4.1 for all tendons.

Measured prestress losses for the north and center spans were approximately the same at 28 days. Because of erratic data in center span tendon 2W at the time testing began, averages could not be compared. Losses in the south span were typically smaller than in the other two spans. This difference may have been caused by reduced creep in the concrete of the south span. Also, a different concrete supplier was used for the segments in the south span.

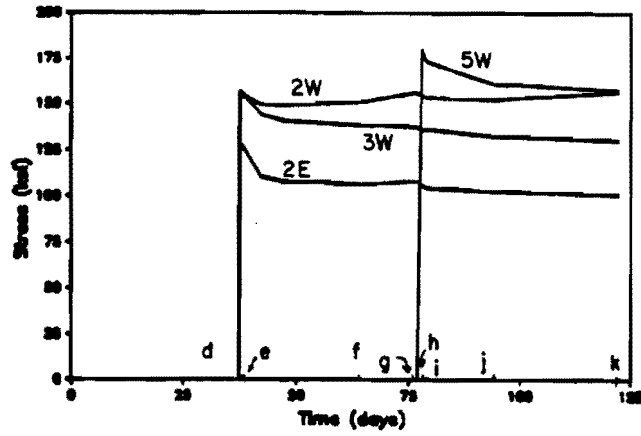
4.3 Deflections

The deflections of the model structure were monitored during all stages of construction with the instrumentation described in Section 3.7. The measured deflections, at key times during construction, are shown in Fig. 4.6. The deflections are plotted for each structural configuration with the initial deflections in each case equal to zero. The deflections that are shown are therefore the deflections occurring during the particular structural configuration. The final deflections from each of the three construction stages were then superimposed. The deflected shape of the completed structure is shown in Fig. 4.7. Time dependent deflections continued to occur while testing procedures were being finalized. The final pretest deflected shape is also shown in Fig. 4.7. The results from an elastic analysis are also shown for each stage of construction and for the final pre-test condition.

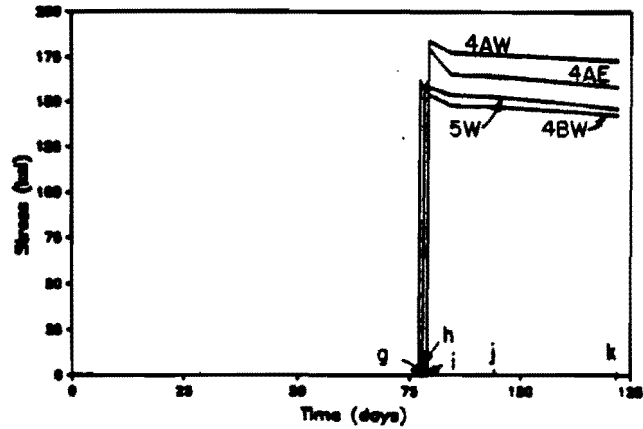
TENDON STRESS vs TIME



(a) North Span Tendons at Joint (5, 6)



(b) Center Span Tendons at Joint (15, 16)



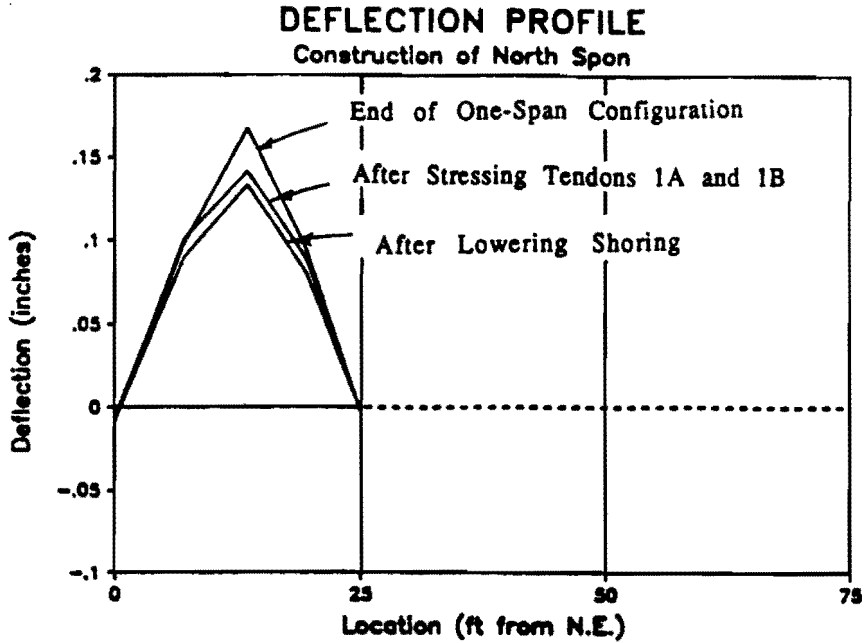
(c) South Span Tendons at Joint (25, 26)

Fig. 4.5 Tendon Stress History

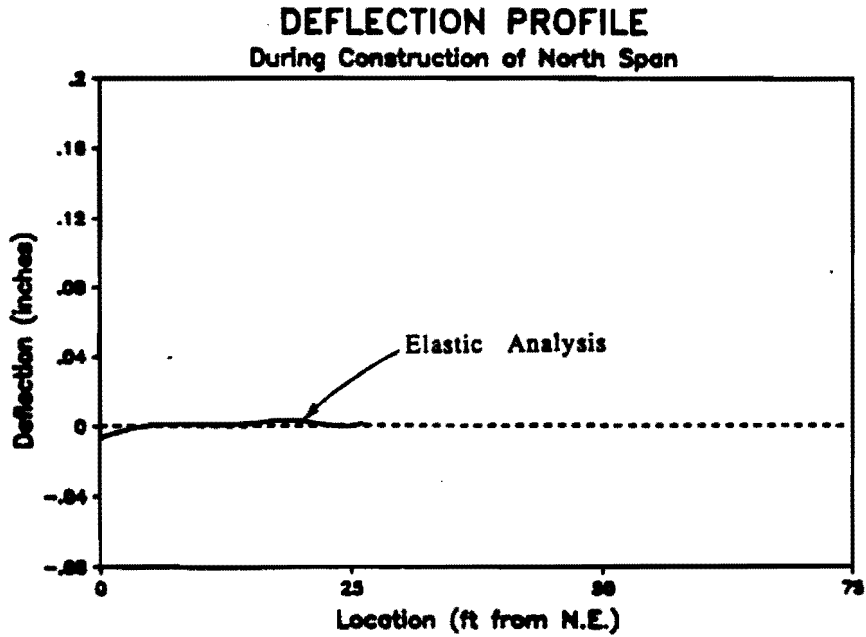
Table 4.1 Summary of Tendon-Stress Losses

Location	Tendon	Stress at Release (ksi)	3 Days Loss (ksi)	% fsi	7 Days Loss (ksi)	% fsi	28 Days Loss (ksi)	% fsi	Start Test Loss (ksi)	% fsi	Age (days)
North Span Joint (5,6)	1aW	169.63	4.03	2.38	7.68	4.53	13.01	7.67	24.29	14.32	122
	1aE	157.17	8.95	5.69	13.11	8.34	20.72	13.18	33.39	21.24	122
	1bW	164.75	8.72	5.29	14.77	8.97	21.69	13.17	29.99	18.20	122
	3W	160.36	5.34	3.33	8.08	5.04	14.64	9.13	24.54	15.30	85
	AVG.			4.17		6.74		10.79		17.27	
Center Span Joint (15,16)	2W	156.27	4.78	3.06	7.46	4.77	5.23	3.35	*	*	85
	2E	130.85	12.64	9.66	21.70	16.58	24.72	18.89	30.07	22.98	85
	3W	156.84	7.32	4.67	14.54	9.27	18.73	11.94	26.60	16.96	85
	5W	179.98	8.35	4.64	19.10	10.61	20.53	11.41	22.43	12.46	44
	AVG.			5.51		10.31		11.40		*	
South Span Joint (25, 26)	4aW	184.06	4.00	2.17	6.91	3.75	7.11	3.86	6.24	3.39	43
	4aE	179.79	8.00	4.45	14.63	8.14	18.52	10.30	21.71	12.08	43
	4bW	162.21	6.94	4.28	14.27	8.80	17.24	10.65	20.20	12.45	45
	5W	158.26	.05	.03	4.58	2.89	8.67	5.48	12.61	7.97	44
	AVG.			2.73		5.90		7.57		8.97	

*Obviously flawed data omitted

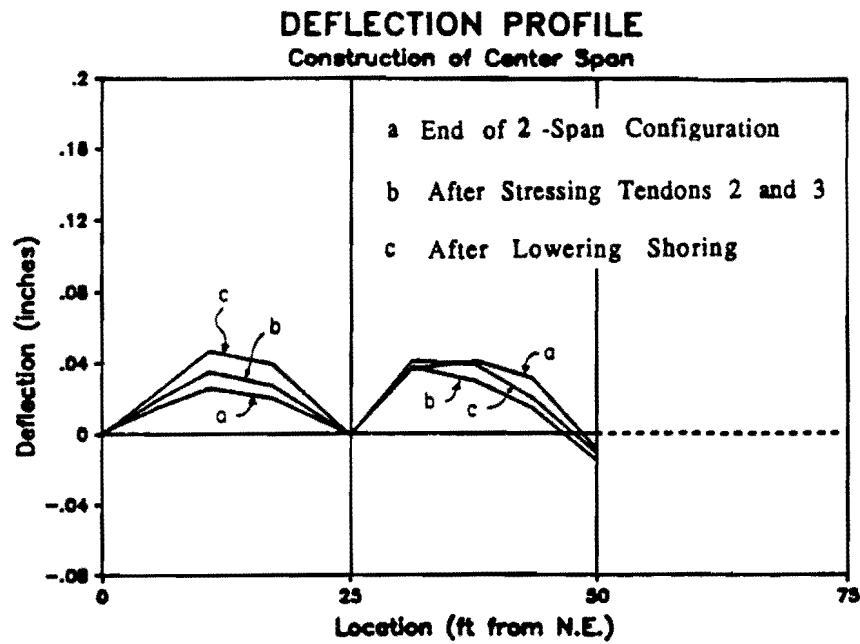


(a) Measured During Construction of North Span

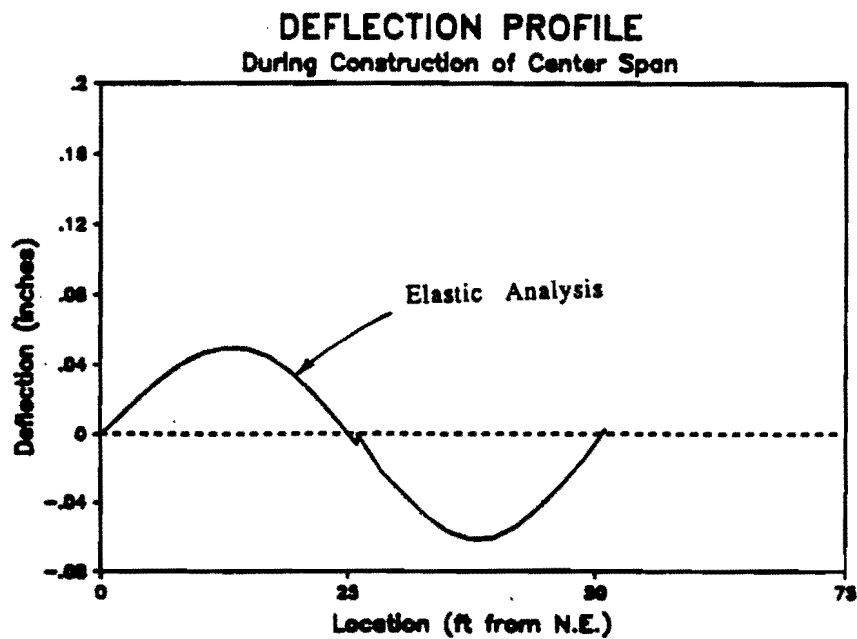


(b) Analysis for Construction of North Span

Fig. 4.6 Deflection Profiles

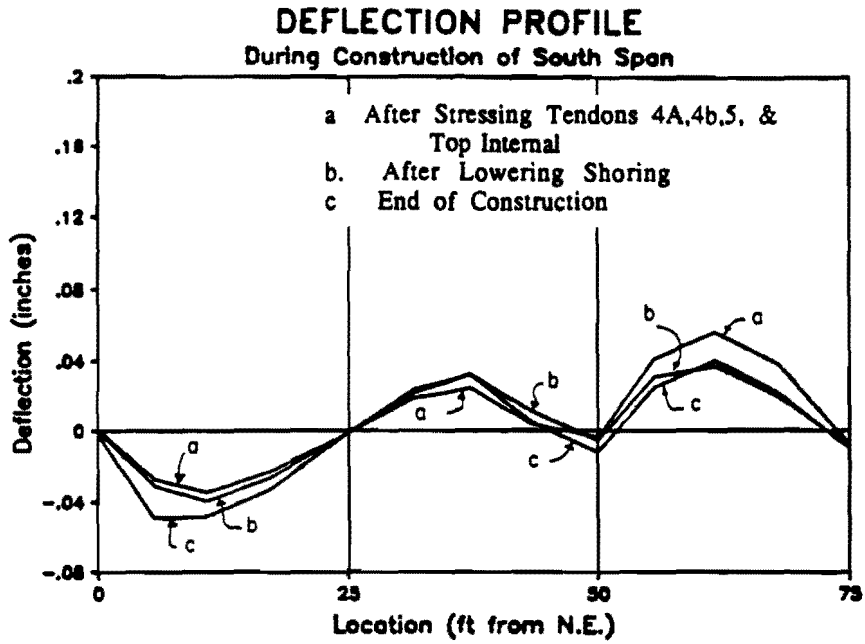


(c) Measured During Construction of Center Span

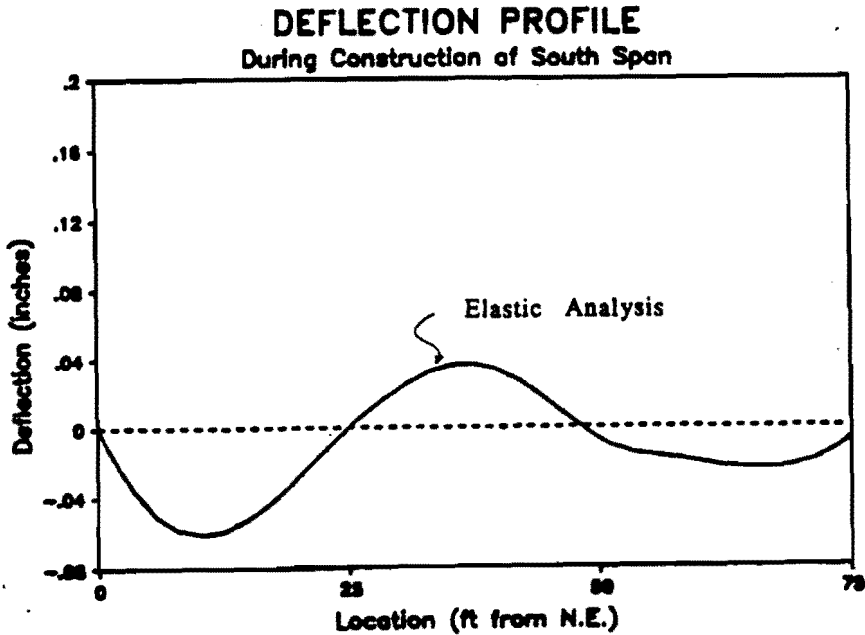


(d) Analysis for Construction of Center Span

Fig. 4.6 Deflection Profiles - continued

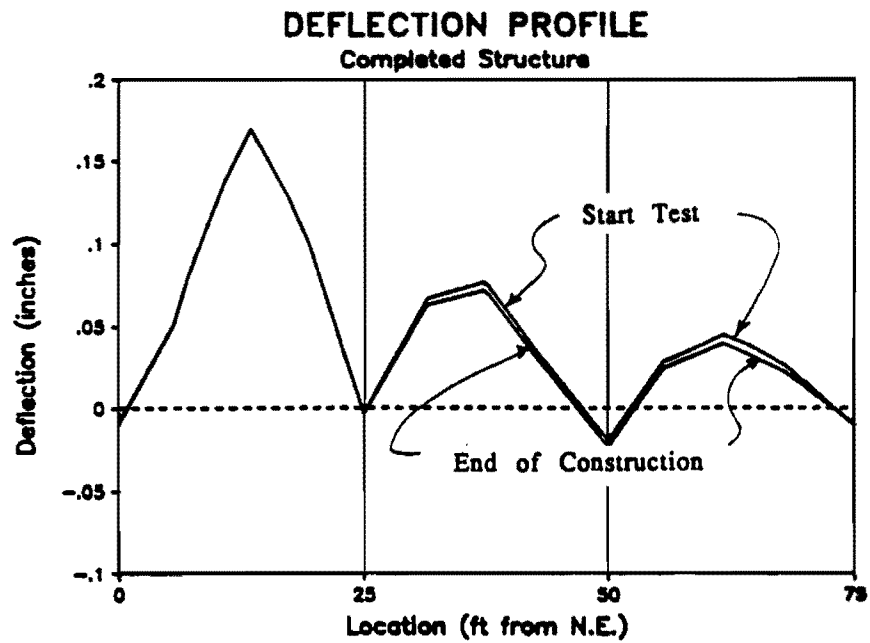


(e) Measured During Construction of South Span

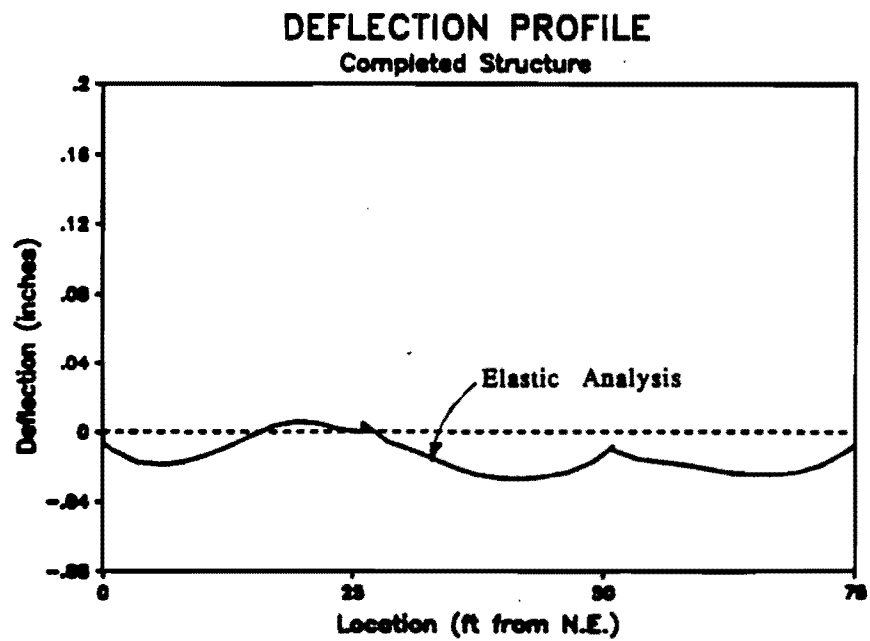


(f) Analysis for Construction of South Span

Fig. 4.6 Deflection Profiles - continued



(a) From Measurements



(b) From Analysis

Fig. 4.7 Resultant Deflected Shape after Construction

spans between the supports. With relatively flexible supports, as with neoprene bearing pads, the structure remains in contact with the stiff shoring close to the flexible support. This phenomenon was evident in all the spans erected. In the north span, the north end was supported on the flexible bearing assembly while the south end was supported on a firm bearing. The north end of the span remained in contact with the shoring while the south end lifted completely off the shoring. In the south span, both ends were supported on flexible bearing assemblies, and subsequently both ends remained in contact with the shoring.

This outward shifting of the contact point has caused problems with prototype construction. A common method of temporarily shoring a span of segments is to use a pair of trusses supporting the segments under each overhanging top-flange. In the initial condition with the span weight carried uniformly along the length of the span, the top-flange moments are small and evenly distributed. As the contact point shifts towards the support, a significant portion of the weight of the span is transferred to the shoring near the support. If this force path is not accounted for, the increased top-flange moments at the contact point can cause flexural cracking in the top-flange. The design of shoring decentering methods must also consider the potentially large forces carried by the shoring following stressing.

4.4 Support Reactions

Reactions were monitored during all stages of construction in an attempt to record the load distribution and the redistribution caused by time dependent effects. Unfortunately, the load cells that were used exhibited a considerable amount of drift with time. Subtle changes in support reactions were clouded by equal or larger variations caused by electrical drift. For example, in the statically determinate single-span configuration, the reactions should remain constant with time. Figure 4.8 shows the variation of recorded reactions at the north exterior bearings for the one-span configuration. The dotted line indicates the theoretical reaction based on measured weights and statics. The measured total reaction immediately after lowering the shoring was equal to the theoretical value. The total reaction remained within approximately 5 percent of the theoretical value for approximately 1.5 days. Over an extended period, however, the measured reactions drifted away from the calculated reaction. The west side exhibited the majority of the drift while the east side remained relatively constant. This drift was noticed in all the load cells and was most pronounced in the older 100-kip load cells. For this reason a continuous record of reactions during erection was not possible.

The drift in the load cell measurements occurred under sustained loads with small deviations occurring in the first day. It was therefore believed that short-term changes in reactions during testing could be adequately measured with the load-cells.

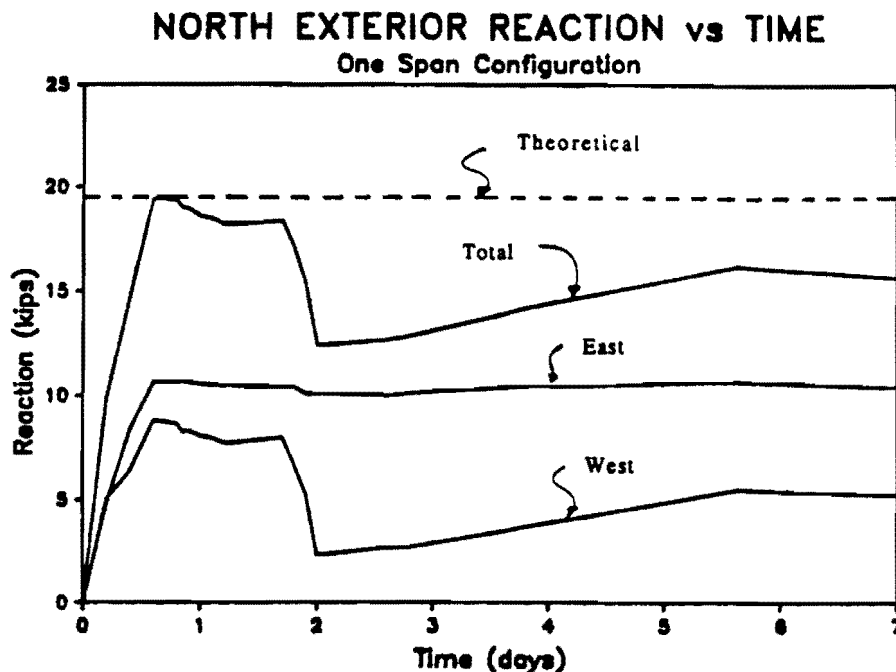


Fig. 4.8 Measurement of North Exterior Reactions

As was discussed in Chapter 2, the measured reactions were modified by hydraulically lifting the pier segments and inserting shims at supports during construction. This was done to equalize reactions under each web at a particular support as well as to equalize the total reactions at the two ends of the structure. Starting at the North Exterior support and proceeding southward, each of the measured reactions were set. Because of the long-term drift in the load cells, each reaction was initialized by lifting the structure from the bearing, taking a zero reading for each of the load cells, and then setting the structure back onto the bearing. This provided an initial reading of the as-constructed condition.

Determination of the force at which the structure lifted from the bearings provided an additional calibration for the measured reactions at the two exterior supports. At the exterior supports the lift-off force was easily determined. As the lifting force is applied to the underside of the pier segment, the reaction force shifts from the bearings to the hydraulic system. Upward movement during this stage is limited to the compressive deformation of the bearing assembly under the reaction force. When the reactive force is finally exceeded, the response changes dramatically. The additional lifting forces are then acting on the end of a long cantilever with a length equal to one span. The structure becomes very flexible, with small changes in lift-force causing relatively large upward movements at the pier segment. The dramatic change in load response is clearly seen in Fig. 4.9 for lift-off at the north exterior support.

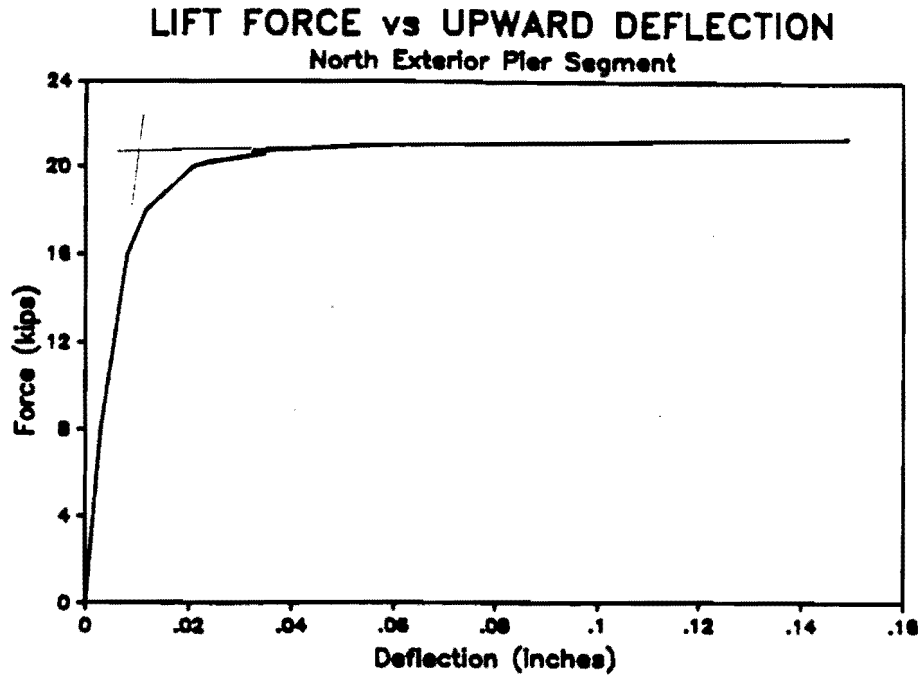


Fig. 4.9 Lift-Off Force Determination

The lift-off force at an interior support is not as easily determined. Once the reactive force is exceeded, then the lifting force is resisted by the structure spanning in both directions. This continuous system is considerably stiffer than the cantilever. Therefore an exact determination of the lift-off force was not determined for the interior pier.

The lift-off forces and measured total reactions (after setting the structure down) are tabulated in Table 4.2 for the two exterior supports. At the north exterior support the lift-off force was measured to be approximately 5 percent more than the measured reactions in the load cells. At the south exterior support the lift-off force was measured to be approximately 80 percent of the reactions measured by the load cells. Since the lift-off force was measured precisely with rams calibrated immediately before the procedure, this force was believed to be accurate. Reactions at the north and south exterior piers were therefore corrected by the factors of 1.05 and 0.80 respectively.

Table 4.2 Exterior Reaction Corrections

Location	Lift-off Force	Load-Cell Measurement	Correction	Corrected Reaction
North Exterior	20.40	19.40	1.05	20.40
South Exterior	22.40	28.03	.80	22.40

$$(N.E.)_{corrected} = 1.05 * [(N.E.) \text{ load cell }]$$

$$(S.E.)_{corrected} = 0.80 * [(S.E.) \text{ load cell }]$$

This correction was subsequently checked for symmetrical load cases and found to give accurate results. The cause of this discrepancy is not known.

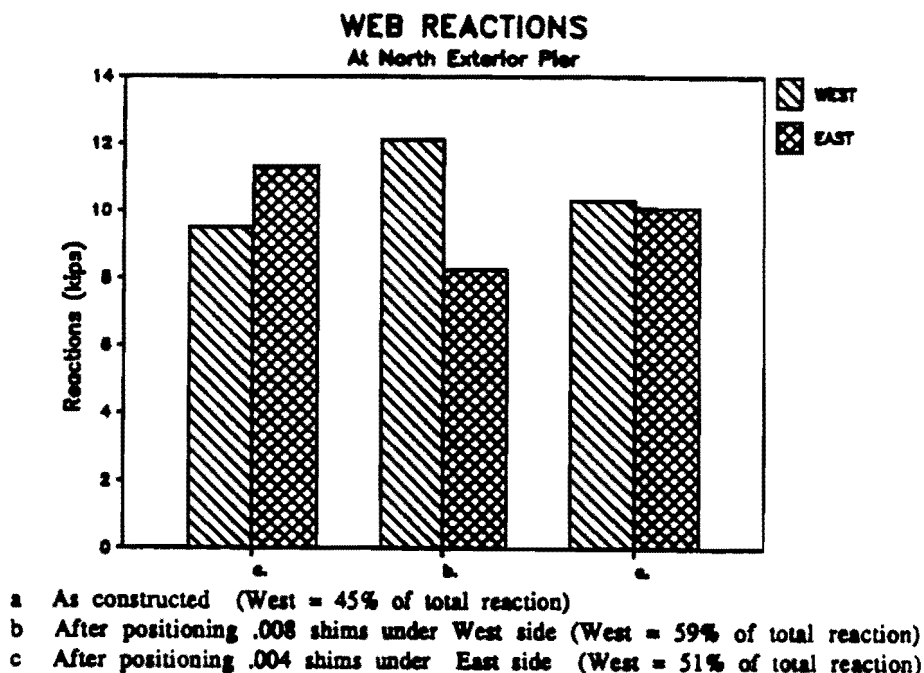


Fig. 4.10 Equalization of North Exterior Reactions

The corrected web reactions at the north exterior and south interior piers during the adjustment process are shown in Figs. 4.10 and 4.11, respectively. The reactions in each of the webs at the north exterior pier after initializing the load cells are shown in Fig 4.10a, with the east side carrying 55 percent of the total reaction. The structure was then lifted and a 0.008 inch thick shim was placed under the west side. This caused the west side reaction to increase excessively, as shown in Fig. 4.10b. The pier segment was lifted again, and a 0.004 inch shim was placed under the west web. This provided approximately equal reactions under each of the webs, as shown in Fig. 4.10c. The reactions under each of the webs at the south interior pier, after initialization, are shown in Fig. 4.11a. The web reactions after positioning various thicknesses of shims are shown in Figs. 4.11b-e.

Figs. 4.10 and 4.11 illustrate the importance of providing the ability to equalize the web reactions after erection. In the constructed condition, the web reactions were not necessarily equal, and in some cases were considerably different. If the web reactions at

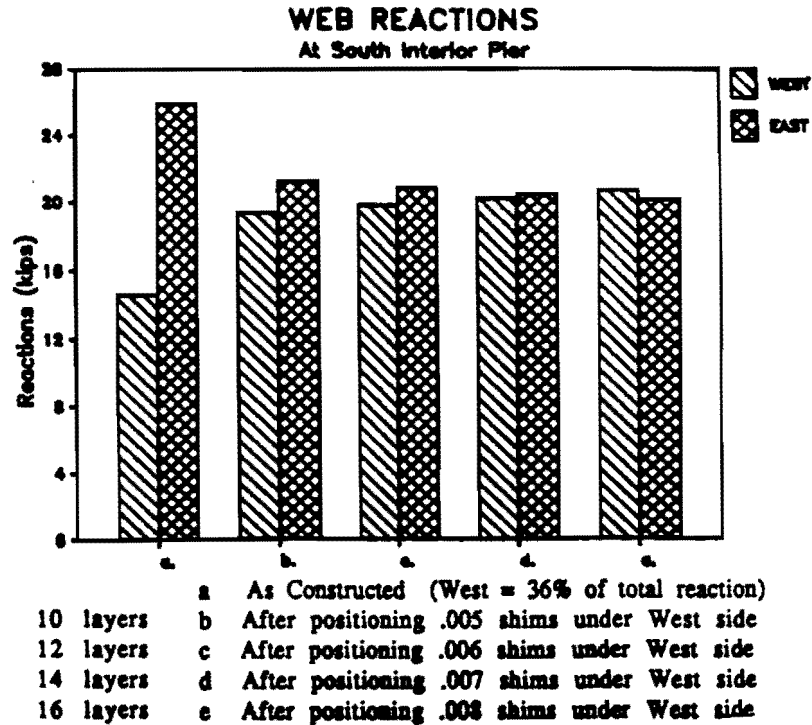


Fig. 4.11 Equalization of South Interior Reactions

the south interior pier were left as they were constructed, the east web would carry approximately 25 percent more vertical shear than the usual design value of half the total vertical shear. Additionally, very thin shims were required to equalize the reactions under the webs, or conversely, very small deformations are necessary to unbalance the web reactions. Unequal web reactions can therefore be expected for construction of this type, and provisions should be made for equalizing reactions after erection.

4.5 Summary of Observations Made During Erection

Several important observations were made from the erection data. Higher-than-expected friction losses were measured at the live end of the post-tensioning tendons. Research is needed to quantify friction losses that occur using standard industry hardware and stressing equipment. Lower than expected friction losses were measured at the deviators. Research is also needed to determine the friction losses that occur through concentrated angle changes at deviators.

As the primary tendons are stressed, the structure lifts off the shoring at midspan regions first. If flexible supports are used, then the stressed structure will remain in contact with the shoring. This load path must be considered for design of the shoring system and segment reinforcement.

Finally, unequal web reactions can be expected in segmental systems erected on shoring. Provision should be made to equalize web reactions after erection.

This page replaces an intentionally blank page in the original.

-- CTR Library Digitization Team

CHAPTER 5 ANALYSIS OF ERECTION STRESSES

Several analysis methods were used during design, construction, and testing of the model structure. Preliminary sizing and serviceability checks were made using moment distribution techniques. After the geometry of the model was established, a plane frame elastic analysis was used to finalize design and to investigate the in-situ condition of the completed structure. The "in-situ" structure was also analyzed to estimate the limits of elastic behavior. A nonlinear finite element program was developed to estimate the full range of flexural behavior of the structure. Finally an upper-bound plastic mechanism analysis was conducted to design the testing apparatus and to predict the location of critical joint mechanisms.

5.1 Nonlinear Finite Element Analysis

In conjunction with this research project, a nonlinear finite element program was developed, by El Habr (10). The program uses several types of structural elements, material models, and an iterative solution technique to estimate the full range of flexural behavior of externally post-tensioned box- girders. A description of the finite elements and solution technique is provided in Ref. 10.

5.2 Plastic Mechanism Analysis

An upper-bound plastic mechanism analysis was conducted to obtain forces for the design of the testing apparatus, and to predict which joints would open during testing. Several plastic mechanisms were considered for each test-load location. Hinge locations were assumed to occur at segment joints, and ultimate moment capacities were calculated at key joints along the structure. Two cases were considered to bound the solution. As an upper limit, the ultimate moment capacities were calculated assuming yield of the tendons, or for low relaxation strands

$$f_{ps} = f_{py} = 0.9 \cdot f_{pu} = 243 \text{ ksi}$$

As a lower limit, the mechanism load was determined from the effective prestress, f_{se} , the specified concrete compressive strength, f'_c , and the unbonded post-tensioning reinforcement ratio, P_p , using the ACI formula for unbonded tendons (17)

$$f_{ps} = f_{se} + 10,000 + ((f'_c)/(100 \cdot P_p))$$

$$< f_{py}$$

$$< f_{se} + 60,000$$

to predict the stress in the tendons corresponding to nominal flexural strength. This second solution used the measured tendon stresses at the start of testing as the effective prestress force, f_{se} .

The critical mechanism loads for each test load, and for each ultimate tendon stress assumption, are summarized in Fig. 5.1. For testing the exterior spans, two mechanisms displayed approximately equal strengths. For testing the interior span, one mechanism was critical.

The mechanism analysis revealed important information regarding the behavior of the structure near ultimate loads. Because mechanisms gave almost equal strengths for testing of the exterior spans, "complex" mechanisms with several joints opening, as shown in Fig. 5.2, could be expected in the dry jointed span. The mechanism analysis also revealed the location of the critical joints in the support regions. For loading in the exterior spans, the negative-moment hinge was found to occur at the interior face of the first interior pier segment, as shown in Fig 5.1. This occurred because the interior span had reduced flexural requirements and therefore less tendon area.

5.3 Plane Frame Analysis

A plane frame elastic analysis, PFT, was used during all stages of design, construction, and testing to predict the elastic behavior of the structure. Dead loads, equivalent prestress forces, and construction live loads were considered for each structural configuration during construction. The completed structure was further analyzed to reflect measured dead loads, concrete properties, support stiffness, and external tendon forces. Design live-load cases were checked for conformance with design serviceability limits. Finally, test load cases were analyzed for comparison with measured behavior.

An elevation of the completed three span structure is shown in Figure 5.3a. The analytical models used for the three phases of construction are shown in Figures 5.3b-d. The analytical models consist of a linear "frame" with nodes located at every segment joint. The members are continuous through the nodes to form a long continuous beam. An additional node was also provided at the center of each "pier-segment" to correspond with the bearing location. For simplicity the closure strip width (3 in.) was added to the adjacent span-segment at each location. To model the flexible bearing assemblies, additional nodes and members were added at each measured reaction location.

The properties of the members were determined from the measured properties of the model structure. The cross-sectional properties of the span and pier-segments were calculated from a transformed section analysis which included the longitudinal reinforcement. The concrete modulus was measured for representative cylinders from each type of concrete. An elastic modulus was determined for each segment, and then segments were

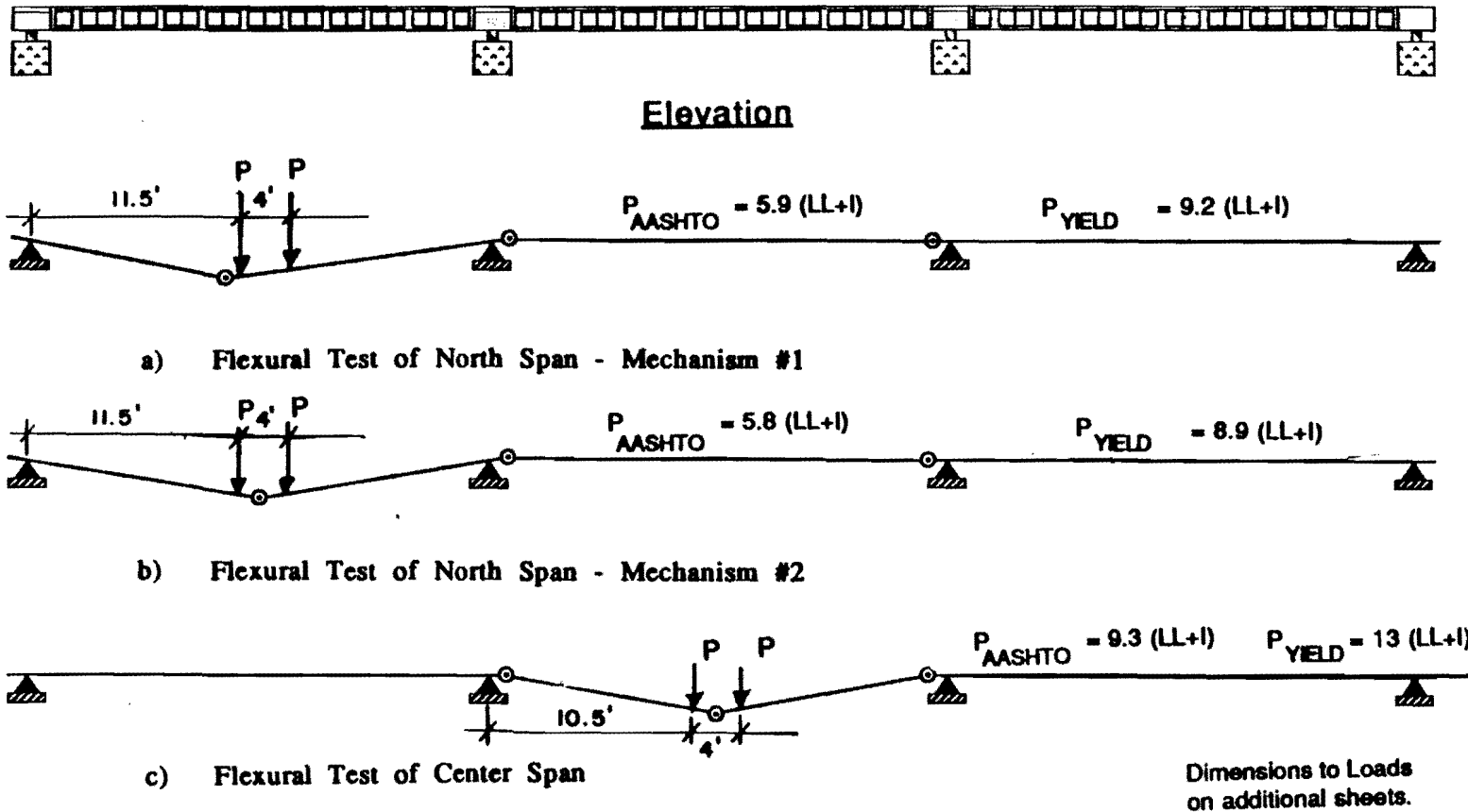
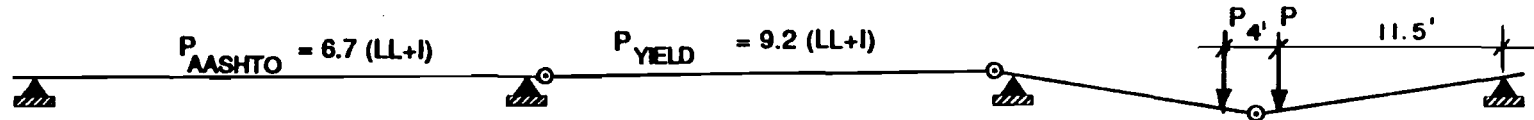


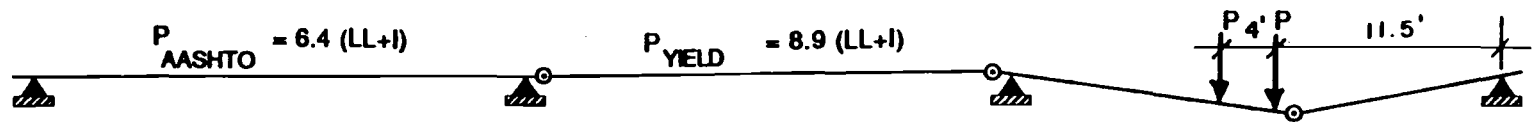
Fig. 5.1 Plastic Mechanism Analysis



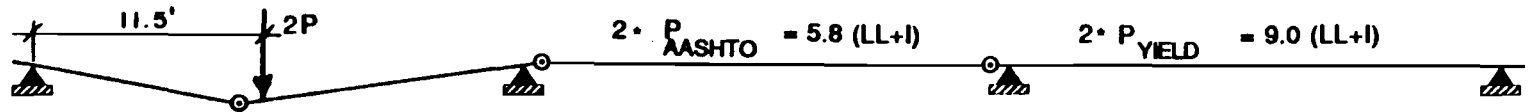
Elevation



d) Flexural Test of South Span - Mechanism #1

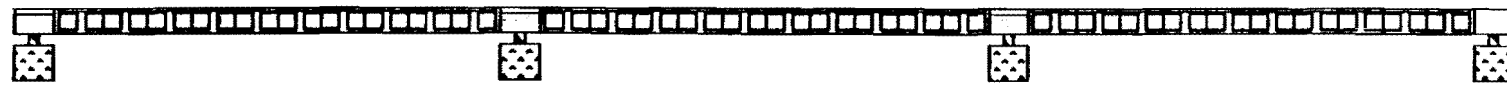


e) Flexural Test of South Span - Mechanism #2



f) Shear Test of North Span - Mechanism #1

Fig. 5.1 Plastic Mechanism Analysis – continued



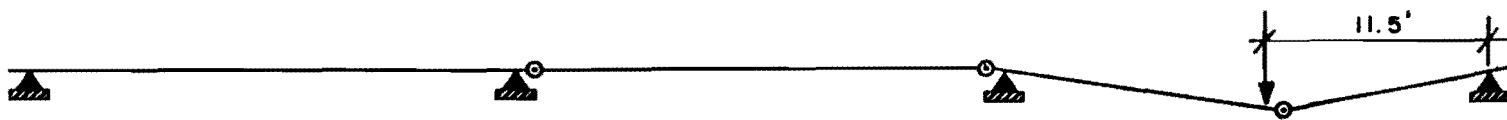
Elevation



g) Shear Test of North Span - Mechanism #2



h) Shear Test of South Span - Mechanism #1



i) Shear Test of South Span - Mechanism #2

Fig. 5.1 Plastic Mechanism Analysis – continued

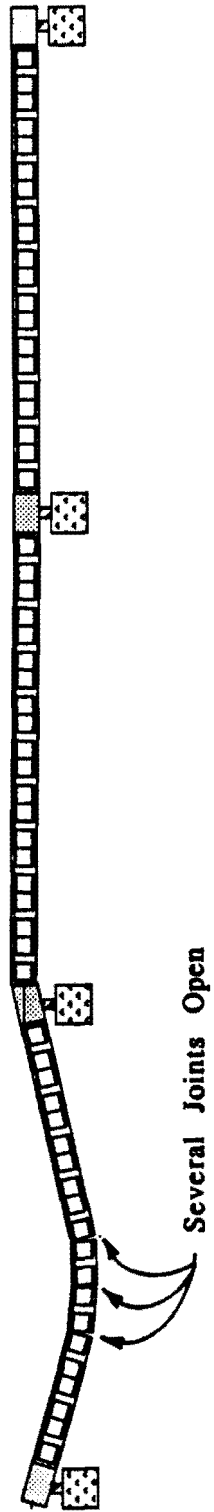
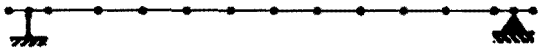


Fig. 5.2 Possible Complex Mechanism in Dry Jointed Span



a) Elevation of Completed Structure



b) One Span Configuration



c) Two Span Configuration



d) Three Span Configuration

Fig. 5.3 Plate Frame Elastic Analysis Models

grouped into five groups of span-segments and two groups of pier-segments. The member properties were then input as the transformed section properties and the average modulus of elasticity for the particular group of segments. The cross-section and concrete properties for all the members of the analytical model are tabulated in Table 5.1.

The flexibility of the load-cell bearing assemblies was modeled with short, axially stiff members. The cross-sectional area of these members was determined from the axial stiffness of the load-cells as measured during calibration. These members were assigned a low moment of inertia so that longitudinal restraint was not added to the model structure. The "load-cell" members also had a hinge at the structure/load-cell interface, so that rotational restraint would not be added to the superstructure.

Several types of loadings were applied to the analytical model. Dead loads consisting of segment self weight, dead load compensating weight, and factored dead loads were applied as uniformly distributed loads on each member. Construction and service live load cases, and test load cases were applied as concentrated loads on members. The post-tensioning forces were applied to members and nodes as a series of vertical and horizontal forces, and concentrated moments.

The model structure was erected in a sequential span-by-span manner. The internal forces and curvatures that exist after erecting a span are additive to the forces and curvatures induced by erecting subsequent spans. To properly predict the in-situ condition of the structure it is necessary to analyze each structural configuration of the evolving structure. Dead loads, equivalent prestress forces, and construction or service live loads were applied to each intermediate structure. The resultant internal forces and deflections from a particular configuration were then superposed with subsequent configurations using a spread sheet.

Several types of dead loads existed during construction and testing of the model structure, and are tabulated in Table 5.2. Self weight of the segments was calculated from the measured segment dimensions. The weight of the cast-in-place closure strip was calculated from its measured dimensions and added to the weight of the adjacent span segment. The dead load compensating blocks comprised a large portion of the total dead load (approximately 75 percent), so each dead load block was weighed prior to erection. The weights ranged from 360 to 396 pounds. Finally, additional dead weight was placed on the structure for application of the factored dead load during testing.

The effect of the post-tensioning was applied to the analytic model by calculating an equivalent prestress force for each tendon and applying this force to the appropriate structural configuration. The equivalent prestress forces were calculated from the measured tendon strains and theoretical tendon geometries. Vertical, lateral, and longitudinal forces, and moments were calculated for each tendon deviation point and anchorage location. To

Table 5.1 Member Properties for Elastic Analysis

Model Segment No.	P.F.T. Member No.	i Mode	j Mode	Length (ft)	Area (in ²)	Ubertua (in ⁴)	Ec (kai)	Type	Comment:
N.E.	1	1	2	1.00	894	20741	6644	Pier Segment	
N.E.	2	2	3	1.00	894	20741	6644	Pier Segment	
1	3	3	4	2.50	450	16540	3976	Span Segment	Include Pour Strip
2	4	4	5	2.25	450	16540	3675	Span Segment	
3	5	5	6	2.25	450	16540	3675	Span Segment	
4	6	6	7	2.25	450	16540	3976	Span Segment	
5	7	7	8	2.25	450	16540	4261	Span Segment	
6	8	8	9	2.25	450	16540	3976	Span Segment	
7	9	9	10	2.25	450	16540	3675	Span Segment	
8	10	10	11	2.25	450	16540	3675	Span Segment	
9	11	11	12	2.25	450	16540	3675	Span Segment	
10	12	12	13	2.50	450	16540	3976	Span Segment	Includes Pour Strip
N.I.	13	13	14	1.00	894	20741	5738	Pier Segment	
N.I.	14	14	15	1.00	894	20741	5738	Pier Segment	
11	15	15	16	2.50	450	16540	4261	Span Segment	Includes Pour Strip
12	16	16	17	2.25	450	16540	3976	Span Segment	
13	17	17	18	2.25	450	16540	3976	Span Segment	
14	18	18	19	2.25	450	16540	4261	Span Segment	
15	19	19	20	2.25	450	16540	4261	Span Segment	
16	20	20	21	2.25	450	16540	4261	Span Segment	
17	21	21	22	2.25	450	16540	3976	Span Segment	
18	22	22	23	2.25	450	16540	3976	Span Segment	
19	23	23	24	2.25	450	16540	4261	Span Segment	
20	24	24	25	2.50	450	16540	4261	Span Segment	Includes Pour Strip
S.I.	25	25	26	1.00	894	20741	6644	Pier Segment	
S.I.	26	26	27	1.00	894	20741	6644	Pier Segment	
21	27	27	28	2.50	450	16540	4561	Span Segment	Includes Pour Strip
22	28	28	29	2.25	450	16540	4561	Span Segment	
23	29	29	30	2.25	450	16540	4561	Span Segment	
24	30	30	31	2.25	450	16540	4561	Span Segment	
25	31	31	32	2.25	450	16540	4561	Span Segment	
26	32	32	33	2.25	450	16540	4561	Span Segment	
27	33	33	34	2.25	450	16540	4561	Span Segment	
28	34	34	35	2.25	450	16540	4561	Span Segment	
29	35	35	36	2.25	450	16540	4561	Span Segment	
30	36	36	37	2.50	450	16540	4940	Span Segment	Includes Pour Strip
S.E.	37	37	38	1.00	894	20741	6644	Pier Segment	
S.E.	38	38	39	1.00	894	20741	6644	Pier Segment	
N.E.B.	39	2	40	.83	20510	1	1	Bearing	2 - 100 kips load cells
S.I.B.	40	26	41	.83	34920	1	1	Bearing	2 - 200 kip load cells
S.E.B.	41	38	42	.83	30510	1	1	Bearing	2 - 100 kip load cells

Table 5.2 Dead Loads for Elastic Analysis

Model Segment No.	P.F.T. Member No.	Length (ft)	Calc. Segment Weight (lbs)	Pour Strip Weight (lbs)	Dead Load Comp. Weights (lbs)	Total Weight (lbs)	Uniform Distrib. Load plf
N.E.	1	1.00	1000			1000	1000
N.E.	2	1.00	1000			1000	1000
1	3	2.50	1055	153	3078	4286	1714
2	4	2.25	1054		2961	4015	1785
3	5	21.25	1037		3009	4046	1798
4	6	2.25	1057		3007	4064	1806
5	7	2.25	1021		3059	4080	1813
6	8	2.25	1040		3072	4112	1828
7	9	2.25	1050		3097	4147	1843
8	10	2.25	1037		32065	4102	1823
9	11	2.25	1054		3077	4131	1836
10	12	2.50	1056	153	2972	4181	1672
N.I.	13	1.00	1000			1000	1000
N.I.	14	1.00	1000			1000	1000
1	15	2.50	1022	153	2991	4166	1666
12	16	2.25	1039		3075	4114	1828
13	17	2.25	1035		3022	4057	1803
14	18	2.25	1041		3069	4110	1827
15	19	2.25	1054		2955	4009	1782
16	20	2.25	1045		3093	4138	1839
17	21	2.25	1046		3079	4125	1833
18	22	2.25	1041		3087	4128	1835
19	23	2.25	1048		3089	4137	1839
20	24	2.50	1036	153	3006	4196	1678
S.I.	25	1.00	1000			1000	1000
S.I.	26	1.00	1000			1000	1000
21	27	2.50	1057	153	3074	4284	1714
22	28	2.25	1046		3051	4097	1821
23	29	2.25	1051		3055	4106	1825
24	30	2.25	1061		3059	4120	1831
25	31	2.25	1033		3087	4120	1831
26	32	2.25	1037		3088	4125	1833
27	33	2.25	1043		3049	4092	1819
28	34	2.25	1035		3090	4125	1833
29	35	2.25	1043		3066	4109	1826
30	36	2.50	1026	153	3057	4235	1694
S.E.	37	1.00	1000			1000	1000
S.E.	38	1.00	1000			1000	1000

simplify the analysis, and to ensure that vertical, longitudinal, and rotational equilibrium were maintained, all tendon deviations were assumed to occur at a point.

For each structural configuration, two types of equivalent prestress forces were applied. The equivalent prestress forces for tendons stressed during a particular structural configuration were calculated from the measured stresses at the completion of that configuration. In addition, the losses that occurred in tendons that were stressed during previous configurations were applied as the difference between the equivalent prestress forces calculated at the beginning of construction of the current configuration and end of construction of the previous configuration. These forces were applied to the current structure, and act in a direction opposite to the original equivalent prestress forces.

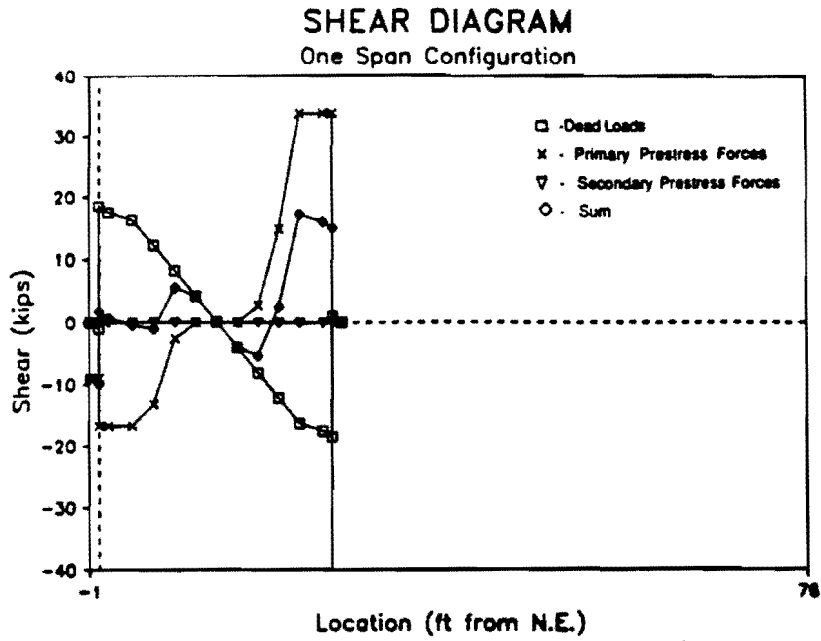
The top internal tendons were not instrumented, so in-situ stresses are not known. These tendons were stressed to a jacking force of $0.74 \cdot f_{pu}$, and the wedge anchors were seated with the internal seating device of the monostrand stressing ram. With approximately $3/8$ inch loss due to anchorage set averaged over 77 feet between anchors, the stress in the internal tendons was assumed to be approximately $0.70 \cdot f_{pu}$ (189 ksi) after seating. With approximately 10 percent time-dependant losses occurring between the end of construction and the start of the test, the effective prestress force in the internal tendons at the start of testing was assumed to be $.63 \cdot f_{pu}$ (170 ksi).

5.4 Estimate of Conditions in the Structure Before Testing

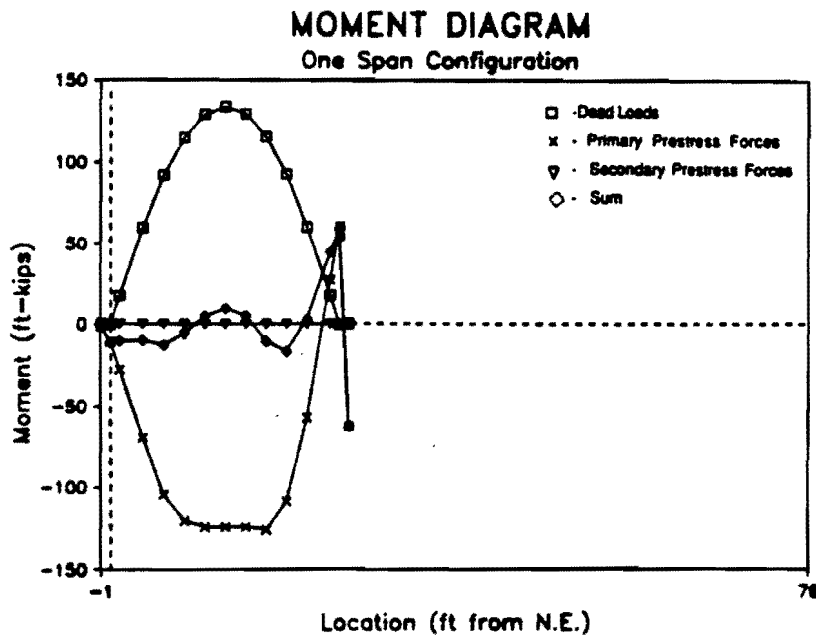
The structure was analyzed using the plane frame model and loading conditions described above. Each structural configuration was analyzed for forces occurring during that stage of construction, and internal forces (shears, moments, and axial forces) and deflections were determined for each case. The forces and deflections from each stage were added to subsequent stages to determine the in-situ condition of the structure. Top and bottom stresses were also determined from calculated internal forces and cross-sectional properties.

Shears, moments, and top and bottom fiber stresses are plotted for each structural configuration in Figures 5.4 through 5.6. The sign convention for stresses assumes compression stress as positive. Each force type is divided into components caused by dead loads, primary prestress forces, and secondary prestress forces. In each case the forces represent the total from each component at the end of the current stage of construction. The sum of the three components is also shown in each case.

The forces existing in the one-span configuration are shown in Fig. 5.4. The dead-load shears and moments are counteracted by the prestress forces, with some reserve

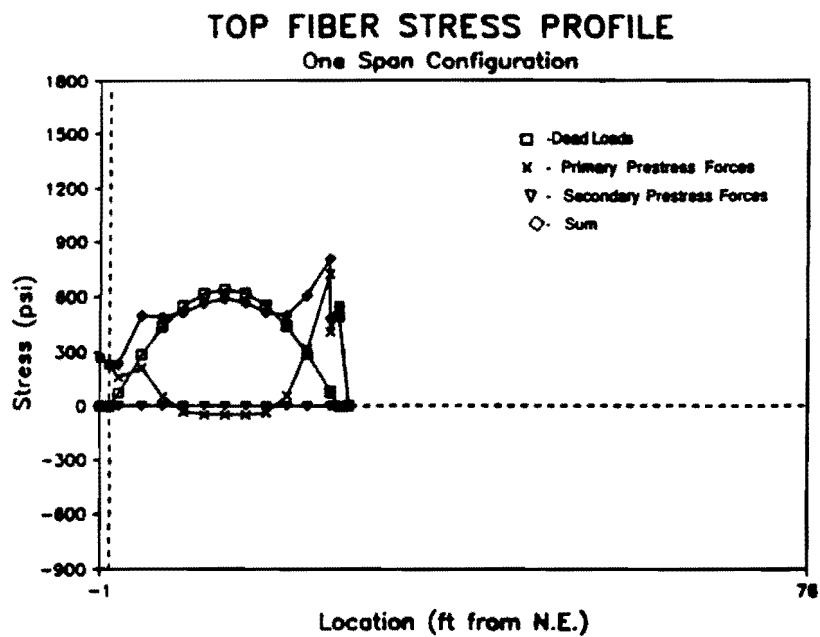


(a) Shear Force Diagram

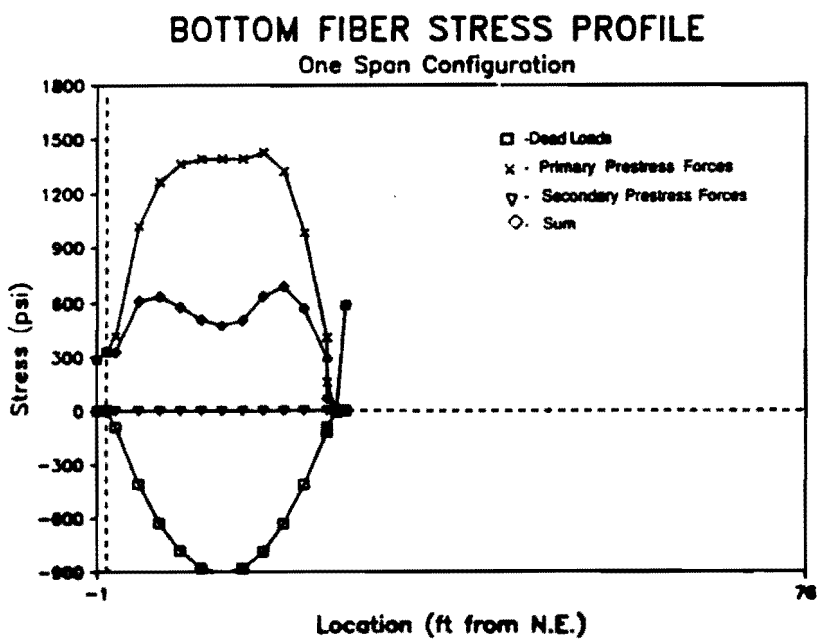


(b) Bending Moment Diagram

Fig. 5.4 One Span Configuration

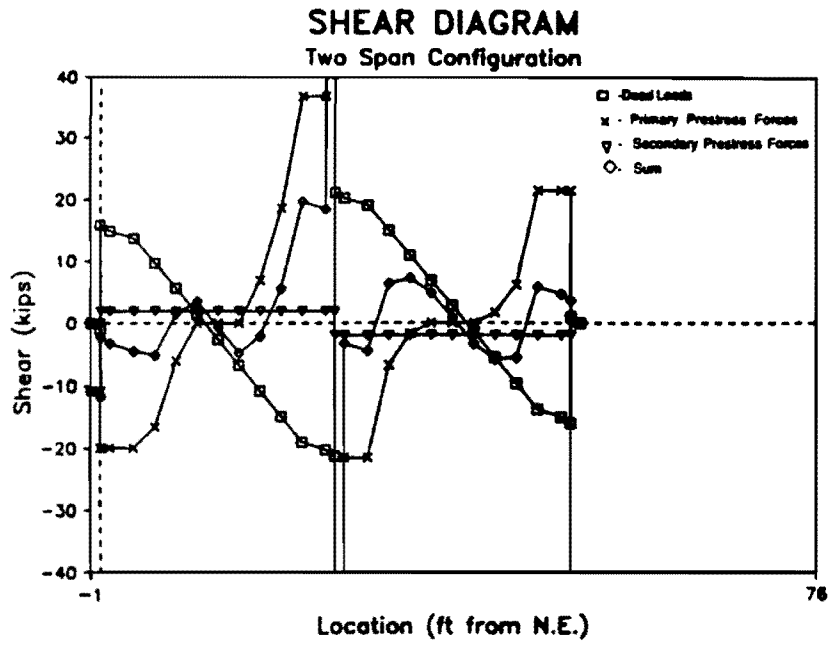


(c) Top Fiber Stress Profile

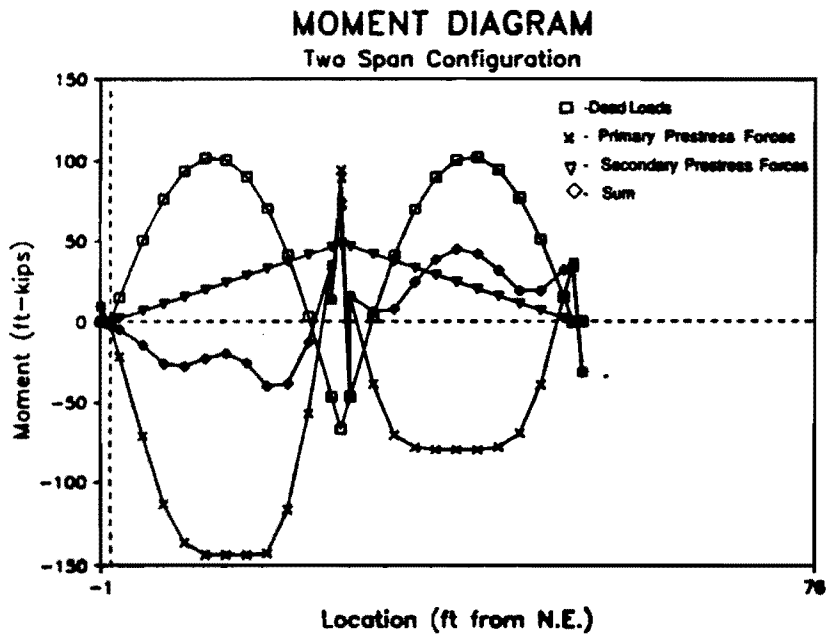


(d) Bottom Fiber Stress Profile

Fig. 5.4 One Span Configuration – continued

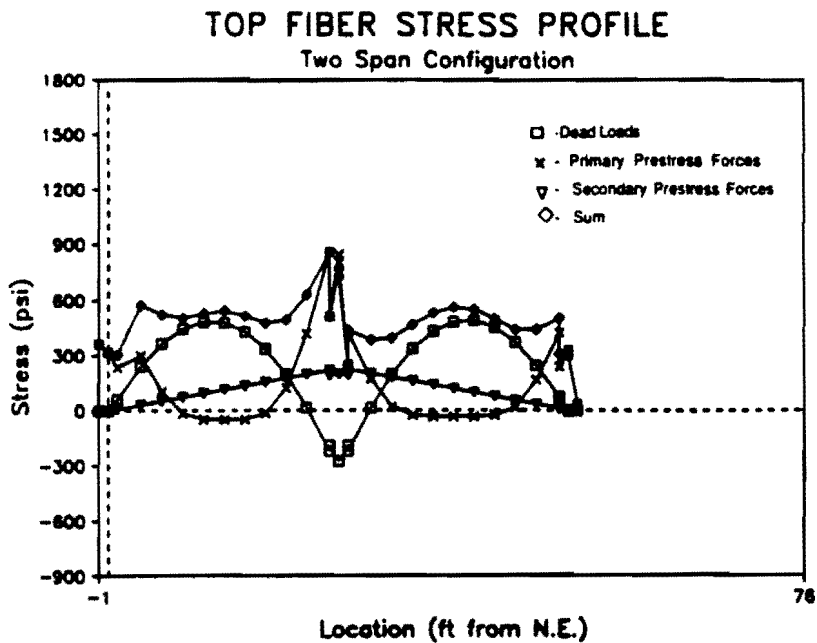


(a) Shear Force Diagram

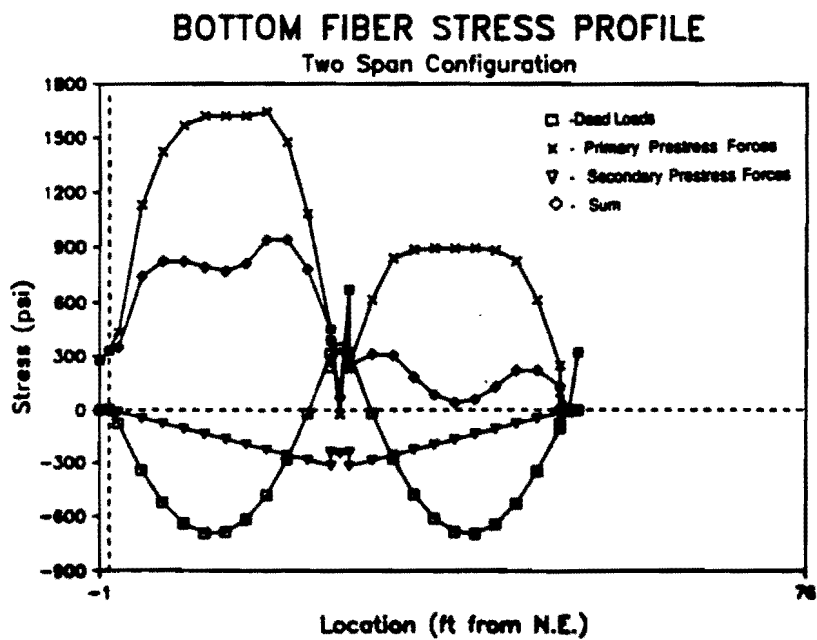


(b) Bending Moment Diagram

Fig. 5.5 Two Span Configuration

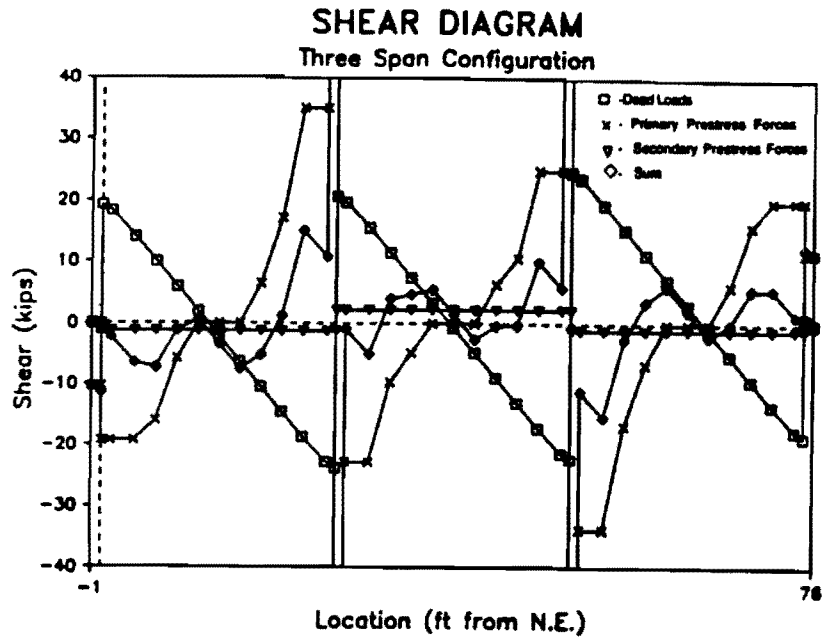


(c) Top Fiber Stress Profile

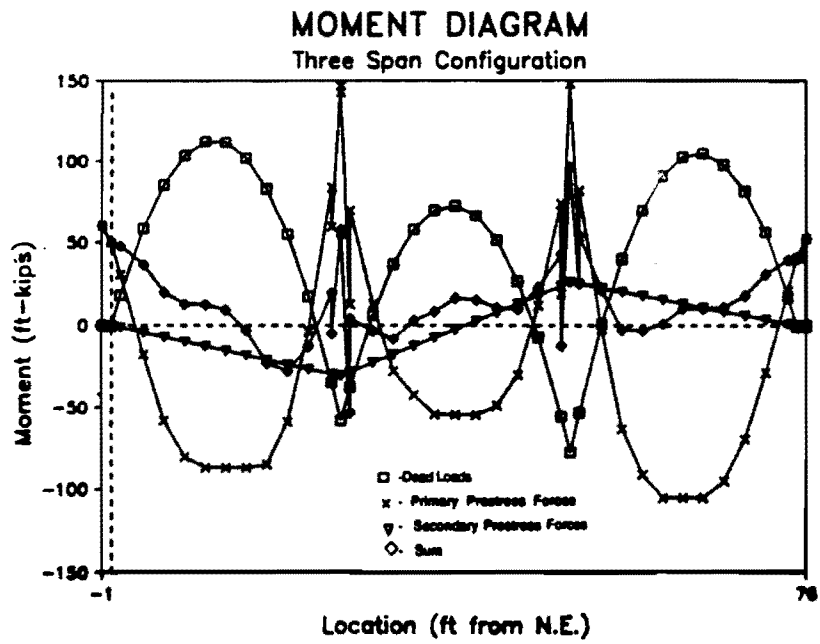


(d) Bottom Fiber Stress Profile

Fig. 5.5 Two Span Configuration – continued

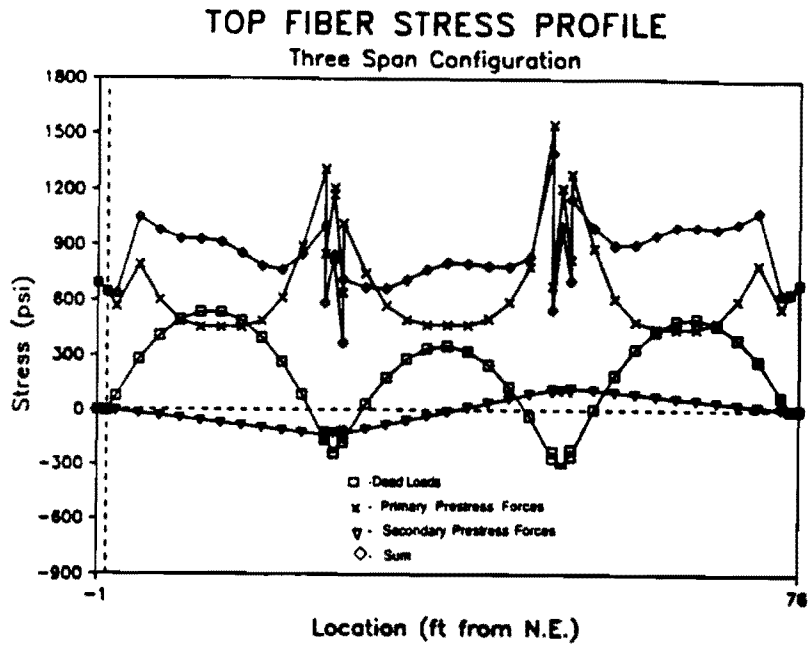


(a) Shear Force Diagram

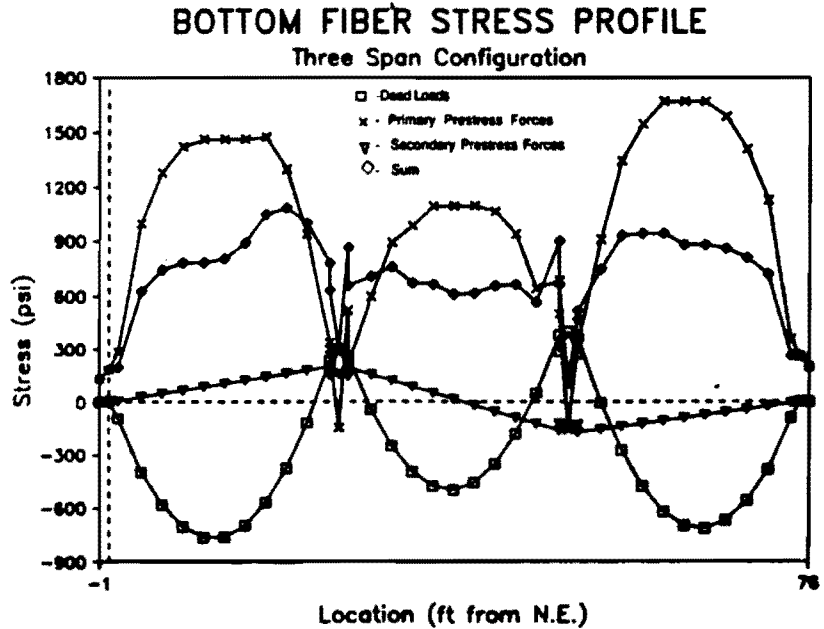


(b) Bending Moment Diagram

Fig. 5.6 Three Span Configuration



(c) Top Fiber Stress Profile



(d) Bottom Fiber Stress Profile

Fig. 5.6 Three Span Configuration – continued

provided for shear at the south end. The extreme fiber stresses range from 450 to 700 psi in the middle portion of the span, providing reserve stress for application of construction live load. In this statically determinate system, the secondary prestress forces are zero.

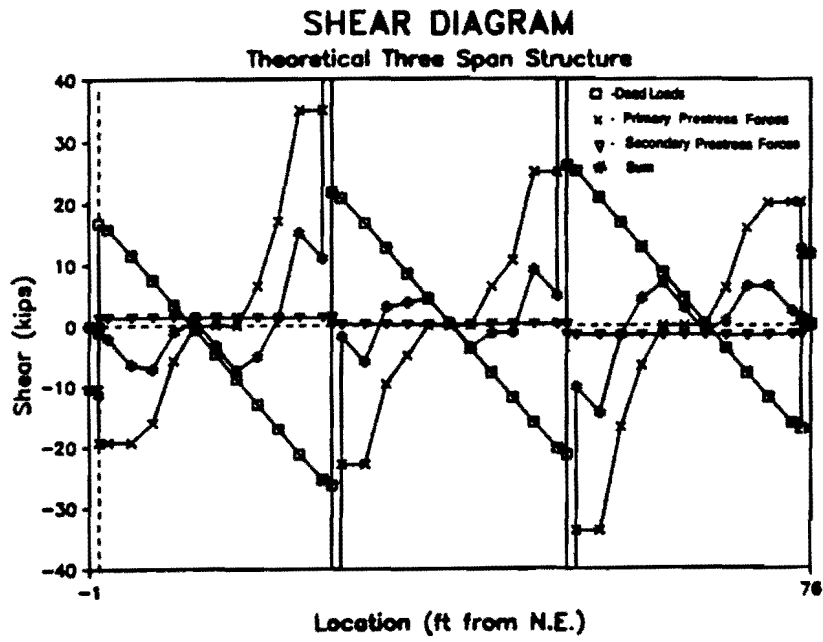
The forces existing in the two-span configuration are shown in Fig. 5.5. In the north span the dead load forces are balanced by the prestress forces with reserve for construction live-loads at all locations. In the "center" span the prestress forces only partially offset the dead load forces leaving almost no reserve for construction live loads. The top fiber stresses range from approximately 400 to 600 psi compression in both spans while the bottom fiber stresses are almost zero in the midspan region of the "center" span. The low stresses in the "center" span at this stage are a result of the construction sequence in which a portion of the "center" span tendons are not stressed until after erection of the south span. High friction losses also occurred in the primary "center" span tendon 2. Also, the secondary prestress forces in the continuous structure contribute to the low combined stresses in the "center" span.

The estimated forces that exist in the structure at the beginning of testing are shown in Fig. 5.6. The dead load shears are more than offset by the prestress forces with some reserve provided for service live loads. The resultant moments at all midspan locations are less than 20 percent of the corresponding dead load moments. The extreme-fiber stresses in the center of all spans range between 600 and 1100 psi compression.

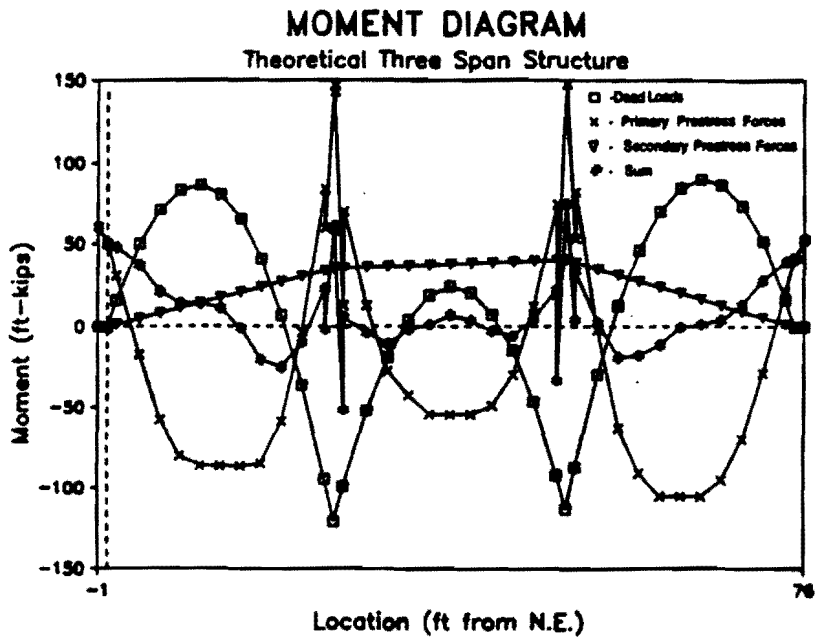
The "Span-by-Span" construction method causes hyperstatic forces to be locked into each structural configuration. A three-span structure with post-tensioning forces applied simultaneously to all spans was analyzed for comparison with results of the true sequential construction method. The resultant forces for this structure are shown in Fig. 5.7. The primary difference between the two structures is the distribution of secondary forces. In the sequentially constructed structure, shown in Fig. 5.6, the secondary prestress forces are anti-symmetric about the center of the structure. This results from stressing each span individually, and causes reduced shears at the north end and increased shears at the south end. In the structure that is post-tensioned in one operation, the secondary prestress forces are approximately symmetrical about the center line. This causes both exterior reactions to increase by approximately the same amount.

The resultant dead load forces are also distributed differently in the two structures. In the sequentially constructed structure the dead loads are resisted primarily by positive-moment bending with a ratio of positive to negative moments in the exterior spans of approximately two. In the three-span structure that is post-tensioned in one operation, the dead load forces are carried by a more equal distribution of positive and negative moments, with a positive-to-negative moment ratio of approximately one.

The resultant extreme-fiber stresses from the two structures are compared in Fig. 5.8. In the north span, the differences in secondary-force distribution are offset by the

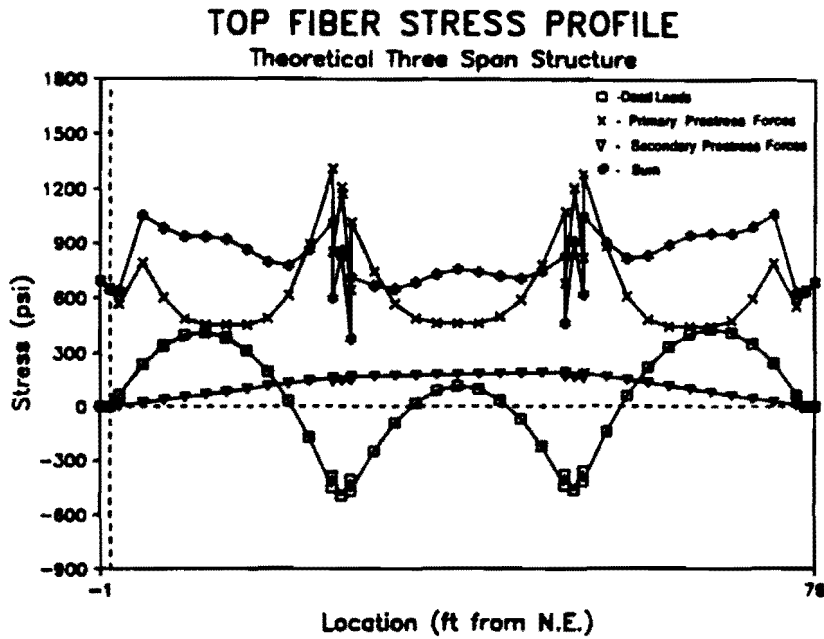


(a) Shear Force Diagram

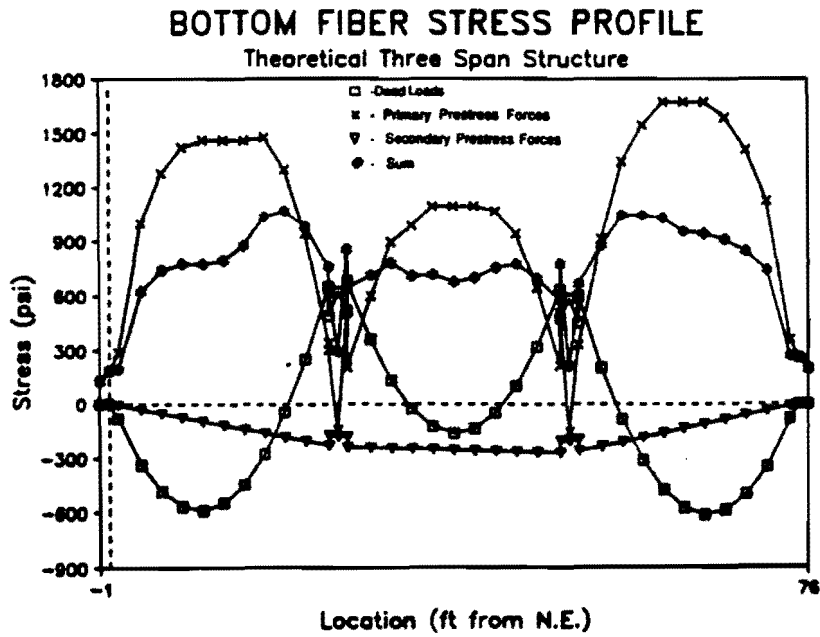


(b) Bending Moment Diagram

Fig. 5.7 Theoretical Three Span Structure

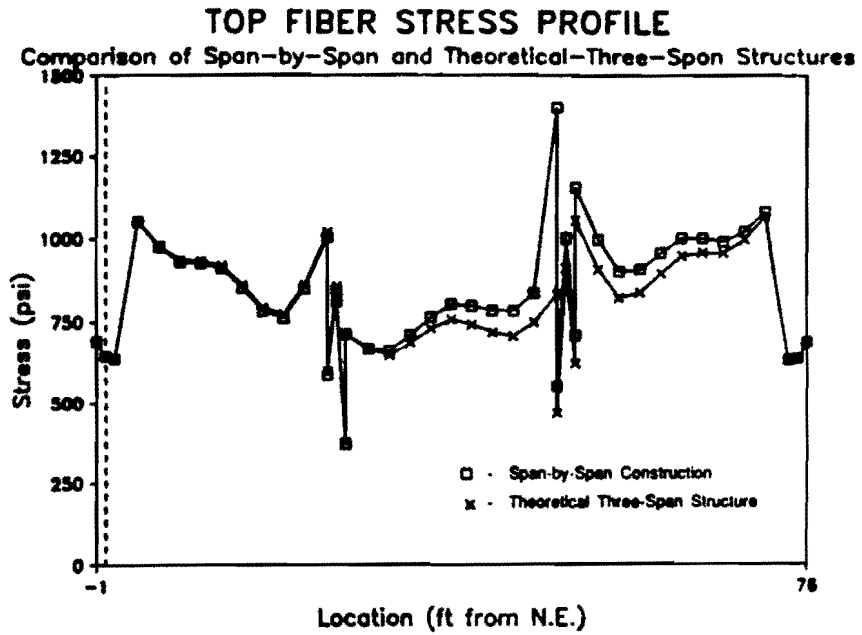


(c) Top Fiber Stresses

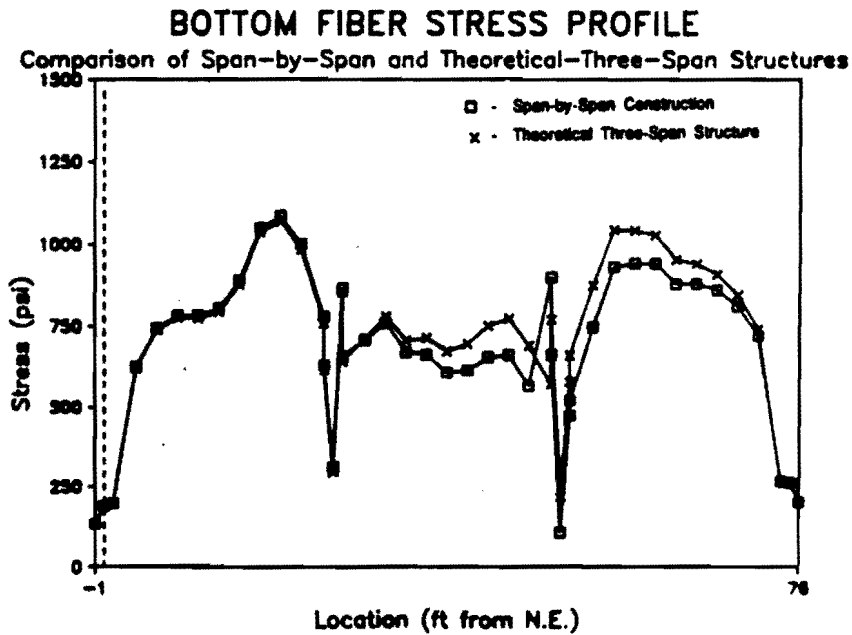


(d) Bottom Fiber Stresses

Fig. 5.7 Theoretical Three Span Structure – continued



(a) Top Fiber Stresses



(b) Bottom Fiber Stresses

Fig. 5.8 Comparison of Extreme Fiber Stresses for As-Built and Theoretical Structures

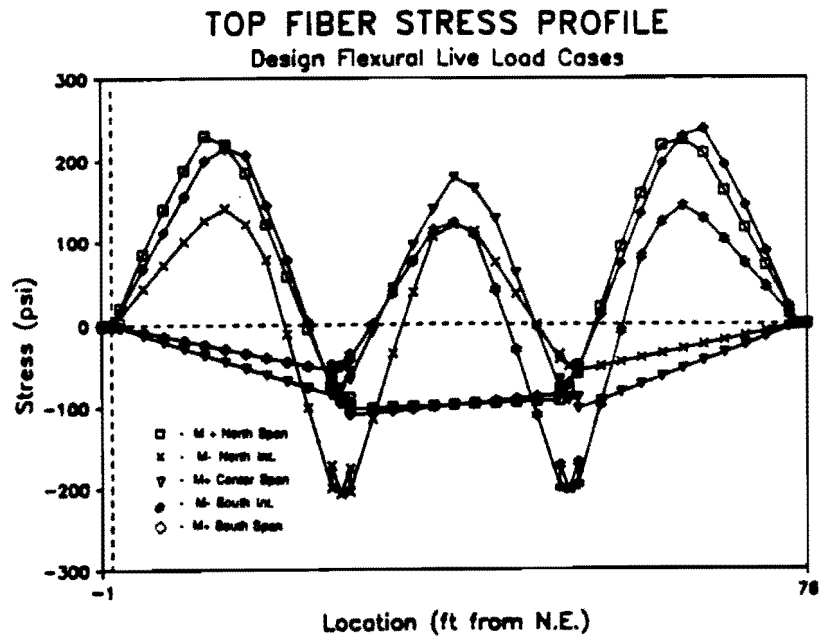
differences in dead-load force distribution to yield almost no change in extreme fiber stress. In the center and south spans the differences in dead load and secondary-force distributions lead to reduced top fiber stresses and increased bottom fiber stresses for the simultaneously post-tensioned structure. Changes in stress as high as 10 percent were computed.

Table 5.3 Concrete Stress Limits for Model Structure

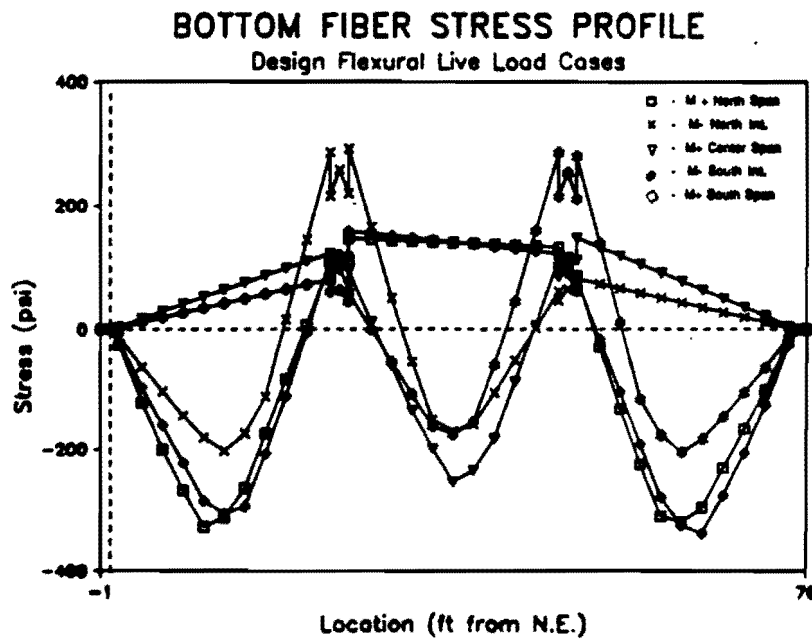
Condition:		
<ul style="list-style-type: none"> - Segmental Construction - Stresses at Service Loads after Losses have Occurred - Less than 50% bonded Prestressed Reinforcement - Without bonded mild reinforcement crossing joints - Design Specified Concrete Strength (f'_c) of 6000 psi 		
	Jan. 1987 Draft ⁽²⁰⁾ Limit:	Feb. 1988 Final Report ⁽¹⁴⁾ Limit:
Compression All Members	$0.40f'_c$	$0.40f'_c$
Tension Precompressed Tensile Zones:		
Dry Joints:	$6.0 \sqrt{f'_c}$ (Comp.)	200 psi compression
Epoxyed Joints:	$3.0 \sqrt{f'_c}$ (Comp.)	0 tension

The service live loads were input to the completed analytical model to check conformance with design serviceability criteria. The design concrete stress limits for all types of segmental construction are also described in Chapter 2. For externally post-tensioned precast segmental box-girders, the newly proposed AASHTD stress limits (14,20) are summarized in Table 5.3. The table shows the initial proposal of Jan. 1987 (20) as well as the finally agreed on values of Feb. 1988 (14). When the bridge model was designed and constructed, the values used in design were those of the Jan. 1987 proposal. These provided that if bonded reinforcement is not provided across segment joints (as is the case in the model), then a residual compression is required in flexural tension zones. The required amount of residual compression depends on whether the segment joints are dry or epoxyed. The allowable concrete compressive stress is independent of the type of construction.

The extreme-fiber stresses that result from only the design service loads are shown in Fig. 5.9. The service load stress envelopes were then superimposed on the calculated in-situ stresses to yield the range of service level stresses in the completed structure. The service load stress range and the design stress limits for the top and bottom fibers are shown in Fig. 5.10. The service stresses in the completed structure are all within the

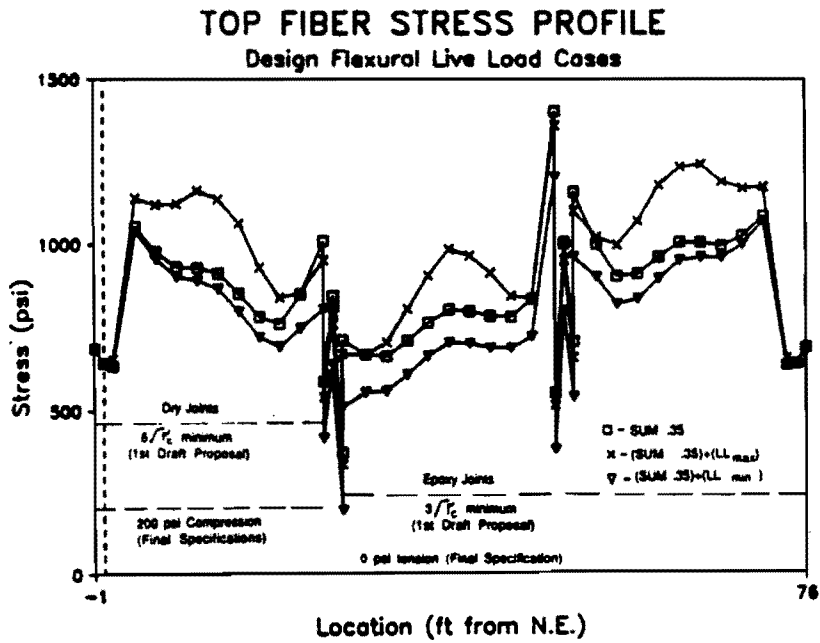


(a) Top Fiber Stresses

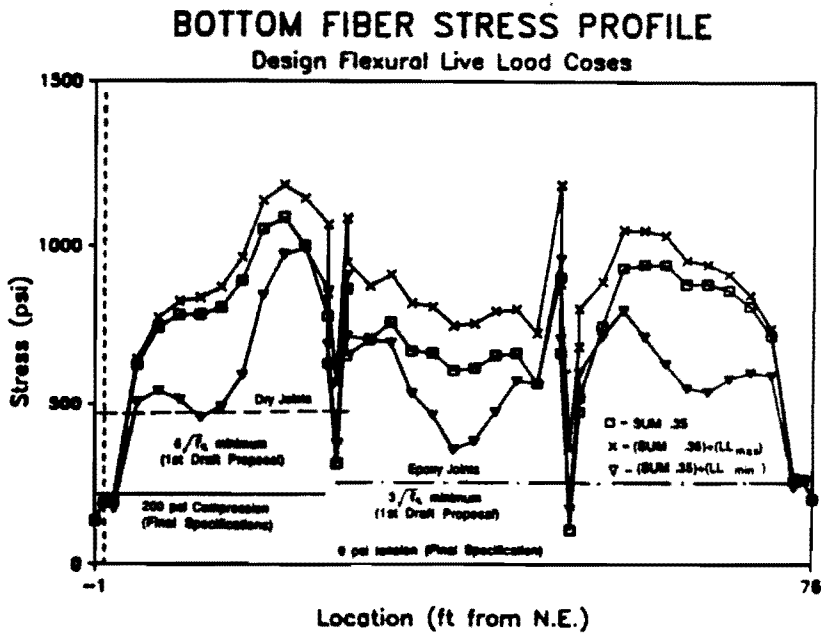


(b) Bottom Fiber Stresses

Fig. 5.9 Extreme Fiber Live Load Stresses



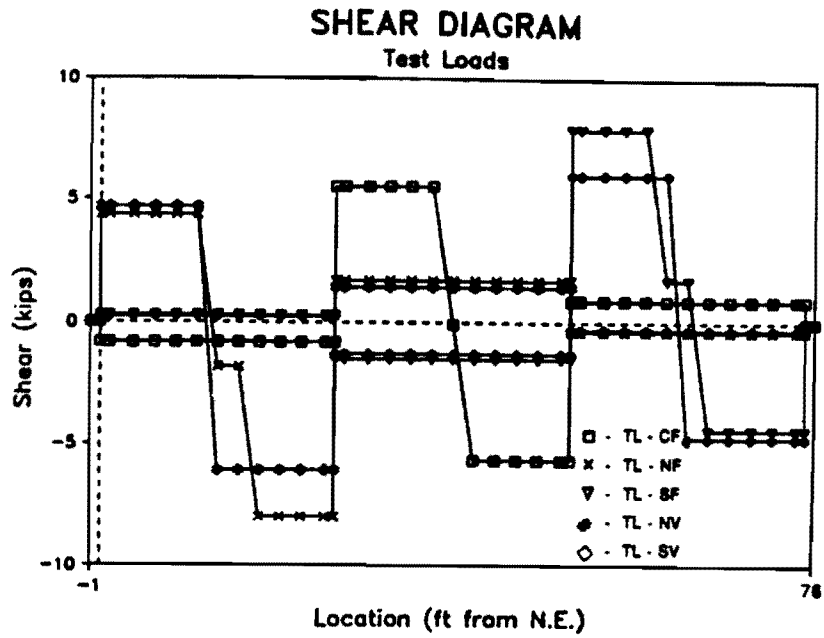
(a) Top Fiber Stresses



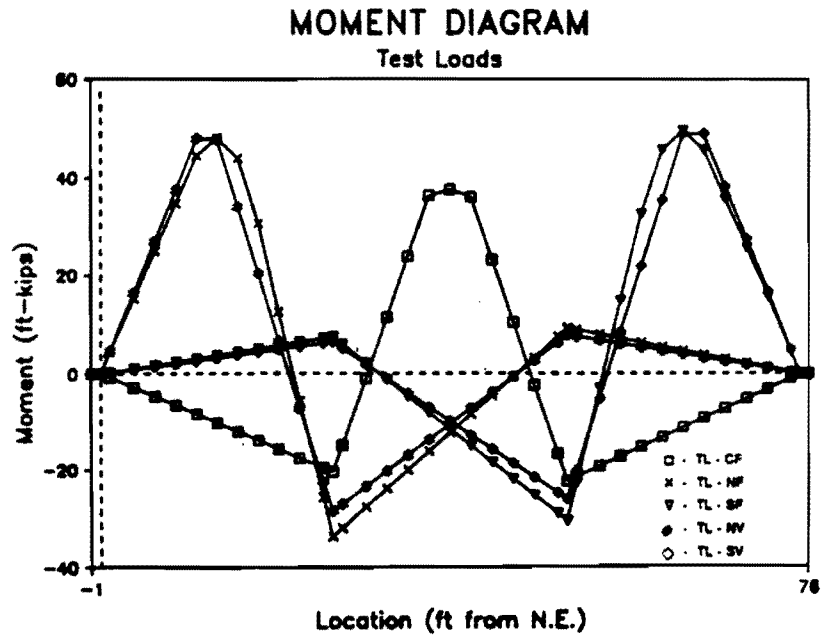
(b) Bottom Fiber Stresses

Fig. 5.10 Service Stress Range

specified limits. The maximum compressive stresses are well below the limiting stress of 2400 psi, shown in Table 5.3. In the flexural tension zones, the PTI initial draft minimum allowable residual concrete compression is 465 psi ($6.0 \cdot (\sqrt{f'_c})$) in the dry span and 232 psi ($3.0 \cdot (\sqrt{f'_c})$) in the epoxied exterior span. These values were used in the model design and are more conservative than the final proposal. Examination of the service load stress range in Fig. 5.10 reveals that the dry exterior span meets the 1st Draft (20) residual compression requirement almost exactly and has a residual compression about 2.4 times the new AASHTO requirement (14), the epoxy joint span has a residual compression of approximately 2.4 times the 1st Draft (20) required residual compression and has a residual compression almost 500 psi above the new AASHTD requirement (14). This extra over-design in the epoxy span was required in the model to provide similar exterior spans. Note both exterior spans are designed quite conservatively. The smallest compression stress at an extreme fiber in the center span is approximately 1.6 times the required compression for epoxy spans. Critical placements of the test load cases corresponding to the equivalent model live load plus impact factor were determined for each space (N=North, C=Center, S=South) for flexure (F) and for shear (V). These test load cases were also applied to the completed structure to determine the internal force distribution and the onset of joint opening assuming no tensile strength at the joint. The shear forces, bending moments, and extreme fiber stresses resulting from the five different test loads are shown in Fig. 5.11. The level at which joints would open (neglecting the tensile capacity of the epoxy) were estimated by determining the multiple number of test loads required to overcome the precompression and induce tensile stress at critical joints. Table 5.4 summarizes the estimates for the joint decompression load levels for each test load case. From this table it is seen that no joint opening would be expected until approximately 2.4 (L&I) load in the dry joint north span and substantially higher load levels in the epoxy jointed center and south spans. Elastic deflections for each test load case were also determined and compared with deflections recorded during testing (see Chapter 6).

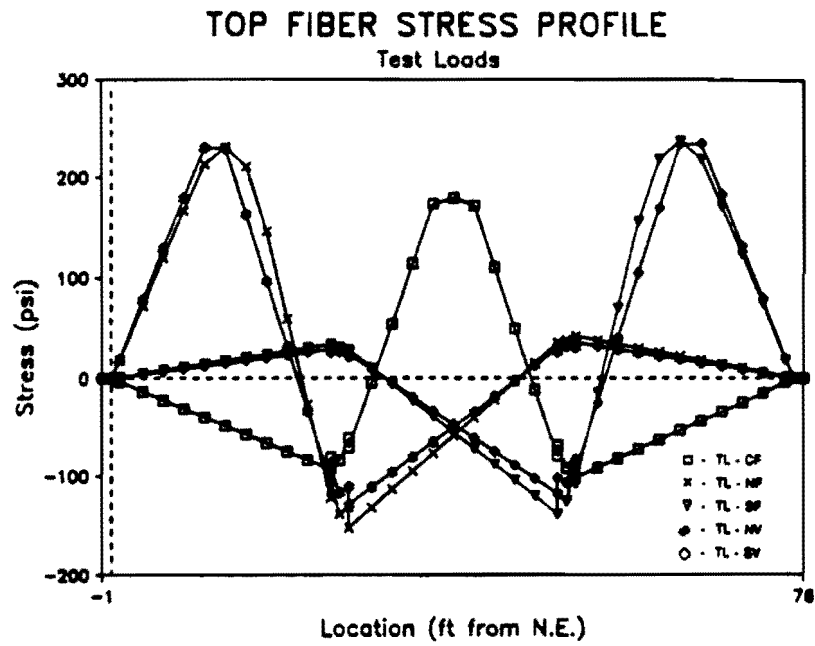


(a) Shear Force Diagram

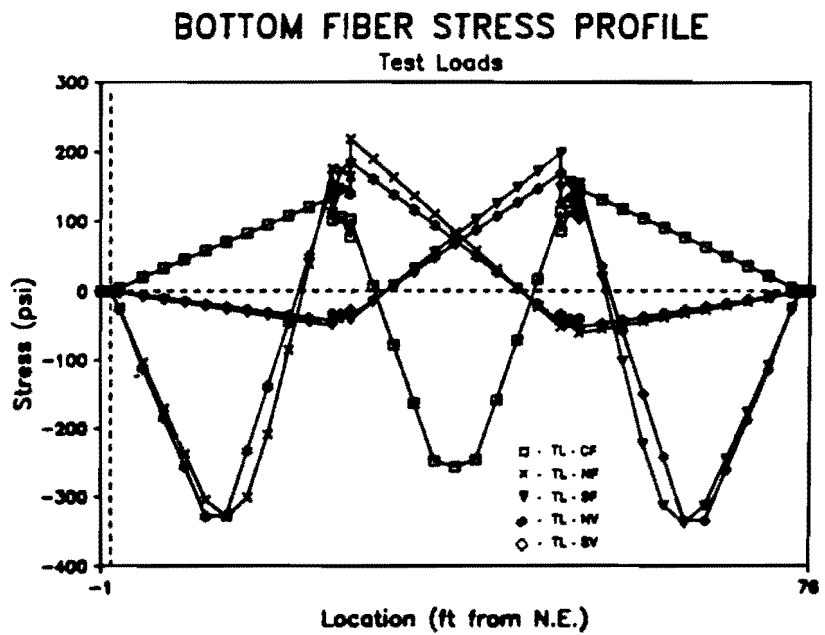


(b) Bending Moment Diagram

Fig. 5.11 Test Load Forces



(c) Top Fiber Stresses



(d) Bottom Fiber Stresses

Fig. 5.11 Test Load Forces – continued

**Table 5.4 Multiple of Line Plus Impact Loads Required
for Joint Decompression**

Test Load Case	Span Loading	Critical Joint No.	Construction Joint Stress (psi)	Joint Stress from Test Load (psi)	Multiple of Test Loads Required for Joint Decompression
TL-CF	Center Flexure	(15, 16)	609	257	2.37
TL-NF	North Flexure	(4, 5)	783	304	2.57
		(5, 6)	805	329	2.45
TL-SF	South Flexure	(25, 26)	878	339	2.59
		(26, 27)	879	313	2.81
TL-NV	North Shear	(4, 5)	783	329	2.38
		(5, 6)	805	327	2.46
TL-SV	South Shear	(25, 26)	878	335	2.62
		(26, 27)	879	335	2.62

CHAPTER 6
LOAD TESTS OPERATIONS

6.1 Loading Program

The model structure was load tested to investigate the complete range of flexural behavior and to conduct preliminary tests of shear and torsional behavior. The test program, shown in Table 6.1, consisted of three distinct phases:

Table 6.1 Loading Program

	North Span (Dry)	Center Span (Epoxy)	South Span (Epoxy)
A. Phase 1 - Structural Characterization			
Design Service Load Cycles 4 Cycles:	3/15/88	3/11/88	3/11/88
Cracking Cycle 1 Cycle:	N/A	3/11/88	3/11/88
Decompression Load Cycles 3 Cycles:	3/17/88*	3/14/88	3/16/88
Torsional Load Cycles Cycles:	3/18/88	N/A	3/18/88
B. Phase 2 - Factored Load Tests			
Design Factored Load Cycles 3 Cycles:	3/29/88/**	N/A	3/31/88
C. Phase 3 - Ultimate Strength Tests			
Flexural Strength Test - Joint Opening Cycles 3 Cycles:	4/5/88	N/A	4/18/88
Flexural Strength Test - Ultimate Cycle 1 Cycle:	4/12/88***	N/A	4/19/88
Shear Strength Test 1 Cycle:	4/21/88	N/A	4/26/88

*Three additional cycles on 3/15/88 with bad rams

**Three additional cycles on 3/25/88 with restraining load system

***Testing conducted on 4/5/88 and 4/7/88 also

Phase 1 - structural characterization

Phase 2 - factored load tests

Phase 3 - ultimate strength tests

The first phase of testing involved loading the structure to the design service-level live loads and then increasing loads to higher levels to establish the decompression loads at critical joints along the structure. In the second phase of testing, the structure was loaded with the increased factored loads used for strength design. In the final phase of testing, the structure was loaded until the ultimate strength was reached. The initial failure tests were flexural. Exploratory tests were then carried out on the partially damaged structure to investigate shear behavior at an opening joint. Phase 1 testing was conducted on all three spans, while Phases 2 and 3 were conducted on the exterior spans only. At all levels of loading, comparisons were made between the dry-jointed and epoxy-jointed exterior spans.

The structural characterization phase of testing, summarized in Table 6.1a, was designed to define and characterize the in-situ condition of the structure. Each of the three spans was tested in a similar manner on the dates shown in Table 6.1a. First, four cycles of service live load were applied to each span. A cracking cycle was then conducted on the epoxy jointed spans (center and south), and then three additional load cycles were applied on all spans to determine the decompression load. The decompression load is the applied load that is necessary to reduce the initial compressive stress to a zero stress level in the extreme flexural-tension fiber, and was determined by a subtle change in stiffness as indicated by load deflection curve. Three additional decompression cycles were applied with an unacceptable pair of rams to the north-span (see Section 6.2.1.2). The data from these load cycles are not presented here. Finally, three cycles of eccentrically applied service load were applied to the two exterior spans to investigate service level torsional behavior.

After completing the first phase of testing, all spans of the structure were loaded with additional dead weight to provide the design factored dead load.

Each exterior span was then subjected to three cycles of the factored design loads. Three additional factored load cycles were applied to the north-span with a loading system that offered restraint to the structure, (see Section 6.2.1.2). These data are also not presented here.

The ultimate strength phase of testing, shown in Table 6.1c, is divided into two stages, flexural strength and shear strength. Each exterior span of the structure was initially subjected to three cycles of load large enough to cause visible opening at a segment joint(s). After completing the "joint-opening" cycles, the load was then continuously increased until the flexural strength was reached. Three separate load cycles were applied to the north-span before flexural strength was achieved. Larger low-level load increments were used on the

south-span, and ultimate strength was achieved on the first "ultimate" cycle. The flexural-strength test was discontinued when the stiffness of the span being loaded had reduced to a very small fraction of the initial elastic stiffness. Both exterior spans experienced approximately the same maximum deflection.

After completing the flexural strength stage of testing, an exploratory test was conducted on each exterior span in which significant shear was transferred across an opening joint. Only one cycle of load applied to each exterior span. Loading was applied to each span until the measured stiffness reached approximately the same stiffness as measured at the conclusion of the flexural strength test.

6.2 Description of Loading System

6.2.1 *Reduced Scale Truck Loads.*

6.2.1.1 *Location of Loads.* The reduced-scale representation of two lanes of AASHTO HS20 truck load with impact, derived in Section 2.1.3, consists of a series of three concentrated loads spaced at 42-in. on-center, as shown in Fig. 2.3. To simplify the load frame, rams were provided only at locations in-line with the rod-clusters in the test floor. Also, two identical rams were used and were operated on the same hydraulic system. These two requirements lead to the use of two equal loads spaced at 48-in. on-center. The rams were attached to heavy steel cross-beams which were tied down to the test floor with 1-in. diam. rods at each end (see Section 6.2.1.2).

With the basic test-configuration described above there were only a few possible locations for the test load. For flexural tests, two rams were spaced at 48-in. measured along the longitudinal axis of the structure. For the shear tests, to increase the shear transfer across an opening joint, the two rams were located at one section along the length of the structure. For the torsion tests, the rams were spaced 48-in. apart along the longitudinal axis of the structure, and were located directly over the west web of the box-girder model. The three types of test load configurations are shown schematically in Fig. 6.1.

The flexural test load configuration provides a reasonable representation of the design AASHTO truck load. The model design load has three loads spaced at 3.5 feet on center, with a percent distribution of total load to the axles of 12%, 44%, and 44%, respectively, and a radius of gyration of force equal to 2.33 feet. The actual flexural test load has two loads spaced at 4.0 feet on center, with 50 percent of the total load distributed to each ram, and a radius of gyration of force equal to 2.0 feet. The radius of gyration of force provides a measure of the global distribution of force within the load case. A smaller value indicates the load group is more concentrated and will result in higher shears and larger peak moments in the critical midspan flexure region.

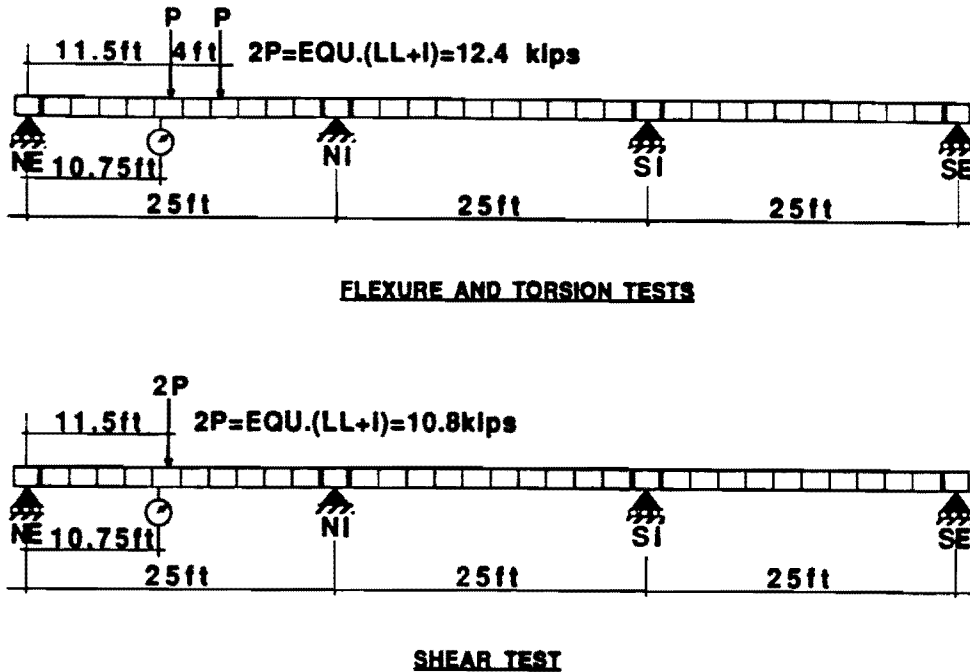


Fig. 6.1 Test Load Configurations

Each possible load configuration was analyzed using a plastic mechanism analysis (Section 5.2) to determine the locations of critical joints. Each test load configuration was also analyzed using an elastic analysis (Section 5.4) to determine the elastic internal forces at the critical mechanism joints. The flexural and shear test load locations were chosen so that the same joints were critical for both tests. If a different joint was critical for the flexure test of the cracked epoxied space, then the desired critical shear mechanism may not have developed properly. The final test load locations were therefore chosen so that flexure and shear test mechanisms involved the same critical joint with the largest shear transfer across the joint.

6.2.1.2 Load Application Equipment. The load frame consisted of a rectangular tension structure that was tied down to the test-floor at its four corners (see Fig. 6.2). The cross-beams were braced to each other with two secondary beams. In the unloaded condition the frame was supported at each corner with adjustable post shores and was tied to the model for stability.

The rams were placed between the load frame and the structure. For all flexural tests the centrally located rams applied load to the webs of the box girder located through a spherical bearing and spreader beam. For the torsion and shear tests the rams were positioned directly above the box-girder webs and located through spherical bearings.

Two types of bearing conditions were used to transfer the applied ram force to the concrete model. During low load-level testing, the spreader beam was hydrastoned to

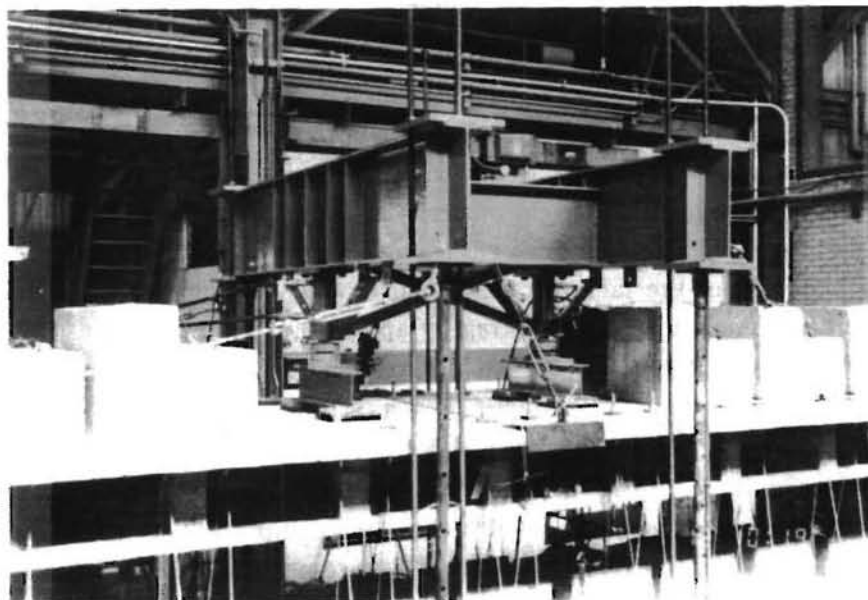


Fig. 6.2 Load Frame

the top of the model to ensure uniform bearing. After several tests it was found that the stiff hydrastone was providing a load path through the load frame which was restraining the top flange of the structure. For all subsequent tests (all factored load and ultimate strength tests) the spreader beam bore on a 1/2-in. thick layer of neoprene. This provided a flexible support between the load frame and the structure so that longitudinal restraint of the top flange of the structure was not induced.

Two double-action 30 ton rams were operated in parallel using a single pump. The applied test force was controlled manually with a pressure transducer connected to a strain indicator box and monitored by a second pressure transducer which was connected to the electronic data acquisition system.

6.2.2 Equivalent Live Load with Impact. So that comparisons could be made with the AASHTO service truck load, it was necessary to determine the magnitude of test load that was equivalent to the reduced-scale service live load. Since the tests were planned to primarily examine flexural behavior, the joint moments were used as the conversion between the service design loads and test loads. The "Equivalent Live Load with Impact" was chosen to provide the same moment at the critical joint as the maximum design service load moment determined at any location. Maximum design moments were determined from the design service loads using influence diagrams developed for each joint. Then, using the influence line for moments at the critical joint, the magnitude of the test load was calculated to give the same moment at the critical joint. The "Equivalent Live Load

with Impact [Equivalent (LL+I)]" is defined as the test load that causes the maximum design live-load moment to occur at the critical joint.

6.2.3 Factored Dead Load. Additional dead weight blocks were added on top of the structure as shown in Fig. 6.2 to simulate the factored dead load for loading above normal service levels. The extra factored dead load consists of 30% of the model dead weight (segment weight plus weight of dead-load compensating blocks). A space was left between adjacent segment-blocks to ensure arching did not occur. Because of interference with the load frame, the factored dead load blocks were left off three central segments. This deficit was made up during testing by applying a small ram load prior to application of additional service live loads.

6.3 General Test Procedure

All tests were conducted with the same equipment and the same general procedure. At the start of each test, ram force was zeroed and reaction load cells, deflection potentiometers, joint opening potentiometers, and pressure transducers were all initialized. Initial readings were also taken on all manually-recorded instrumentation. Using this procedure, the data from the test measurements represented the structural response due to test loads only. The tendon strains were never zeroed, so the measured strain data represented the actual tendon strain.

Test loads were applied in small increments until the desired maximum level was reached. If the maximum level was defined by a specific load, as for service and factored load tests, then the range of force was divided into approximately equal increments. If the maximum level was defined by the model behavior, as for cracking, decompression, and ultimate strength tests, then the load increments were chosen to highlight important observations. An attempt was made, although not always successful, to use the same load increments for testing of both of the exterior spans, so that direct behavioral comparisons could be made.

The first load cycle was started immediately after zeroing the instrumentation. A small load was applied (approximately 2 kips total load) to stabilize the load frame, and then the temporary restraining brackets for the load frame were loosened. The loads were then increased to the first load increment.

The load was increased to the desired level and then held for approximately 5 seconds to enable scanning of all channels by the data acquisition system. The hydraulic line pressure was allowed to equalize until all other manual readings had been made. Midspan deflections were manually read and plotted with applied load during the test to provide information for control of the test.

6.4 Presentation of Test Data

For comparison, most of the data has been presented as a function of the applied test load. In all figures, and for discussion purposes the applied test load is expressed in terms of its reduced-scale equivalent, including impact (i.e., the Equivalent (LL+I), as described in Section 6.2.2). The data are plotted against multiples of equivalent (LL+I), with the origin located to reflect the unloaded state. For the service level tests the unloaded state corresponds with the actual dead load (DL). For the factored and ultimate load tests the unloaded state corresponds approximately with the factored dead load (1.3DL). Because the concrete blocks comprising the additional 30% load for the factored dead load could not be positioned on the segments near the test frame, a small load of about $0.30(LL+I)$ was necessary to bring the loading up to the factored dead load condition. This load was applied prior to application of the live load. Therefore, the applied load starts with this small negative value for all factored and ultimate strength data.

The test data is presented in several standard figures which are described below. In most cases only the loading portion of a complete load cycle is shown.

Applied Load vs Deflections: The deflection represents the net deflection of the structure at the location shown on the schematic after adjustment for support deflections.

Reaction vs Applied Load: The reaction represents the total force measured by the two load cells at a particular support, corrected as described in Section 4.4. Each of the four reactions of the structure are plotted. The reaction at the north interior pier was calculated from the other three reactions and the applied loads.

Joint Moment vs Applied Load: Joint moments were calculated from the corrected reactions and applied loads. The calculated joint moments are presented for all opening joints for a particular test.

Change in Tendon Stress vs Applied Load: The change in the tendon stress represent the average change in stress in two strands of the tendon, corrected as described in Section 4.1. The values indicate the change in stress resulting from the applied test load, and are shown for all measurement locations.

Joint Opening vs Applied Load: The relative movement between points on the bottom flange of adjacent segments at a joint was measured using potentiometers crossing the segment joints, as described in Section 3.9. Relative movements are presented for all opening joints for a particular test.

Joint Opening Profiles: The relative movements between points at various depths of adjacent segments at a joint were measured using grid crack monitors as described in Section 3.9. The relative movements are presented as a profile at a particular

6.5.1 Live Load Cycles for Center-span. Four cycles of service live load were applied to the center-span using the load set-up shown on the schematic in Fig. 6.3. In the first cycle the applied force was increased from zero to the service live load in $0.09(LL+I)$ increments in the first cycle and in $0.18(LL+I)$ increments in the last three cycles. Each of the four cycles provided approximately the same response to the applied loads.

The measured deflected shape of the three-span structure is shown in Fig. 6.3 for a typical service load cycle. The midspan deflection of 0.040 inches corresponds to a deflection/span ratio of $L/7500$. Also shown is the calculated deflected shape from the elastic analysis (see Section 5.4). The elastic analysis overestimates the measured deflection by approximately 20 percent. The tendon data indicated a live-load stress range of about 1 ksi. No tendon slip was noticed at this load level.

6.5.2 Cracking Cycle for Center-span. After completing the live load cycles it was necessary to initially crack the epoxied center-span in order to determine the decompression load. The applied load was increased from zero to a maximum load level of almost $6.0(LL+I)$ in increments of $0.18(LL+I)$. The structure cracked in two stages at approximately 5.2 and $5.7(LL+I)$.

The applied load-deflection response during the cracking cycle is shown in Fig. 6.4. The measured reactions and the calculated joint-moments are plotted with respect to the applied load in Fig. 6.5. The change in tendon stress due to applied load is shown for all center-span tendons in Fig. 6.6.

2.6(LL+I): The structure exhibited linear behavior up to a level of approximately $2.6(LL+I)$. As loading was increased beyond this level the deflection response remained linear but had a slightly lower stiffness.

5.2(LL+I): The applied load was increased until visible cracking occurred in the concrete in segment 16, adjacent to joint (15,16) at approximately $5.2(LL+I)$. Cracking at joint (15,16) of the center-span reduced the stiffness at that point and caused the internal forces to redistribute. After cracking, a larger portion of the load was carried at the interior reactions as the applied load tended to cantilever from the stiff uncracked support region.

The midspan tendon stresses remained linear with applied load up to the point that the concrete section cracked. As cracking occurred, the tensile force that was previously carried by the concrete was transferred to the post-tensioning tendons. This caused a sudden increase in tendon stresses and corresponding strains to equilibrate these forces. With unbonded tendons, considerable elongation was necessary to develop the increased tendon forces. This caused concentrated rotations to occur at the midspan and subsequently increased vertical deflection.

Tendon 5 began slipping from the north end towards the midspan region of the center-span. Tendon 5 also began slipping from the north end of the south-span (21,22) through the pier segment to the south end of the north-span (19,20).

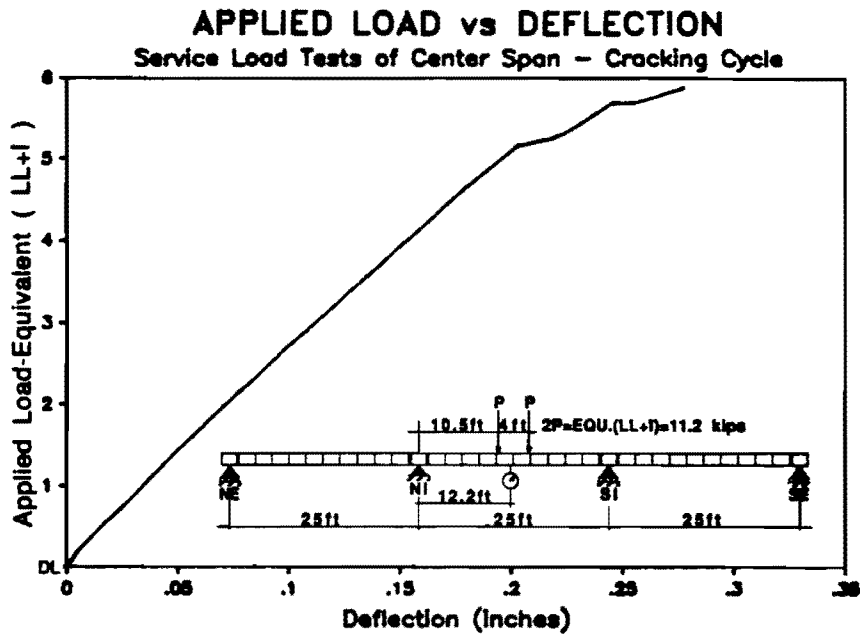


Fig. 6.4 Center Span Cracking Cycle Applied Load vs. Deflection

5.7(LL+I): As loads were increased further, additional cracking occurred at approximately 5.7(LL+I).

5.9(LL+I): The test was discontinued when a hydraulic fitting sprung a leak and pressure reduced rapidly. The cracking cycle is summarized in Tables 6.2, 6.3, and 6.4.

Table 6.2 Center-span Cracking Cycle - Maximum Response Values

	Cracking 5.2(LL+I)	5.9(LL+I)
Deflections	.20 (L/1500)	.28 inches (L/1071)
Reactions	35 kips at NI and SI	39 kips at NI and SI
Moments M+ve	180 ft-kips at (15,16)	190 ft-kips at (15,16)
M-ve	-100 ft-kips at (NI,11)	-130 ft-kips at (NI,11)

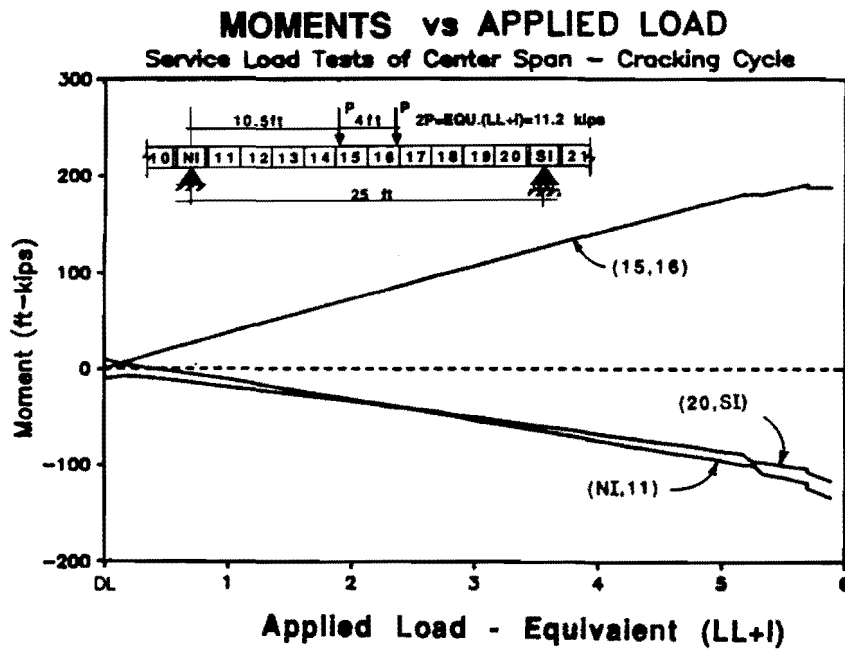
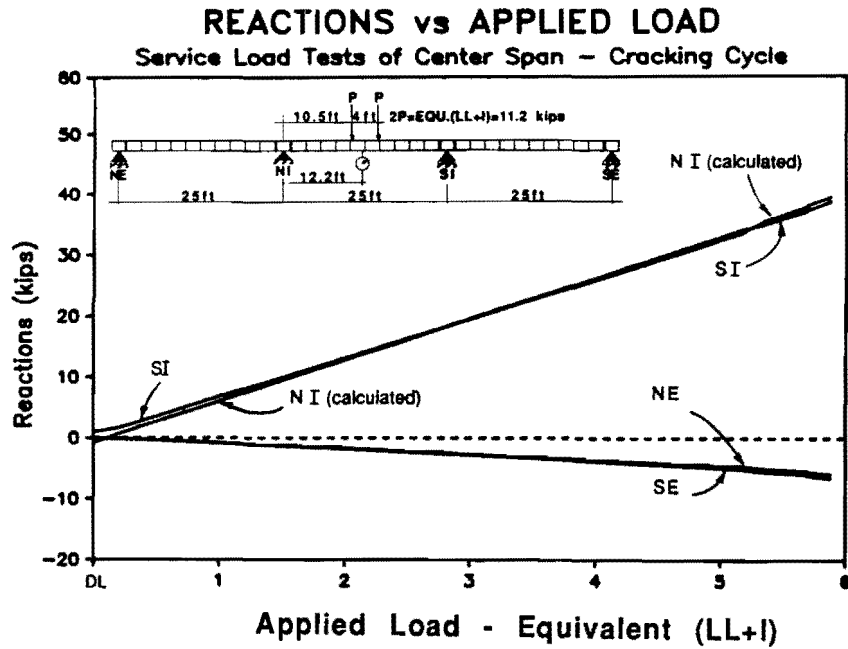


Fig. 6.5 Center Span Cracking Cycle Reactions and Joint Moments

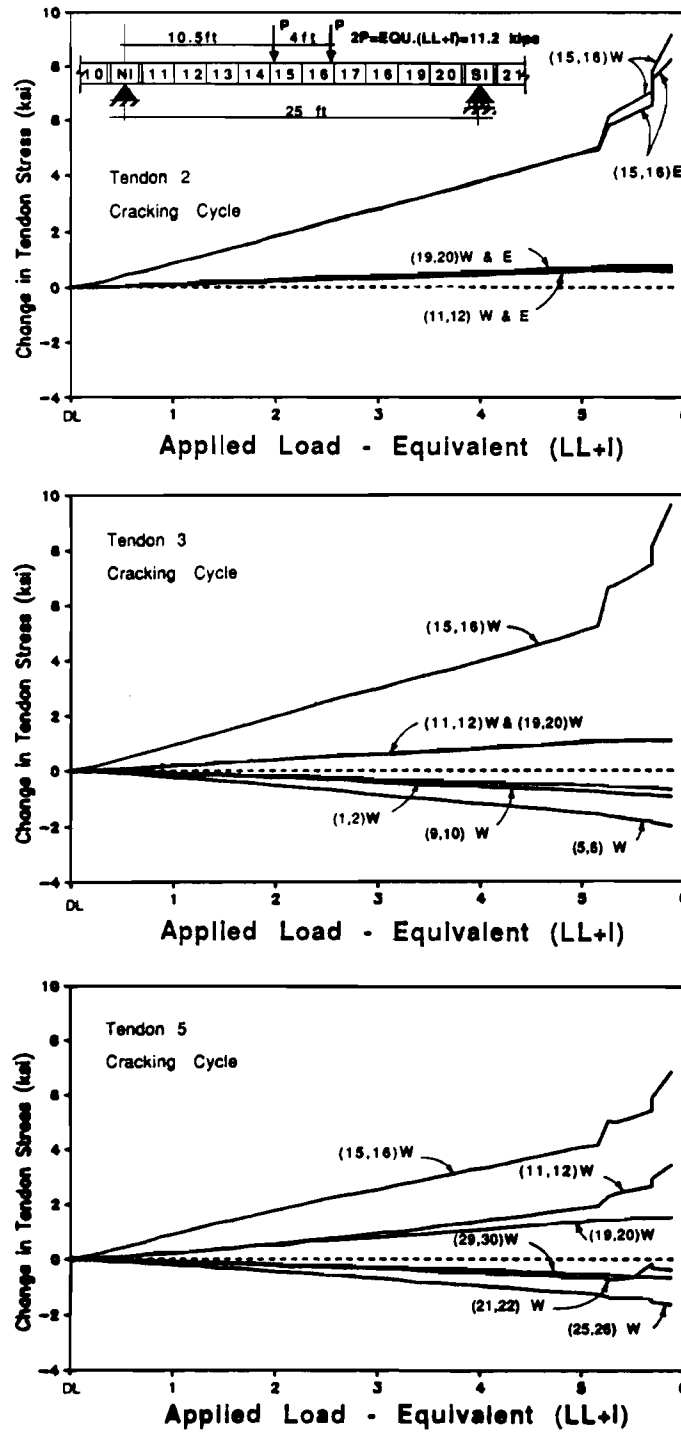


Fig. 6.6 Center Span Cracking Cycle - Change in Tendon Stress vs. Applied Load

Table 6.3 Center-span Cracking Cycle - Change in Tendon Stress (ksi)

	Before Cracking	
	5.2(LL+I)	5.9(LL+I)
Tendon 2:	.5 / 5 / 0.5	1 / 9 / 1
Tendon 3:	1 / 5 / 5	1 / 10 / 1
Tendon 5:	2 / 4 / 2	3 * 7 / 2

* denotes slip towards midspan

key = (11,12)/(15,16)/(19,20)

= north-end/midspan/south-end

Table 6.4 Summary of Center-span Cracking Cycle

<i>P_{applied}</i> :	Description:
DL only	-Start Test ($P_{rms}=0$)
DL+2.7(LL+I)	-Stiffness reduces slightly in P-delta curve
DL+5.2(LL+I)	-Cracking occurs in Segment 16 adjacent to joint (15,16) -Tendon 5 (center-span) begins to slip from the north end towards the midspan region -Tendon 5 (south-span) begins to slip from the north end of the south-span (21,22) through the pier segment to the south end of north-span (19,20).
DL+5.7(LL+I)	-Cracking propagates further
DL+5.9(LL+I)	-Test discontinued

6.5.3 Decompression Load Test of Center-Span. After initially cracking the center joint, three load cycles were applied to the center-span to determine the magnitude of the decompression load. The applied load was increased in $0.54(LL+I)$ increments up to a load level of approximately $2.1(LL+I)$, and then in $0.18(LL+I)$ increments up to a maximum load of $4.1(LL+I)$, or approximately 70 percent higher than the measured decompression load, $2.4(LL+I)$.

The applied load-deflection response was almost identical for all three decompression cycles, and cycle 1 is shown in Fig. 6.7. The measured reactions and the calculated joint-moments are plotted with respect to the applied load in Fig. 6.8. The change in tendon stress due to applied load is shown for all center-span tendons in Fig. 6.9.

2.4(LL+I) Decompression Load: The structure exhibited linear behavior up to the level of the decompression load, at $2.4(LL+I)$. Beyond this load, the load-deflection, response reactions, and joint-moment response all diverge from linear behavior. The midspan stiffness reduces as the joint opens under increased loading, causing a larger portion of the load to be carried by negative bending at the supports.

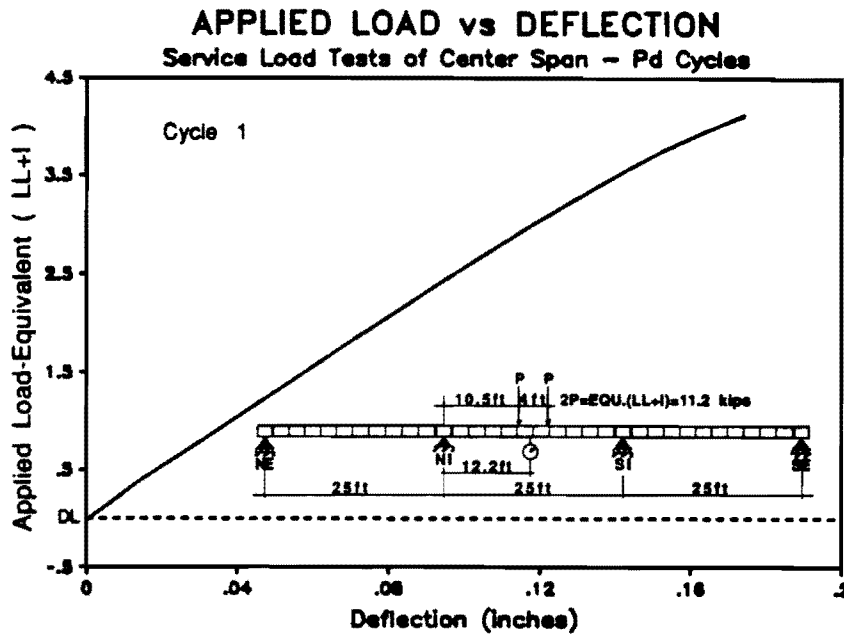


Fig. 6.7 Center Span Decompression Cycles Applied Load vs. Deflection

2.8(LL+I): The midspan tendon stresses remained linear up to approximately 2.8(LL+I). Beyond this load level the tendon stresses began to diverge from the linear response at an increasing rate.

4.1(LL+I): The maximum load level reached during the decompression load cycles for the center-span was 4.1(LL+I). The decompression load cycles for the center-span are summarized in Tables 6.5, 6.6, and 6.7.

Table 6.5 Center-span Decompression Cycles - Maximum Response Values

	Decompression Load 2.4(LL+I)	4.1(LL+I)
Deflections	0.09 L/3333	0.17 inches L/1764)
Reactions	16 kips at NI and SI	27 kips at NI and SI
Moments M+ve	90 ft-kips at (15,16)	150 ft-kips at (15,16)
M-ve	-40 ft-kips at (NI,11)	-70 ft-kips at (NI,11)

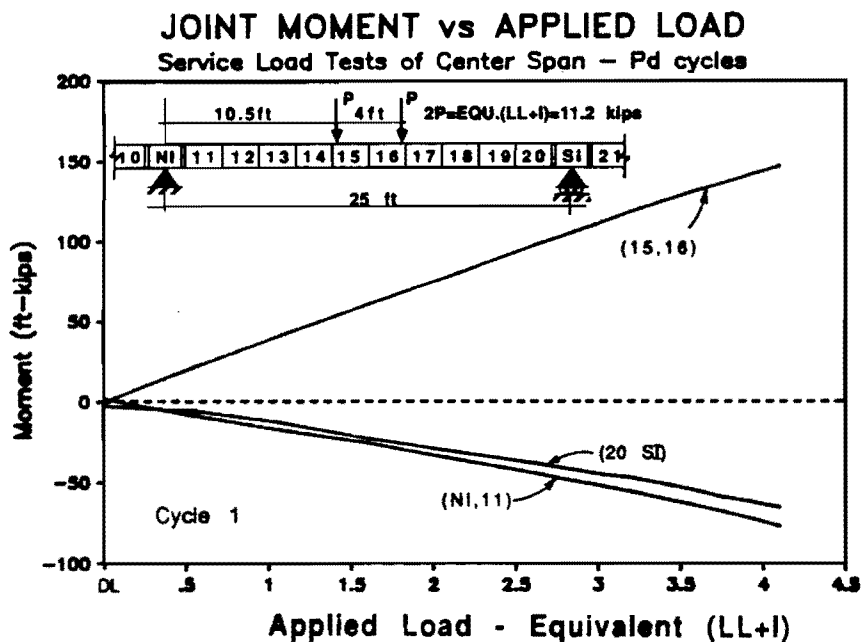
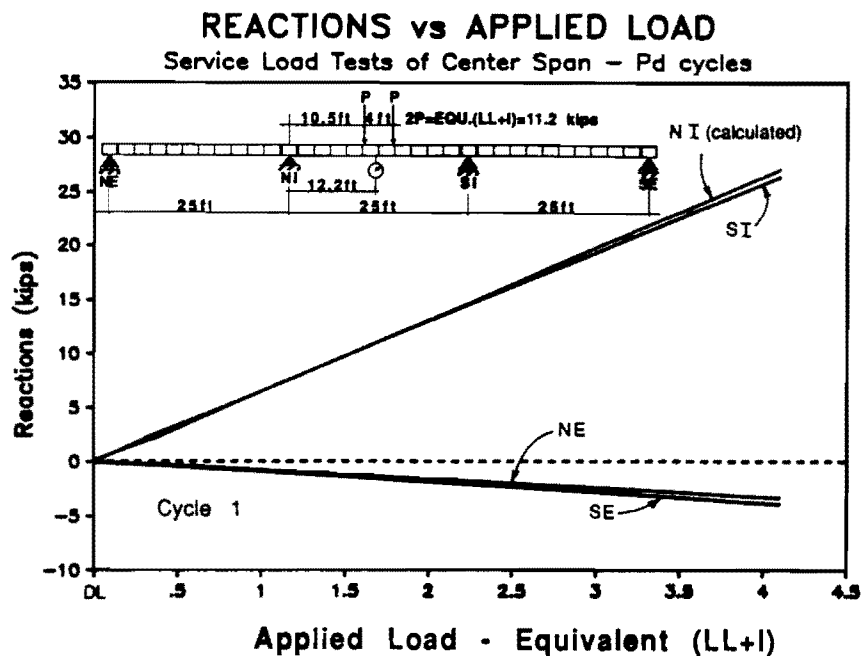


Fig. 6.8 Center Span Decompression Cycles Reactions and Joint Moments

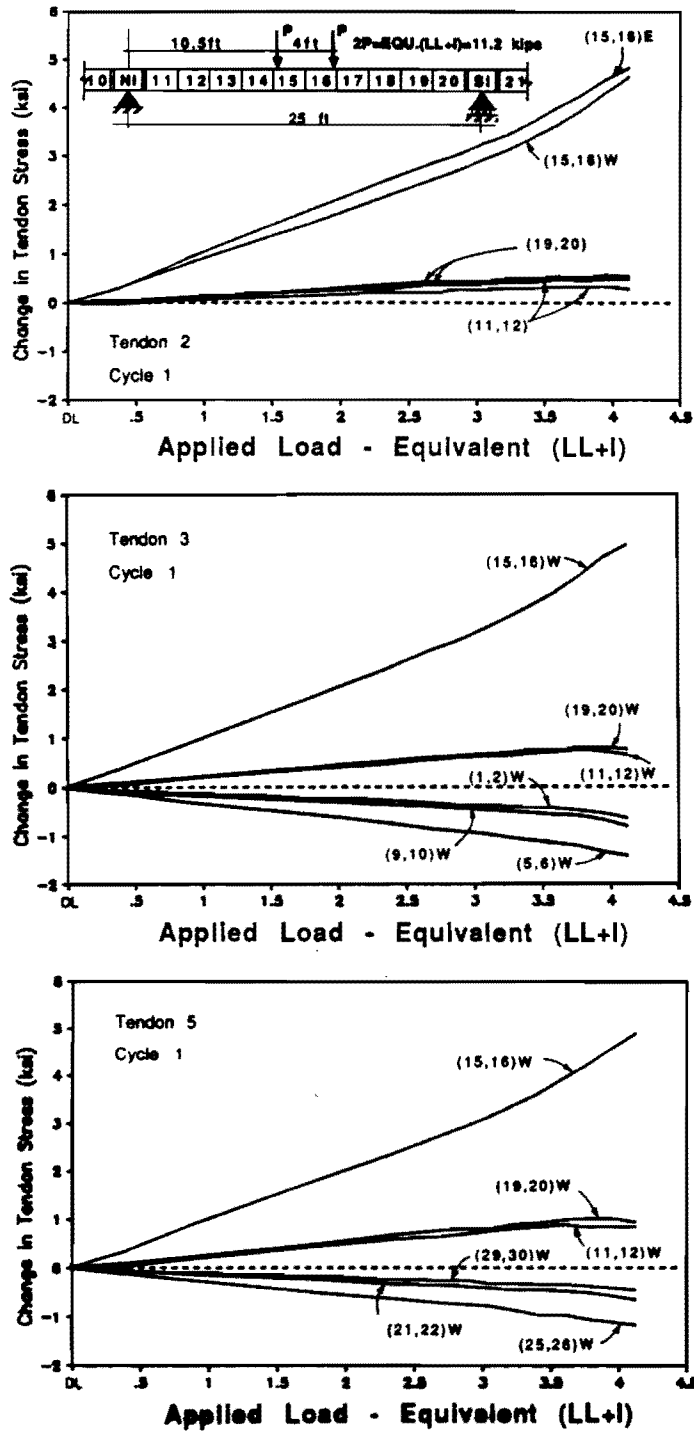


Fig. 6.9 Center Span Decompression Cycles Change in Tendon Stress vs. Applied Load

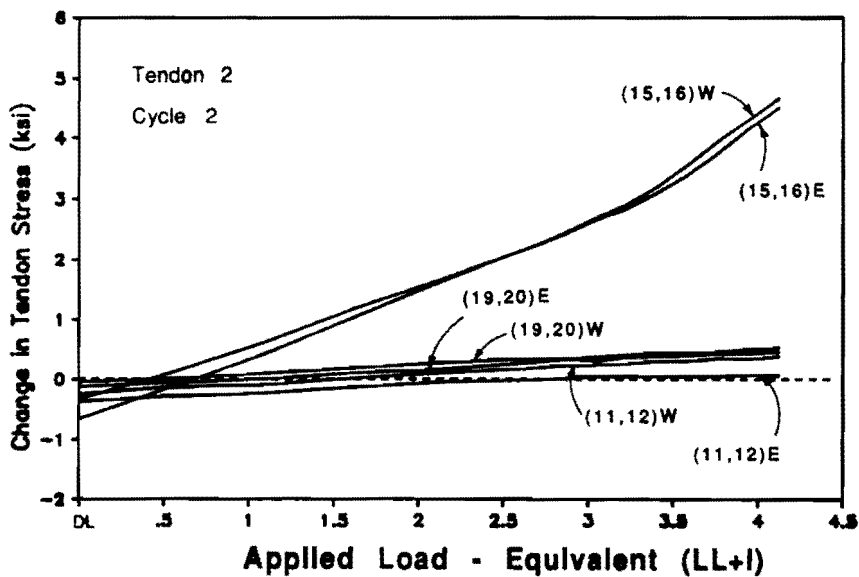
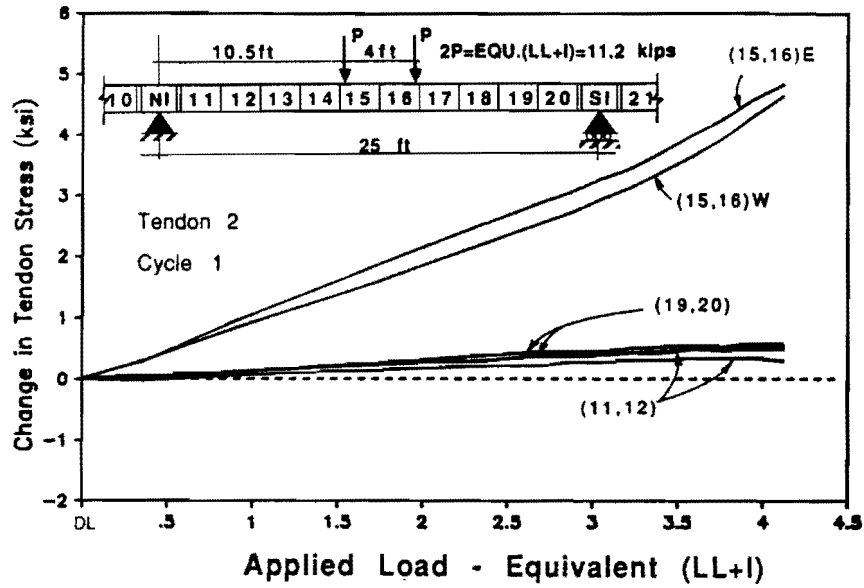


Fig. 6.10 Change in Tendon Stress vs. Applied Load Comparison Between First and Second Cycles

Table 6.6 Center-span Decompression Cycles - Change in Tendon Stress

	Decompression Load	
	2.4(LL+I)	4.1(LL+I)
Tendon 2:	0 / 2 / 0	.5 / 5 / 0.5
Tendon 3:	.5 / 2 / 0.5	1 / 5 / 1
Tendon 5:	.5 / 2 / 0.5	1 / 5 / 1

key = (11,12)/(15,16)/(19,20)
 = north end/midspan/south end

Table 6.7 Summary of Center-span Decompression Cycles

$P_{applied}$:	Description:
DL only	-Start Test ($P_{rams}=0$)
DL+2.4(LL+I)	-Decompression Load
DL+2.8(LL+I)	-The midspan tendon stresses began to deviate from initially linear behavior
DL+4.1(LL+I)	-Maximum applied load

In all tendons of the center-span there appeared to be a small change in stress between the first and second decompression cycles, as shown in Fig. 6.11 for tendon 2. After unloading from the first load cycle there was a net reduction in tendon stress of approximately 0.5 ksi. When the load was reapplied, the tendon stress still increased to the same level as the first cycle. It appears that slip may have occurred at the pier segments during the first cycle causing a reduction of tendon force in cycle 2.

6.6 North-span Load Tests (Dry Jointed)

The north-span was subjected to all levels of loading ranging from design service loads to loads producing ultimate flexural and shear strength.

6.6.1 Service Load Tests of North-Span.

6.6.1.1 Live Load Cycles of North-Span. Four cycles of service live load were applied to the north-span using the load set-up shown in the schematic on Fig. 6.11. The load was applied in $0.16(LL+I)$ increments for all four cycles. Each of the four cycles provided approximately the same response to the applied loads.

The measured deflected shape of the three span structure is shown in Fig 6.11 for a typical service load cycle. The midspan deflection of 0.053 inches corresponds to a deflection/span ratio of $L/5660$. Also shown is the calculated deflected shape from the

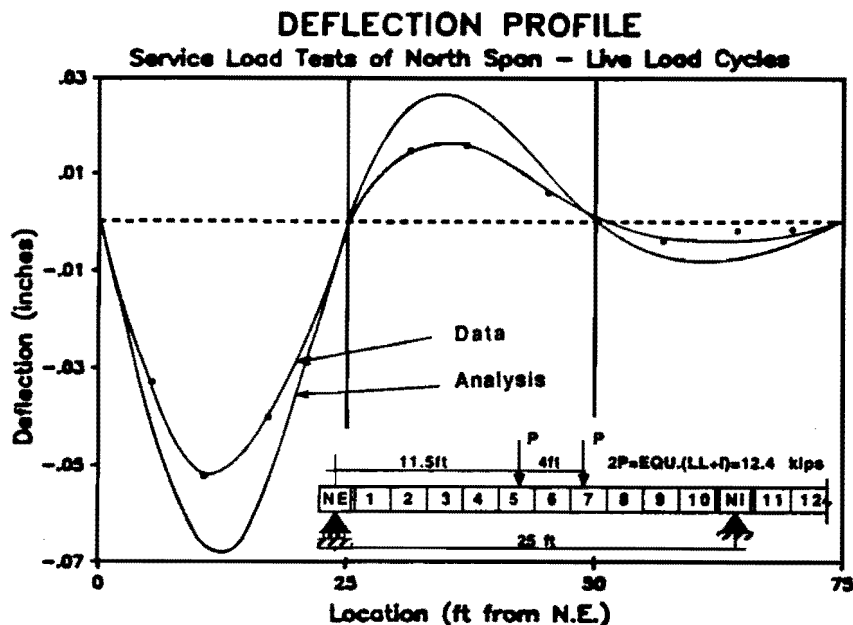


Fig. 6.11 North Span Service Load Tests Deflection Profile

elastic analysis (see Section 5.4). The elastic analysis overestimates the measured deflection by approximately 28 percent. The tendon data indicated a live load stress range of about 1 ksi. No tendon slip was noticed at this load level.

6.6.1.2 Decompression Load Cycles for North-Span. Because the north-span was erected with dry joints it was not necessary to initially crack the span prior to conducting the decompression load tests. A total of six decompression cycles were applied to the north-span. For the first three cycles, a pair of rams was used which displayed erratic behavior possibly caused by higher ram friction. A different pair of rams were used for subsequent tests.

The final three decompression cycles produced more consistent results. The load was applied in $0.32(LL+I)$ increments up to $1.6(LL+I)$, and then in $0.16(LL+I)$ increments up to a maximum load of $2.6(LL+I)$, or approximately 37 percent higher than the measured decompression load of $1.9(LL+I)$.

The applied load-deflection response was identical for all three decompression cycles, and cycle 1 is shown in Fig. 6.12. The measured reactions and the calculated joint-moments are plotted with respect to the applied load in Fig. 6.13.

1.9(LL+I) Decompression Load: The decompression load was estimated to be approximately $1.9(LL+I)$. The structure exhibited bi-linear elastic behavior with a very slight reduction in stiffness for loads above the decompression load.

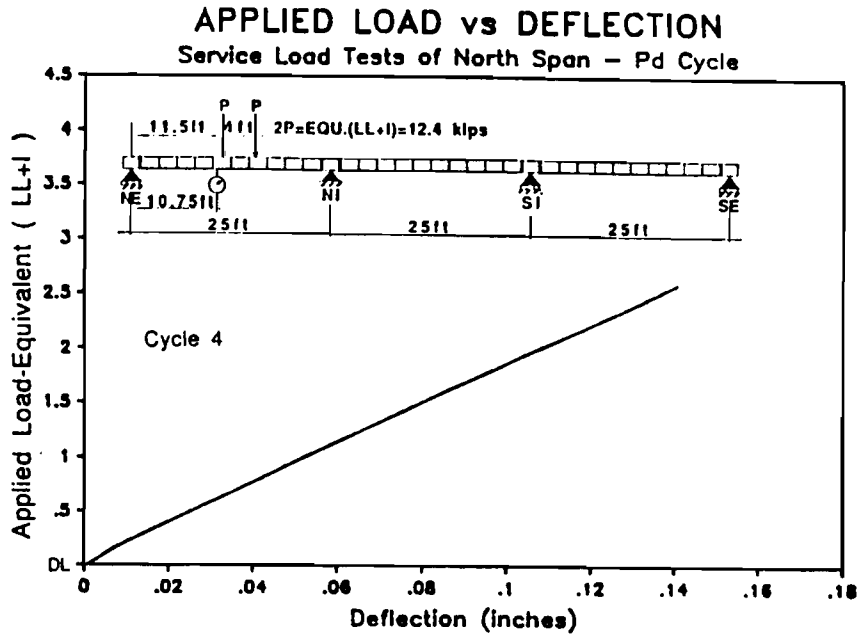


Fig. 6.12 North Span Decompression Cycles: Applied Load vs. Deflection

The reaction and joint moment data show very slight redistribution of internal forces towards the interior support for load levels above the decompression load.

2.6(LL+I): The maximum load level reached during the decompression load cycles for the north-span was 2.6(LL+I). The decompression load cycles are summarized in Tables 6.8, 6.9, and 6.10.

Table 6.8 North-span Decompression Cycles - Maximum Response Values

	Decompression Load 1.9(LL+I)	2.6(LL+I)
Deflections	0.10 (L/3000)	0.14 inches (L/2143)
Reactions	18 kips at NI	25 kips at NI
Moments M +ve	92 ft-kips at (5,6)	120 ft-kips at (5,6)
M -ve	-56 ft-kips at (NI,11)	-79 ft-kips at (NI,11)

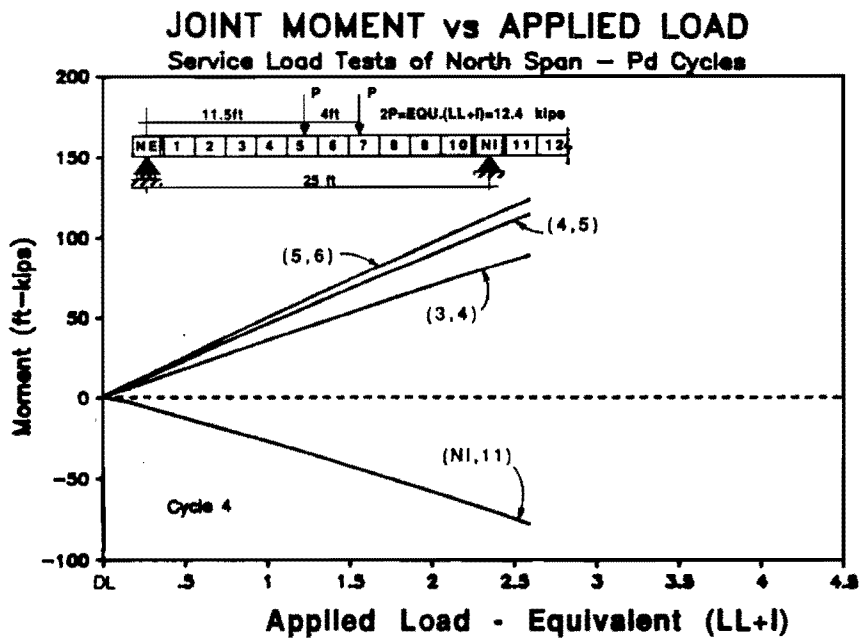
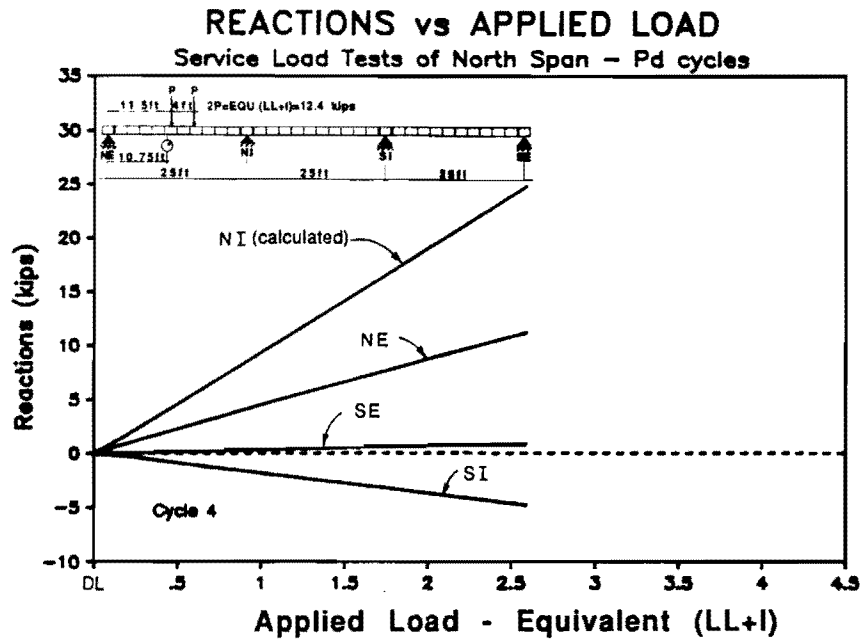


Fig. 6.13 North Span Decompression Cycles Reactions and Joint Moments

Table 6.9 North-span Decompression Cycles - Change in Tendon Stress (ksi)

	Decompression Load	
	1.9(LL+I)	2.6(LL+I)
Tendon 1a:	0 / 2 / 0.5	.5 / 3 / 0.5
Tendon 1b:	.5 / 3 / 0.5	1 / 4 / 1
Tendon 3:	1 / 2 / 1	1 / 3 / 1

key = (1,2)/(5,6)/(9,10)
 = ext.end/midspan/int.end

Table 6.10 Summary of North-span Decompression Cycles

$P_{applied}$:	Description:
DL only	-Start Test ($P_{rams}=0$)
DL+1.9(LL+I)	-Decompression Load
DL+2.6(LL+I)	-Maximum Applied Load

The change in the tendon stresses due to applied load appeared to be linear throughout the entire load cycle, with a maximum stress range of approximately 3.5 ksi at midspan.

6.6.1.3 Torsional Load Cycles. After completing the service load cycles, a final test series was conducted to investigate the torsional response of the structure. The exterior spans were each subjected to three cycles of applied load with the rams positioned directly over the west web. The maximum applied torsional load was representative of a single lane of traffic positioned directly over the west web. The load was applied in 0.16(LL+I) increments to a maximum applied load of 1.0(LL+I).

To measure the torsional response of a structure, rotations must be precisely measured at critical locations along the span. In the model, the rotations were measured by a pair of potentiometers at each support and midspan region, located symmetrically about the longitudinal axis of the structure, as described in Section 3.7. The rotation was calculated from the difference in measured deflection and the spacing between the potentiometers. The magnitude of the measured deflections were very small leading to considerable error in calculating the rotations at a particular section. In addition, the load cell bearings, described in Section 3.6, were relatively flexible compared with the torsional stiffness of the box-section. This caused the torsional forces to distribute in the girder. Further uncertainty existed because the applied ram-force was less than 5 percent of the ram capacity. Therefore, the only observation that can be made from the torsional test is to confirm that the box-section has very high torsional stiffness.

6.6.2 Factored Load Cycles for North Span. After completing the service load tests of all three spans additional dead weight was erected onto the structure to simulate

the factored dead load requirement. Loads were then applied to the dry joint north-span to simulate the factored live-load condition.

A total of six factored load cycles were applied to the north-span. For the first three cycles, the load frame configuration (Section 6.2.1.2) induced longitudinal restraint to the top flange of the model. The longitudinal restraining forces induced lateral forces on the ram pistons which may have caused high friction.

The final three factored load cycles, and all subsequent tests, were conducted with a revised load frame which allowed relative movement between ram locations. The load was applied in approximately $0.16(LL+I)$ increments up to the factored design load of $1.3DL+2.86(LL+I)$. The applied load-deflection response was the same for all three factored load cycles, and cycle 1 is shown in Fig. 6.14. The measured reactions and the calculated joint-moments are plotted with respect to the applied load in Fig. 6.15.

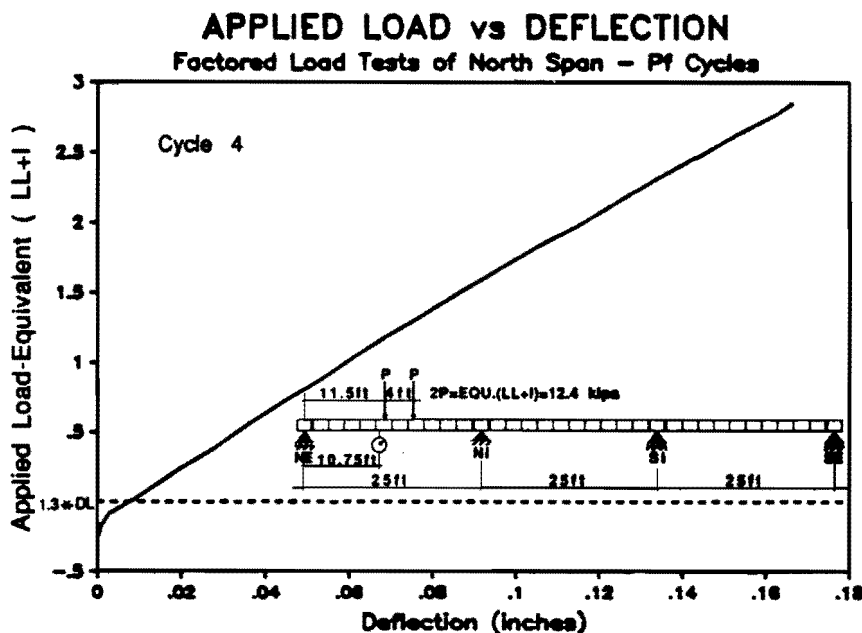


Fig. 6.14 North Span Factored Load Cycles Applied Load vs. Deflection

1.4(LL+I) Decompression Load: In this case, with the structure preloaded with 30 percent more dead load, less applied force was necessary to cause tension at the extreme fiber. The decompression load is consistent with the previous estimation of the decompression load ($1.9(LL+I)$) determined without the additional dead weight. The difference between these two loads is equal to the test load that produces the same moment at the critical joint as 30 percent of the dead load, which is approximately $0.5(LL+I)$.

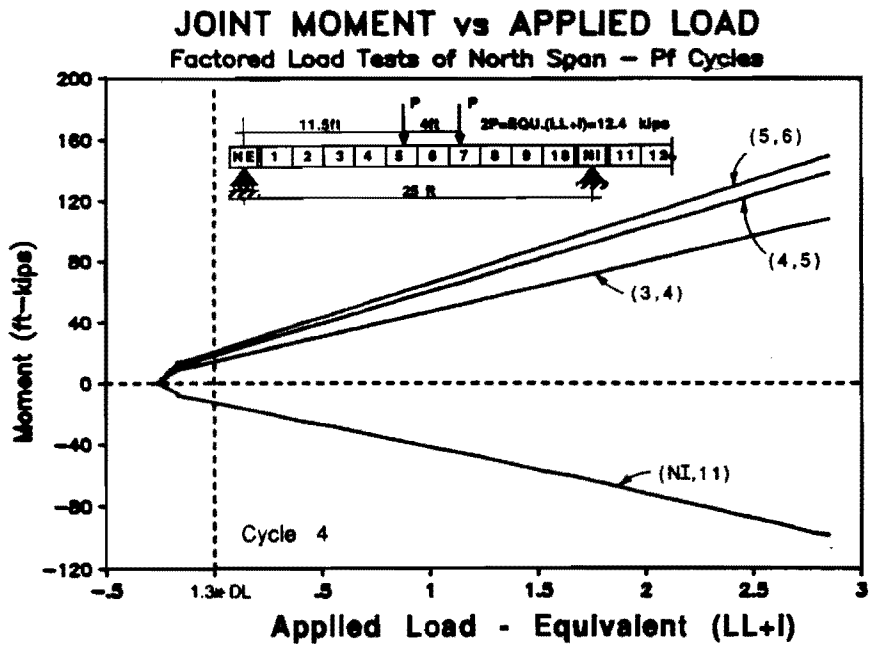
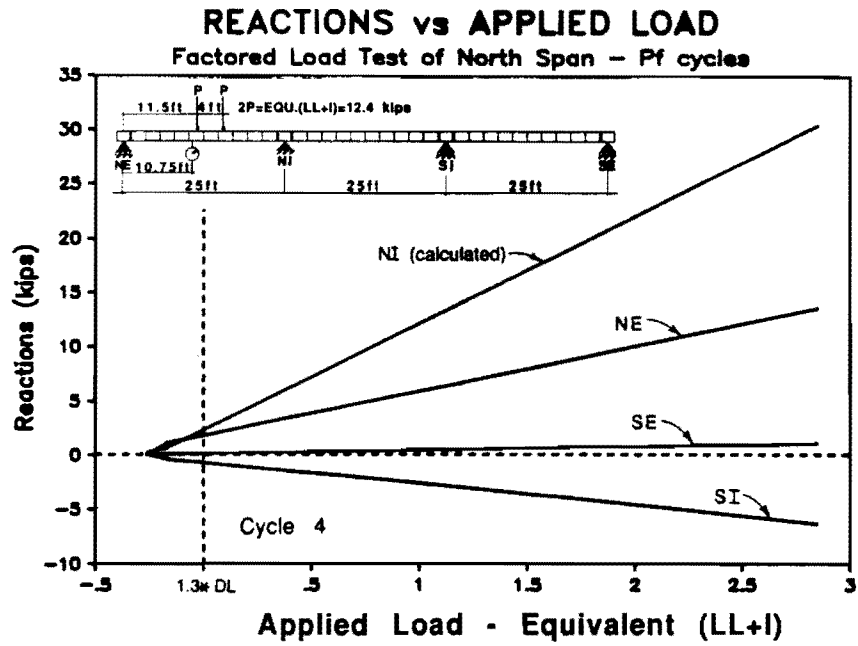


Fig. 6.15 North Span Factored Load Cycles Reactions and Joint Moments

2.9(LL+I) Factored Live Load: The span was loaded to the factored live load level of 2.9(LL+I). Both the reactions and the calculated joint moments show linear behavior indicating minimal internal force redistribution. All tendons exhibited linear behavior with a maximum stress range at midspan of approximately 4 ksi. The factored load cycles for the north-span are summarized in Tables 6.11, 6.12, and 6.13.

Table 6.11

**North Span Factored Load Cycle - Maximum Response
Values at Factored Load = 2.9(LL+I)**

Deflections	0.17 inches (L/1764)
Reactions	30 kips at NI
Moments M +ve	150 ft-kips at (5,6)
M -ve	-100 ft-kips at (NI,11)

**Table 6.12 North Span Factored Load Cycle
Change in Tendon Stress at Factored Load = 2.9(LL+I)**

	(1,2) ext.end	(5,6) midspan	(9,10) int.end
Tendon 1a:	1	4	1
Tendon 1b:	1	4	1
Tendon 3:	1	4	1

Table 6.13 Summary of North Span Factored Load Cycles

$P_{applied}$:	Description:
1.3DL-0.28(LL+I)	-Start Test ($P_{rams}=0$)
1.3DL	-Start Live Load application from the factored dead load condition
1.3DL+1.4(LL+I)	-Decompression Load
1.3DL+2.9(LL+I)	-Factored Load

6.6.3 Flexural Strength Tests of North Span

6.6.3.1 Joint Opening Cycles for North Span. Load was then increased beyond factored load levels to investigate the ultimate flexural behavior of the system. The first stage of the flexural strength test was to apply load to the structure to visibly open a midspan joint. Load was applied in 0.32(LL+I) increments to the factored load level, 2.9(LL+I), and then in 0.16(LL+I) increments to a maximum applied load of

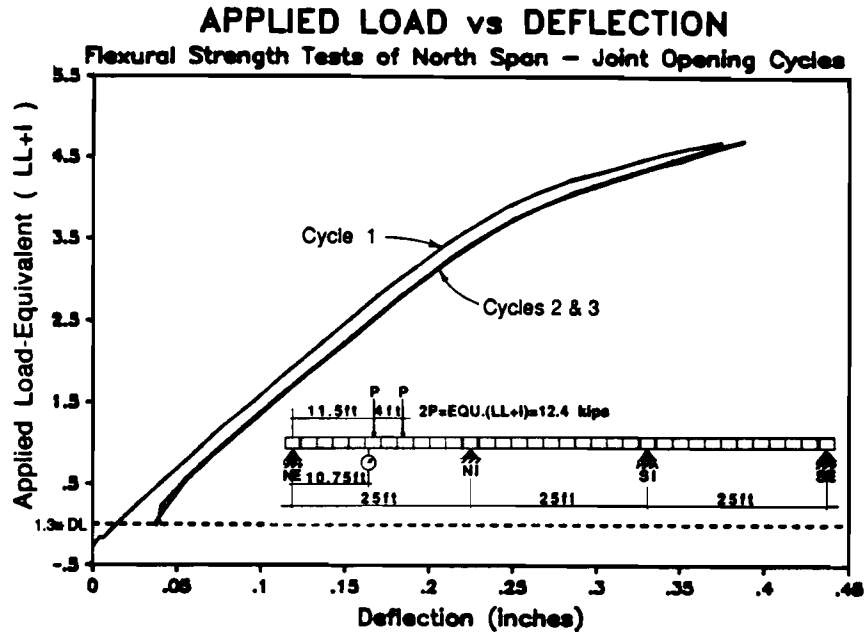


Fig. 6.16 North Span Joint Opening Cycles Applied Load vs. Deflection

4.7(LL+I). The corresponding joint opening at this load level was approximately 0.02 in., which translates into 0.08 in. in the prototype structure.

The applied load-deflection response for all three joint opening cycles is shown in Fig. 6.16. The measured reactions and the calculated joint-moments are plotted with respect to the applied load in Fig. 6.17. The change in tendon stress due to applied load is shown for all north-span tendons in Fig. 6.18. The measured joint openings are plotted with respect to applied load in Fig. 6.19.

1.4(LL+I) Decompression Load: The structure exhibited linear behavior up to the level of the decompression load, at 1.4(LL+I). Beyond this load, the load-deflection, reactions, and joint-moment response all diverge from linear behavior as applied load begins redistributing to the interior support.

1.8(LL+I): The midspan region of all the tendons in the north-span exhibited linear response up to approximately 1.8(LL+I). For load levels higher than 1.8(LL+I) the rate of change in tendon stress increased.

3.0(LL+I): Joints (4,5) and (5,6) began opening at approximately 3.0(LL+I). This resulted in rapidly reducing stiffness at midspan, increased deflections, and redistribution of internal forces towards the interior support.

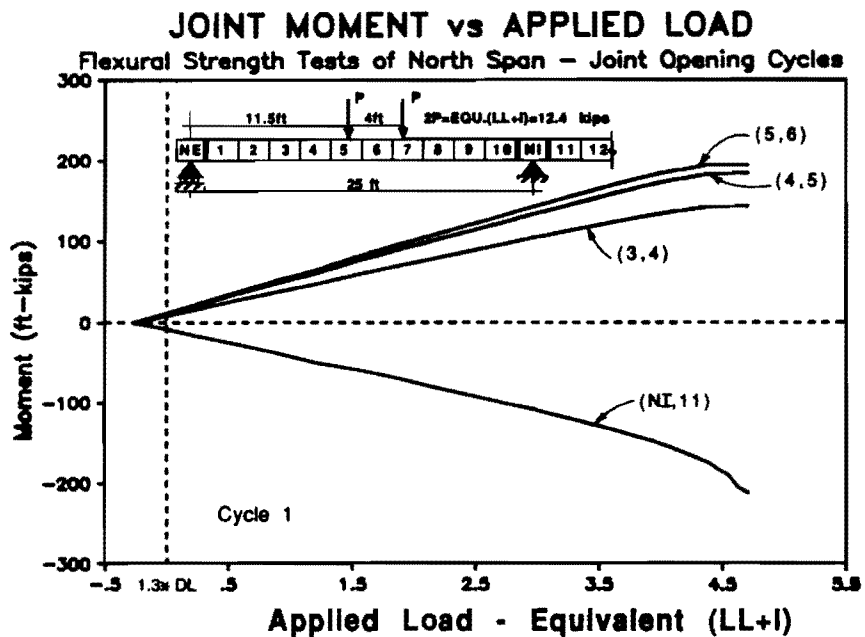
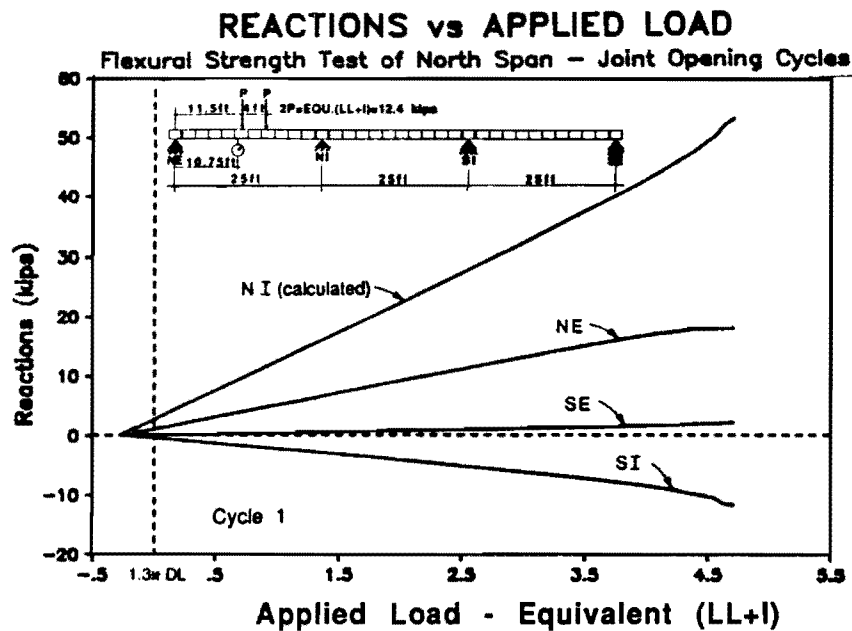


Fig. 6.17 North Span Joint Opening Cycles Reactions and Joint Moments

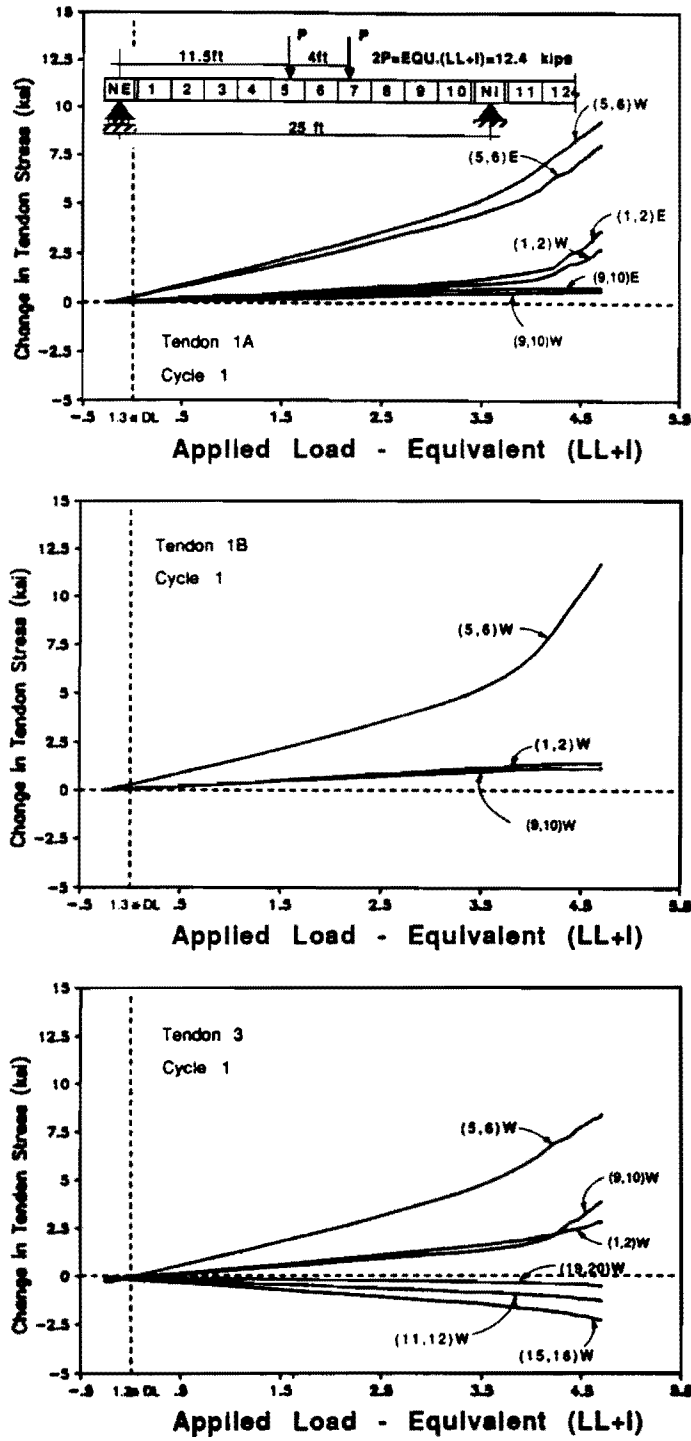
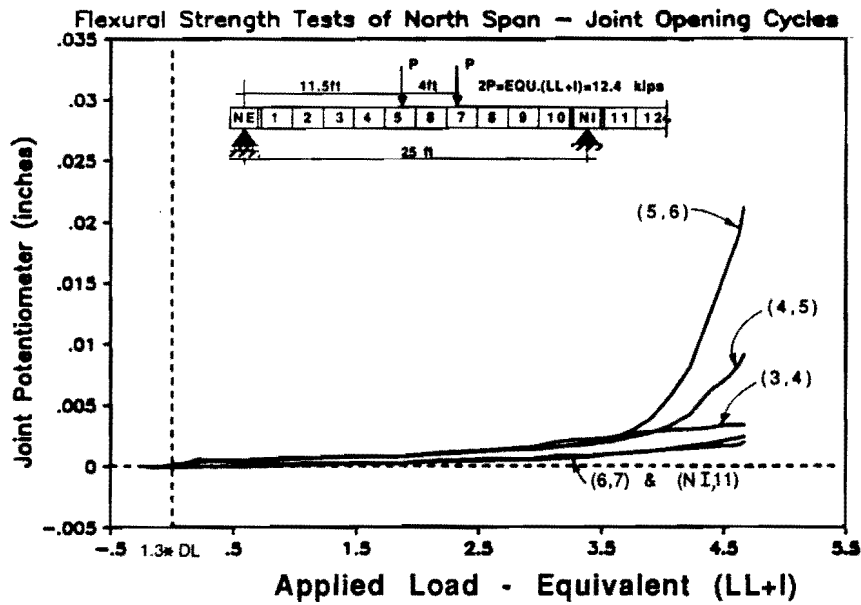


Fig. 6.18 North Span Joint Opening Cycles – Change in Tendon Stress vs. Applied Load

JOINT OPENING POTENTIOMETER vs APPLIED LOAD



JOINT OPENING POTENTIOMETER vs APPLIED LOAD

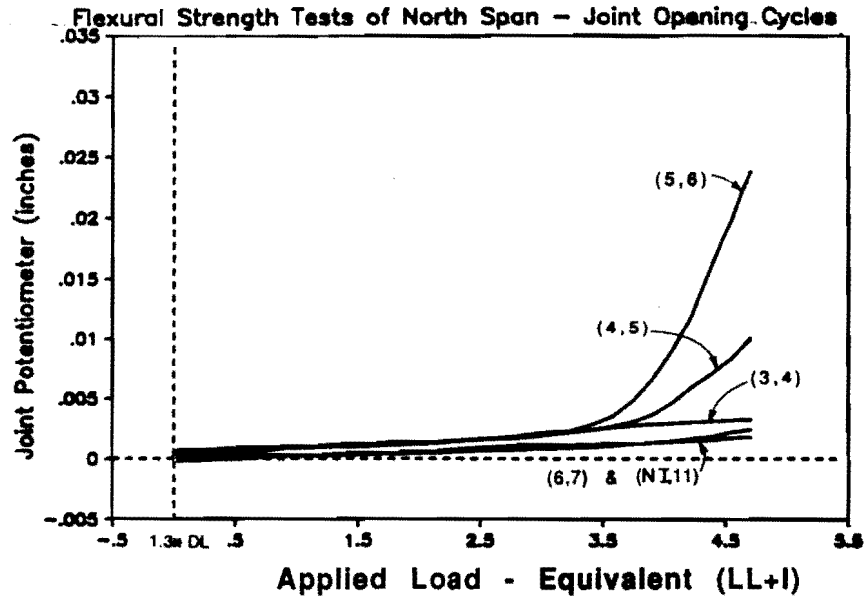


Fig. 6.10 North Span Joint Opening Cycles Joint Opening Potentiometer vs. Applied Load

The tendon stresses began increasing at a faster rate as the joint opened further. This increase in force caused Tendon 1a to begin to slip from the midspan region towards both ends of the span.

3.5(LL+I): Tendon 3 began slipping from both ends towards the midspan region.

4.2(LL+I): Slipping in tendon 1a began slowly at 3.0(LL+I) until major slip occurred at 4.2(LL+I). As tendon 1a slipped freely, the reactions and joint-moments indicated that "hinging" was occurring at the midspan region, and negative moments increased rapidly. Much larger elongations were necessary to develop the same force in the slipping tendon, leading to large rotations at the open joint region. Joints (4,5) and (5,6) opened at a faster rate as shown at the top of Fig. 6.19 for the first joint opening cycle.

4.7(LL+I): The applied load was increased until joint (5,6) was visibly open at a maximum load of 4.7(LL+I). The tangent stiffness at the beginning and end of the joint opening cycle was calculated as 18(LL+I)/inch and 5.9(LL+I)/inch, respectively. The joint opening cycles for the north-span are summarized in Tables 6.14, 6.15, and 6.16.

Table 6.14
North Span Joint Opening Cycles
Maximum Response

Values at Load = 4.7(LL+I)

Deflections	0.37 inches (L/810)
Reactions	53 kips at NI
Moments M +ve	190 ft-kips at (15,16)
M -ve	-210 ft-kips at (NI,11)

Table 6.15
North Span Joint Opening Cycles
Change in Tendon

Stress at Load = 4.7(LL+I)

	(1,2) ext.end	(5,6) midspan	(9,10) int.end
Tendon 1a:	4 *	10	1
Tendon 1b:	2	12	2
Tendon 3:	3 *	9 *	4

* denotes slip towards midspan

Table 6.16 Summary of North Span Joint Opening Cycles

<i>P_{applied}</i>:	Description:
1.3DL-0.28(LL+I)	-Start Test ($P_{rams}=0$)
1.3DL	-Start Live Load application from the factored dead load condition
1.3DL+1.4(LL+I)	-Decompression Load
1.3DL+1.8(LL+I)	-The midspan stresses of all the tendons begin to increase at a faster rate
1.3DL+3.0(LL+I)	-Joints (4,5) and (5,6) begin to open widely causing tendon stresses to increase at a faster rate -Tendon 1a begins to slip slowly from both ends towards the midspan region
1.3DL+3.5(LL+I)	-Tendon 3 begins to slip from both ends towards the midspan region.
1.3DL+4.2(LL+I)	-Tendon 1a begins to slip rapidly from the midspan section towards both ends. The resultant elongations cause "Hinging" to occur at midspan.
1.3DL+4.7(LL+I)	-Maximum Load for Joint Opening Cycles

As mentioned above, tendon slip was noticed in tendons 1a and 3 during the first decompression load cycle. The applied load-tendon stresses are shown for the first two joint opening cycles in Fig. 6.20. The tendon stresses were set equal to zero at the start of the first cycle. After applying one cycle of load there was a net change in tendon stress at the start of the second cycle. The exterior-end stresses had increased and the midspan stresses had decreased. This is also illustrated by the tendon stress profile (Fig. 6.21) for the unloaded condition preceding each load cycle. With slip occurring towards the midspan section of the tendon, the "unstressed" length of that portion had increased, leading to decreased tendon stresses when the applied load was removed. Conversely, because the tendon had slipped away from the exterior region the "unstressed" length had decreased leading to increased tendon stresses when the applied load was removed.

The slip that occurred in the first cycle also changed the distribution of moments in subsequent cycles. Figure 6.22 is a comparison between the joint moments in the first two joint-opening cycles. In the first cycle, described above, the structure appears to hinge at the midspan region at approximately 4.2(LL+I). In subsequent cycles to the same load level the moment increased smoothly throughout the load cycle with a maximum moment equal to the first cycle.

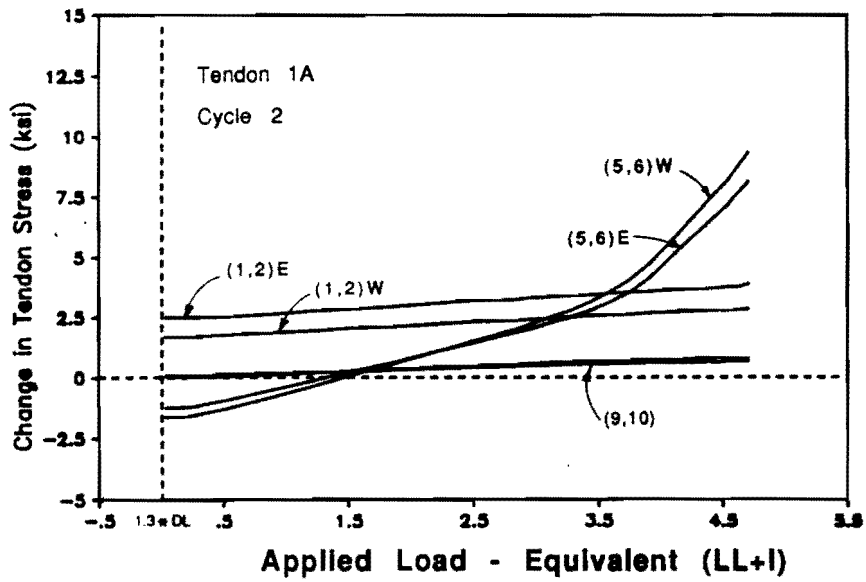
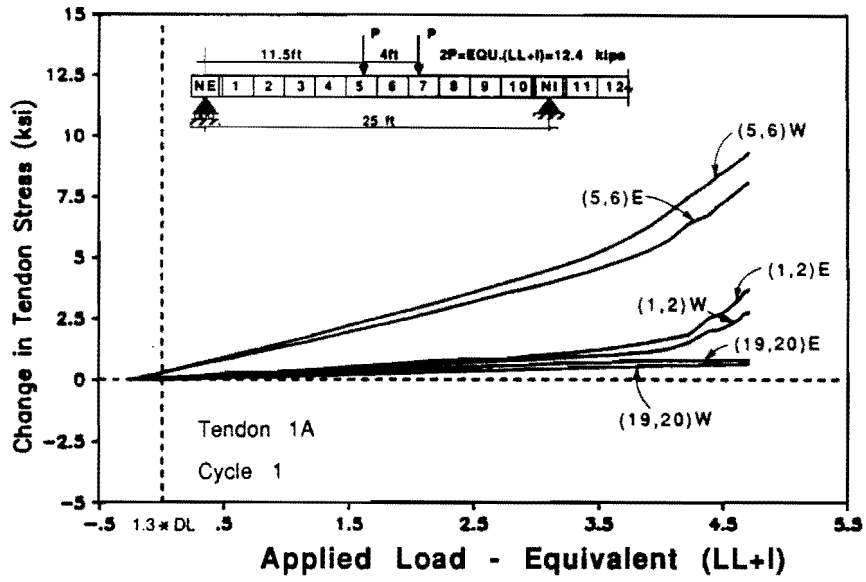


Fig. 6.20 North Span Joint Opening cycles Comparison of Tendon Stresses for Cycles 1 & 2

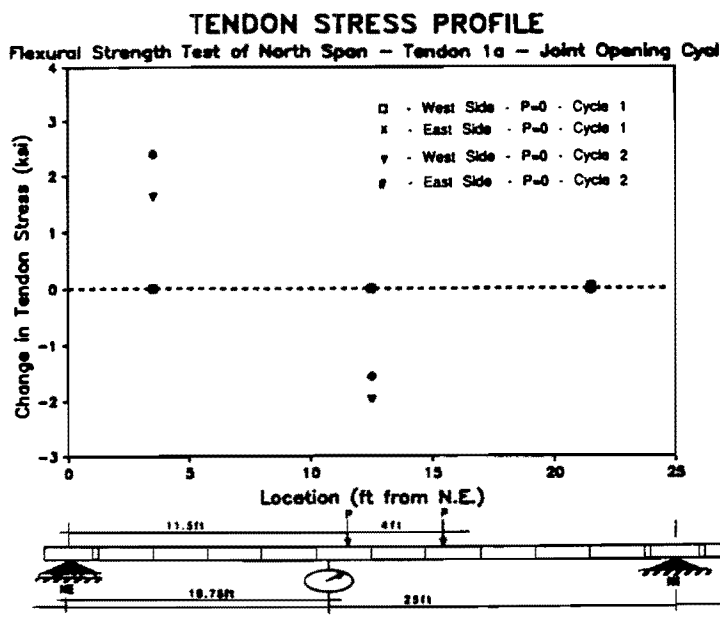


Fig. 6.21 North Span Joint Opening Cycles – Tension Stress Profile

The slip in the tendons during the first cycle also changed the behavior of the opening joints. In the first cycle, shown at the top of Fig. 6.19, the critical joint (5,6) (as predicted by the plastic mechanism analysis in Section 5.2) opened 0.021 inches, while the adjacent joint (4,5) opened 0.010 inches. All other joints remained visibly closed, with joint (3,4) measuring 0.003 inches. In the second cycle, shown at the bottom of Fig. 6.19, joint (5,6) opened widely at a lower load level and reached a higher maximum opening of 0.025 inches. joint (4,5) displayed more gradual opening to a maximum opening of 0.011 inches.

No cracking was visible in the concrete following the north-span joint-opening tests.

6.6.3.2 Flexural Strength Cycles for North Span. After completing the joint-opening cycles, the structure was loaded to higher levels to determine the flexural strength of the system. Because the strength of the structure could not be precisely determined, and because of the possible brittle nature of the failure mode, the load was increased above the previous joint opening load levels in very small increments (0.04 to 0.08(LL+I)). Subsequently, due to time constraints, the ultimate flexural strength test for the north-span was conducted in three sessions, each time to a higher load level. The flexural strength of the north-span was measured to be 6.8(LL+I) with an ultimate midspan deflection of 1.62 inches.

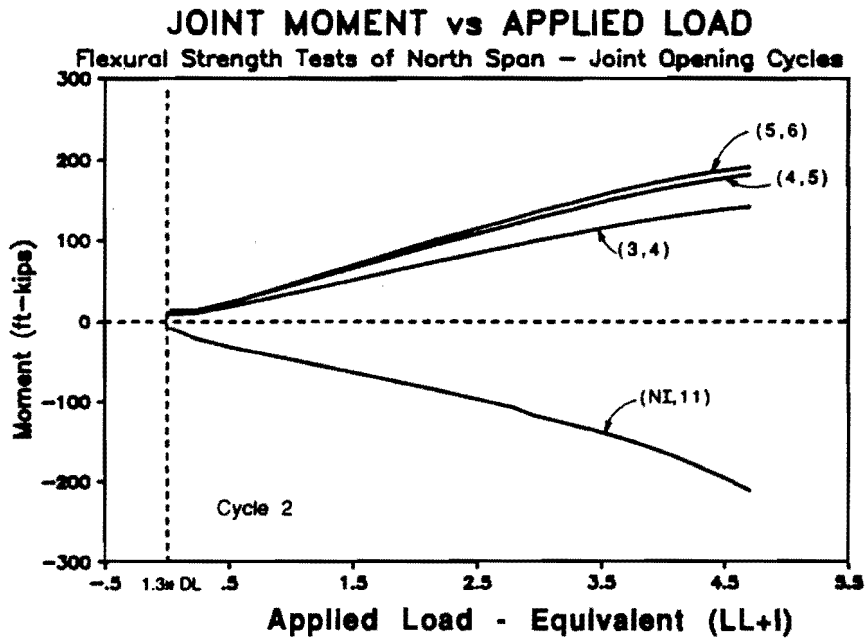
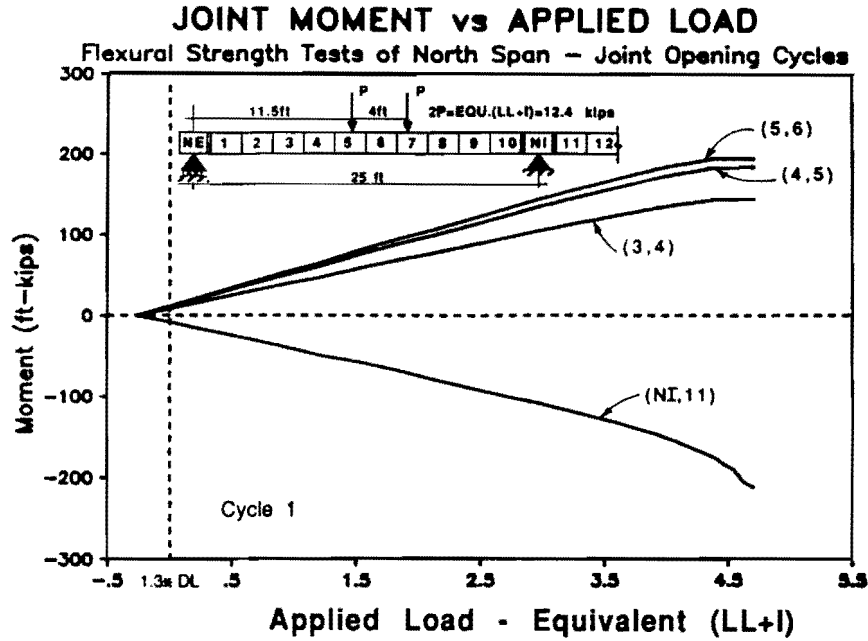


Fig. 6.22 North Span Joint Opening Cycles Comparison of Joint Moments for Cycles 1 & 2

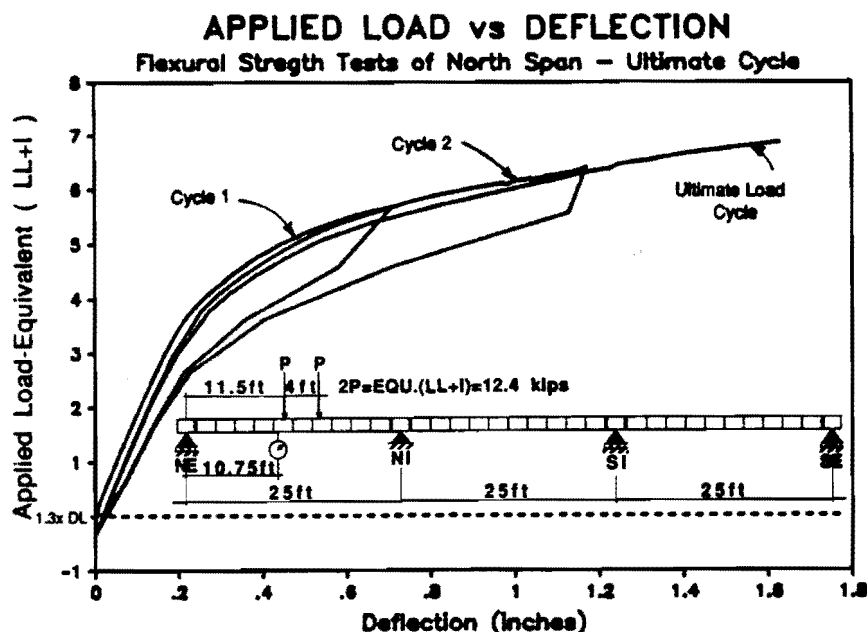


Fig. 6.23 North Span Flexural Strength Test - Applied Load Vs. Deflection

The applied load-deflection response for all three flexural strength cycles is shown in Fig. 6.23 and the last cycle alone is shown in Fig. 6.24. The measured reactions and the calculated joint-moments for the ultimate cycle are plotted with respect to the applied load in Fig. 6.25. The change in tendon stress due to applied load is shown for all north-span tendons in Fig. 6.26. Because the critical negative-moment joint occurs on the interior side of the first interior pier segment (see plastic mechanism in analysis in Section 5.2), the change in tendon stress due to applied load is shown for all center-span tendons in Fig. 6.27. The joint behavior, as measured by potentiometer and grid crack-monitors, is illustrated in Fig. 6.28.

Response of the structure at load stages corresponding to $1.4(LL+I)$, $1.8(LL+I)$, and $3.0(LL+I)$ was essentially the same as that measured in the previous joint-opening cycles.

3.8(LL+I): Joint (4,5) began opening at approximately $3.8(LL+I)$ causing the tendon stresses in the midspan sections of tendons 1a and 1b to begin increasing at a faster rate. Tendon 3 began slipping from both ends towards the midspan region.

4.8(LL+I): The support joint, (NI,11) began opening at approximately $4.8(LL+I)$. This shows up as the inflection point in the reaction and moment data (Fig.

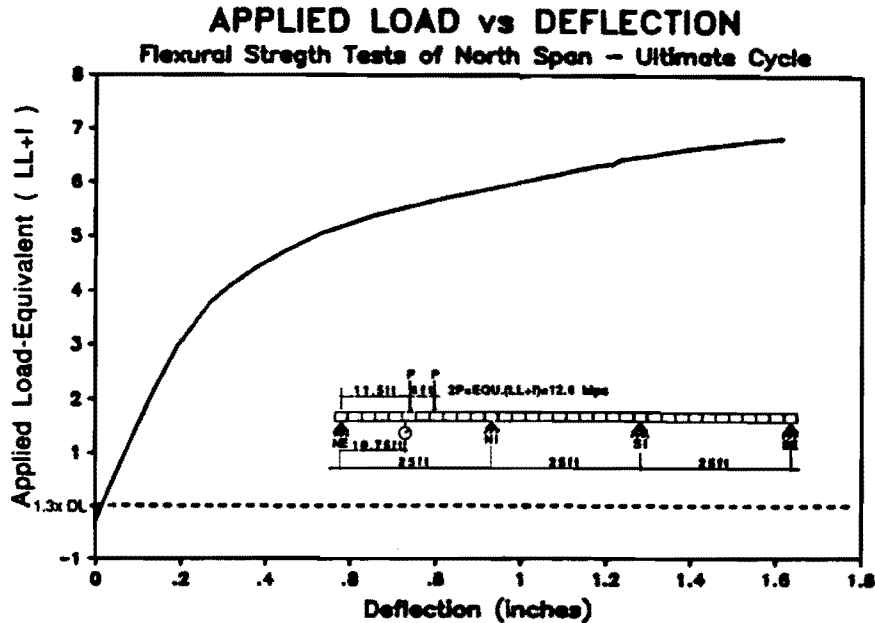


Fig. 6.24 North Span Flexural Strength Tests – Applied Load vs. Deflection

6.26) indicating that the reduced stiffness at the support caused a redistribution of internal forces back towards the midspan region.

All the tendon stresses at the near end of the interior span (tendons 2, 3, and 5) increased as the support joint began opening at approximately 4.8(LL+I). Tendon 1a began slipping from both ends towards the midspan region.

5.0(LL+I): The support joint opened further, reducing stiffness at the support and redistributing the internal forces towards the midspan region. Tendon 1b began slipping from the interior end (9,10) towards the midspan region.

5.3(LL+I): Tendon 5 (interior span) began slipping from the midspan region towards the near end (11,12) of the interior span.

6.2(LL+I): Tendon 1b began slipping from the exterior end (1,2) towards the midspan region. Slipping continued from the interior end as well.

6.4(LL+I): Tendon 2 (Interior span) began slipping from the midspan region towards the near end (11,12) of the interior span.

6.8(LL+I) **Flexural Strength:** The test was discontinued before catastrophic failure when crushing was noticed on the top of a key in joint (5,6) (Fig. 6.29), and the tangent stiffness had reduced to 4 percent of the initial elastic stiffness. The tangent stiffness

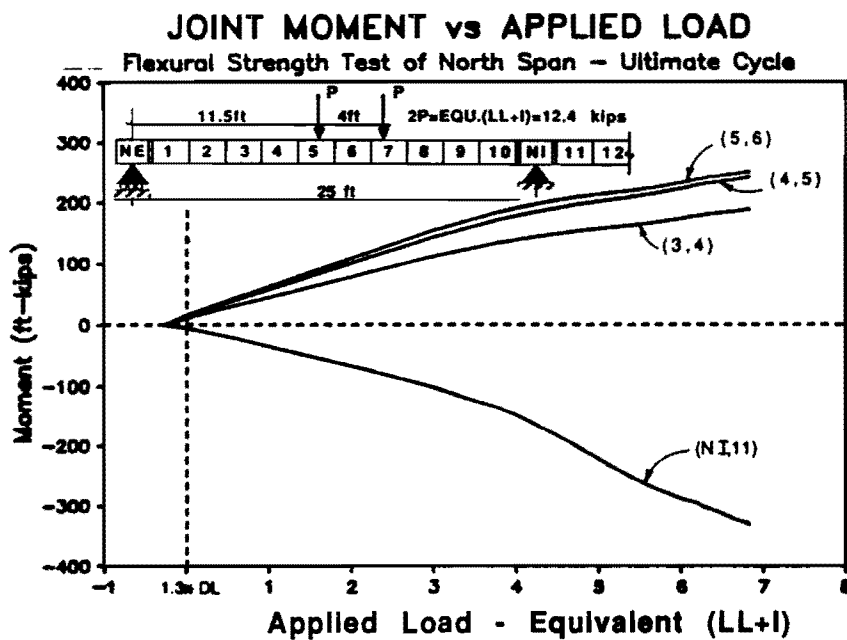
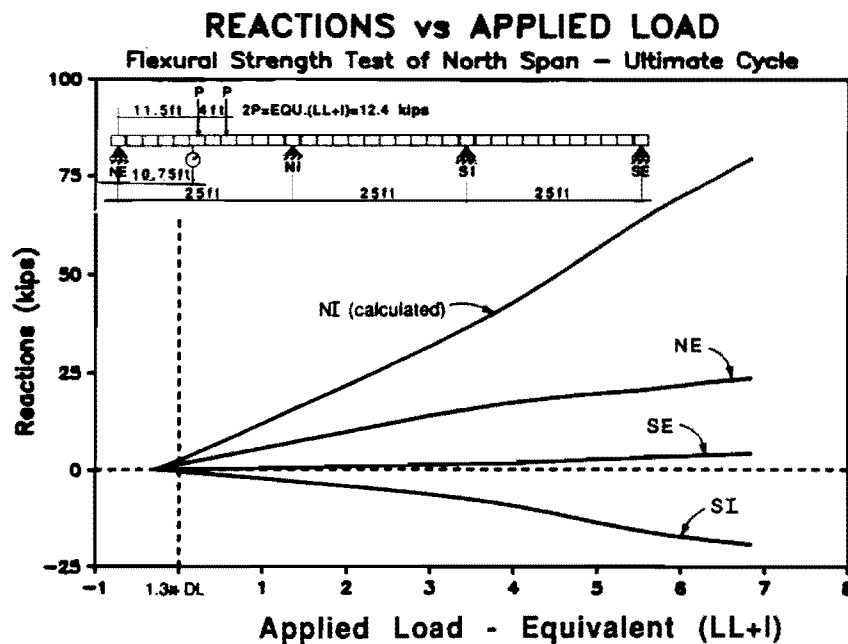


Fig. 6.25 North Span Flexural Strength Tests - Reactions and Joint Moments

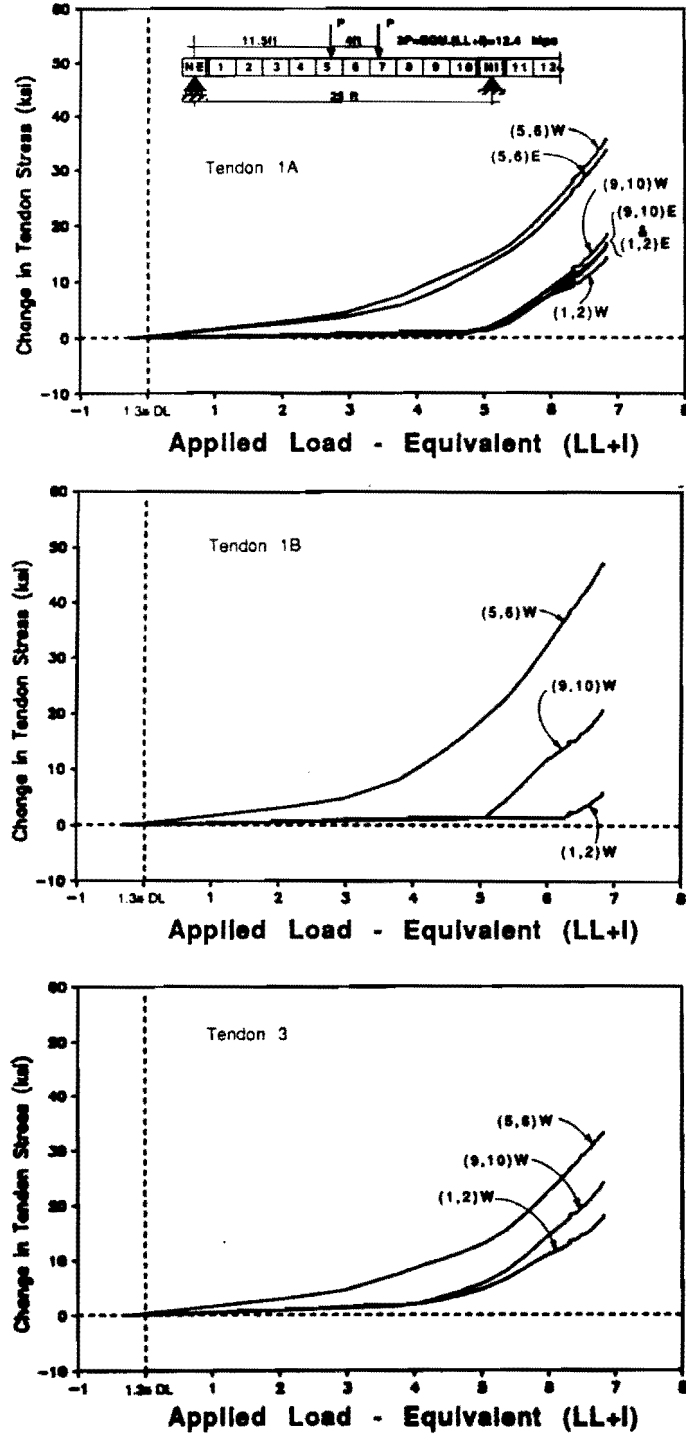


Fig. 6.26 North Span Flexural Strength Tests – Change in Tendon Stress vs. Applied Load (North-Span Tendons)

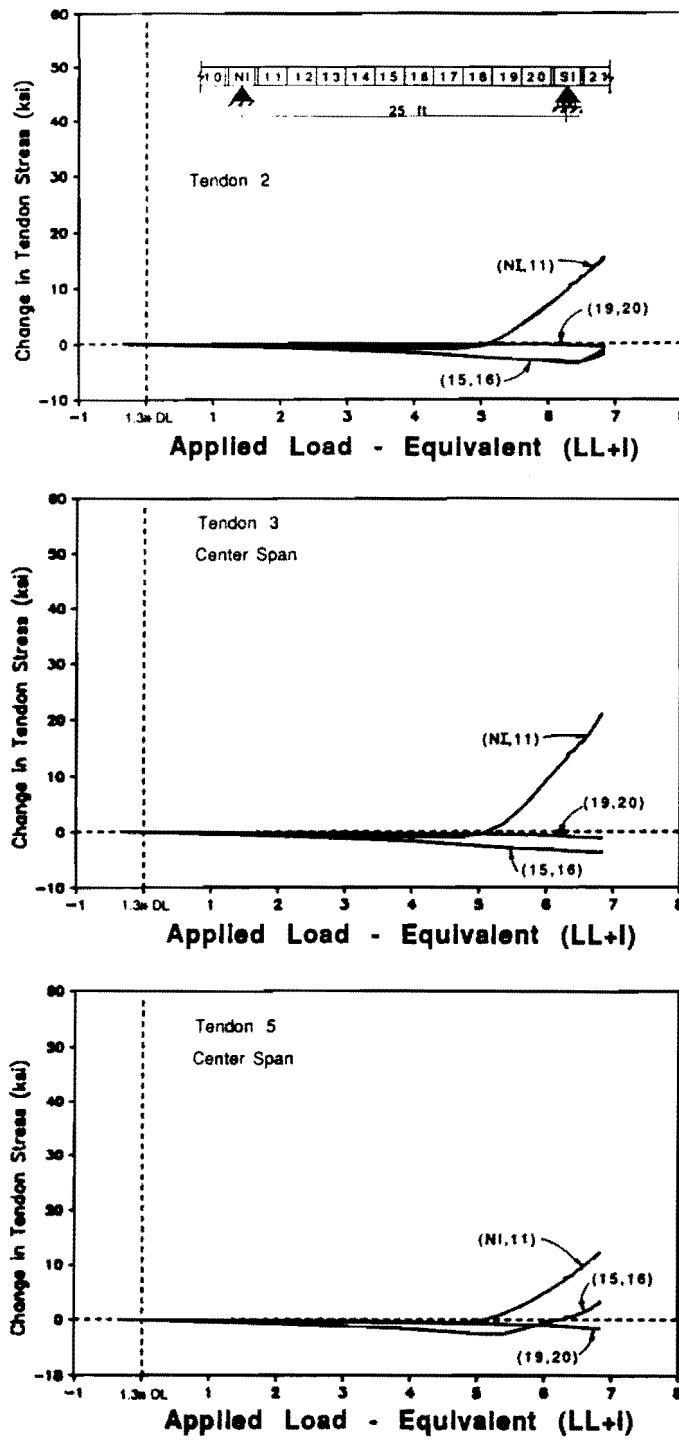
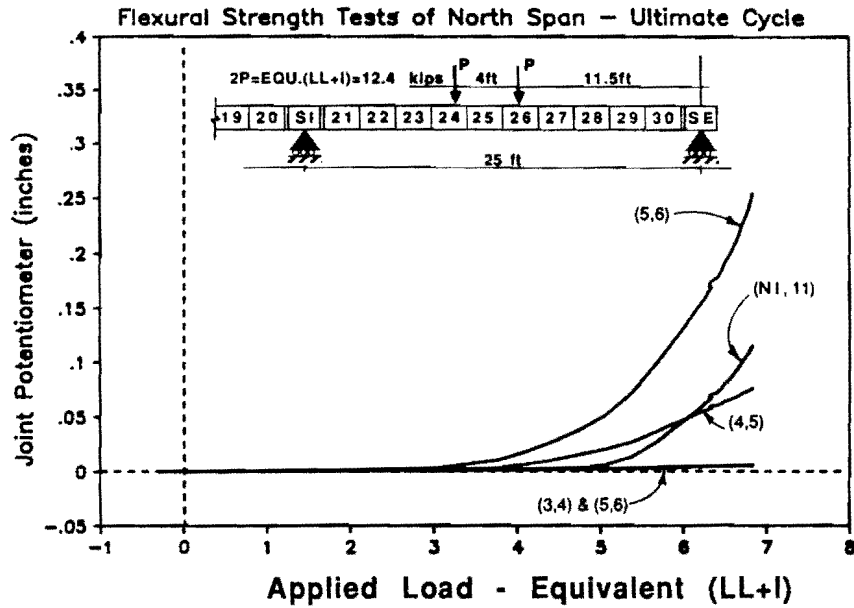


Fig. 6.27 North Span Flexural Strength Tests – Change in Tendon Stress vs. Applied Load (Center-Span Tendons)

JOINT OPENING POTENTIOMETER vs APPLIED LOAD



JOINT OPENING PROFILES

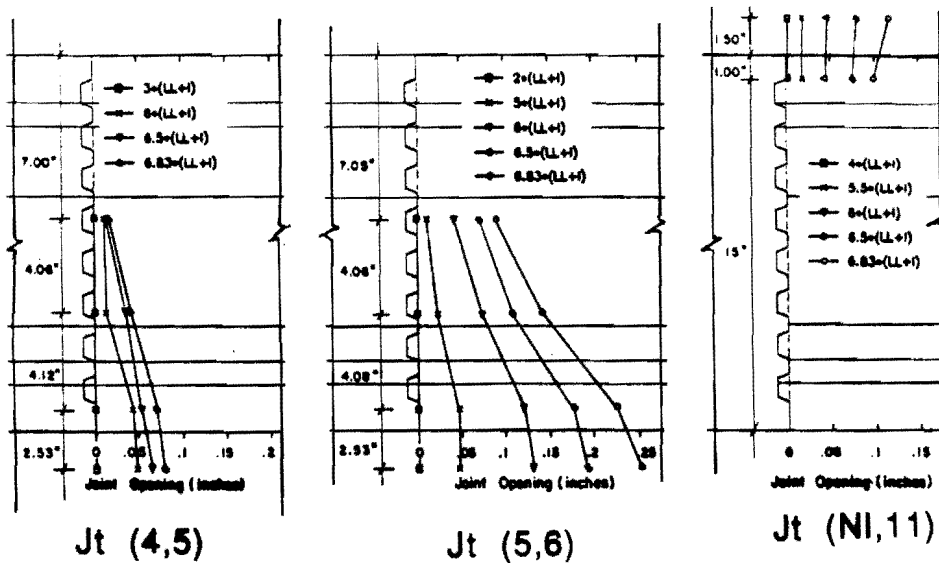


Fig. 6.28 South Span Flexural Strength Tests – Joint Opening Behavior



Fig. 6.29 North Span Flexural Strength Tests – Crushing on Top of Key at Joint (5, 6)

for increasing levels of applied live load was calculated from the load deflection curve, and is tabulated in Table 6.17. The flexural strength cycles for the north-span are summarized in Tables 6.18, 6.19, and 6.20.

Table 6.17
Instantaneous Stiffness During North-Span Tests
 (measured in (LL+I)/inch)

Applied Load	Flexural Test	Shear Test
1(LL+I)	18	18
2(LL+I)	16	17
3(LL+I)	13	11
4(LL+I)	6.2	4.7
5(LL+I)	4.3	3.1
6(LL+I)	1.6	1.3
6.8(LL+I)	.76	N/A
7.2(LL+I)	N/A	.82

Table 6.18
North Span Flexural Strength Cycles - Maximum Response Values
Flexural Strength Load = 6.8(LL+I)

Deflections	1.62 inches (L/185)
Reactions	82 kips at NI
Moments M +ve	250 ft-kips at (5,6)
M -ve	-320 ft-kips at (NI,11)

Table 6.19 - North Span Flexural Strength Cycles
Change in Tendon Stress (ksi) - Flexural Strength Load = 6.8(LL+I)

Exterior Span Tendons	Interior Span Tendons
Tendon 1a: 15 * 36 * 19	Tendon 2: 15 ** 0 / <0
Tendon 1b: 7 * 48 * 21	Tendon 3: 21 / ;0 / <0
Tendon 3: 18 * 33 * 25	Tendon 5: 12 ** 3 / <0
*denotes slip towards midspan key = (1,2)/(5,6)/(9,10) = ext.end/midspan/int.end	**denotes slip towards near end key = (11,12)/(15,16)/(19,20) = near end/midspan/far end

Table 6.20 Summary of North Span Flexural Strength Cycle

<i>P_{applied}</i>:	Description:
1.3DL-0.28(LL+I)	-Start Test ($P_{rams}=0$)
1.3DL	-Start Live Load application from the factored dead load condition
1.3DL+1.4(LL+I)	-Decompression Load
1.3DL+1.8(LL+I)	-Midspan tendon stresses begin to diverge from linear behavior.
1.3DL+3.0(LL+I)	-Joints (4,5) and (5,6) begin to open widely causing Reactions, Joint Moments and Tendon stresses to increase at a higher rate
1.3DL+3.8(LL+I)	-Tendon 3 (north-span) began slipping from both ends towards the midspan region
1.3DL+4.8(LL+I)	-The support joint begins to open causing the near-end interior-span tendon stresses to begin to increase -Tendon 1a began slipping from both ends towards the midspan section
1.3DL+5.0(LL+I)	-Support joint (NI,11) begins to open widely -Tendon 1b began slipping from the interior end towards the midspan region.
1.3DL+5.3(LL+I)	-Tendon 5 (interior span) began slipping from the midspan region towards the near end of the interior span
1.3DL+6.2(LL+I)	-Tendon 1b began slipping from the exterior end towards the midspan region
1.3DL+6.4(LL+I)	-Tendon 2 (interior span) began slipping from the midspan region towards the near end of the interior span
1.3DL+6.8(LL+I)	-Flexural Strength

Table 6.21
North Span Shear Test - Maximum Response Values
Shear Strength Load = 7.2(LL+I)

Deflections	2.19 inches (L/137)
Reactions	74 kips at NI
Moments M +ve	250 ft-kips at (5,6)
M -ve	-380 ft-kips at (NI,11)

Table 6.22 North Span Shear Test
Change in Tendon Stress - Shear Strength Load = 7.2(LL+I)

Exterior Span Tendons	Interior Span Tendons
Tendon 1a: 25 * 42 * 22	Tendon 2: 20 ** 0 / 0
Tendon 1b: 8 * 59 * 30	Tendon 3: 27 ** -1 / 0
Tendon 3: 27 * 41 * 30	Tendon 5: 15 ** 5 * 0.5
* denotes slip towards midspan key = (1,2)/(5,6)/(9,10) = ext.end/midspan/int.end	** denotes slip towards near end key = (11,12)/(15,16)/(19,20) = near end/midspan/far end

Table 6.23 Summary of North-Span Shear Test

$P_{applied}$:	Description:
1.3DL-.30(LL+I)	-Start Test ($P_{rams}=0$)
1.3DL	-Start Live Load application from the factored dead load condition
1.3DL+1.4(LL+I)	-Decompression Load
1.3DL+1.8(LL+I)	-Midspan tendon stresses begin to diverge from linear behavior.
1.3DL+3.0(LL+I)	-Joints (4,5) and (5,6) begin to open widely resulting in increased deflections, redistribution of internal forces toward the interior support, and causing tendon stresses to increase at a higher rate.
1.3DL+3.9(LL+I)	-Tendon 3 (north-span) began slipping from both ends towards the midspan region.
1.3DL+4.4(LL+I)	-The support joint begins to open causing the near-end interior-span tendon stresses to begin to increase. -Internal forces begin to redistribute back towards midspan
1.3DL+4.6(LL+I)	-Tendon 1a began slipping from both ends towards the midspan region.
1.3DL+4.9(LL+I)	-Tendon 1b began slipping from the interior end (9,10) towards the midspan region.
1.3DL+5.5(LL+I)	-Tendon 5 (interior span) began slipping from the midspan region towards the near end (north) of the interior span.
1.3DL+5.7(LL+I)	-Joint (11,12) (support joint) begins to open widely causing the internal forces to shift back towards the midspan region, and an abrupt change in the reaction and joint-moment responses (Fig. 6.35).
1.3DL+6.2(LL+I)	-Tendon 2 (interior span) began slipping from the midspan region towards the near end of the interior span
1.3DL+6.4(LL+I)	-Tendon 1b began slipping from the exterior end (1,2) towards the midspan region.
1.3DL+7.0(LL+I)	-Tendon 3 (interior span) began slipping from the midspan region towards the near end (north) of the interior span.
1.3DL+7.1(LL+I)	-Tendon 5 (interior span) began slipping from the far end of the interior span (south) towards the midspan region.
1.3DL+7.2(LL+I)	-Ultimate strength limited by flexural capacity.

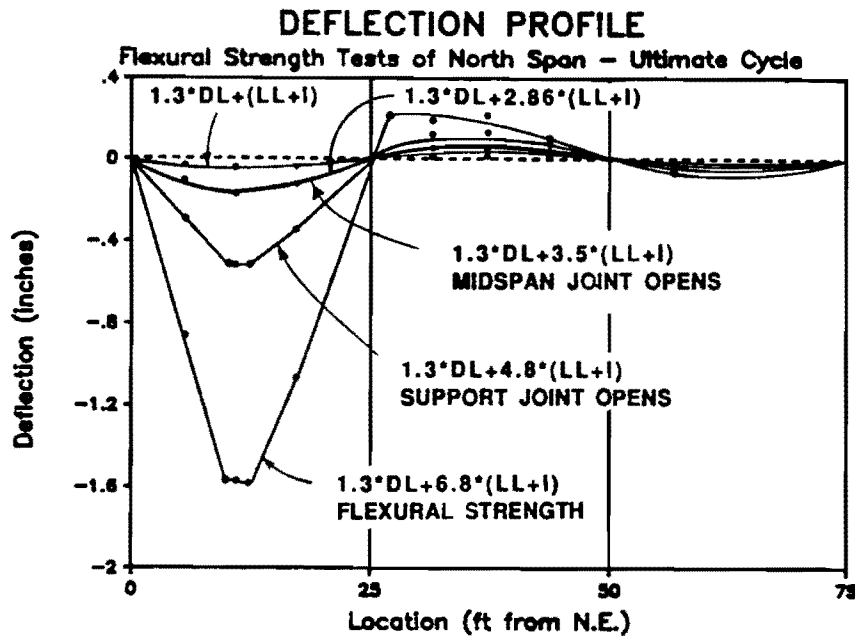


Fig. 6.30 North Span Flexural Test – Deflection Profile

The applied load-deflection response during the first two ultimate load cycles are also shown on Figure 6.23. The unloading portions of these cycles have also been shown. The structure exhibited non-linear elastic behavior with very small permanent deformations after loading to 82% and 93% of the ultimate strength. This was noticed for all cycles of testing with small permanent deformations caused by cracking and tendon slip.

The measured deflected shapes of the three-span structure for increasing levels of applied load are shown in Fig 6.30. At the service load ($1.0(LL+I)$) and the factored load ($2.9(LL+I)$) the deflections are small and the deflected shape is a smooth curve. The deflected shape remains smooth until the midspan joints begin to open at $3.0(LL+I)$. Beyond this load, “hinging” occurs at the opening joints, and the midspan deflections increase considerably. When the support joint opens at $4.8(LL+I)$ the mechanism forms and deflections begin to increase very rapidly. The final deflected shape of the structure clearly illustrates the mechanism behavior of the structure at ultimate load levels.

The reaction and joint-moment curves exhibit double curvature (slight S- shape). As the midspan joints open, the midspan stiffness reduces causing internal forces to redistribute towards the support. When the support joint opens, the support stiffness reduces and internal forces are redistributed back towards midspan.

The concentrated rotations that occurred at critical opening joints were measured with manually recorded crack-monitors distributed over the height of the joint, as described

in Section 3.9. A profile of each opening joint during the flexural test of the north-span is shown at the bottom of Fig. 6.28. Large rotations occurred at two midspan joints (joints (4,5) and (5,6)), and one support joint (joint (NI,11)). The measured profiles indicate that the joint opened linearly with the compressive stresses gradually concentrating in the top flange. The neutral axis for all ultimate load cases can be extrapolated from the joint profiles, and was within the compression flange at all opening joints.

The concentrated angle changes that occurred at each joint mechanism can be roughly calculated from the joint opening profiles. The concentrated rotations that occurred at the midspan joints were approximately 0.3 degrees at joint (4,5) and 0.9 degrees at the primary joint mechanism (5,6) for a total midspan concentrated angle change of approximately 1.2 degrees. The concentrated angle change that occurred at the support joint (NI,11) was approximately 0.4 degrees. The total midspan angle change was approximately three times the magnitude of the concentrated angle change at the support. This is roughly consistent with the plastic mechanism rotations that occur in a propped cantilever beam, shown in Fig. 6.31, which for ideal conditions would predict the midspan-to-support angle changes of between 2 and 3. The relative magnitude of the plastic rotation at the support joint is a function of the critical mechanism for the load case, continuity with the adjacent span, and the initial deformations caused by secondary prestress effects.

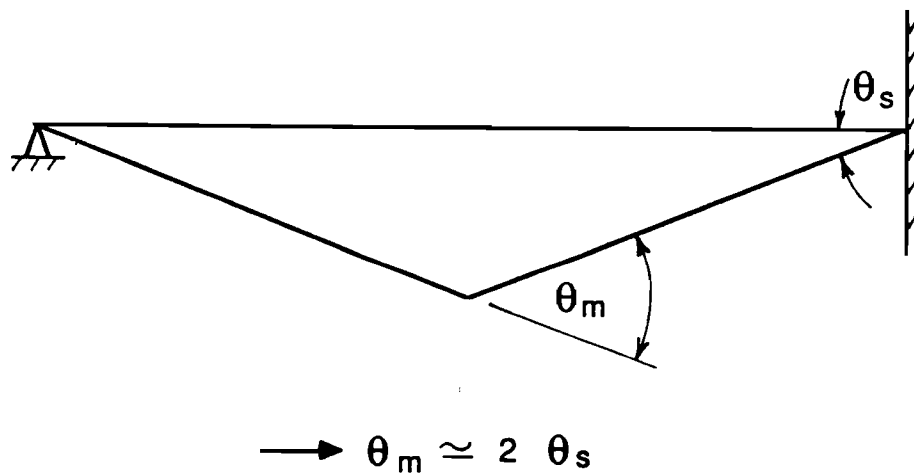


Fig. 6.31 Plastic Mechanism Rotations for Propped Cantilever

The cracking behavior of the midspan region on the west and east sides of the north-span during the flexural strength test is summarized in Figure 6.32. The lines indicate the total length of cracks when the flexural strength ($6.8(LL+I)$) was reached. The initial extension and load at which the crack length was recorded are also indicated (as a multiples of $(LL+I)$). The shear transfer at the segment joints when the ultimate flexural moment was reached is also shown. The shear in segment 5 is distributed almost equally in both directions with a joint transfer shear of approximately $2.0(LL+I)$ at both joints.

The large rotations required for increased tendon stresses occurred primarily at the dry segment joints. Inclined web cracking first occurred in the second ultimate strength cycle at an applied load of approximately $5.8(LL+I)$.

The cracking extended from the open joint and generally fanned towards the load point. The width of the inclined web cracks remained small throughout the flexural test. Horizontal cracking was also noticed at the web/top-flange junction at joint (5,6). At ultimate loads the neutral axis had shifted into the top flange as indicated by cracking in the bottom face of the top flange.

6.6.4 Shear Strength Test of North Span. The final test that was run on the north-span was a shear test in which the load was applied in such a way that significant shear was transferred across an opening joint. One cycle of load was applied in $0.36(LL+I)$ increments up to $3.3(LL+I)$, $0.18(LL+I)$ increments to $4.7(LL+I)$, and $0.09(LL+I)$ increments up to a maximum load of $7.2(LL+I)$.

The applied load-deflection response for the shear strength cycle is shown in Fig. 6.33. The measured reactions and the calculated joint-moments are plotted with respect to the applied load in Fig. 6.34. The change in tendon stress due to applied load is shown for all north-span tendons in Fig. 6.35 and all center-span tendons in Fig. 6.36. The joint behavior, as measured by potentiometer and grid crack-monitors, is illustrated in Fig. 6.37.

1.4(LL+I) Decompression load: The test load that is equivalent to the service live load is calculated to cause the same moment at the critical joint as the design live load. The decompression load should therefore be approximately the same as for the flexural test load since the Equivalent $(LL+I)$ adjusts for the load location.

The test was discontinued at $7.2(LL+I)$ before catastrophic failure when the tangent stiffness of the applied load-deflection response reached approximately the same stiffness as measured at the conclusion of the flexural strength test. The tangent stiffness at increasing levels of applied load is also tabulated in Table 6.17. The strength was ultimately limited by the flexural strength, although the shear transfer at the opening joints caused markedly different local behavior.

The measured deflected shape of the three-span structure for increasing levels of applied load is shown in Fig 6.38. At the service load, $1.0(LL+I)$, and the factored load,

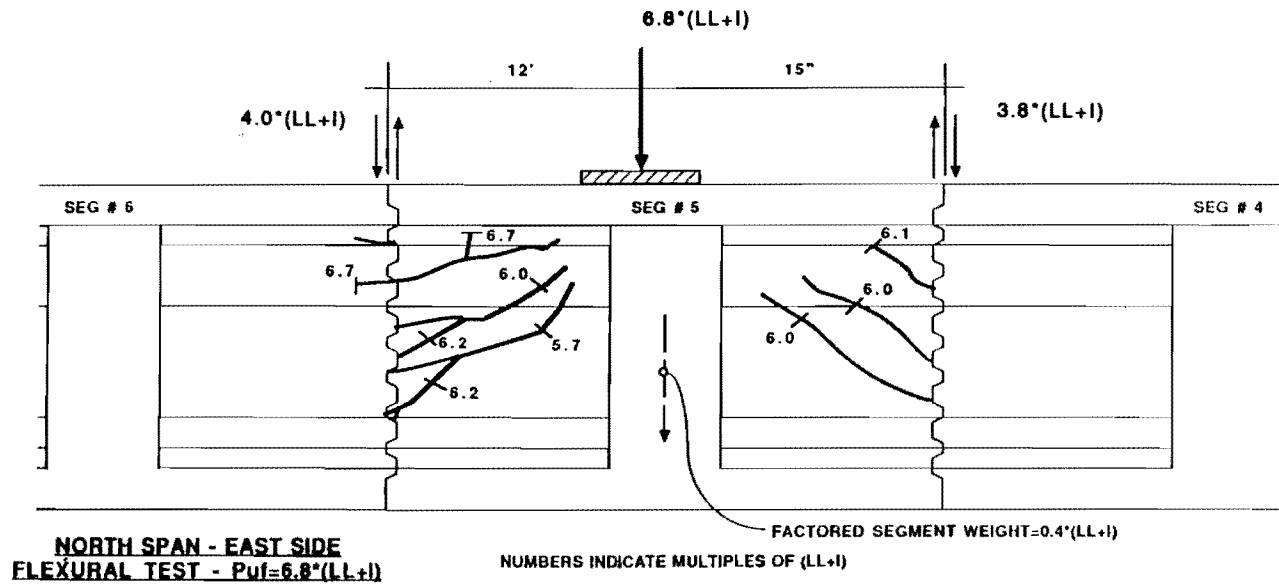
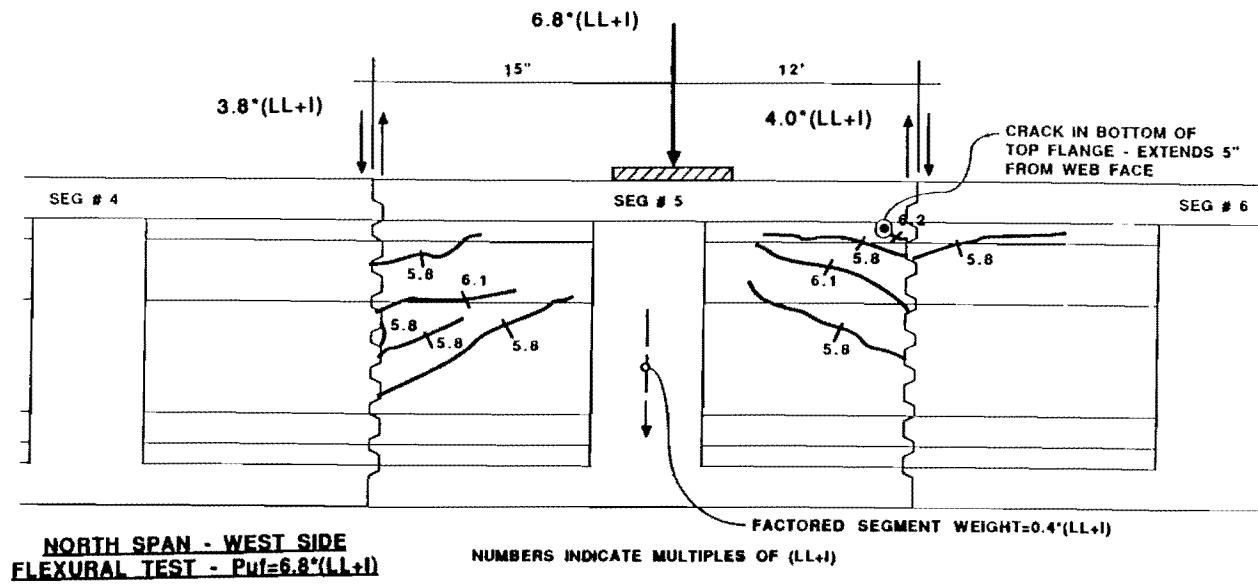


Fig. 6.32 North Span Flexural Test - Cracking Summary

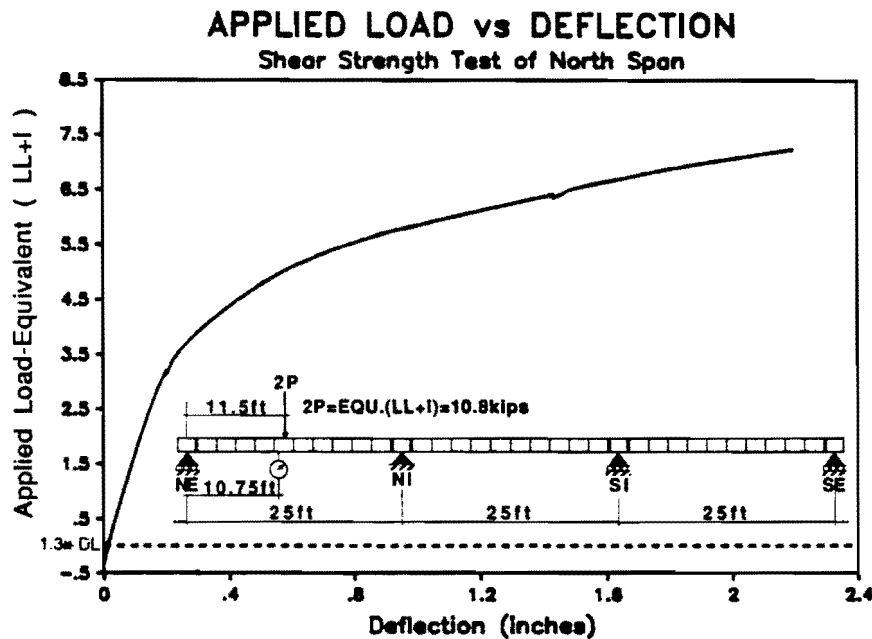


Fig. 6.33 North Span Shear Strength Test – Applied Load Vs. Deflection

2.9(LL+I), the deflections were small and the deflected shape is a smooth curve. The deflected shape remains smooth until the midspan joints begin opening at 3.0(LL+I). Beyond this load, “hinging” occurred at the opening joints and the midspan deflections increased considerably. When the support joint opened at 4.8(LL+I), the mechanism formed and deflections increased very rapidly. The final deflected shape of the structure clearly illustrates the mechanism behavior of the structure at ultimate load levels.

The reaction and joint-moment curves again exhibited double curvature (S-shape). As the midspan joints opened the midspan stiffness reduced causing internal forces to redistribute towards the support. When the support joint opened, the support stiffness reduced and internal forces were redistributed back towards midspan.

A profile of each opening joint during the shear test of the north-span is shown at the bottom of Fig. 6.37. Large rotations occurred at two midspan joints, Joints (4,5) and (5,6) and one support joint, joint (NI,11). In this case, with significant shear transferred across the opening joint, the concentrated rotations occurred at an inclined crack which extended from the load point to the bottom of the web adjacent to the joint (shown in the cracking summary in Fig. 6.39). The apparent joint openings measured by the crack monitors occurred at cracks in the concrete section while the match-cast dry joints remained closed.

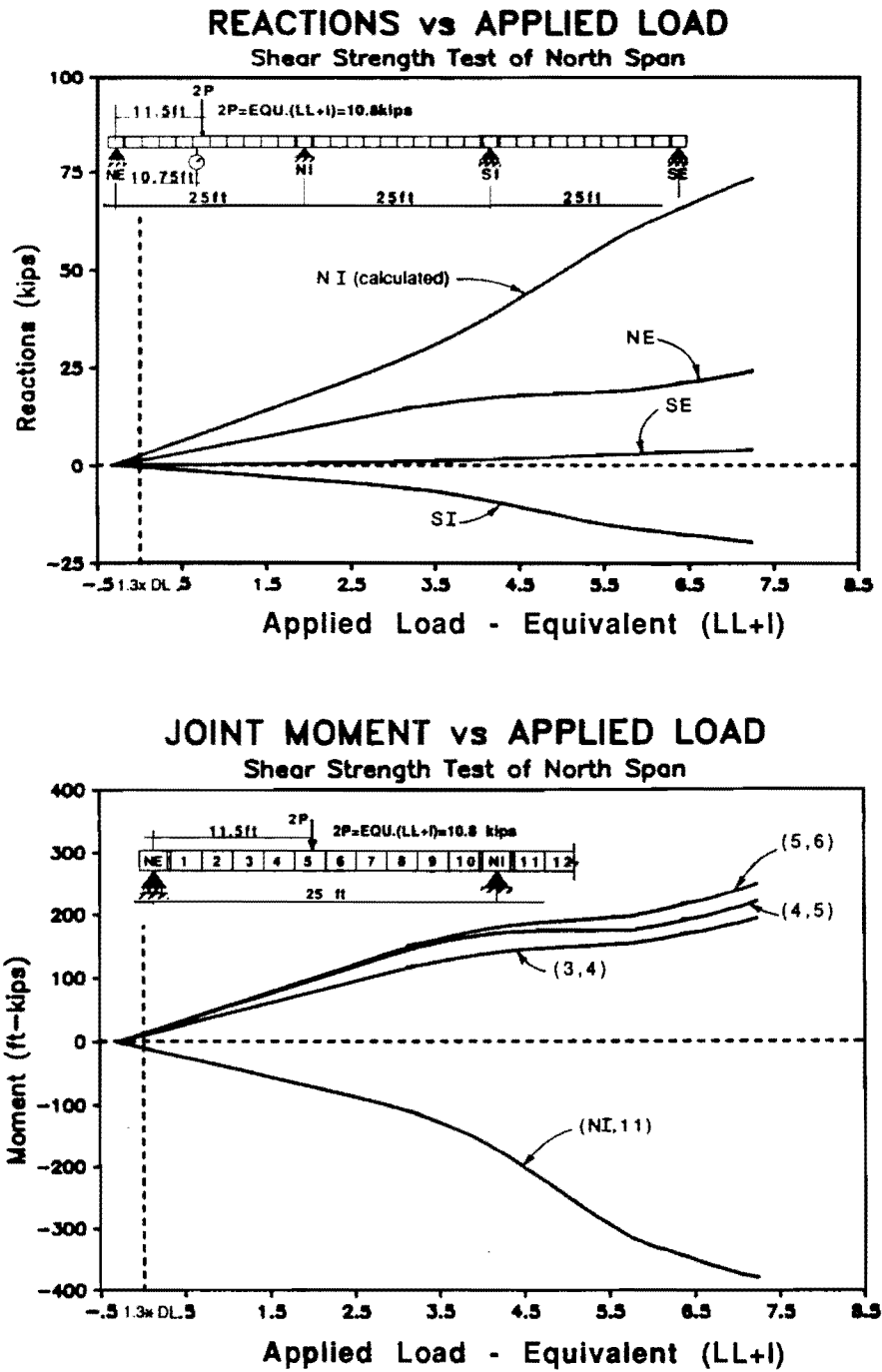


Fig. 6.34 North Span Shear Strength Test – Reactions and Joint Moments

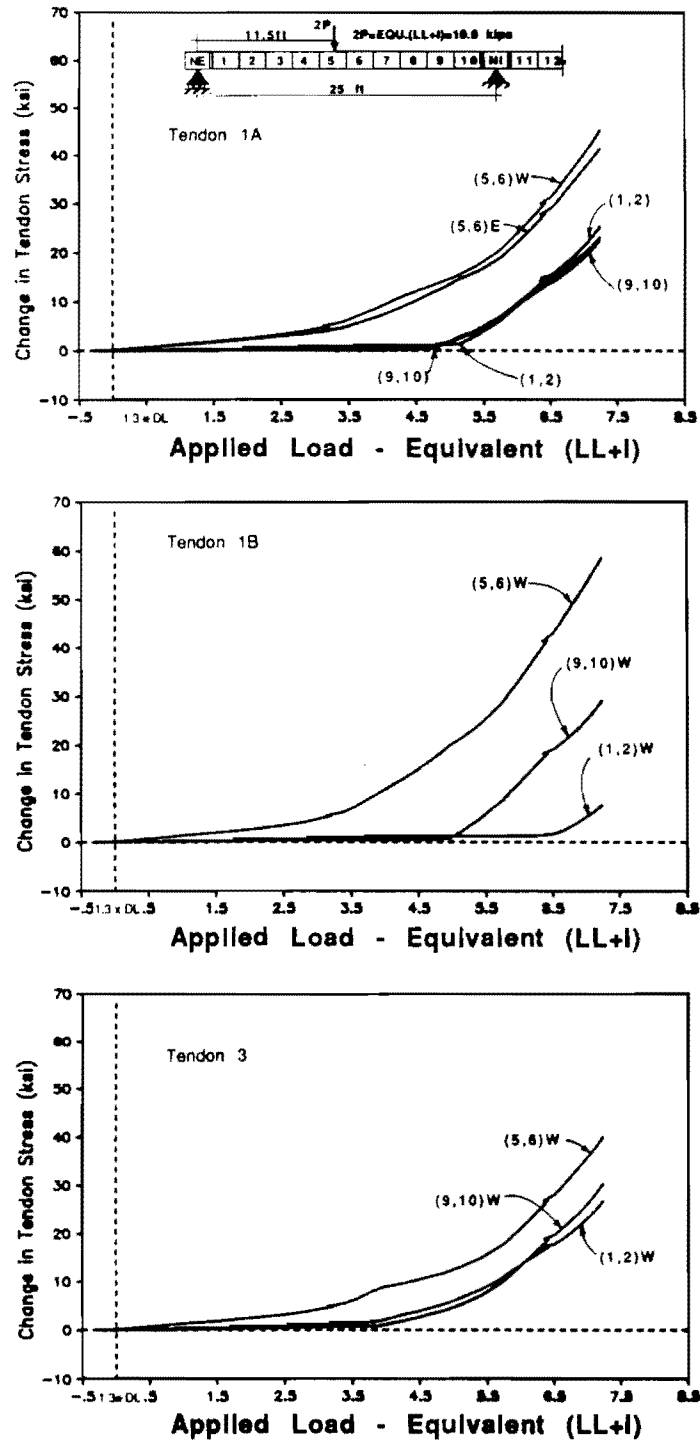


Fig. 6.35 North Span Shear Strength Test – Change in Tendon Stress vs. Applied Load (North Span)

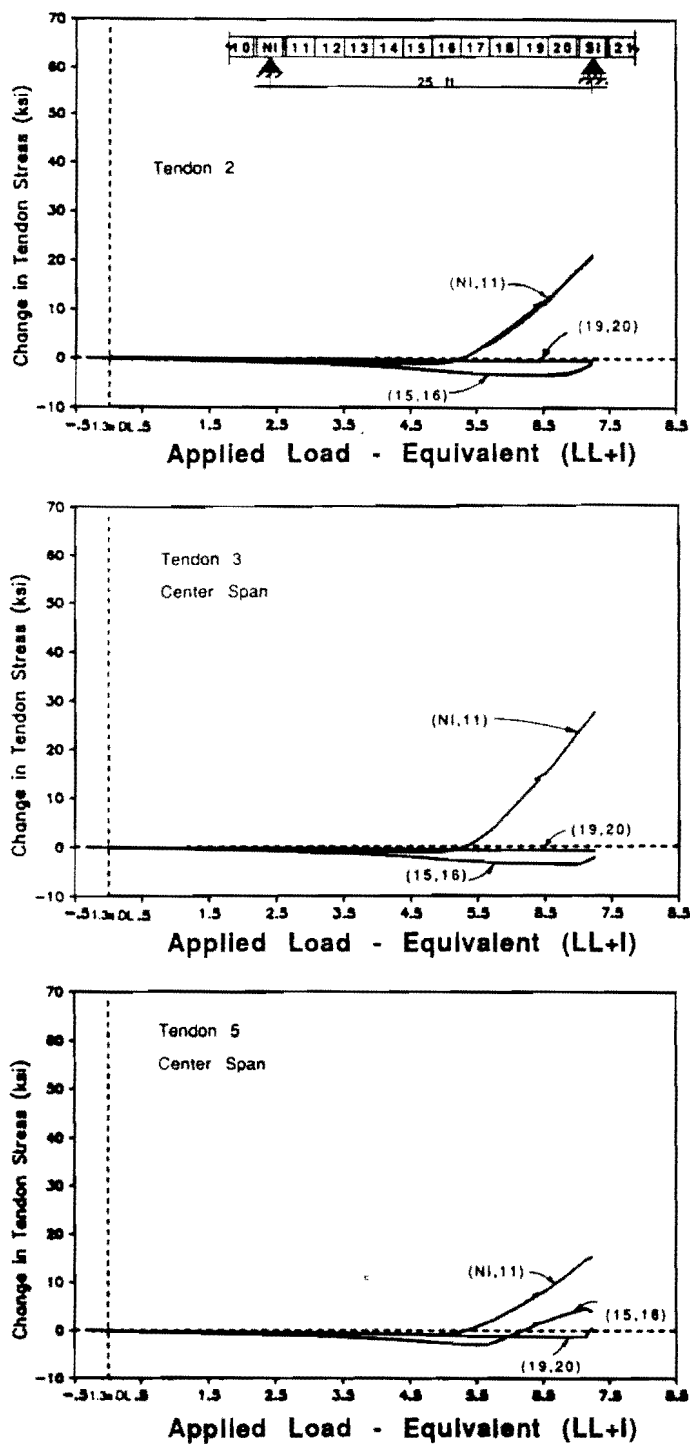
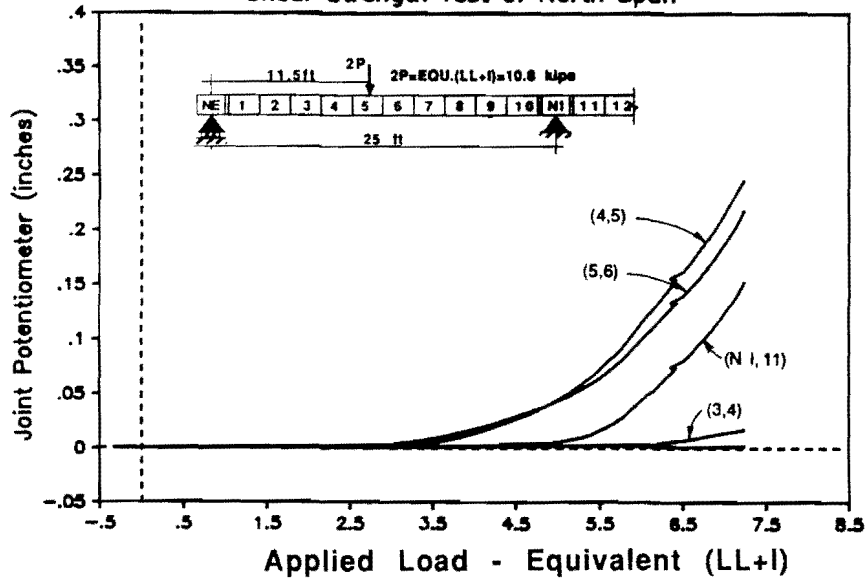


Fig. 6.36 North Span Shear Strength Test – Change in Tendon Stress vs. Applied Load (Center Span)

JOINT OPENING POTENTIOMETER vs APPLIED LOAD
 Shear Strength Test of North Span



JOINT OPENING PROFILES

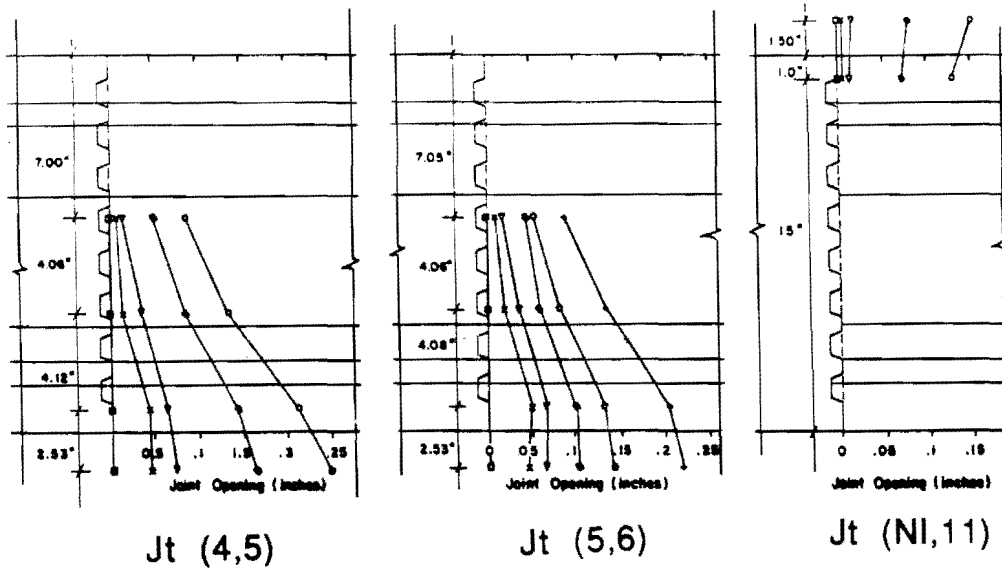


Fig. 6.37 North Span Shear Strength Test – Joint Opening Behavior

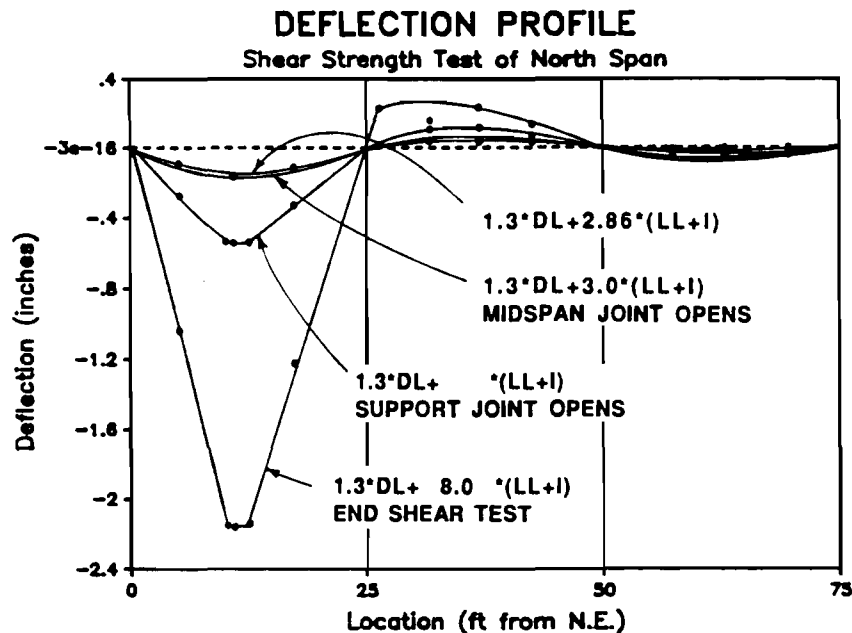


Fig. 6.38 North Span Shear Test – Deflection Profiles

The concentrated rotations can again be calculated from the measured joint-opening profiles. The measured concentrated rotations were approximately 0.8 degrees at each of the two midspan joints (Joints (4,5) and (5,6)), and approximately 0.5 degrees at the support joint (NI,11). The ratio of total midspan rotation to support rotation is again approximately 3.

The cracking behavior of the midspan region on the west and east sides of the north-span during the shear test is summarized in Figure 6.39. The lines indicate the total length of the crack when the test was discontinued at $(7.2(LL+I))$. The previous cracking from the flexural tests is shown shaded, and the new cracking or opening of previous cracks is shown as solid lines. The initial extension and the load at which it first occurred are also indicated as multiples of $(LL+I)$. The shear transfer at the segment joints at the end of the test is also shown. The shear in segment 5 is distributed primarily towards the interior support with a joint shear transfer of $5.4(LL+I)$ at joint (5,6).

The cracks that formed during the flexural test began to reopen at approximately $4.1(LL+I)$. In addition, at joint (5,6), new cracks formed which extended from the base of the web at the match-cast joint up to a previous crack.

At approximately $5.4(LL+I)$ an additional inclined crack formed on the west side of joint (5,6). This new crack crossed several of the cracks which had been formed during the flexural test. As load was increased, joints (4,5) and (5,6) opened at approximately the

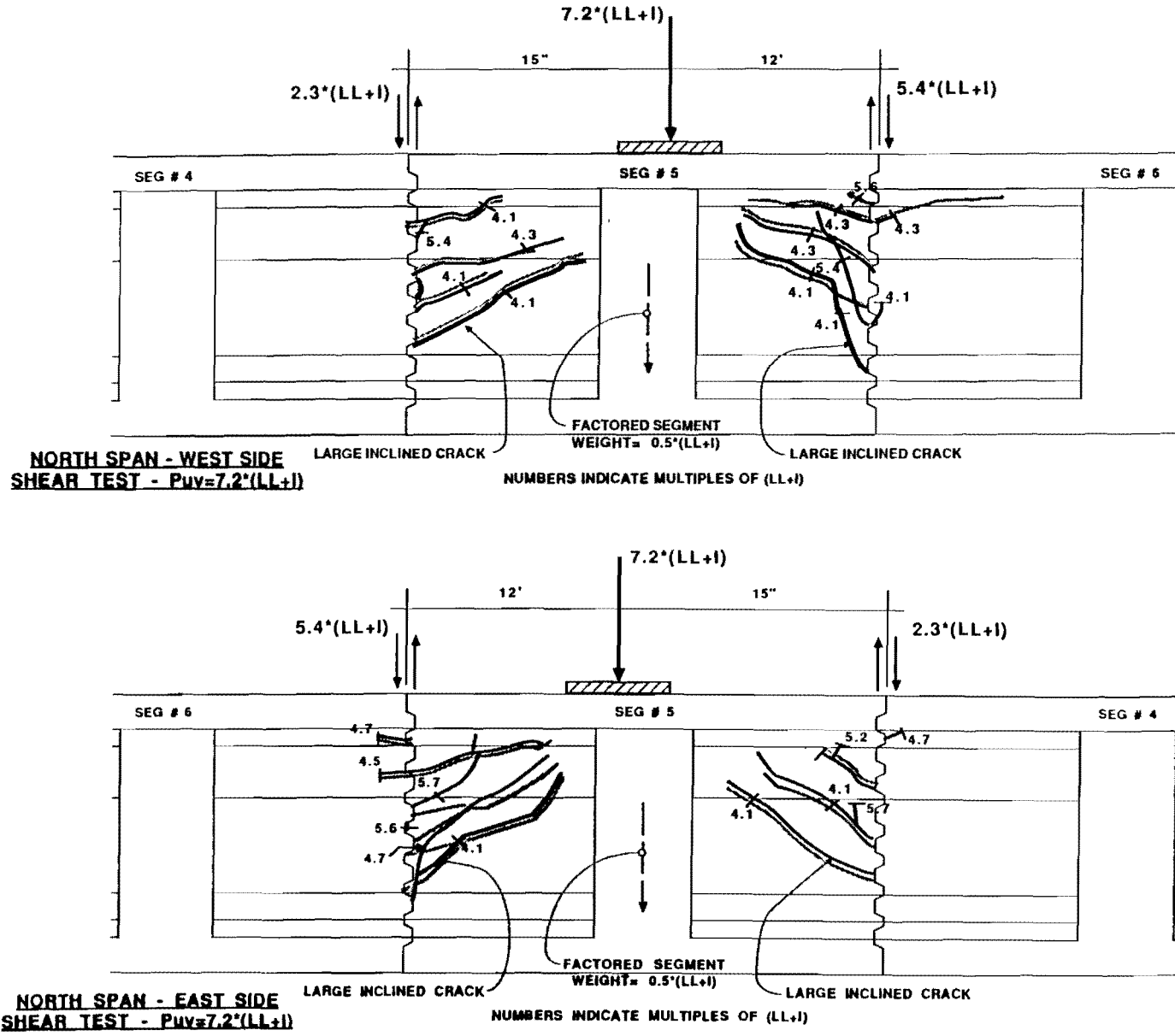


Fig. 6.39 North Span Shear Test - Cracking Summary

same rate, with the concentrated rotations occurring at the primary inclined cracks. At the conclusion of the test the dry match-cast joint was closed, with all of the hinge rotations occurring at the inclined cracks. This allowed the shear forces to utilize the entire height of the web to transfer across the joint.

6.7 South-span Load Tests (Epoxyed Joints)

6.7.1 Service Load Tests of South-Span.

6.7.1.1 Live Load Cycles for South-Span. Four cycles of service live load were applied to the epoxy jointed south-span using the load set-up shown in the schematic of Fig. 6.40. For all four cycles the load was applied in $0.16(LL+I)$ increments up to the service live load $1.0(LL+I)$. Each of the four cycles provided approximately the same response to the applied loads.

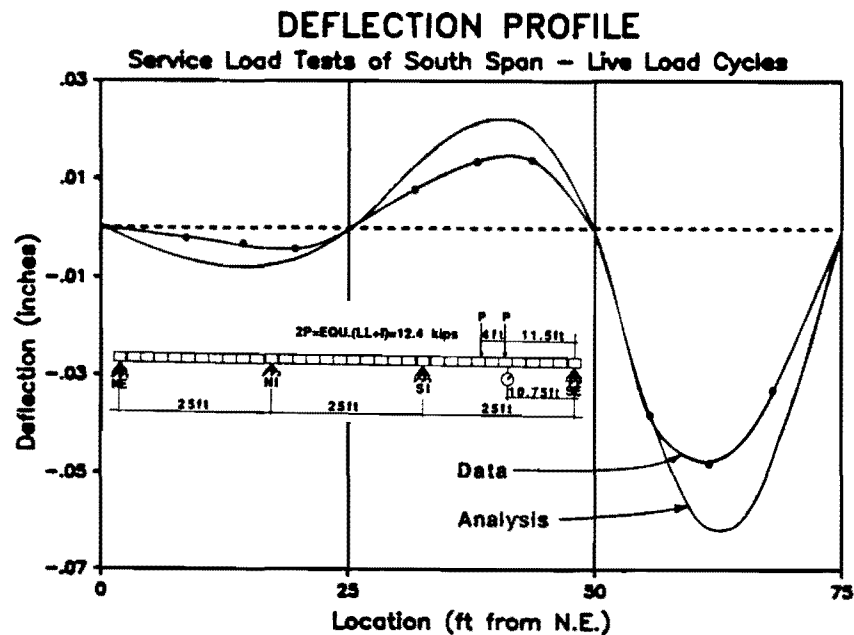


Fig. 6.40 South Span Service Load Tests - Deflection Profile

The measured deflected shape of the three-span structure is shown in Fig 6.40 for a typical service load cycle. The midspan deflection of 0.048 inches corresponds to a deflection/span ratio of $L/6250$. Also shown on Fig. 6.40 is the calculated deflected shape from the elastic analysis (see Section 5.4). The elastic analysis overestimates the measured deflection by approximately 29 percent.

The tendon data indicated a Live Load Stress range of about 1 ksi. No tendon slip was noticed at service-load levels.

6.7.1.2 Cracking Cycle for South-Span. After completing the live load cycles it was necessary to initially crack the epoxy-jointed south-span before the decompression load could be determined. The applied load was increased from zero to $3.2(LL+I)$ in $0.16(LL+I)$ increments, and from $3.2(LL+I)$ to a maximum load of $5.7(LL+I)$ at $0.08(LL+I)$ increments. The south-span cracked in segment 26 adjacent to joint (25,26) at approximately $5.4(LL+I)$. The crack was clearly through the concrete and the epoxy joint was uncracked.

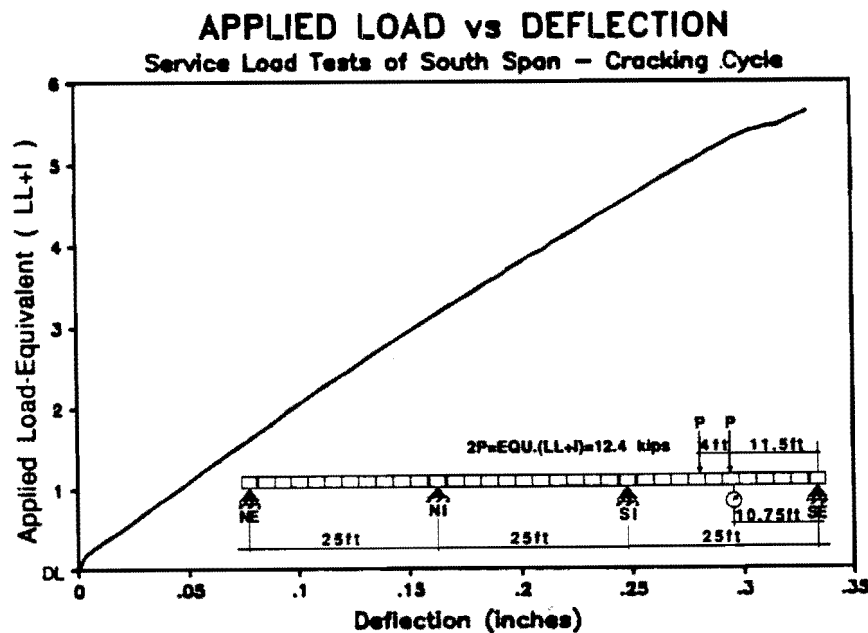


Fig. 6.41 South Span Cracking Cycle - Applied Load vs. Deflection

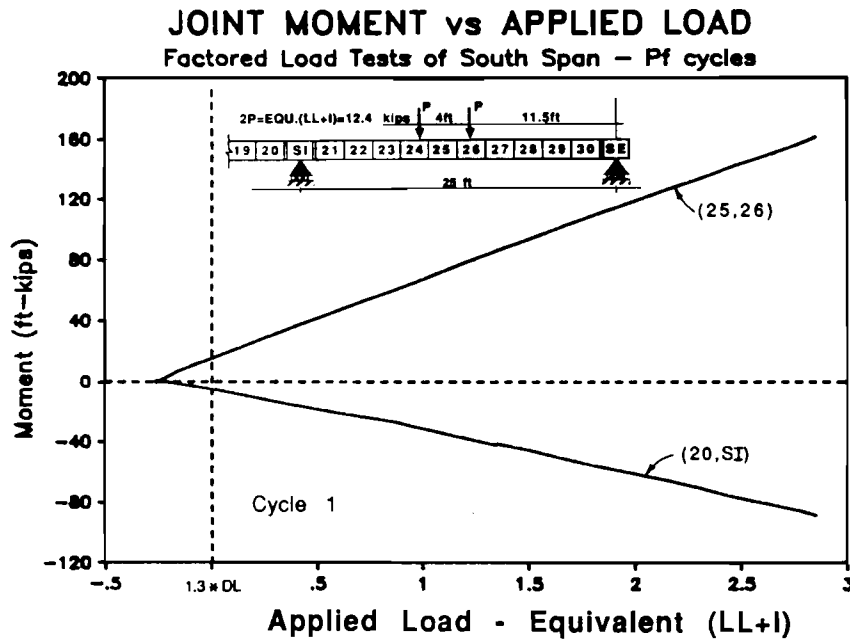
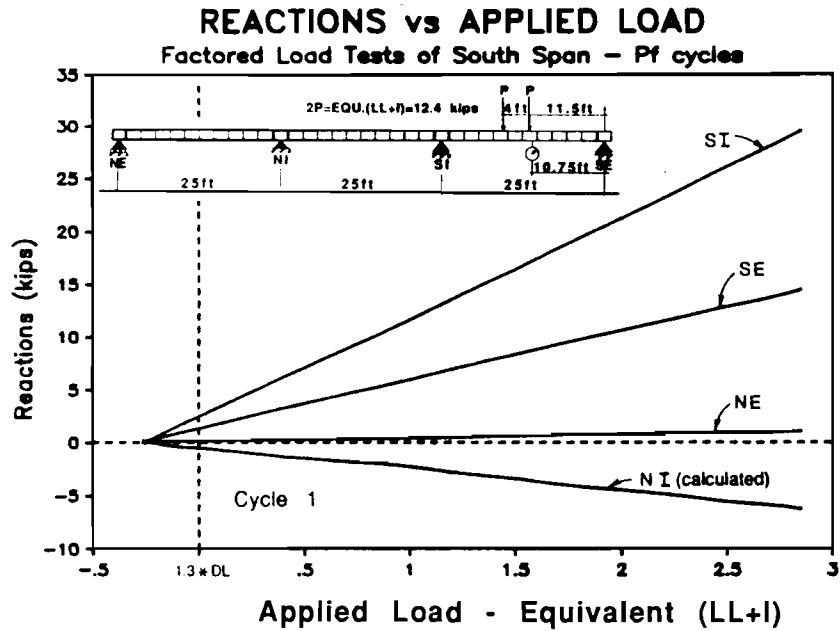


Fig. 6.42 South Span Cracking Cycle - Reactions and Joint Moments

The applied load-deflection response during the cracking cycle is shown in Fig. 6.41. The measured reactions and the calculated joint-moments are plotted with respect to the applied load in Fig. 6.42. The change in tendon stress due to applied load is shown for all south-span tendons in Fig. 6.43.

2.4(LL+I): As noticed in the epoxied center-span, the load deflection response exhibits bi-linear behavior with a reduction in stiffness at approximately 2.4(LL+I). This change in behavior is also noticed as a subtle change in the reactions, joint-moments, and tendon stress responses.

5.4(LL+I) Cracking Load: Cracking occurred through the concrete in segment 26 adjacent to joint (25,26). As for the north and center-spans, after cracking, the loads tended to redistribute towards the continuous support because of the reduced stiffness at midspan.

The midspan tendon stresses remained linear with applied load up to the point that the concrete cracked. As cracking occurred, the tensile force that was previously carried by the concrete was transferred to the post-tensioning tendons. This caused a sudden increase in tendon stresses. For unbonded tendons, considerable elongation was necessary to develop the increased tendon forces. This caused concentrated rotations to occur at the crack and resulted in vertical deflection. The west side of tendon 4a slipped from the exterior end (29,30) towards the midspan region during cracking. Slip was not noticed at any other locations.

5.7(LL+I): The test was discontinued at 5.7(LL+I) at 10 percent above the cracking load. Although the bottom flange appeared to be cracked all the way through at the end of this cycle, subsequent testing to higher load levels indicated that only partial cracking had occurred at this load stage. The joint opening response, shown in Fig.6.44, also illustrates larger crack opening on the west side with only limited cracking on the east side. The cracking-load cycle for the south-span is summarized in Tables 6.24, 6.25, and 6.26.

Table 6.24 South-span Cracking Cycle - Maximum Response Values

	Cracking Load	
	5.4(LL+I)	5.7(LL+I)
Deflections	0.30 (L/1000)	0.33 inches (L/909)
Reactions	50 at SI	53 kips at SI
Moments M +ve	270 at (25,26)	280 ft-kips at (25,26)
M -ve	-150 at (20,SI)	-170 ft-kips at (20,SI)

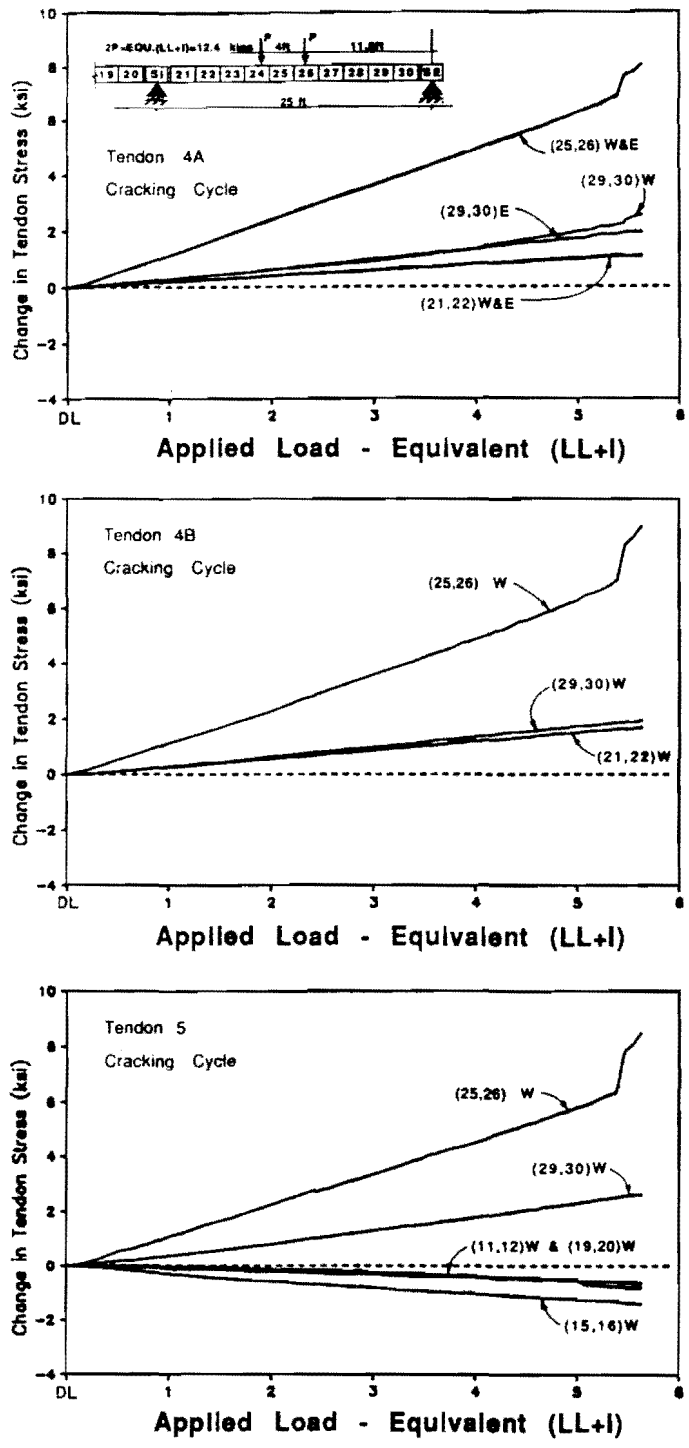


Fig. 6.43 South Span Cracking Cycle – Change in Tendon Stress vs. Applied Load

JOINT OPENING POTENTIOMETER vs APPLIED LOAD Service Load Tests of South Span - Cracking Cycle

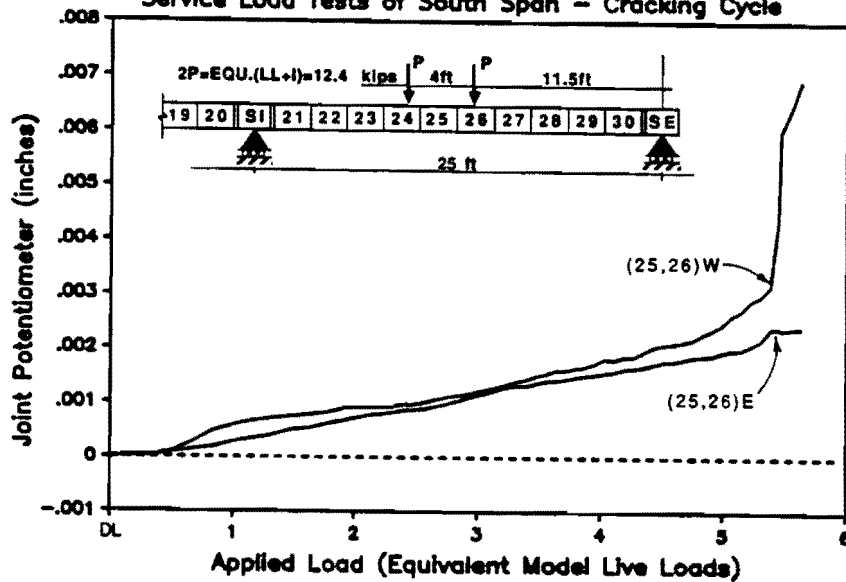


Fig. 6.44 South Span Cracking Cycle - Joint Opening Potentiometer vs. Applied Load

Table 6.25 South-Span Cracking Cycle - Change in Tendon Stress

	Before Cracking 5.4(LL+I)	After Cracking 5.7(LL+I)
Tendon 4a:	2 * 7 / 1	2 * 8 / 1
Tendon 4b:	2 / 7 / 2	2 / 9 / 2
Tendon 5:	2 / 6 / X	2 / 8 / X

X: denotes inactive strain gage
 * denotes slip towards midspan
 key = (29,30)/(25,26)/(21,22)
 = ext.end/midspan/int.end

Table 6.26 Summary of South-Span Cracking Cycle

$P_{applied}$:	Description:
DL only	-Start Test ($P_{rams}=0$)
DL+2.4(LL+I)	-Stiffness reduces slightly as bottom of uncracked girder goes into tension
DL+5.4(LL+I)	-Cracking occurs in Segment 26 adjacent to joint (25,26)
DL+5.7(LL+I)	-Test discontinued

6.7.1.3 **Decompression Load Cycles for South-Span.** After initial cracking at joint (25,26), three load cycles were applied to the south-span to determine the magnitude of the decompression load. The applied load was increased in $0.32(LL+I)$ increments to a load level of approximately $1.6(LL+I)$, and then in $0.16(LL+I)$ increments to a maximum load of $3.4(LL+I)$, or approximately 30 percent higher than the measured decompression load, $2.6(LL+I)$.

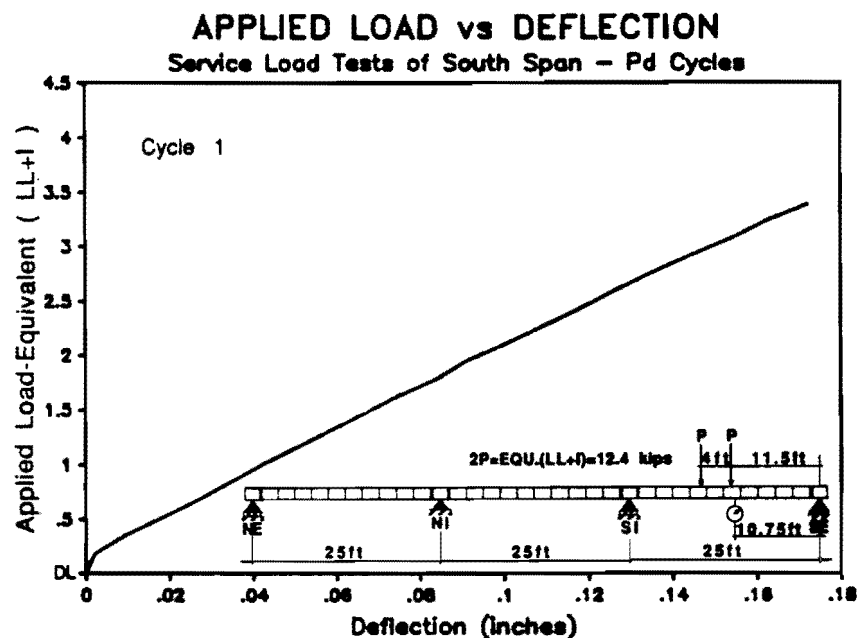


Fig. 6.45 South Span Decompression Cycles – Applied Load vs. Deflection

The applied load-deflection response during the cracking cycle is shown in Fig. 6.45. The measured reactions and the calculated joint-moments are plotted with respect to the applied load in Fig. 6.46.

2.6(LL+I) Decompression Load: The data was erratic throughout these cycles, perhaps as the result of friction in the rams. The decompression load was estimated from a large-scale plot of manually recorded data. This data showed a change in behavior at approximately $2.6(LL+I)$.

The reactions and joint moments show very subtle changes in response at the decompression load indicating only slight redistribution of internal forces towards the interior support.

3.4(LL+I): The maximum test load applied during the decompression load test of the south-span was $3.4(LL+I)$. The south-span decompression cycles are summarized in Tables 6.27, 6.28, and 6.29.

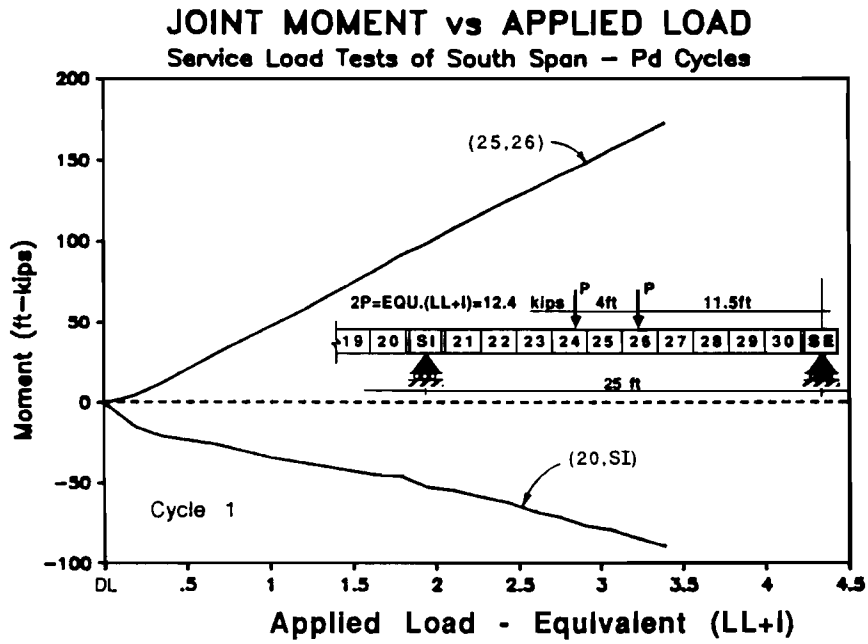
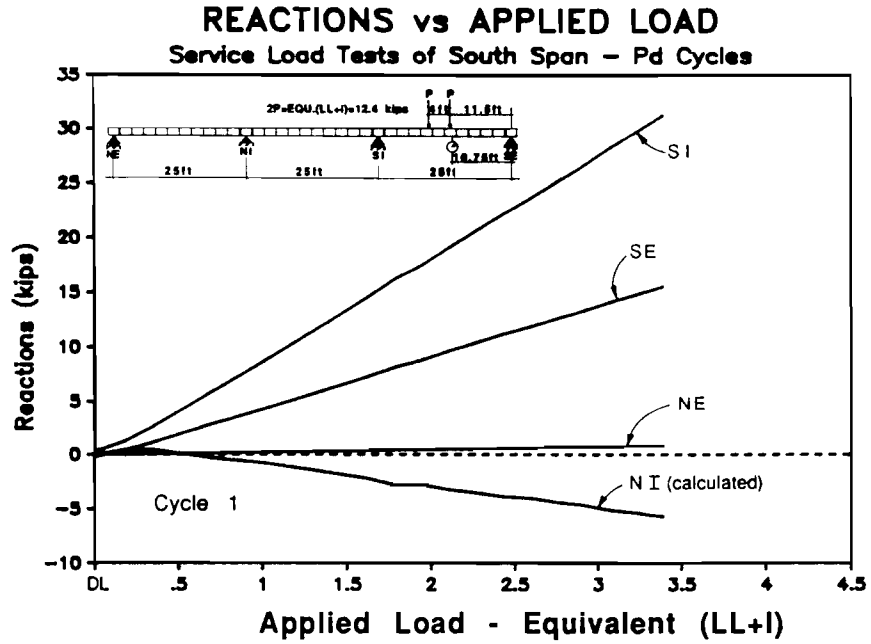


Fig. 6.46 South Span Decompression Cycles - Reactions and Joint Moments

Table 6.27 South-Span Decompression Cycles - Maximum Response Values

	Decompression Load 2.6(LL+I)	3.4(LL+I)
Deflections	0.13 inches (L/2307)	0.14 inches (L/2142)
Reactions	24 kips at SI	32 kips at SI
Moments M +ve	130 ft-kips at (25,26)	120 ft-kips at (15,16)
M -ve	-70 ft-kips at (20,SI)	-75 ft-kips at (NI,11)

Table 6.28 South-Span Decompression Cycles - Change in Tendon Stress (ksi)

	Decompression Load 2.6(LL+I)	3.4(LL+I)
Tendon 4a:	1 / 3 / 0.5	1 / 4 / 0.5
Tendon 4b:	1 / 3 / 1	1 / 4 / 1
Tendon 5:	1 / 3 / X	1 / 4 / X

X: denotes inactive strain gage
key = (29,30)/(15,16)/(21,22)
= ext.end/midspan/int.end

Table 6.29 Summary of South-Span Decompression Cycles

$P_{applied}$:	Description:
DL only	-Start Test ($P_{rams}=0$)
DL+2.6(LL+I)	-Decompression Load
DL+3.4(LL+I)	-Maximum load for Test Cycles

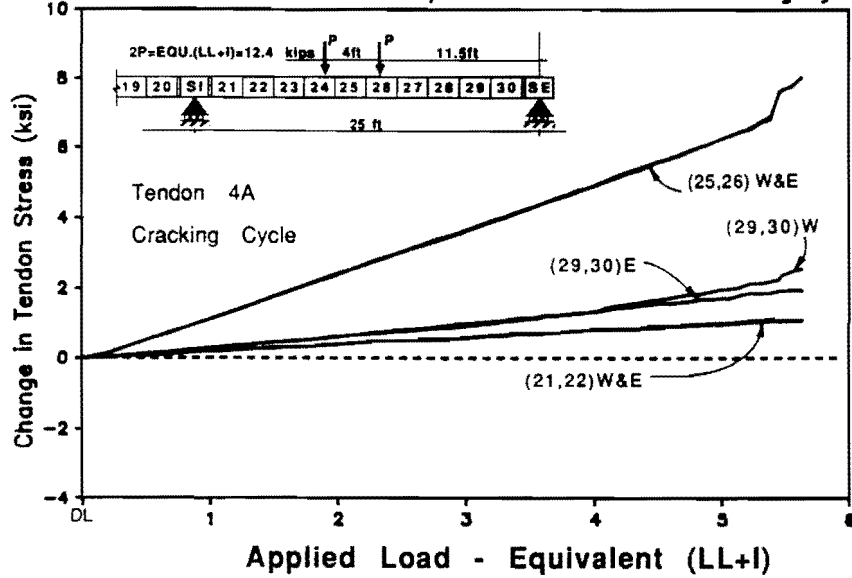
The change in the tendon stresses due to applied load appeared to be linear throughout the entire load cycle, with a maximum stress range of approximately 3.5 ksi at midspan.

Tendon slip in all tendons was noticed between the previous cracking cycle and the current decompression cycles. Figure 6.47 shows the applied load versus stress response in tendon 4a for the cracking cycle and the first decompression- load cycle. After the cracking cycle there was residual tension in the tendons. This is illustrated in the tendon stress profile (Fig.6.48) for the unloaded condition preceding each load cycle. The two-span continuity tendon (tendon 5) illustrates similar behavior with slip occurring across the pier segment (Figs. 6.49 and 6.50).

6.7.2 Factored Load Cycles for South-Span. After completing the service load tests additional dead weight was added to the structure to simulate the factored dead

CHANGE IN TENDON STRESS vs APPLIED LOAD

Service Load Tests of South Span - Tendon 4a - Cracking Cycle



CHANGE IN TENDON STRESS vs APPLIED LOAD

Service Load Tests of South Span - Tendon 4a - Pd Cycles

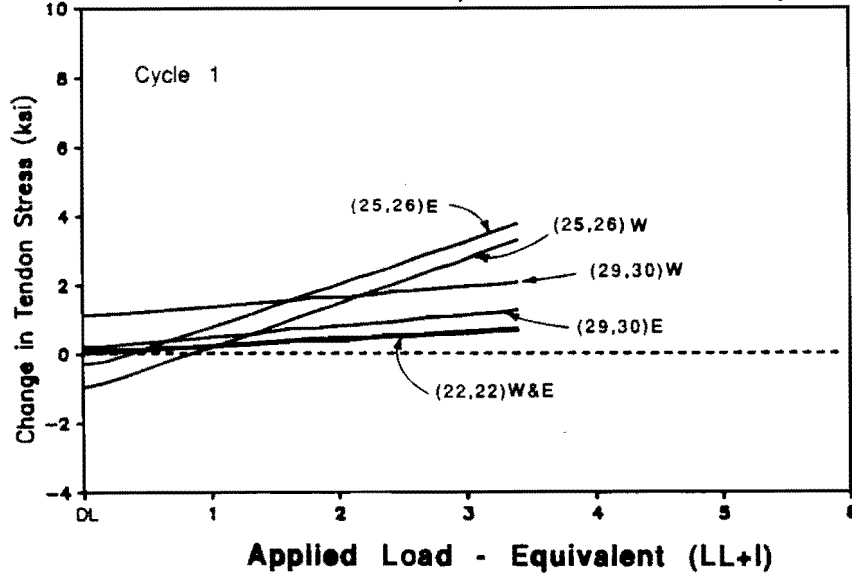


Fig. 6.47 Comparison of South Span Cracking Cycle and Decompression - Load Cycle Response for Tendon 4a

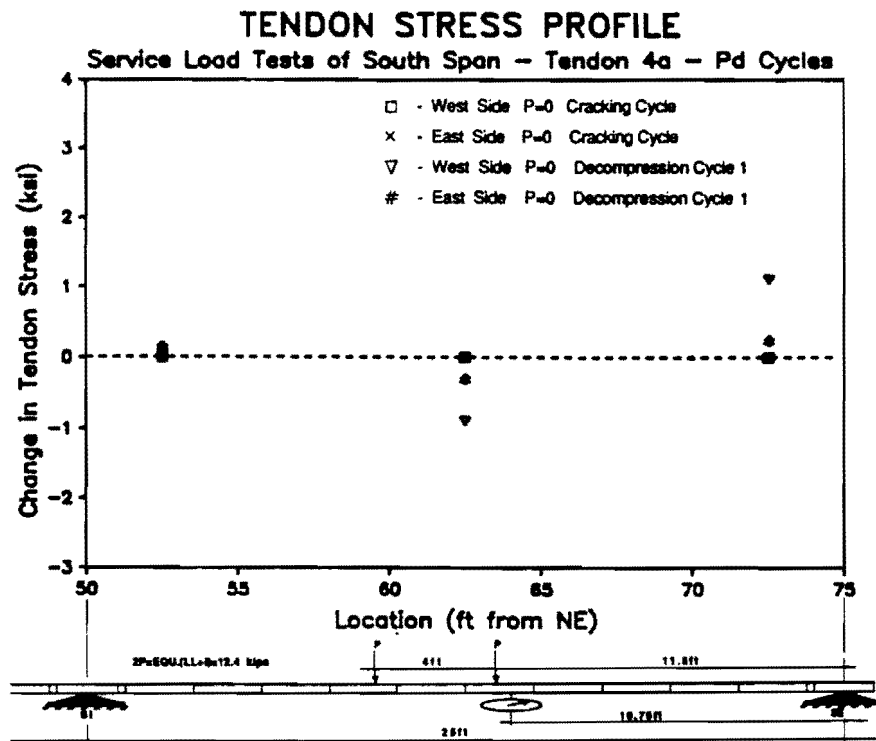


Fig. 6.48 South Span - Tendon 4a Stress Profile

load requirement. Three factored load cycles were conducted on the south-span with loads applied in $0.16(LL+I)$ increments up to the factored design load of $1.3DL+2.86(LL+I)$.

The applied load-deflection response was the same for all three factored load cycles, and cycle 1 is shown in Fig. 6.51. The measured reactions and the calculated joint-moments are plotted with respect to the applied load in Fig. 6.52.

2.2(LL+I) Decompression Load: In this case, with the structure preloaded with 30 percent more dead load, less applied force was necessary to cause tension at the extreme fiber. The decompression force of $2.2(LL+I)$ is consistent with the previous estimation of the decompression load ($2.6(LL+I)$) determined without the additional dead weight. The difference between these two loads is approximately equal to the test load that produces the same moment at the critical joint as 30 percent of the dead load.

2.9(LL+I) Factored Live Load: The south-span was loaded to the factored live load level of $2.9(LL+I)$. The factored load cycles are summarized in Tables 6.30, 6.31, and 6.32.

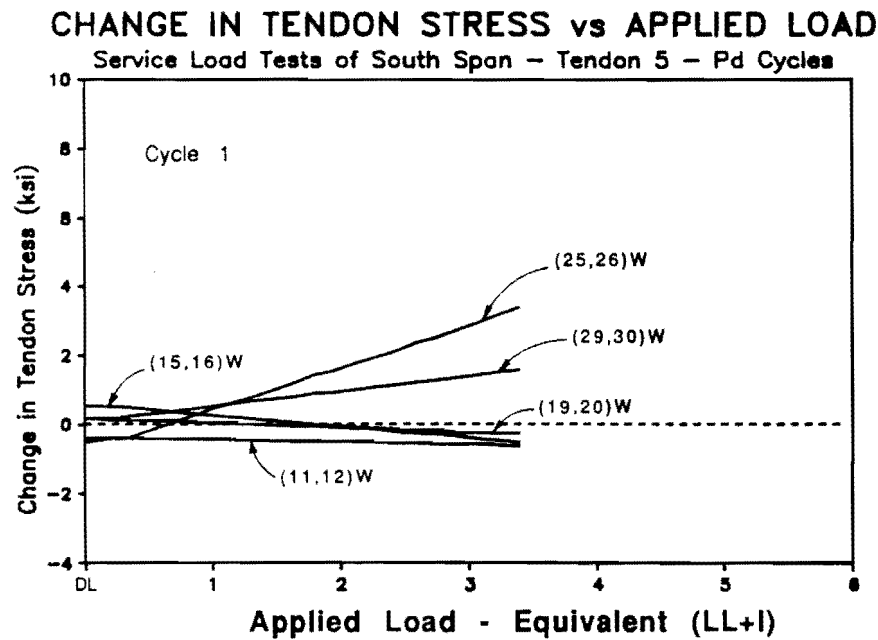
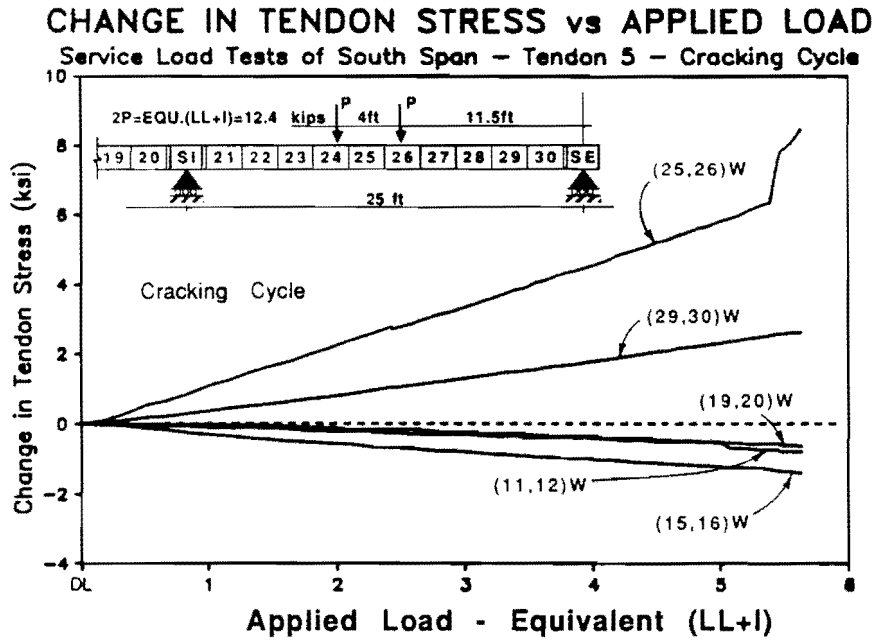


Fig. 6.49 Comparison of South - Span Cracking Cycle and Decompression - Load Cycle Response for Tendon 5

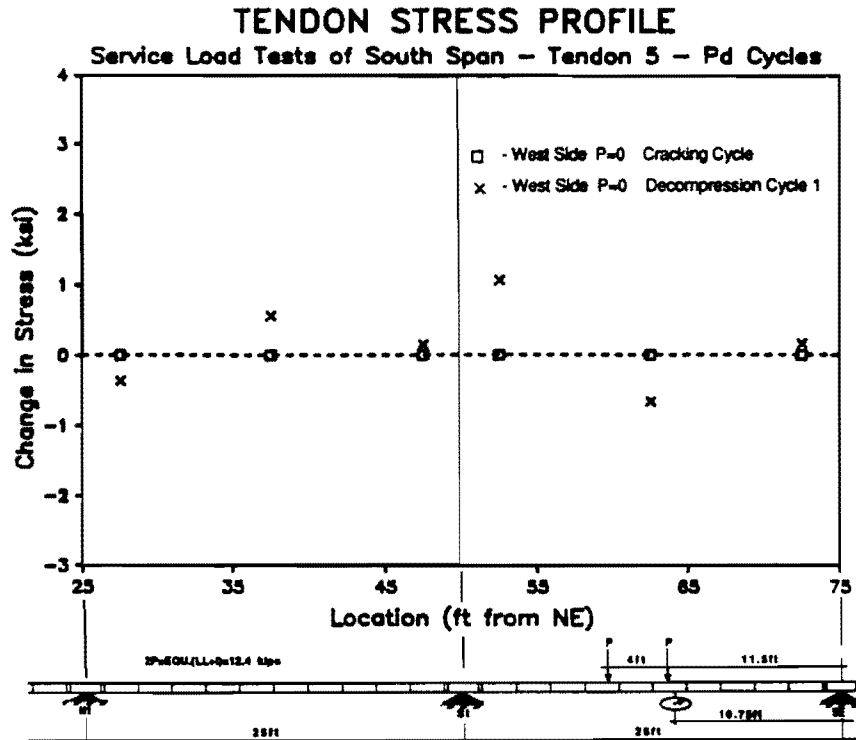


Fig. 6.50 Tendon Slip After Cracking Cycle

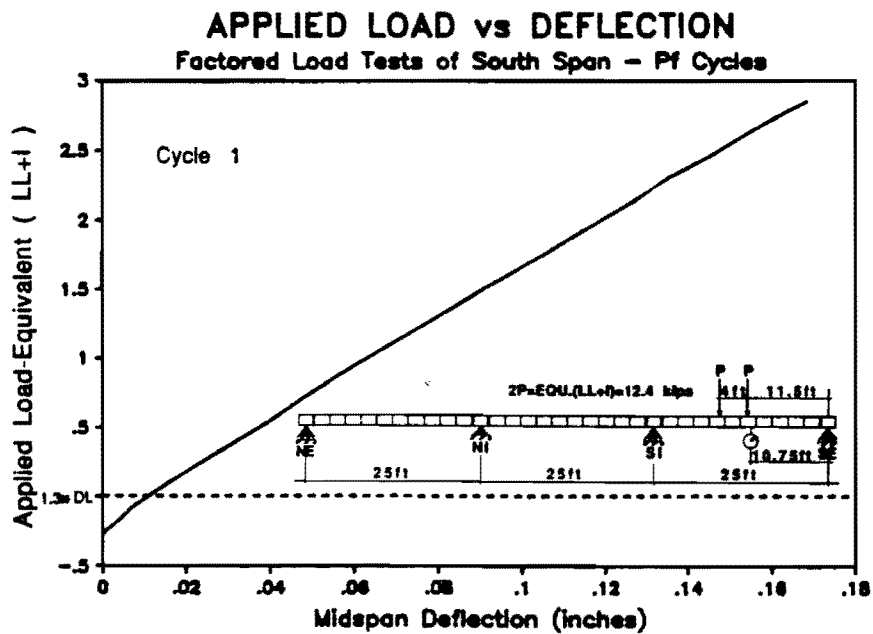


Fig. 6.51 South Span Factored Load Cycles – Applied Load vs. Deflection

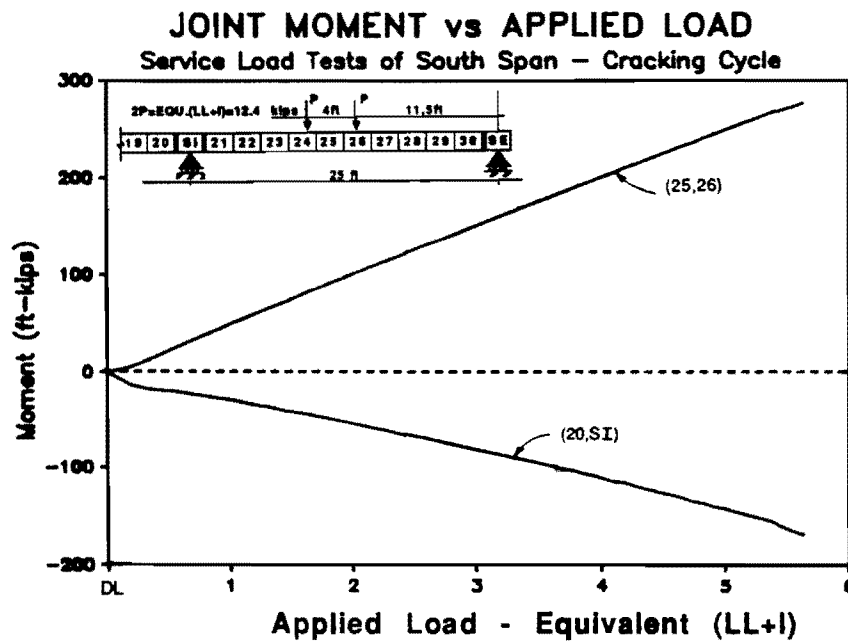
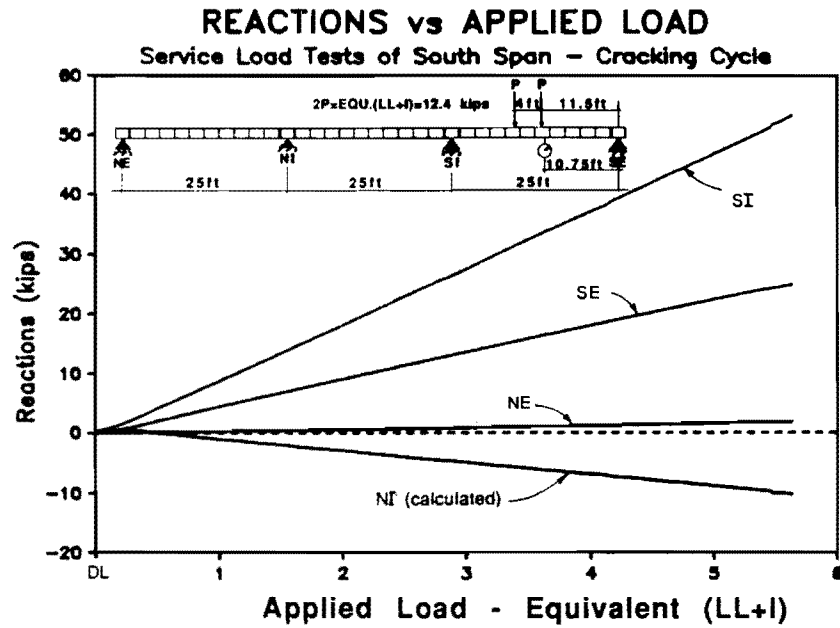


Fig. 6.52 South Span Factored Load Cycles – Rections and Joint Moments

Table 6.30 South-span Factored Load Cycles
Maximum Response Values at Factored Load = 2.9(LL+I)

Deflections	0.17 inches (L/1765)
Reactions	29 kips at SI
Moments M +ve	160 ft-kips at (25,26)
M -ve	-90 ft-kips at (20,SI)

Table 6.31 South-span Factored Load Cycles
Change in Tendon Stress (ksi) at Factored Load = 2.9(LL+I)

	(29,30) ext.end	(25,26) midspan	(21,22) int.end
Tendon 1a:	1	4	.5
Tendon 1b:	1	4	1
Tendon 3:	1	3	1

All gages are active.

Table 6.32 Summary of South-span Factored Load Cycles

$P_{applied}$:	Description:
1.3DL-0.28(LL+I)	-Start Test ($P_{rams}=0$)
1.3DL	-Start Live Load application from the factored dead load condition
1.3DL+2.2(LL+I)	-Decompression Load
1.3DL+2.9(LL+I)	-Factored Load Condition

Both the reactions and the calculated joint-moments show extremely linear behavior indicating minimal internal force redistribution. All tendons exhibited linear behavior with a maximum stress range of approximately 4.5 ksi.

6.7.3 Flexural Strength Tests Of South-Span

6.7.3.1 Crack Opening Cycles for South-Span. Load was increased beyond factored load levels to investigate the ultimate flexural behavior of the system. The first stage of the flexural strength test was to apply load to the structure to visibly open a midspan crack. Three cycles of load were applied to open the midspan crack. The load was applied in $0.32(LL+I)$ increments to the factored load level of $2.9(LL+I)$, and then in $0.16(LL+I)$ increments to a maximum applied load of $4.8(LL+I)$. Because the crack had only partially progressed during the initial cracking cycle (Section 6.7.1.2), additional cracking occurred during the first crack-opening cycle. The corresponding crack opening at this load level was approximately 0.03 in., which translates to 0.12 in. for the prototype structure.

After fully cracking the south-span in cycle 1, the structure behaved quite differently in the second and third crack-opening cycles. The flexural stiffness reduced for loads higher than the decompression load just as it did for the dry-jointed north-span.

The applied load-deflection response for the three crack-opening cycles is shown in Fig. 6.53. The measured reactions and the calculated joint-moments are plotted with respect to the applied load in Fig. 6.54.

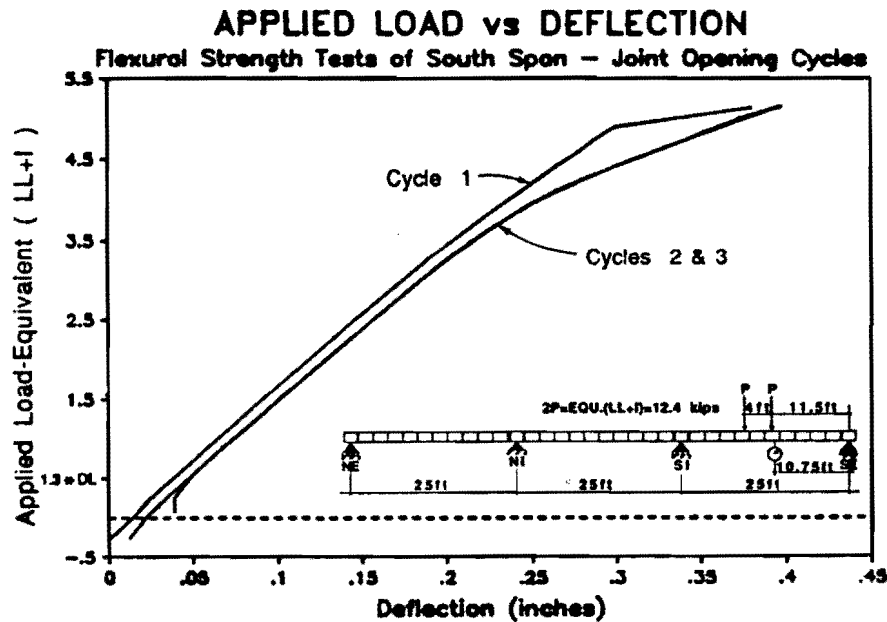


Fig. 6.53 South Span Crack Opening Cycles – Applied Load vs. Deflection

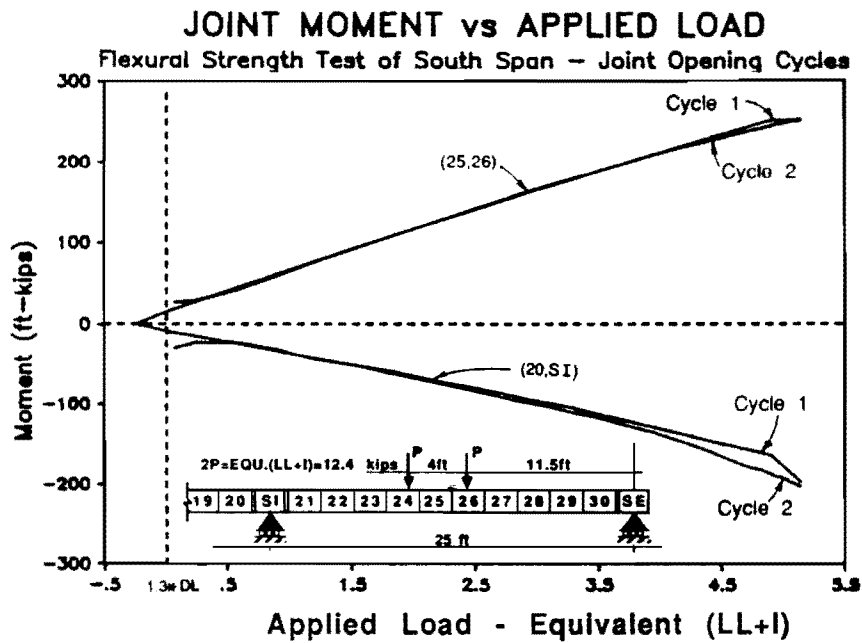
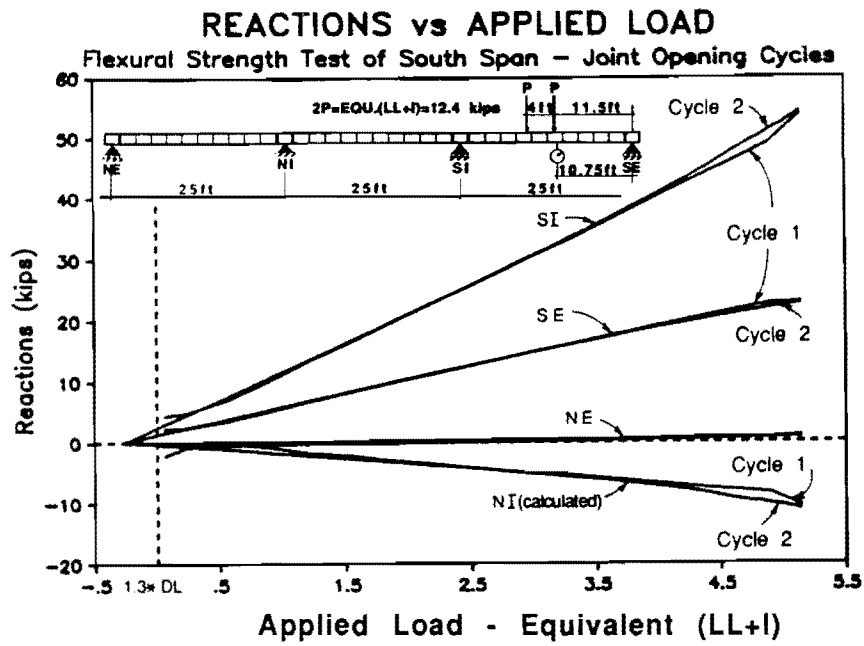


Fig. 6.54 South Span Crack Opening Cycles – Reactions and Joint Moments

2.2(LL+I) Decompression Load: At load levels higher than the decompression load the load-deflection, reaction, and joint-moment responses all exhibited the same behavior as observed for the dry-jointed north-span. After decompression, the midspan stiffness reduced and internal forces were redistributed toward the interior support.

2.4(LL+I): For cycles 2 and 3 the midspan region of all the tendons in the south-span exhibited linear response up to approximately $2.4(LL+I)$ with a corresponding stress range of approximately 3 ksi. For load levels higher than $2.4(LL+I)$ the tendon stresses increased at a higher rate.

2.8(LL+I): The crack-opening response near joint (25,26) for the first and second cycle is shown in Fig.6.55. For the first cycle, only the west side of the crack began opening at $2.8(LL+I)$. During the later two cycles, after fully cracking the joint, both sides of the crack opened symmetrically. The crack also opened slightly wider in the later cycles.

4.8(LL+I): The applied load was increased until the crack adjacent to joint (25,26) was visibly open at a maximum load of $4.8(LL+I)$. The tangent stiffness computed for the crack-opening response at the beginning and end of the crack-opening cycle was calculated as $18(LL+I)/\text{inch}$ and $7.8(LL+I)/\text{inch}$, respectively. The crack-opening cycles for the north-span are summarized in Tables 6.33, 6.34, and 6.35.

**Table 6.33 South-span Crack-Opening Cycles
Maximum Response Values at Load = $4.8(LL+I)$**

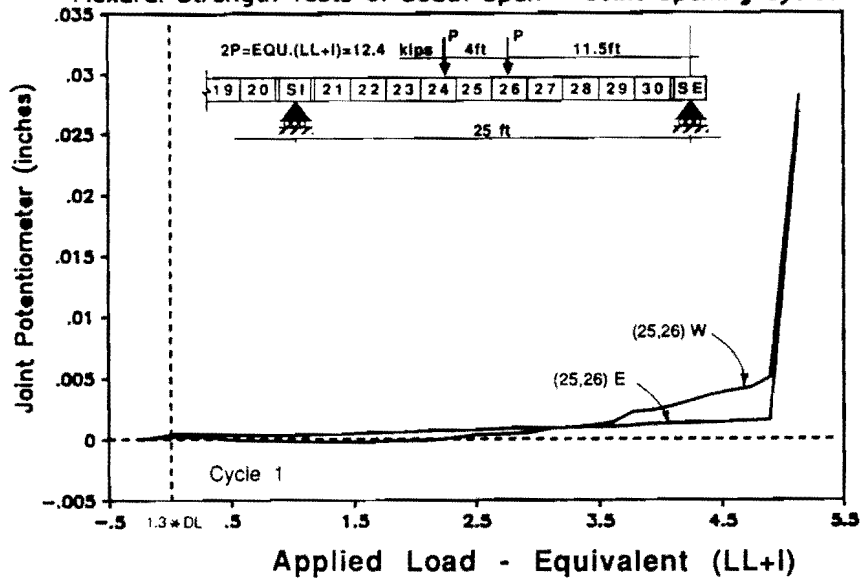
	(end of cycle 2)
Deflections	0.40 inches (L/750)
Reactions	54 kips at SI
Moments M +ve	250 ft-kips at (25,26)
M -ve	-200 ft-kips at (20,SI)

**Table 6.34 South-span Crack-Opening Cycles
Change in Tendon Stress (ksi) at Load = $4.7(LL+I)$ Cycle 1**

	(29,30) ext.end	(25,26) midspan	(21,22) int.end
Tendon 4a:	3	11	1
Tendon 4b:	2	13	2
Tendon 5:	2	13	2

JOINT OPENING POTENTIOMETER vs APPLIED LOAD

Flexural Strength Tests of South Span – Joint Opening Cycles



JOINT OPENING POTENTIOMETER vs APPLIED LOAD

Flexural Strength Tests of South Span – Joint Opening Cycles

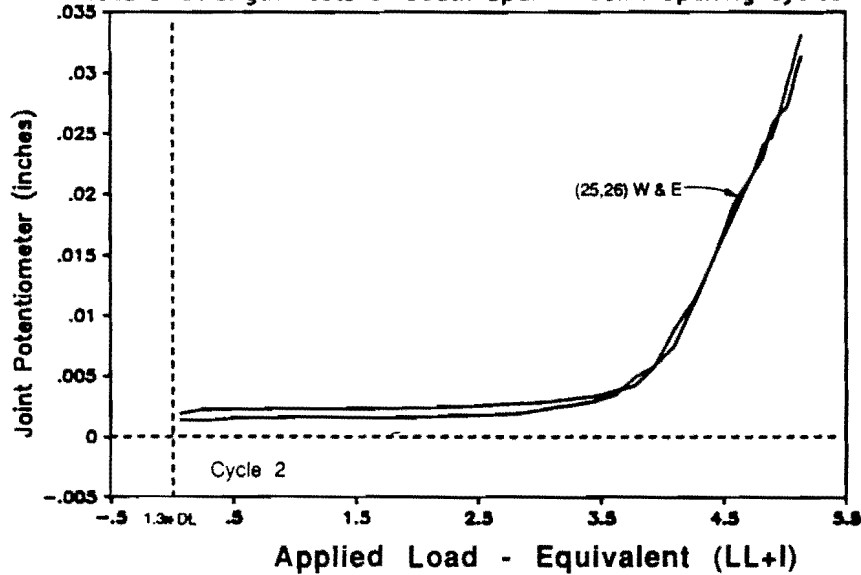


Fig. 6.55 South Span Crack Opening Cycles – Joint Opening Potentiometer vs. Applied Load

Table 6.35 Summary of South-span Crack-Opening Cycles

$P_{applied}$:	Description:
1.3DL-0.28(LL+I)	-Start Test ($P_{rams}=0$)
1.3DL	-Start Live Load application from the factored dead load condition
1.3DL+2.2(LL+I)	-Decompression Load
1.3DL+2.4(LL+I)	-The midspan stresses for all the south-span tendons begin to increase at a faster rate
1.3DL+2.8(LL+I)	-Crack near joint (25,26) begins to open
1.3DL+4.8(LL+I)	-Maximum Load for Crack-Opening Cycles

The applied load tendon stress response for the south-span crack-opening cycles was similar for all tendons. The applied load-stress response during the first and second crack-opening cycles for Tendon 4a is shown in Fig. 6.56. In the first cycle the tendons remained linear to approximately the decompression load, and then the tendon stresses started increasing at a slightly higher rate. The tendon stresses increased suddenly to a maximum stress increase of approximately 11 ksi when the section cracked. Slip was also apparent from the exterior end towards the midspan region.

After applying one cycle of load there was a net change in tendon stress at the start of the second cycle. The exterior end stresses had increased and the midspan stresses had decreased. This is also illustrated by the tendon stress profile (Fig.6.57) for the unloaded condition preceding each load cycle. With slip occurring towards the midspan section of the tendon, the "unstressed" length of that portion had increased, leading to decreased tendon stresses when the applied load was removed. Conversely, because the tendon had slipped away from the exterior region, the "unstressed" length had decreased, leading to increased tendon stresses when the applied load was removed.

As load was applied for Cycle 2 the tendon-stress response histories had approximately the same initial slopes. At 2.4(LL+I) the stresses began deviating from the initial linear behavior, slowly at first and then at a higher rate at approximately 3.5(LL+I). Note also that stress range for the later crack-opening cycles was slightly higher in the midspan region and lower at the exterior end. However, the net stress increase from the start of the first cycle was the same for all cycles. No slipping was noticed in the later two crack-opening cycles.

Apart from the crack extension described above, there was no other cracking during the crack-opening cycles for the south-span. Only a single crack through the concrete adjacent to joint (25,26) was visible at the end of this cycle.

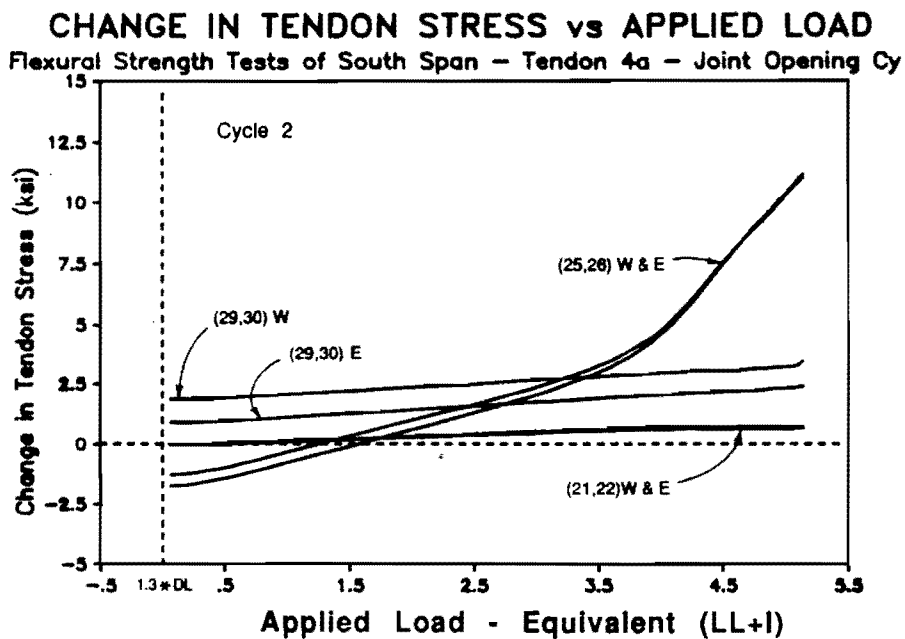
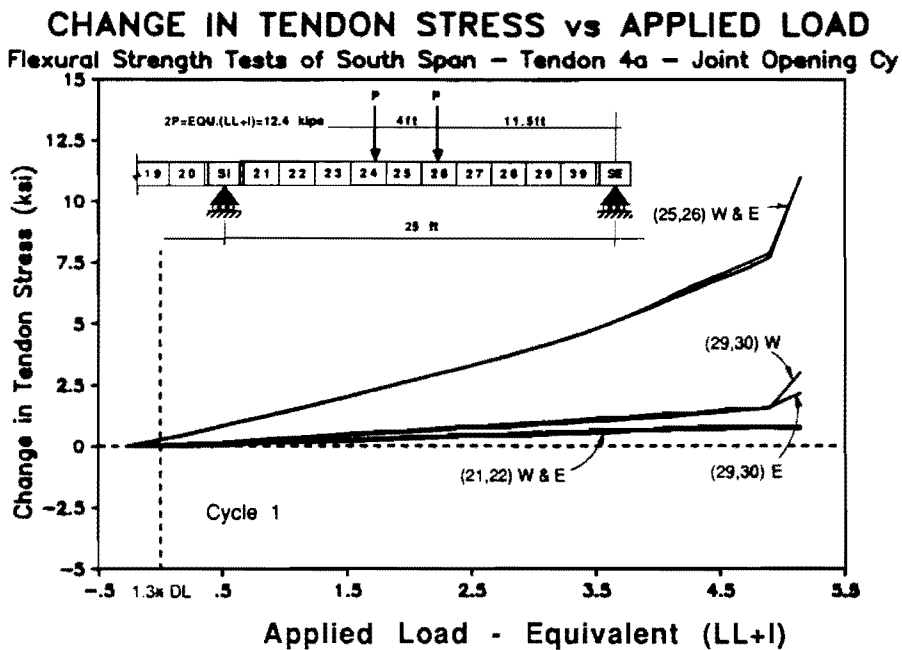


Fig. 6.56 South Span Cracking Cycle – Joint Opening Potentiometer vs. Applied Load

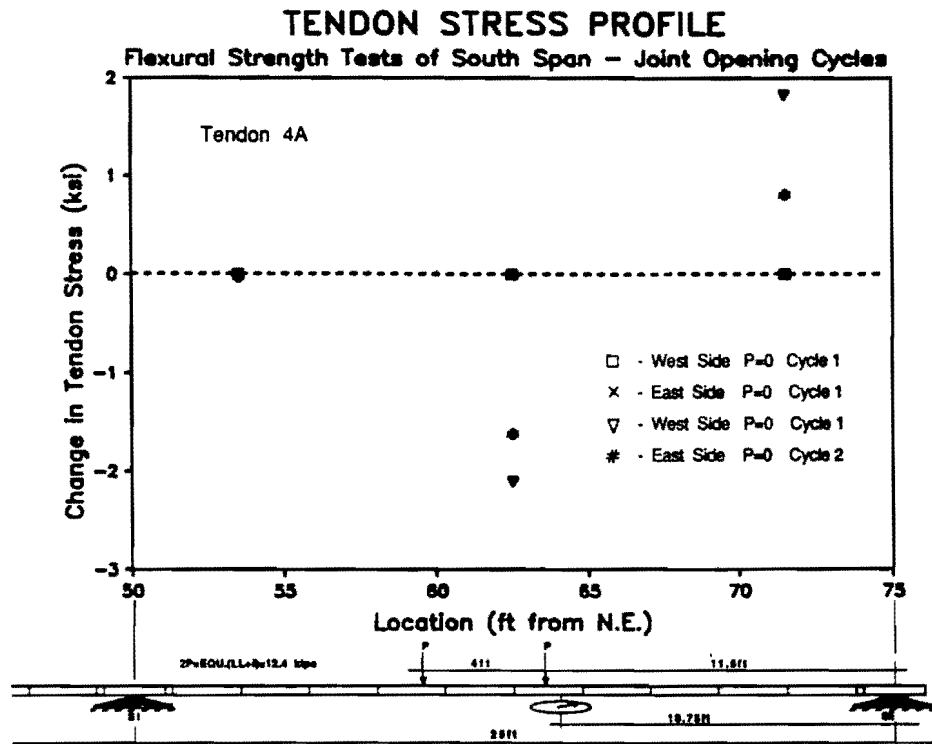


Fig. 6.57 South Span Crack Opening Cycles - Tendon 4a Stress Profile Before Cycles 1 & 2

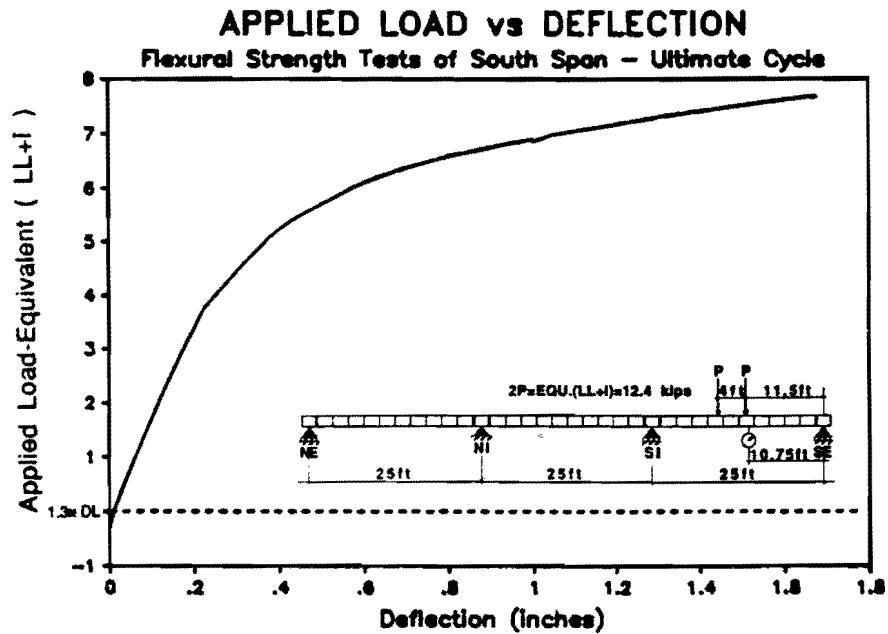


Fig. 6.58 South Span Flexural Strength Test - Applied Load vs. Deflection

6.7.3.2 Flexural Strength Cycle for South-Span. After completing the crack-opening cycles the structure was loaded to higher levels to determine the flexural strength of the system. The load was applied in $0.81(LL+I)$ increments to the previous cracking load, in $0.16(LL+I)$ increments to $6.0(LL+I)$, in $0.08(LL+I)$ increments to $7.0(LL+I)$, and then $0.04(LL+I)$ increments until the flexural strength of the south-span was reached. The flexural strength test was conducted in one load cycle, and the strength was measured to be $7.7(LL+I)$ with an ultimate midspan deflection of 1.69 inches.

The applied load-deflection response for the flexural strength cycle is shown in Fig. 6.58. The measured reactions and calculated joint-moments are plotted with respect to the applied load in Fig. 6.59. The change in tendon stress due to applied load is shown for all south-span tendons in Fig. 6.60, and for all center-span tendons in Fig. 6.61. The joint behavior, as measured by potentiometer and grid crack-monitors, is illustrated in Fig. 6.62.

The south-span displayed essentially the same behavior for loads up to $2.4(LL+I)$ as was observed for the later cycles of the crack-opening load cycles.

3.8(LL+I): The crack adjacent to the midspan joint began opening widely causing internal forces to redistribute more rapidly and also causing all the tendon stresses in the midspan of the south-span to begin increasing at a higher rate.

5.2(LL+I): Tendon 5 (south-span) began slipping from the exterior end towards the midspan region.

5.3(LL+I): Tendon 4a began slipping from the exterior end towards the midspan region.

5.4(LL+I): Tendon 4a began slipping from the interior end towards the midspan region.

5.5(LL+I): Tendon 4b began slipping from both ends towards the midspan region.

5.8(LL+I): The crack adjacent to the support joint (20,SI) began to open at approximately $5.8(LL+I)$. This shows up as the inflection point in the reaction and moment data (Fig. 6.59) indicating that the reduced stiffness at the support caused a redistribution of internal forces back towards the midspan region.

All the tendon stresses at the near end of the interior span (tendons 2, 3, and 5) increased as the support crack began opening at approximately $5.8(LL+I)$.

6.2(LL+I): Tendon 5 (interior span) began slipping from the midspan region towards the near the south end of the interior span.

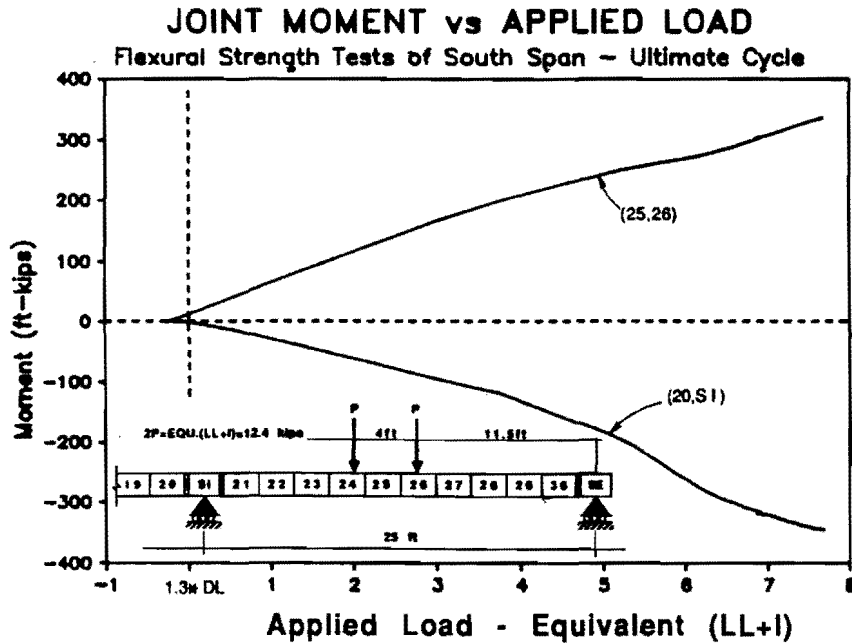
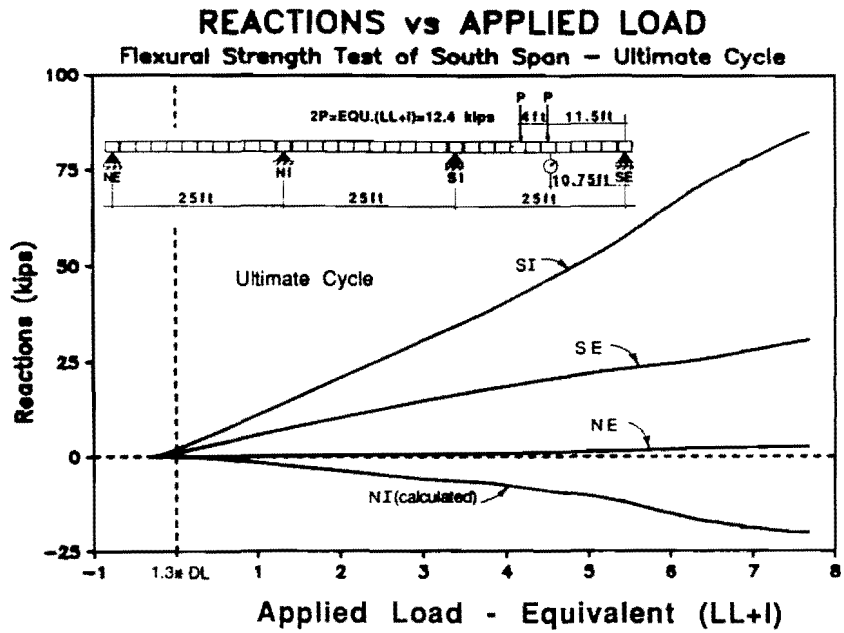


Fig. 6.59 South Span Flexural Strength Test - Reactions and Joint Moments

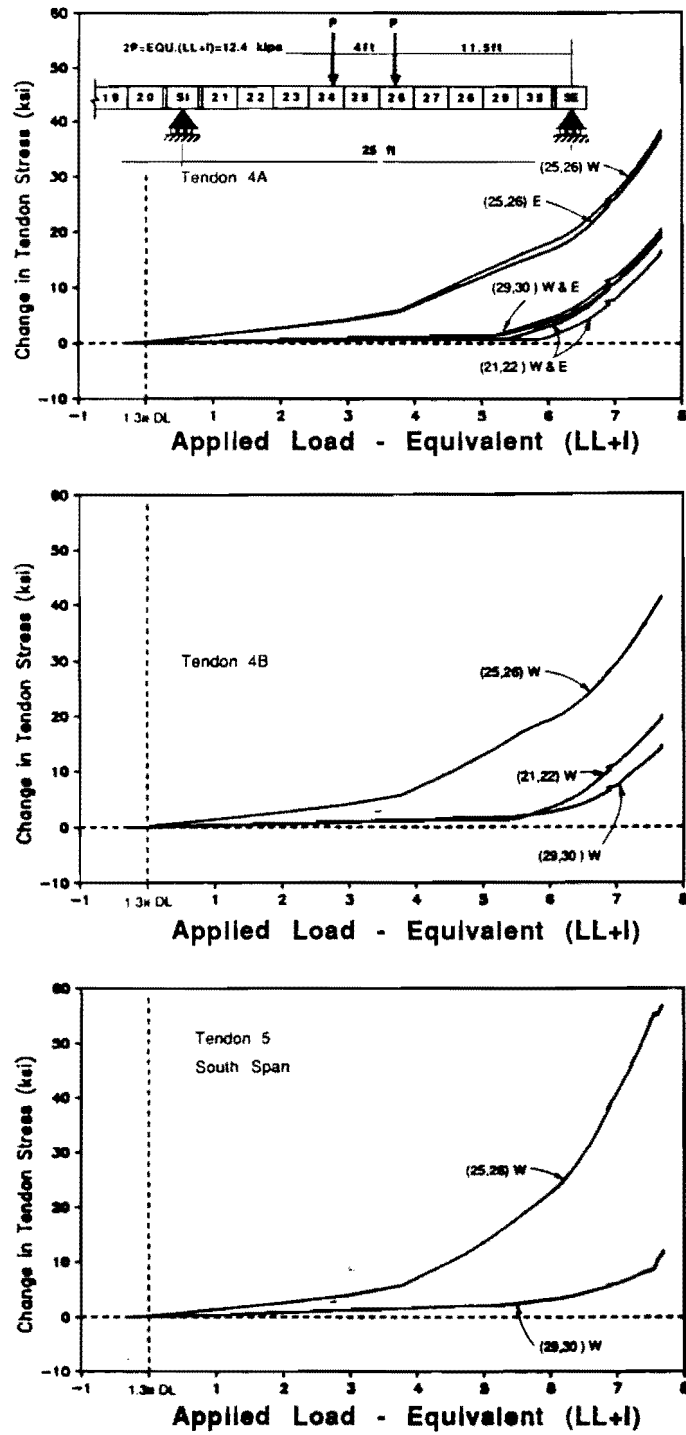


Fig. 6.60 South Span Flexural Strength Test – Change in Tendon Stress vs. Applied Load – South Span Tendons

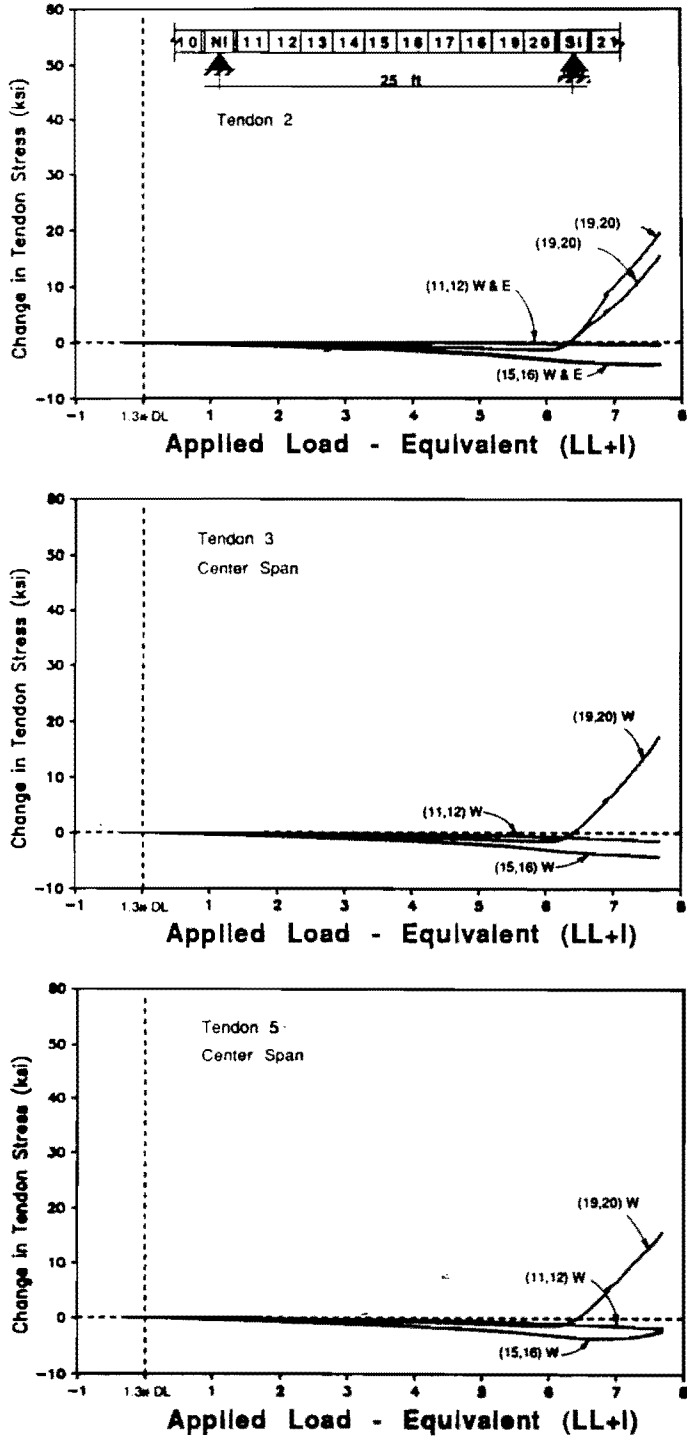
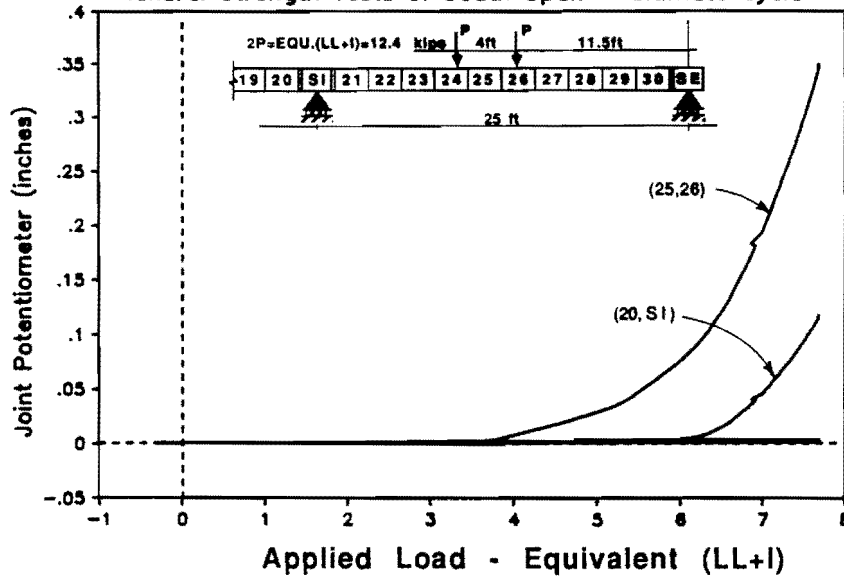


Fig. 6.61 South Span Flexural Strength Test Change in Tendon Stress vs. Applied Load - South Span Tendons

JOINT OPENING POTENTIOMETER vs APPLIED LOAD
 Flexural Strength Tests of South Span - Ultimate Cycle



CRACK OPENING PROFILES

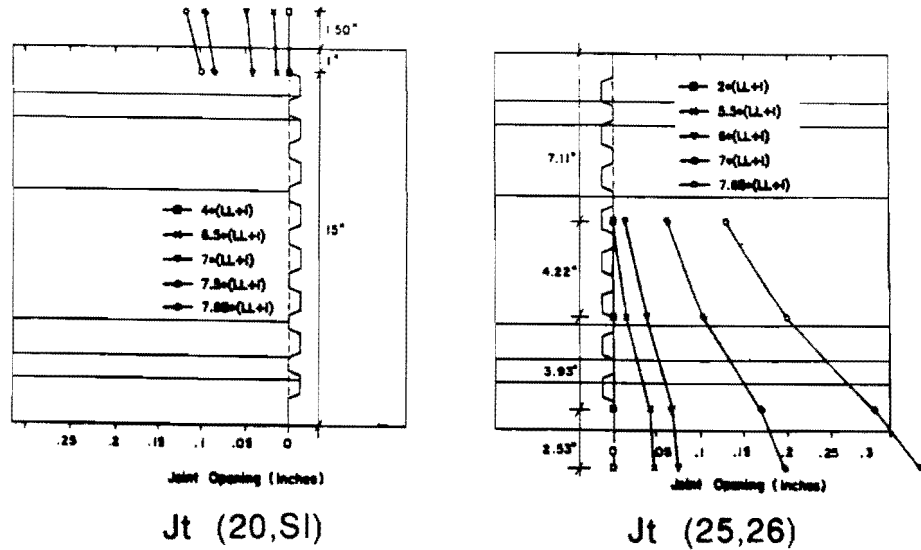


Fig. 6.62 South Span Flexural Strength Test - Crack Opening Behavior

6.4(LL+I): The support crack began opening rapidly, reducing stiffness at the support, and redistributing internal forces back towards the midspan region. The tendon stresses for all tendons in the south-span began increasing at a higher rate.

7.6(LL+I): Tendon 5 (south-span) began slipping from the exterior end towards the midspan region.

7.7(LL+I) **Ultimate Flexural Strength:** The test was discontinued before catastrophic failure when the south-span experience approximately the same level of midspan deflection as the north-span. At this load level the tangent stiffness had reduced to 4 percent of its initial elastic stiffness and was approximately equal to the tangent stiffness at the conclusion of the north-span flexural test. The tangent stiffness for increasing levels of applied live load was calculated from the load-deflection curve, and is tabulated in Table 6.36. The flexural strength cycle for the south-span is summarized in Tables 6.37, 6.38, and 6.39.

Table 6.36 Tangent stiffness During South-span Tests
(measured in (LL+I)/inch)

Applied Load	Flexural Test	Shear Test
1(LL+I)	18	18
2(LL+I)	18	18
3(LL+I)	17	12
4(LL+I)	11	7.8
5(LL+I)	7.3	5.4
6(LL+I)	3.7	2.9
7(LL+I)	1.2	1.6
7.7(LL+I)	0.57	N/A
8.0(LL+I)	N/A	0.73

Table 6.37
South-span Flexural Test - Maximum Response Values
Flexural Strength Load = 7.7(LL+I)

Deflections	1.69 inches (L/178)
Reactions	93 kips at SI
Moments M +ve	340 ft-kips at (25,26)
M -ve	-350 ft-kips at (20,SI)

Table 6.38 - South-span Flexural Test
Change in Tendon Stress (ksi) Flexural Strength Load = 7.8(LL+I)

Exterior Span Tendons	Interior Span Tendons
Tendon 4a: 20 * 38 * 17	Tendon 2: 18 / <0 / <0
Tendon 4b: 14 * 41 * 19	Tendon 3: 18 / <0 / <0
Tendon 5: 12 * 57 / X	Tendon 5: 16 ** <0 / <0
key = (29,30)/(25,26)/(21,22) = ext.end/midspan/int.end	key = (19,20)/(15,16)/(11,12) = near end/midspan/far end

X: denotes inactive strain gauge

* denotes slip towards midspan

** denotes slip towards near end

Table 6.39 Summary of South-span Flexural Strength Cycle

$P_{applied}$:	Description:
1.3DL-.28(LL+I)	-Start Test ($P_{rams}=0$)
1.3DL	-Start Live Load application from the factored dead load condition
1.3DL+2.2(LL+I)	-Decompression Load
1.3DL+2.4(LL+I)	-Midspan stresses for all south-span tendons begin to increase at a higher rate
1.3DL+3.8(LL+I)	-Crack adjacent to joint (25,26) began opening causing increased tendon stresses and redistribution of internal forces towards support region.
1.3DL+5.2(LL+I)	-Tendon 5 (south-span) began slipping from exterior end towards the midspan region.
1.3DL+5.3(LL+I)	-Tendon 4a began slipping from exterior end towards the midspan region.
1.3DL+5.4(LL+I)	-Tendon 4a began slipping from interior end towards the midspan region.
1.3DL+5.5(LL+I)	-Tendon 4b began slipping from both ends towards the midspan region.
1.3DL+5.8(LL+I)	-Crack adjacent to joint (20,S1) began opening causing redistribution of forces back towards midspan. -The tendons at the near end of the interior span begin to develop additional load.
1.3DL+6.2(LL+I)	-Tendon 5 (interior span) began slipping from the midspan region towards the near (south) end of the interior span.
1.3DL+6.4(LL+I)	-The support crack began opening rapidly. -The tendon stresses for all tendons in the south-span begin to increase at a higher rate.
1.3DL+7.6(LL+I)	-Tendon 5 (south-span) began slipping from the exterior end towards the midspan region.
1.3DL+7.7(LL+I)	-Ultimate Flexural Strength

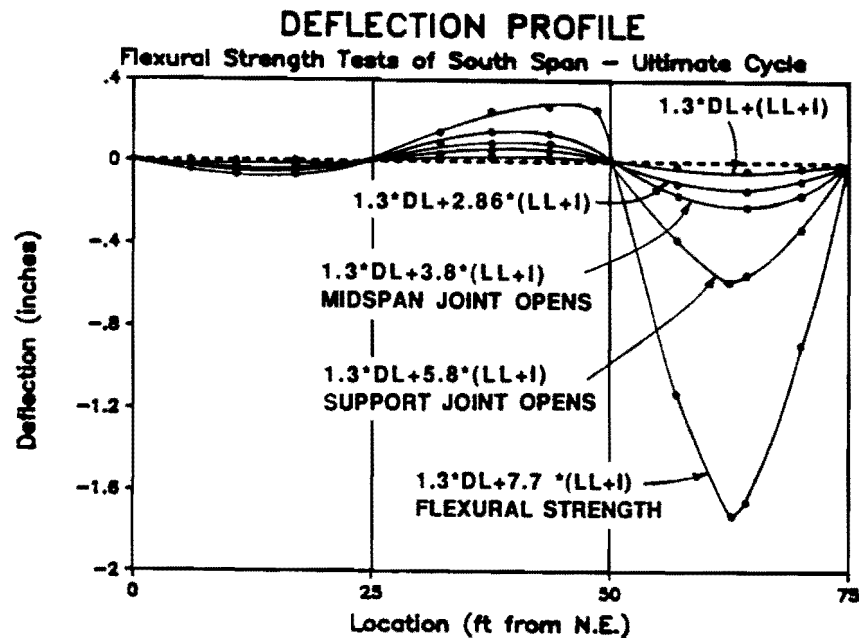


Fig. 6.63 South Span Flexural Strength Test – Deflection Profiles

The measured deflected shapes of the three span structure for increasing levels of applied load are shown in Fig 6.63. At the service load ($1.0(LL+I)$) and the factored load ($2.9(LL+I)$) the deflections are small and the deflected shape is a smooth curve. The deflected shape remained smooth until the midspan crack began opening at $3.8(LL+I)$. Beyond this load, “hinging” occurs at the opening crack, and the midspan deflections increase considerably. When the support crack opens at $5.8(LL+I)$, the mechanism forms and deflections begin to increase very rapidly. The final deflected shape of the structure clearly illustrates the mechanism behavior of the structure at ultimate load levels.

The reaction and joint-moment curves exhibit double curvature (slight S- shape). As the midspan crack opens, the midspan stiffness reduces causing internal forces to redistribute towards the support. When the support crack opens, the support stiffness reduces and internal forces are redistributed back towards midspan.

The concentrated rotations that occurred at critical opening cracks were measured with manually recorded crack-monitors distributed over the height of the crack. A profile of each opening crack during the flexural test of the south-span is shown at the bottom of Fig.6.62. Because of the presence of epoxy, large rotations occurred at only one midspan crack near joint (25,26) and one support crack adjacent to joint (NI,11). The measured profiles indicate that the crack opened linearly, with compressive stresses gradually concentrating in the top flange. The location of the neutral axis at ultimate strength

can be extrapolated from the crack profiles, and was within the compression flange at both opening cracks.

The concentrated angle changes that occurred at each mechanism can be calculated approximately from the crack opening profiles. The concentrated rotations that occurred at the opening cracks were approximately 1.1 degrees at the midspan crack near joint (25,26), and approximately 0.4 degrees at the support joint (20,SI). The midspan angle change is again approximately three times the magnitude of the concentrated angle change at the support.

The cracking behavior of the midspan region of the south-span during the flexural strength test is summarized in Fig. 6.64. The lines indicate the total length of the crack when the flexural strength ($7.7(LL+I)$) was reached. The initial crack length and load at which it was first observed are also indicated. The shear transfer at the segment joints when the ultimate flexural moment was reached is also shown. The shear in segment 26 was distributed primarily towards the exterior support with a shear transfer of approximately $1.6(LL+I)$ at the opening crack.

The rotations required for increased tendon forces occurred primarily at a crack through the concrete adjacent to joint (25,26). Inclined web cracking first occurred at an applied load of approximately $5.1(LL+I)$. The inclined cracking extended from the open flexural crack, and generally fanned towards the load point. The width of the inclined web cracks remained small throughout the flexural test. Horizontal cracking was also noticed near the web/top-flange junction near joint (25,26). At ultimate loads the neutral axis had shifted into the top flange as indicated by cracking in the bottom face of the top flange.

6.7.4 Shear Strength Cycle for South-Span. The final test that was run on the south-span was a shear test in which the load was applied so that significant shear would be transferred across an opening crack adjacent to a joint. One cycle of load was applied in $0.56(LL+I)$ increments to $4.1(LL+I)$, in $0.32(LL+I)$ increments to $5.6(LL+I)$, in $0.16(LL+I)$ increments up to $7.5(LL+I)$, and then in $0.08(LL+I)$ increments to a maximum load of $8.0(LL+I)$. The test was discontinued when the applied load-deflection stiffness had reached approximately the same level as for the flexural strength test. As in the dry-jointed north-span, the strength was ultimately limited by the flexural strength although the shear transfer at the opening crack caused markedly different local behavior.

The applied load-deflection response for the shear strength cycle is shown in Fig. 6.65. The measured reactions and calculated joint-moments are plotted with respect to applied load in Fig. 6.66. The change in tendon stress due to applied load is shown for all south-span tendons in Fig. 6.67, and for all center-span tendons in Fig. 6.68. The crack behavior adjacent to the joint, as measured by potentiometer and grid crack-monitors, is illustrated in Fig. 6.69.

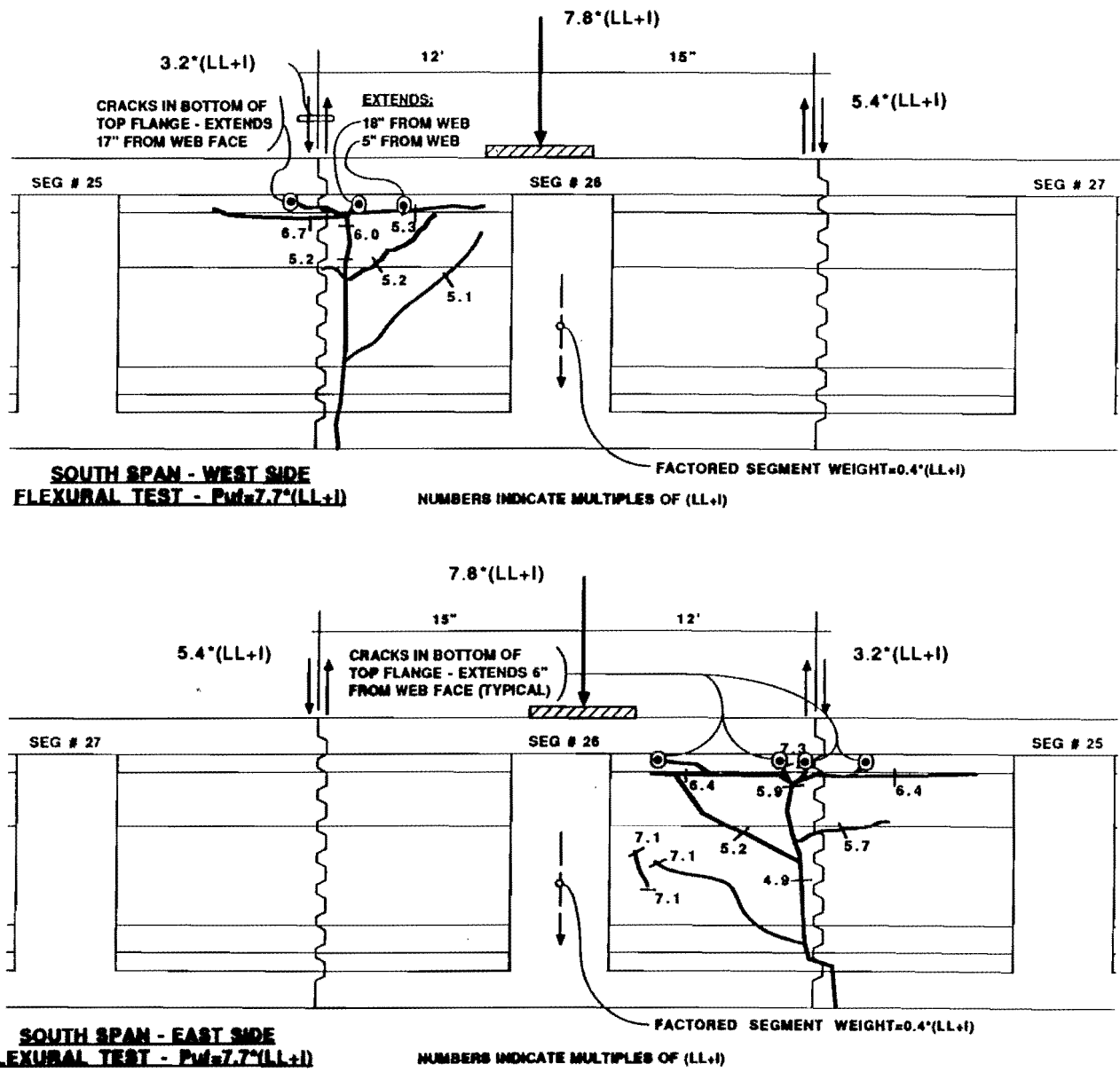


Fig. 6.64 South Span Flexural Strength Test – Cracking Summary

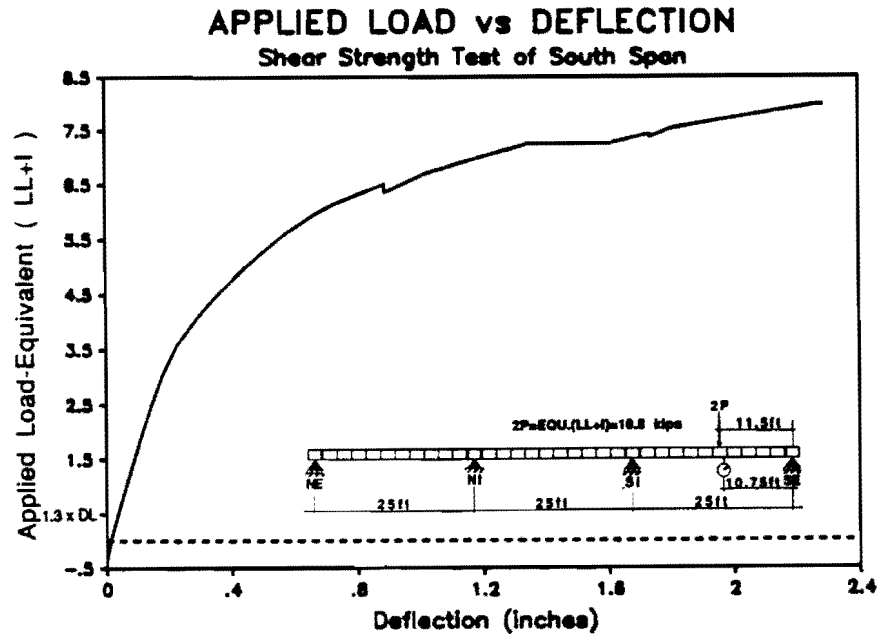


Fig. 6.65 South Span Shear Test – Applied Load vs. Deflection

The sequence of events during the south-span shear test was very similar to that outlined earlier for the flexural strength test (Sec. 6.7.3.2). Detailed highlights of the shear test are summarized in Table 6.42.

The test was discontinued before catastrophic failure at 8.0(LL+I) when the south-span had been subjected to the same level of midspan deflection as the north-span. At this load level the tangent stiffness had reduced to 4 percent of the initial elastic stiffness and was approximately equal to the tangent stiffness at the conclusion of the north-span shear test. The tangent stiffness at increasing levels of applied load is tabulated in Table 6.36. The strength was ultimately limited by the flexural strength although the shear transfer at the opening crack caused markedly different local behavior. The shear strength test of the south-span is summarized in Tables 6.40, 6.41, and 6.42.

Table 6.40
South-span Shear Test
Maximum Response Values Shear Strength Load = 8.0(LL+I)

Deflections	2.29 inches (L/131)
Reactions	74 kips at SI
Moments M +ve	350 ft-kips at (26,27)
M -ve	-340 ft-kips at (20,SI)

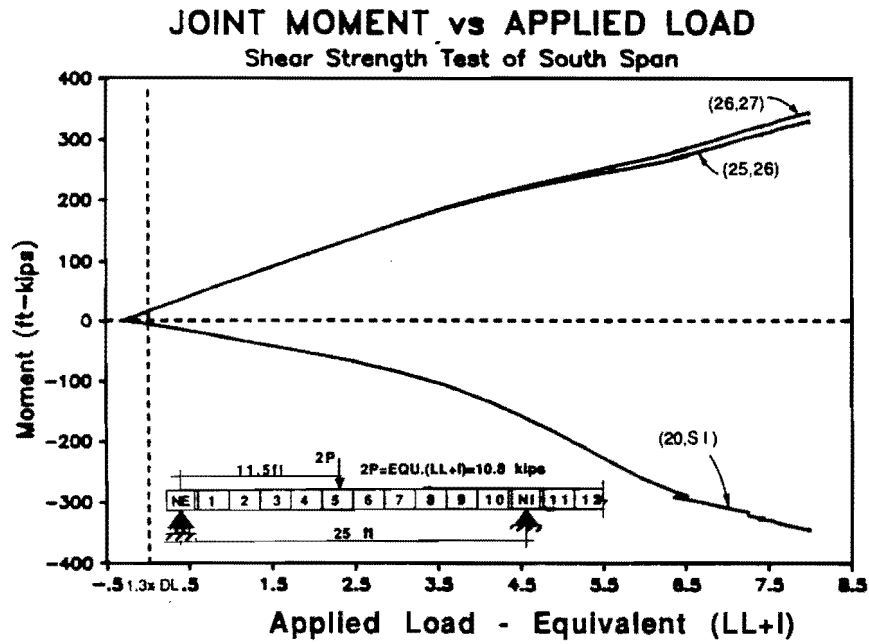
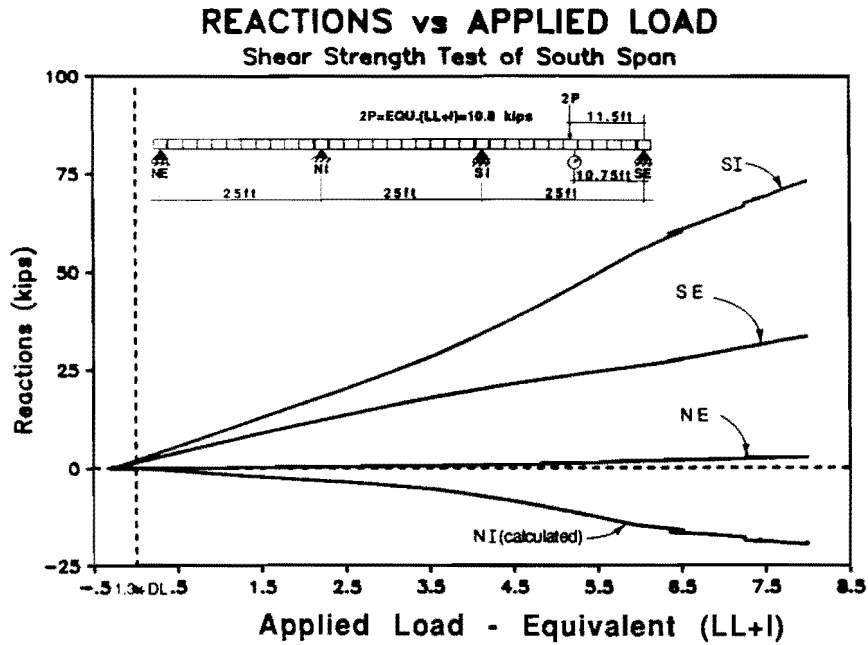


Fig. 6.66 South Span Shear Test – Reactions and Joint Moments

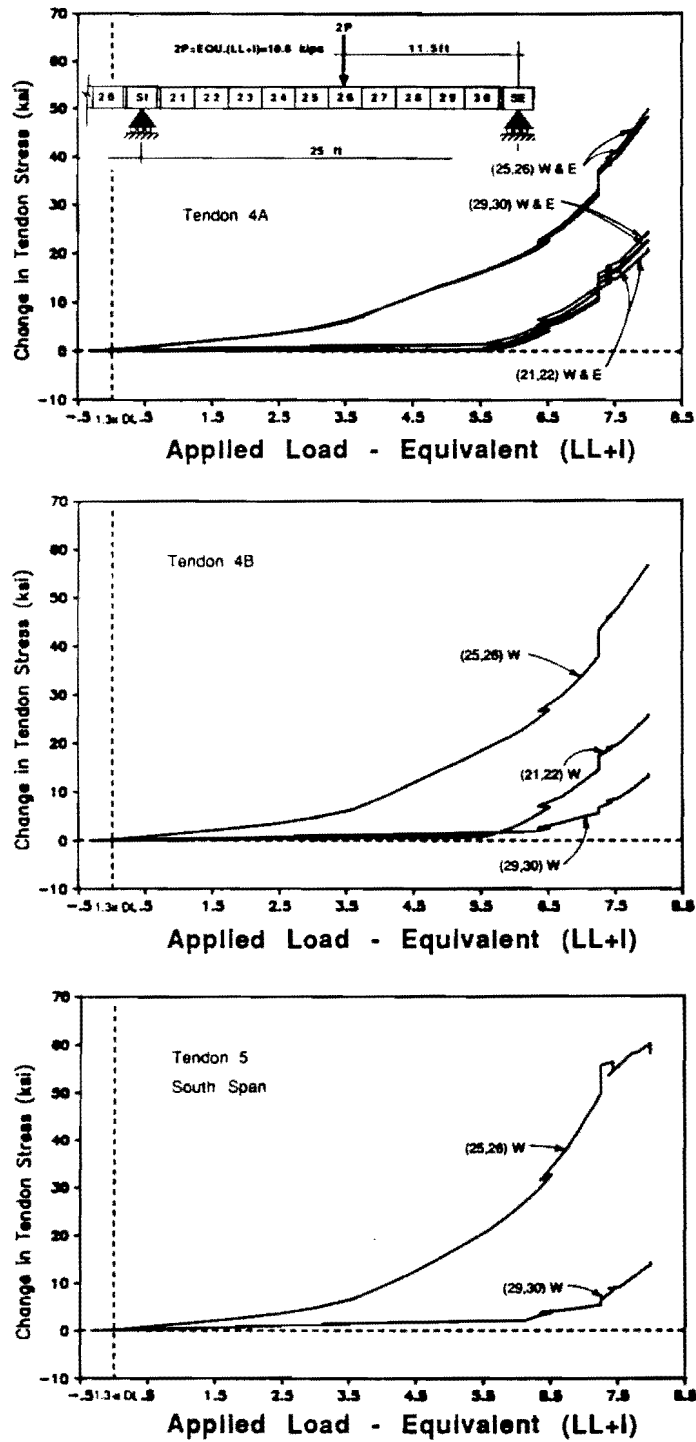


Fig. 6.67 South Span Shear Test – Change in Tendon Stress vs. Applied Load – South Span Tendons

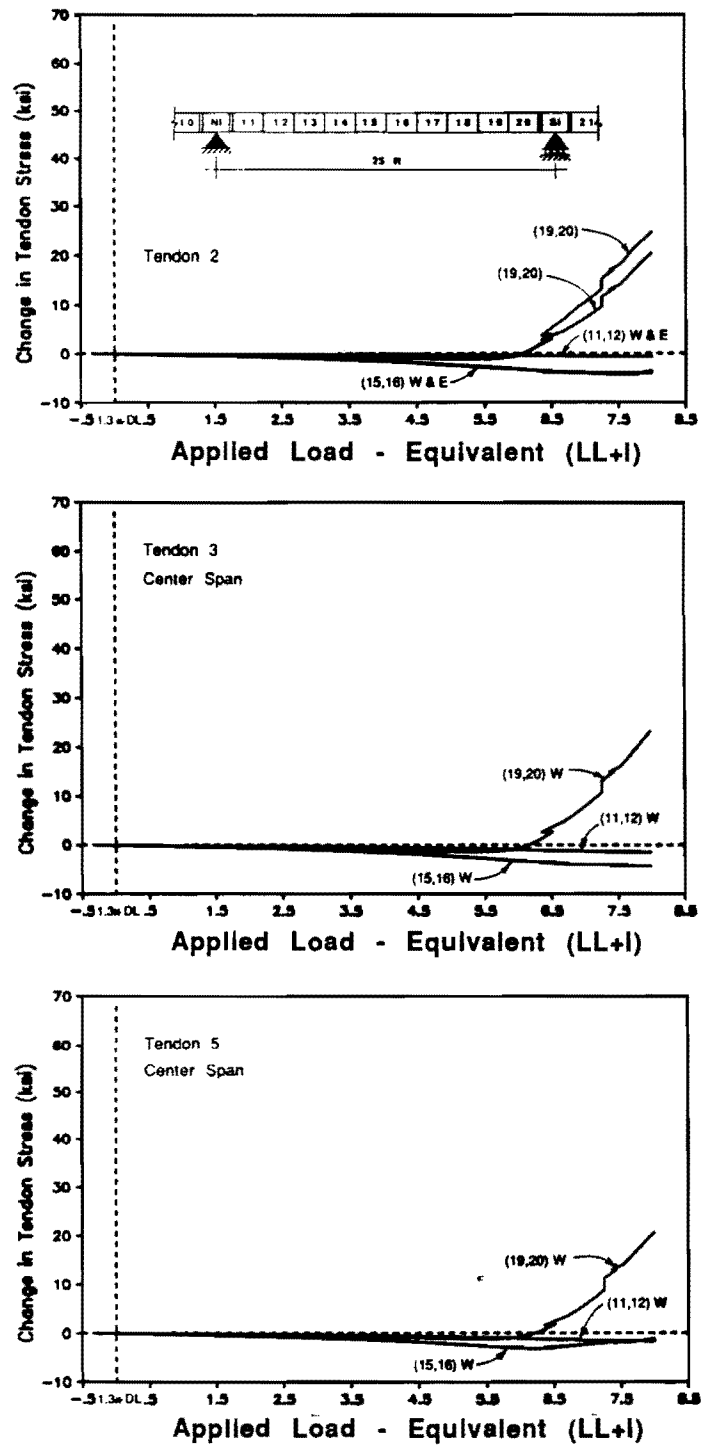
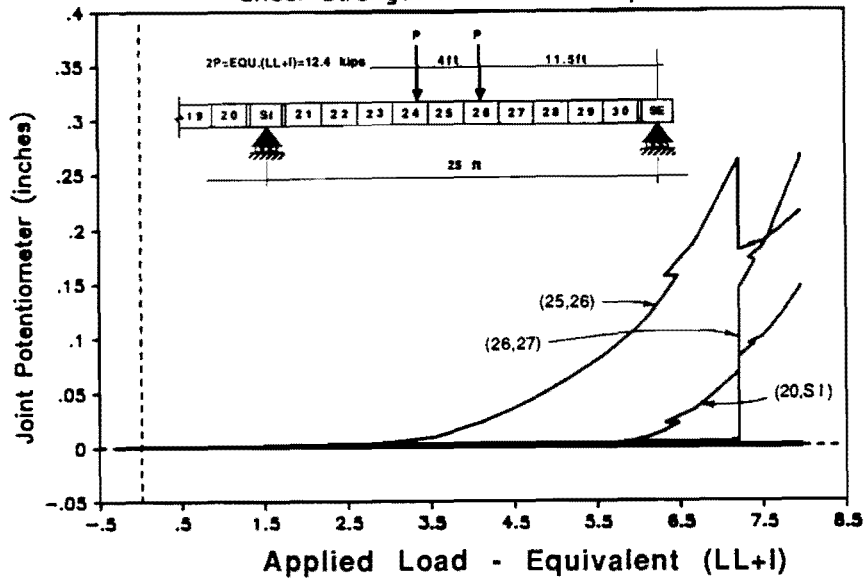


Fig. 6.68 South Span Shear Test - Change in Tendon Stress vs. Applied Load - Center Span Tendons

JOINT OPENING POTENTIOMETER vs APPLIED LOAD
Shear Strength Test of South Span



CRACK OPENING PROFILES

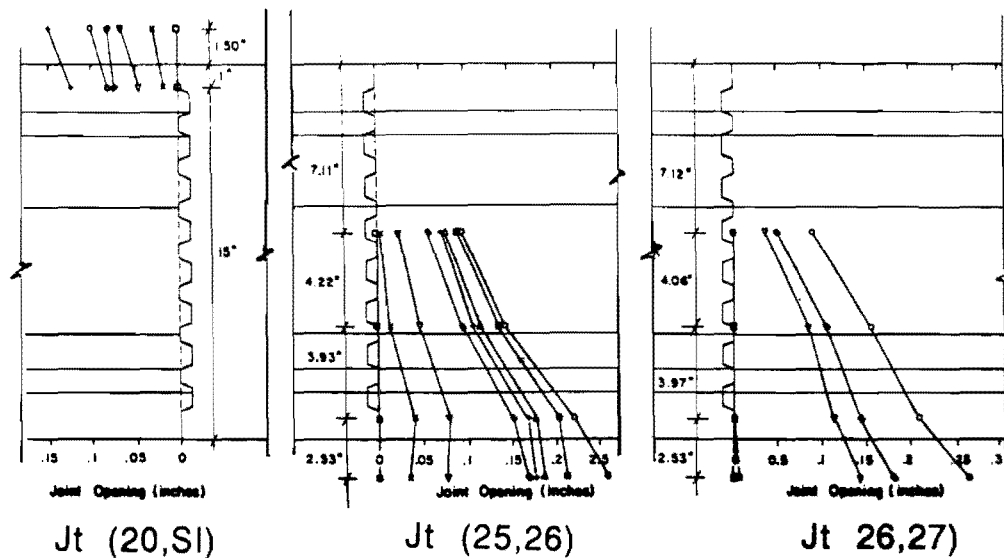


Fig. 6.69 South Span Shear Test – Crack Opening Behavior

Table 6.41
South-span Shear Test
Change in Tendon Stress (ksi)
Shear Strength Load = 8.0(LL+I)

Exterior Span Tendons	Interior Span Tendons
Tendon 4a: 24 / 50 / 23	Tendon 2: 22 / -3 / 0
Tendon 4b: 14 / 57 / 27	Tendon 3: 23 / -3 / -1
Tendon 5: 17 / 60 / X	Tendon 5: 21 ** -1 / -1
key = (29,30)/(25,26)/(21,22) = ext.end/midspan/int.end	key = (19,20)/(15,16)/(11,12) = near end/midspan/far end

X: denotes inactive strain gauge
 * denotes slip towards midspan
 ** denotes slip towards near end

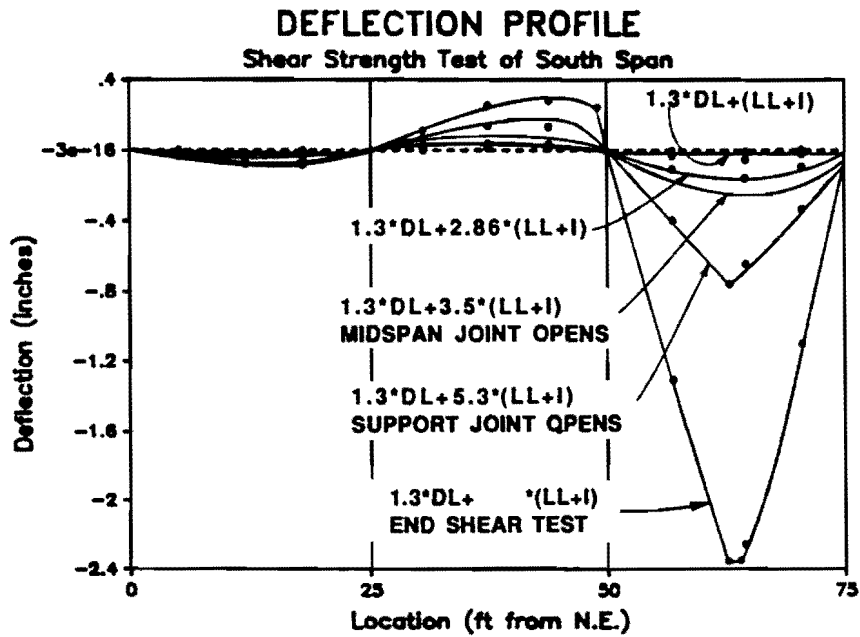


Fig. 6.70 South Span Shear Test - Deflection Profile

Table 6.42 Summary of South-Span Shear Strength Cycle

Applied:	Description:
1.3DL-0.30(LL+I)	-Start Test ($P_{rams}=0$)
1.3DL	-Start Live Load application from the factored dead load condition
1.3DL+2.2(LL+I)	-Decompression load
1.3DL+2.4(LL+I)	-The midspan stresses for all south-span tendons begin to increase at a higher rate. The measured stress range of midspan was approximately 3 ksi.
1.3DL+3.0(LL+I)	-The cracks from the previous flexural test began to open.
1.3DL+3.5(LL+I)	-The crack adjacent to joint (25,26) began opening widely causing increased tendon stresses and redistribution of internal forces towards support region.
1.3DL+4.8(LL+I)	-Cracking occurs through the bottom flange approximately 9 in. south of joint (25).
1.3DL+5.3(LL+I)	-The crack adjacent to joint (20,S1) began opening causing redistribution of forces back towards midspan. -The tendon stresses at the near end of the interior span begin to increase.
1.3DL+5.6(LL+I)	-Tendon 4b began slipping from the interior end towards the midspan region.
1.3DL+5.7(LL+I)	-Tendon 4a began slipping from both ends towards the midspan region.
1.3DL+6.2(LL+I)	-Tendon 5 (south-span) began slipping from the exterior end towards the midspan region. Tendon 5 (interior span) also began slipping from the midspan region towards the near south end of the interior span.
1.3DL+6.3(LL+I)	-Tendon 4b began slipping from the exterior end towards the midspan region.
1.3DL+6.5(LL+I)	-An additional crack forms in the bottom flange of segment 26 at approximately 9 in. north of joint (26,27).
1.3DL+7.2(LL+I)	-Cracking occurs in 26 adjacent to joint (26,27).
1.3DL+7.7(LL+I)	-The primary inclined cracks form in segment 26. Rotations required for increased tendon stress concentrate at these inclined cracks.
1.3DL+7.8(LL+I)	-Tendon 2 (interior span) began slipping from the midspan region towards the near (south) end of the interior span.
1.3DL+8.0(LL+I)	-Ultimate strength limited by flexural capacity.

The measured deflected shapes of the three-span structure for increasing levels of applied load are shown in Fig 6.70. At the service load ($1.0(LL+I)$), and the factored load ($2.9(LL+I)$) the deflections were small and the deflected shape is a smooth curve. The deflected shape remains smooth until the midspan crack began opening at $3.5(LL+I)$. Beyond this load "hinging" occurred at the opening cracks, and midspan deflections increase considerably. When the support crack opened at $5.3(LL+I)$, the mechanism formed and deflections began increasing very rapidly. The final deflected shape of the structure clearly illustrates the mechanism behavior of the structure at ultimate load levels.

The reaction and joint-moment curves again exhibited double curvature (S-shape). As the midspan crack opened the midspan stiffness reduced causing internal forces to redistribute towards the interior support. When the support crack opened, the support stiffness reduced and internal forces were redistributed back towards midspan.

A profile of each opening crack during the shear test of the south-span is shown at the bottom of Fig. 6.69. Up to approximately $6.8(LL+I)$ the midspan rotations were concentrated at a single crack adjacent to joint (25,26). After cracking occurred near joint (26,27), the midspan rotations were equally distributed at the two cracks. Because a significant level of shear was transferred across the opening crack, concentrated rotations occurred at an inclined crack which extends from the load point to the bottom of the web, as shown in the cracking summary in Fig. 6.71

Concentrated rotations were calculated from the measured crack-opening profiles. The measured concentrated rotations were approximately 0.8 degrees at each of the two midspan cracks (adjacent to joints (25,26) and (26,27)), and approximately 0.5 degrees at the support crack adjacent to joint (NI,11). The ratio of total midspan rotation to support rotation is again approximately 3.

The cracking behavior of the midspan region on the west and east sides of the south-span is summarized in Fig. 6.71. The lines indicate the total length of the crack when the test was discontinued at $8.0(LL+I)$. The previous cracking from the flexural test is shown with shaded lines, and new cracks or previous cracks that reopen are shown as solid lines. The initial crack extension and the load at which the crack was first observed occurred are also indicated. The shear transfer at the segment joints at the end of the test is also shown. The shear in segment 26 was distributed primarily towards the interior support, with a shear transfer of $5.2(LL+I)$ at joint (25,26).

Cracks that formed during the flexural test reopened at approximately $3.0(LL+I)$. At approximately $4.8(LL+I)$ the bottom flange of Segment 26 cracked approximately 9 inches south of joint (25,26). At approximately $6.5(LL+I)$ the bottom flange of segment 26 cracked again, this time at approximately 9 inches north of joint (26,27). At an applied load of $7.2(LL+I)$ a major crack formed adjacent to joint (26,27). After this crack formed, the cracks located away from the joints closed slightly as the rotations concentrated at the

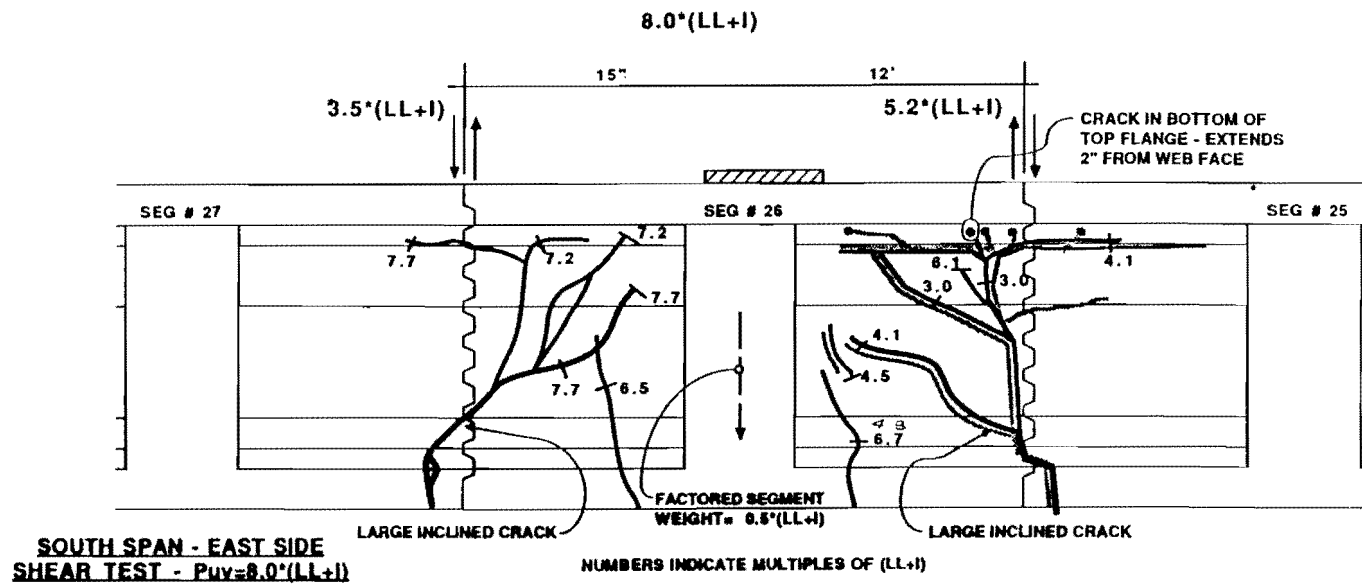
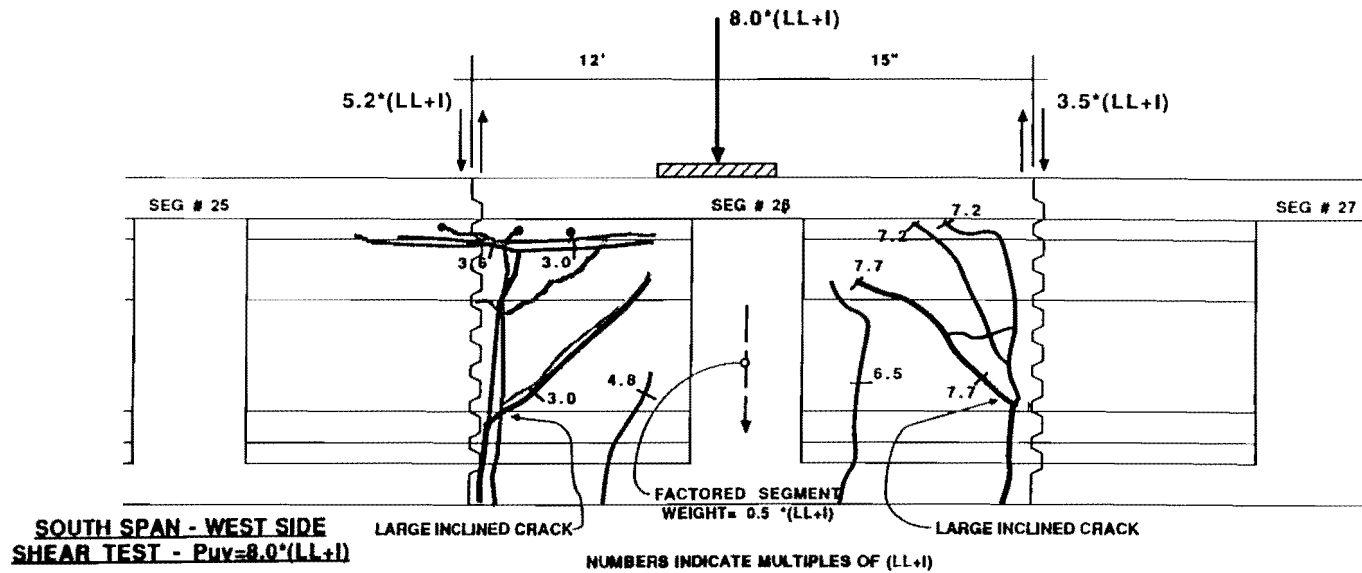


Fig. 6.71 South Span Shear Test - Cracking Summary

crack which formed adjacent to the joints. As load was further increased, cracks adjacent to joints (25,26) and (26,27) opened at approximately the same rate, with concentrated rotations occurring at the primary inclined cracks. At the conclusion of the test the flexural cracks adjacent to the joints were effectively closed with all hinge rotations occurring at the inclined cracks. This allowed the transfer of shear across the joint over the entire height of the web.

7. INTERPRETATION OF TEST DATA

7.1 Observations from Load Tests

7.1.1 Service Load Behavior.

7.1.1.1 **Live Load Response.** The measured deflected shapes of the three span structure for typical service live load application on the dry-jointed north span, epoxy-jointed center span, and the epoxy-jointed south span are shown in Figures 6.5, 6.13, and 6.41 respectively. The measured maximum service live load deflections were $L/5660$ for the dry-jointed exterior span, $L/6250$ for the epoxy-jointed exterior span, and $L/7500$ for the epoxy-jointed interior span. The deflection in the dry-jointed exterior span was approximately 10 percent more than for the epoxy-jointed exterior span. This difference may be caused by a slightly smaller effective cross-section in the dry joints caused by differential shrinkage in the thin flanges of the precast segments. Differential shrinkage in segments, due to variable thicknesses, results in less than full contact between match-cast segments. Epoxy effectively filled any space left by differential shrinkage, and restored full contact between segments.

The live-load tendon-stress increases in the midspan region of the loaded span were measured to be less than 2 ksi in all spans. The stress response remained constant for five consecutive live load cycles indicating that the tendons did not slip at the deviators at service level loads.

7.1.1.2 **Comparison with Elastic Analysis.** The plane frame elastic analysis consistently overestimated the deflections of the model structure. Table 7.1 summarizes the maximum measured and calculated deflections for service load testing of each span. The elastic analysis overestimated the measured deflections by approximately 30 percent in the exterior spans and 20 percent in the interior span.

Some of the increase in measured stiffness might be caused by a higher insitu concrete modulus of elasticity. The concrete modulus used in the analysis was taken from concrete cylinders representative of each type of concrete used (Section 2.2.1). The reinforced concrete in the structure has a higher degree of confinement than the unreinforced cylinders, which may lead to a higher apparent modulus in

Table 7.1 Service Load Deflections

	Span Joint Type	North Dry	Center Epoxy	South Epoxy
Measured	Deflection (in.)	0.53	0.40	0.48
	Δ/L	1/5660	1/7500	1/6250
Calculated	Deflection (in.)	0.68	0.48	0.62
	Δ/L	1/4412	1/6250	1/4839
	$\frac{\text{Calculated}}{\text{Measured}}$	128%	120%	129%

the true structure. In addition, the neglect of the stiffening diaphragms and the relative size of the flange and web thickness, as compared to the thickness of the test cylinder, may contribute to increased stiffness.

Another possible cause for higher measured stiffness is the added stiffness of the secondary cable system. Applied loads are resisted by the combined action of bending stresses in the girder and by a suspension system with the draped external tendons, as shown in Fig. 7.1. The stiffness of each component system contributes to the overall stiffness of the structure. This effect may be further aggravated in the model by the relatively larger grouted ducts.

7.1.1.3 Torsional Response. The model structure exhibited high torsional stiffness with rotational deformations less than could be accurately measured with the instrumentation. The relative flexibility of the load-cell bearing assemblies caused the torsional forces to distribute to adjacent spans causing small distortions throughout the length of the structure.

7.1.1.4 Fretting Fatigue at Deviators. Although the live-load stress range was small, and slip was not apparent during live load cycles, there is need for research to assess the effect of fretting fatigue on external tendons at the deviation locations. The change in tendon force between two adjacent segments of an external tendon occurs by friction while undergoing a concentrated angle change at the deviators (Fig. 7.2). The force transfer occurs over a short length under high

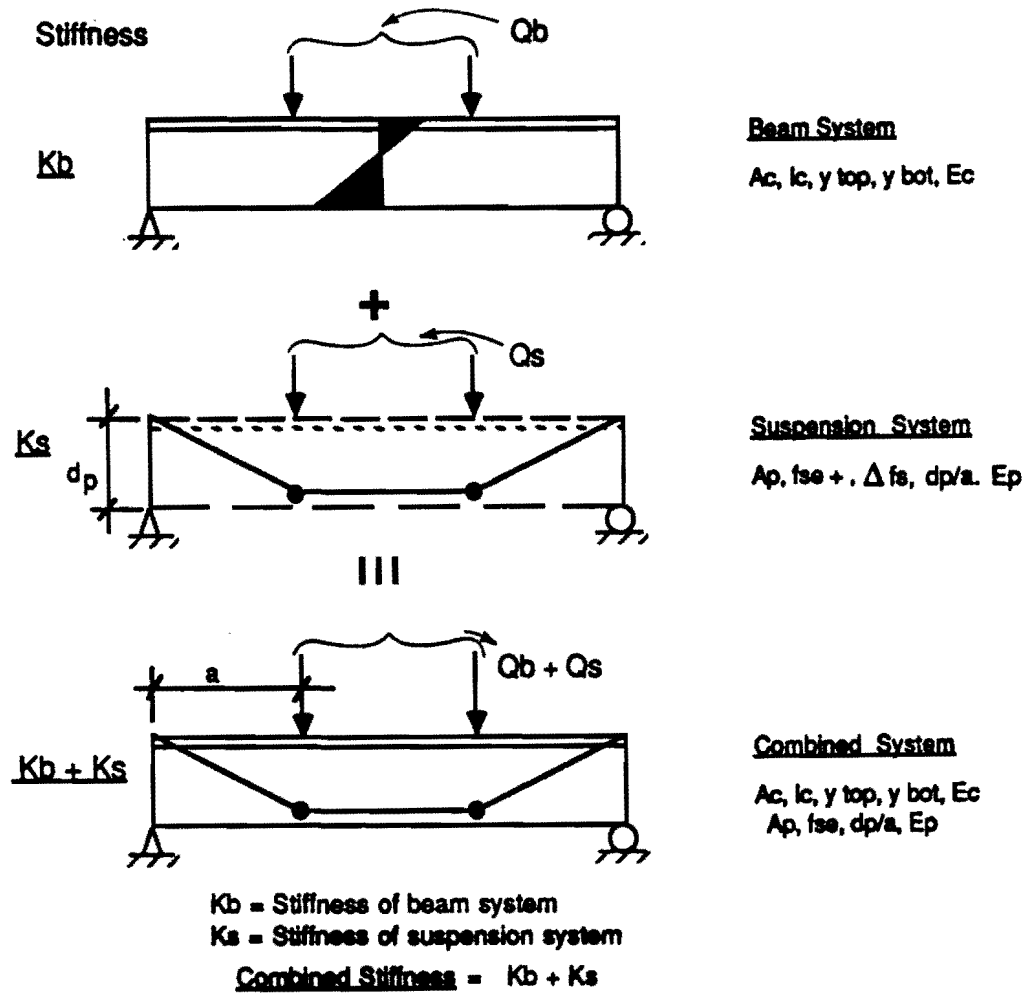
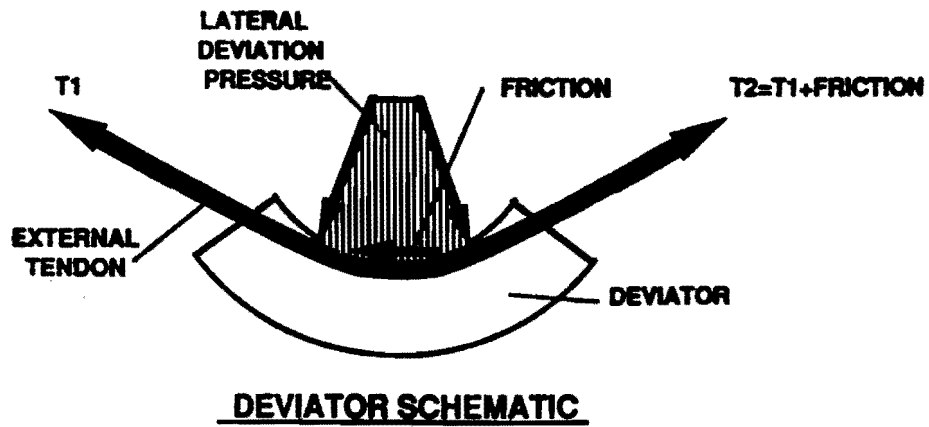


Figure 7.1 Beam and Suspension Systems

lateral deviation pressures. The friction force combines with the lateral pressure to induce a high surface shear on the strand wires that are in contact with the deviation hardware. Figure 7.3 shows the state of stress in an element of the strand in contact with the deviation hardware. As the lateral deviation stresses are increased with high curvatures or multiple strands, for example, the magnitude of the maximum



FRETTING CONCERN

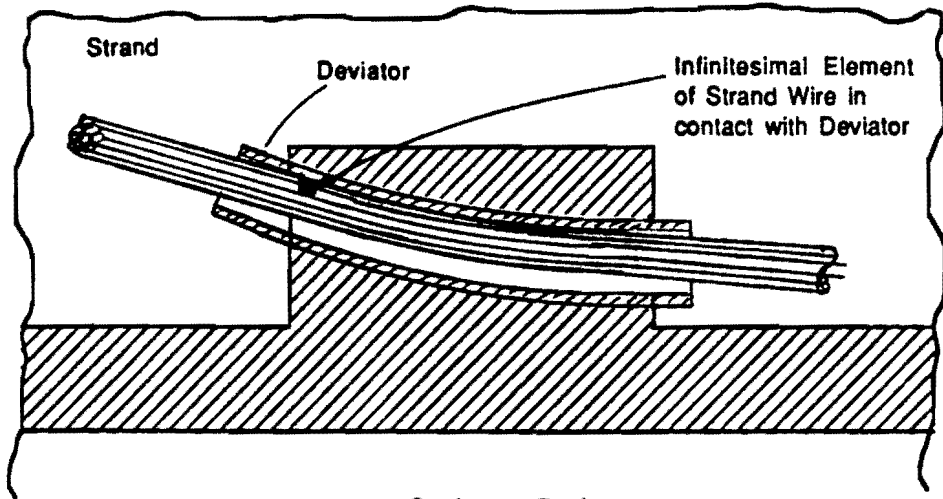
- HIGH LATERAL PRESSURE
- SURFACE SHEAR
- SLIP POTENTIAL

Figure 7.2 Deviator Force Components

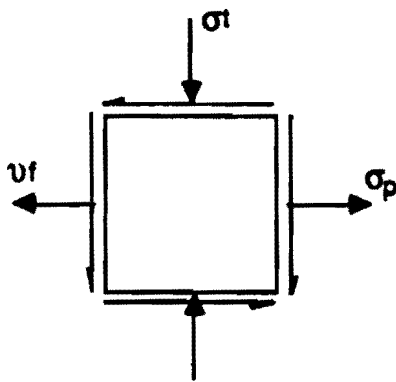
shear stress also increases. The magnitude of the maximum tensile stress remains constant.

The fretting problem is further aggravated by slip at the deviators, perhaps caused by the occurrence of a previous overload or inadvertent cracking. Slip was noticed in both exterior spans at approximately twice the load required for decompression. Once slip has occurred at a grouted deviator, then bond is lost and the potential for further slip is increased.

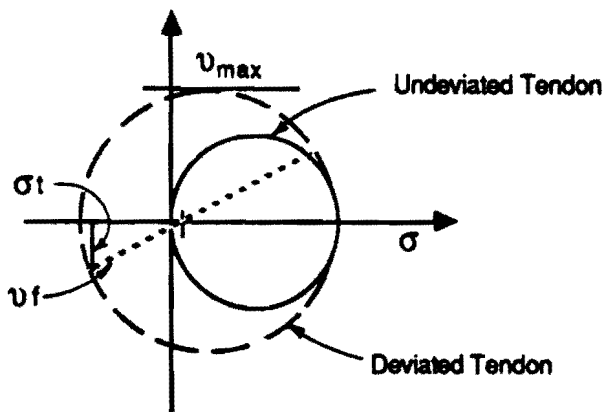
7.1.2 Factored Load Behavior. After completing the service load tests the three-span structure was loaded with additional weight to simulate the factored dead load condition of $1.3 \cdot DL$. Each of the exterior spans of the structure was then individually loaded with the factored design live load plus impact, $2.86 \cdot (LL+I)$. Factored load tests were not conducted on the interior span.



a. Section at Deviator



- σ_p = tendon stress
- σ_t = lateral deviation stress
- ν_f = shear stress from friction forces
- $\approx \mu \cdot \sigma_t$



b. Stress Condition

Figure 7.3 Stress Condition for Strand in Contact with Deviator

The structure behaved linearly throughout the load cycle with a slight reduction in stiffness when midspan joints decompressed. At these higher load levels the measured maximum factored live load deflections, as determined in different load cycles, were $L/1764$ for the dry-jointed exterior span and $L/2310$ for the epoxy-jointed exterior span. In this case the deflections in the dry-jointed span were approximately 25 percent more than in the epoxy-jointed exterior span, with the difference caused by the reduced effective cross-section in the dry joints and the tensile capacity in the uncracked regions of the epoxied joints.

The factored-load tendon-stress increases in the midspan region of the loaded span were measured to be less than 5 ksi in both exterior spans. The tendons did not appear to slip at the deviators for any of the factored load cycles.

7.1.3 Ultimate Flexural Behavior. The applied load is plotted versus the resultant midspan deflection for the ultimate load test of the dry-jointed north span in Fig. 7.4. The deflections represent the net deflection of the structure, after adjustment for support deflections at the location shown on the schematic. The deflections increase linearly with applied load up to the decompression load, P_d . As the midspan joints begin to open, stiffness reduces, and deflections increase at an escalating rate. The stiffness continues to decrease until the support joint opens and a mechanism forms. For load levels higher than the "mechanism load", P_m , the stiffness remains relatively constant with slight decreases as the ultimate strength is approached. The reduction in stiffness beyond the mechanism load is due primarily to slip in the external tendons at deviators.

The measured deflected shape of the three-span structure with factored dead load ($1.3*DL$) and increasing levels of applied load are shown in Fig. 7.5. At the applied service live load, $1.0(LL+I)$, and the applied factored design load, $2.9(LL+I)$, the deflections are small and the deflected shape appears as a smooth curve. The deflected shape remains smooth until the midspan joints open widely at $3.0(LL+I)$. Beyond this load, "hinging" occurs at the midspan joints, and the midspan deflections increase considerably. When the support joint opens at $4.8(LL+I)$ the mechanism forms and deflections begin to increase very rapidly. Due to reduced flexural requirements, the center span has less post-tensioning than the exterior spans. The support joint therefore opened on the interior side of the interior pier segment. The

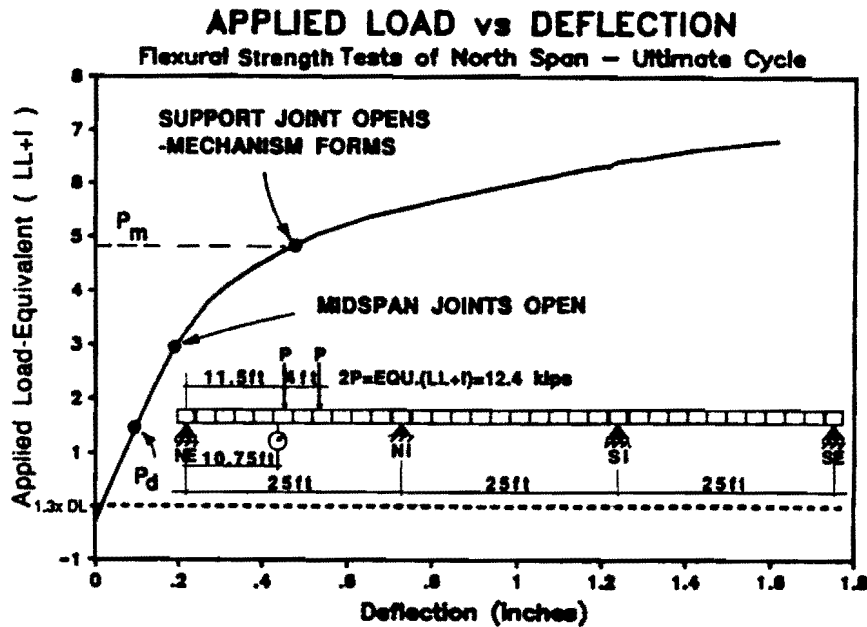


Figure 7.4 Stages of Flexural Behavior

final deflected shape of the structure clearly illustrates the mechanism behavior of the structure at ultimate load levels.

In section 5.2 a plastic mechanism analysis was conducted for each test load case. The plastic hinge capacities were calculated using first, the ACI formula for unbonded tendon stresses, and second, the tendon yield stress. The calculated mechanism capacity is dependent on the hinge capacity used. Using the ACI formula, the calculated mechanism capacity underestimated the measured capacity within 15 percent. Using the tendon yield stress, the calculated mechanism capacity overestimated the measured capacity by as much as 35 percent.

7.1.4 Shear Behavior. The local behavior of the segments near an opening joint was affected by the amount of shear that was being transferred across the joint. In the flexural tests, with the load applied as a series of forces along the longitudinal axis of the structure, small shears were transferred across the critical opening joints. In this case the concentrated rotations occurred either at the joints in the dry span or at a crack adjacent to a precast joint in the epoxied spans. At ultimate load levels

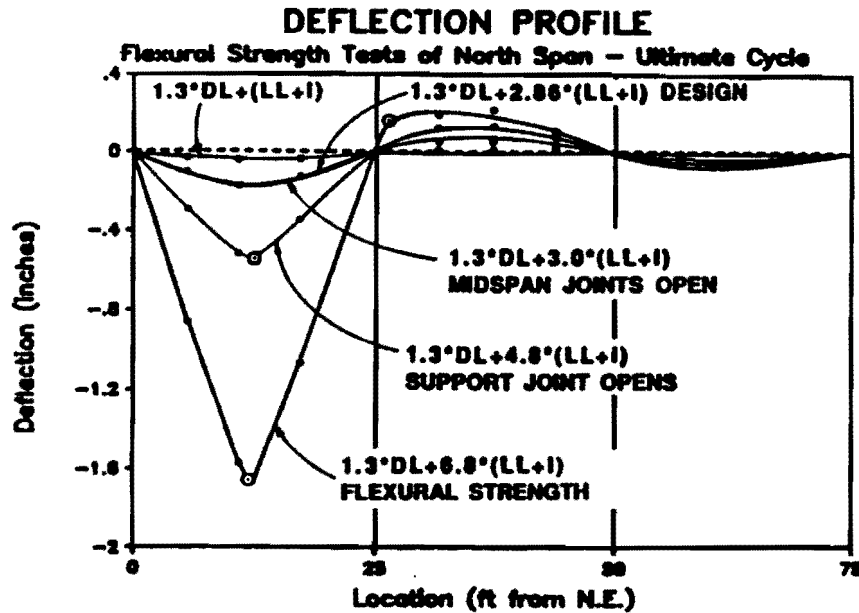


Figure 7.5 Ultimate Deflection Profile

the joint/crack had opened into the top flange of the girder in both the dry-jointed and epoxy-jointed spans.

The local force transfer mechanism in the segments adjacent to the opening joints or cracks when flexural strength was reached is shown schematically in Fig. 7.6a. The joint/crack had opened into the top flange causing the load to arch across the segment joint. The small shears that were transferred across the open joints at this stage were carried by the vertical component of the "arch force" at the joint. The segment reinforcement transferred the shears from the load point to the edge of the segment, and then the arch action transferred the force across the joint.

In the shear tests, a concentrated force was applied to the structure so that significant shear would be transferred across opening joints or cracks. The ratio of shear at joint (5,6) during the flexural and shear tests was approximately 2.5:1. In this case after the joint had opened up through the bottom flange, an inclined crack formed from the load point to the bottom of the web at the edge of the segment, as shown in Fig. 7.6b. As load was increased to ultimate levels, the concentrated

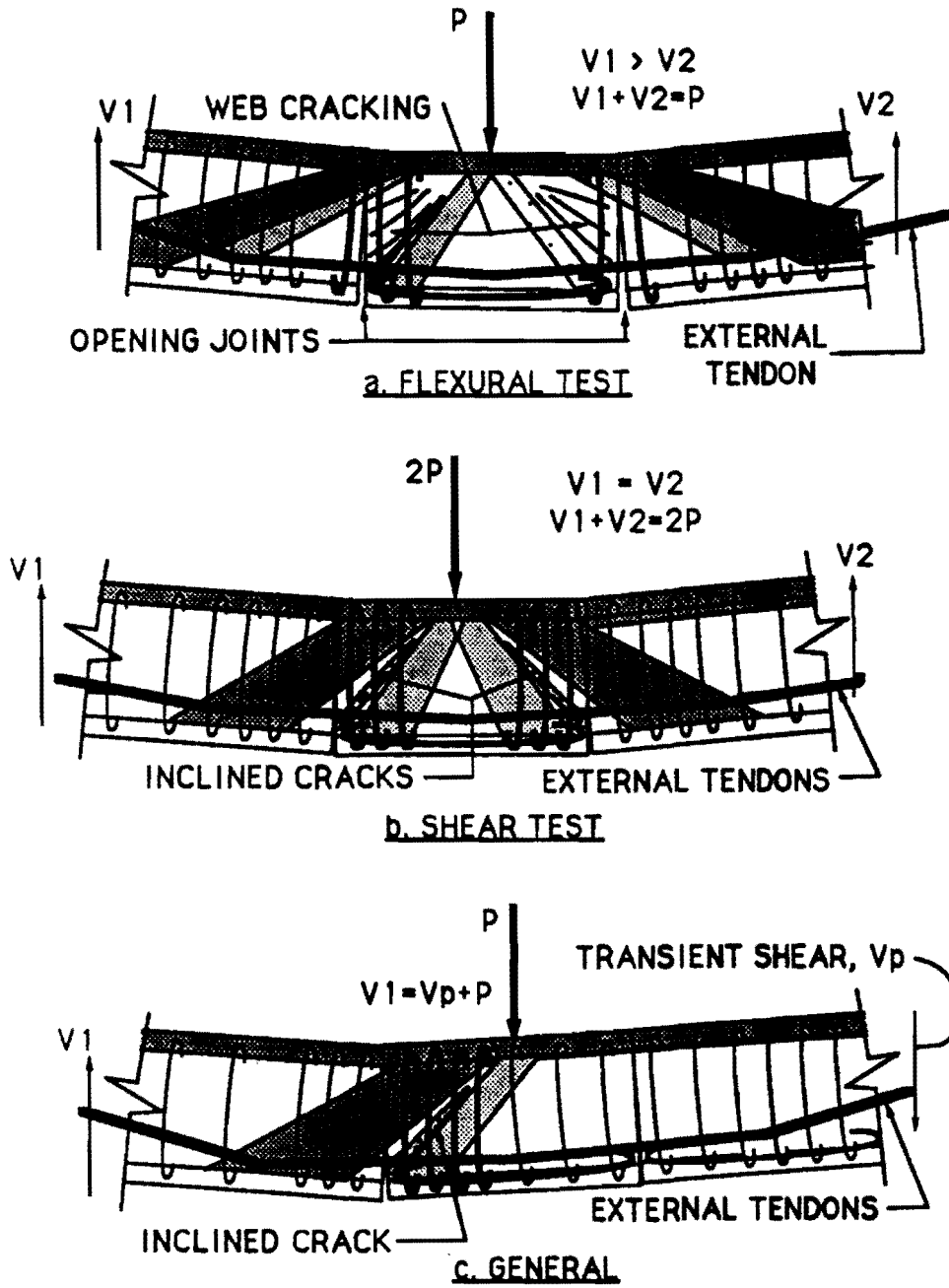


Figure 7.6 Shear Mechanisms at Opening Joints

rotations occurred at the inclined crack leaving the joint region in firm contact. This was true for both the dry-jointed and the epoxy-jointed spans.

The local force transfer mechanism in the segments adjacent to the opening joints/cracks when capacity was reached is also shown in Fig. 7.6b. A compressive strut formed from the load point to the lower corner of the segment. The segment web reinforcement transmitted this force across the inclined crack to the top of the segment. The shear force was then transferred across the joint utilizing much of the web depth.

The reinforcement for the concrete segments near opening joints must be properly detailed to allow the large rotations required for tendon stress increases. Local truss mechanisms, such as shown in Fig. 7.6c, should be developed for the critical segments to ensure that the shear transfer can be made across the joints. The bottom longitudinal reinforcement must be anchored close to the opening joint and must resist the horizontal component from the transient shears (Fig. 7.6c) plus the force in an inclined strut aligned between the load point and the bottom corner of the segment. The web reinforcement must be able to resist the transient shear from global loads plus the vertical component of the force in the inclined strut. The web reinforcement must be anchored under the bottom longitudinal reinforcement and high in the section so that anchorage is maintained when the neutral axis shifts to the top flange of the segment.

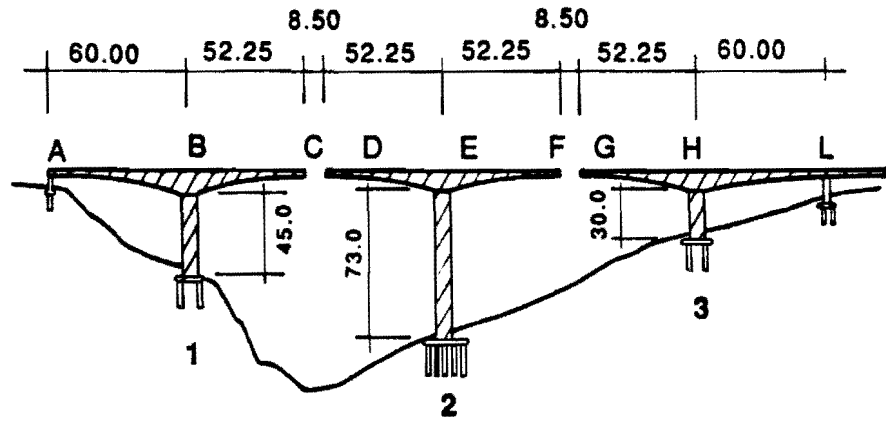
7.1.5 Ductility. Ductility of a structural member or system was defined by Naaman (24) as "a measure of the ability of a material, section, structural element, or structural system to sustain inelastic deformation prior to collapse, without substantial loss in resistance." Ductility is important in structural members so that warning is provided to the occupants of the structure of a possible impending failure. Brittle behavior in which ultimate failure occurs suddenly with little or no warning should be avoided in structural elements or systems.

The use of unbonded reinforcement in structural concrete can present a serious problem with respect to ductility. Because the reinforcement is not bonded to the concrete section, tendon elongations are distributed over the entire free length of the tendon. Large concentrated rotations and deflections are required for increases in tendon stresses.

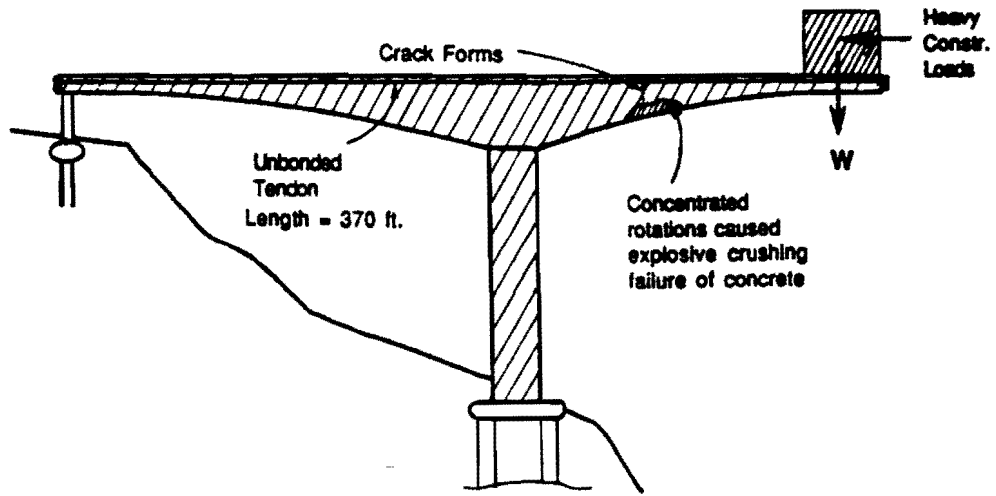
The following example illustrates the critical importance of ductility in unbonded systems. The structure shown in Fig.7.7a (25) was constructed by the balanced cantilever method. During construction, heavy loads were applied to the end of the cantilever which caused flexural cracking to occur at the location shown in Fig. 7.7b. After the concrete section cracked, the forces that were previously carried by tension in the concrete were transferred to the post-tensioning tendon. Because the internal tendons had not yet been grouted, the elongations required for increased tendon strain (and stress) were averaged over the entire length of the unbonded tendon. Large rotations were therefore necessary at the cracked section to develop the required tension forces. The large rotations caused the compressive stresses to concentrate in the top flange until the concrete exploded catastrophically and the segments dropped to the ground.

This example illustrates two important ductility considerations for unbonded tendons in structures. First, details should be provided to ensure that plastic hinges form in a ductile manner (25). This can be achieved by a number of methods, all of which involve providing bonded reinforcement at all locations in the structure. This requirement is especially critical in the case of single hinge mechanisms such as the cantilevered bridge example described. Further, formation of multiple-hinge mechanisms in redundant structures can lead to redistribution of loads and increased capacity. Second, if the moment capacity is less than the cracking moment, then an additional factor of safety on the required capacity should be provided.

Two general types of ductility are important for structural elements, global ductility and local ductility. In a global sense the structure should be able to withstand large deflections before strength is reached. In addition, the structure must have reserve capacity beyond load-levels that cause noticeable distress in the structure (cracking and/or large deflections). In a local sense, the structure must be able to withstand the necessary distortions required for global ductility. For unbonded systems, large concentrated rotations are required to develop increased tendon forces. The concrete in the vicinity of the "plastic-hinge" must be detailed properly to ensure that these large rotations can occur. Confinement of the concrete in the compressive zone at a hinge will allow higher ultimate concrete strains and larger induced



a) Condition of Bridge Prior to Collapse



b) Failure Condition

Figure 7.7 Bridge Collapse During Construction

rotations. In segmental construction, proper anchorage of the tension flange reinforcement in the segments will allow larger concentrated rotations at the critical opening joint.

The inherent flexural strength of the structural system is best reflected by examining moments at midspan. The midspan service load moments (DL+LL) are compared with the midspan ultimate load moments ($1.3DL+6.8(LL+I)$ or $1.3DL+7.7(LL+I)$) in Table 7.2. The difference between the ultimate applied-load moment in the dry and epoxy-jointed spans is caused primarily by a difference in the effective prestress in the two spans (see Section 7.2.2). Two indices of behavior are defined below:

Table 7.2 Factor of Safety and Safety Margin
Service and Ultimate Level
Midspan Moments

		Dead Load	Applied Load	Midspan Moments	
				Dry Joints	Epoxyed Joints
D	Dead Load	DL	0	101	115
S	Service Live Load	0	(LL+I)	50	48
Df	Factored Dead Load	0.3*DL	0	30	34
u	Ultimate Applied Load	0	6.8*(LL+I)	250	—
		0	7.7*(LL+I)	—	340
$\frac{D+Df+u}{D+S}$	Factor of Safety	—	—	2.5	3.0
$\frac{Df+u}{S}$	Safety Margin	—	—	5.6	7.8

1. The Factor of Safety is defined as the total ultimate moment divided by the total service load moment. The factor of safety exceeded 2.5 in the test structure. This means that the ultimate midspan moment was more than 2.5 times the midspan service-level moment.
2. The Safety Margin is defined as the ratio of the ultimate midspan applied-load moment to the service midspan applied-load moment. The safety

margin indicates the number of live-load multiples that can be applied to the structure above the service load condition. The safety margin was more than 5.6 for the model structure. The apparently large difference between the dry and epoxy spans is again due primarily to the larger effective prestress in the epoxy-jointed span.

7.2 Estimation of Insitu Forces

In order that conclusions can be drawn from the test data it is necessary to estimate the condition of the structure before testing. The concrete stress condition in the completed structure at the start of testing is a function of the sequential construction method. The analysis, described in Chapter 5, determined the final forces in the concrete by estimating the equivalent prestress forces from the measured tendon data and then applying these forces to the model structure. The construction process was tracked in a segmental manner with the equivalent prestress forces applied at each step of construction. Losses were accounted for by applying equivalent forces in the opposite direction. The analysis represents the best estimate of the forces which existed in the structure at the start of testing.

To provide a base for tendon stress increases, the effective prestress forces must also be determined. The effective prestress forces can be estimated from the decompression moment if the insitu dead load condition and the concrete section properties are known. This information can also be used to calibrate the analysis if the effective prestress is too dissimilar from the values used in the analysis.

7.2.1 Insitu Dead Load Forces. The reactions and moments from the analysis are compared with the reactions and moments measured with the load cells in Table 7.3. The analysis shears agree closely with the reactions measured at the north end of the structure. The measured reactions were adjusted as described in Section 4.4. At the south end of the structure, the analysis differs from the measured reactions by approximately 9 percent at the interior support and 6 percent at the exterior support. Because of the highly redundant system, a closure of less than 10 percent is considered acceptable.

7.2.2 Effective Prestress Forces at Critical Joints. A primary variable for estimating the ultimate strength of an unbonded system is the stress that exists in

Table 7.3 Insitu Dead Load Forces

Location	NEP	NEP	3:4	4:5	5:6	6:7	NIP	NIP	NIP	NIP	15:16	SIP	SIP	SIP	SIP	24:25	25:26	26:27	27:28	SEP	SEP	Units	
x:	0	0	8	10.3	12.5	14.8	24	25	25	26	37.5	49	50	50	51	60.3	62.5	64.8	67	75	75		
Dead Load Forces:																							
Analysis Shear (DL+PS2)	-1	18.0						-25.	23.0				20.	23.7							-20.	1	kips
Measured Reactions		19.5							49.6					40.2								22.4	kips
1.3* (Analysis Shear)	-1.3	23.4						-33.	29.9					-26.	30.9						-26.	1.3	kips
Analysis Moments (DL+PS2)	-5	-5	93.4	99.4	96.2	83.8	-64.	-89.	-89.	-66.	71.1	-32.	-51.	-51.	-28.	107.	116.	116.	106.	-5	-5	ft-kips	
Measured Moments			97.6	105.	103.	91.4				-60	99.5	19				133.	138.	134.	121.			ft-kips	
1.3* (Analysis Moments)	-6.5	-6.5	121.	129.	125.	109.	-84.	-116	-115	-86.	92.5	-41.	-67.	-67.	-36.	139.	151.	151.	138.	-6.5	-6.5	ft-kips	

the tendon prior to loading the structure. The effective prestress should therefore be calculated for the model structure so that the strength prediction equations can be verified.

The total force in the prestressing tendons can be determined from the moment that causes decompression because the stress at the extreme fiber is known to be zero. The concrete stress resulting from application of the decompression load can be determined from the change in prestress forces and the change in forces resulting from applied load. If the change in prestress force is assumed to be small compared to the effective prestress force, and axial forces from loading are assumed to be zero, then the effective prestress force can be calculated. The effective prestress force is therefore estimated as the ratio of the stresses caused by dead loads, secondary prestress forces, and applied loading to an index which depends on the concrete cross-section and the tendon eccentricity. Note that the tendon eccentricity must include all the tendons crossing the joint.

Table 7.4 summarizes the calculation of the effective prestress forces at each midspan region and also at the interior face of the interior supports. Also shown is the average tendon stress at each location as determined from the tendon strain data. The tendon strain data were used for calculating the equivalent prestress forces for the analysis.

The effective prestress force from the decompression load agrees reasonably well with strain data for the midspan regions of the center and south spans. For the north span however, the decompression load yielded an effective prestress force that was considerably less than was determined from the tendon strain data. During testing, the north span decompressed at a lower load level than in the similar south span, which tends to verify the difference in the calculated effective prestress forces. This indicates that the equivalent prestress force in the north span may be less than was used for the analysis. The result of this is to increase the dead-load deflection in the north and south spans and decrease deflections in the center span.

The effective prestress force was also calculated at the opening joint on the interior face of the interior pier segment. In these cases, the magnitude of the decompression moment at the critical joint was determined from the factored dead load moment plus the applied load moment. These joints did not open until very

Table 7.4 Calculation of Effective Prestress Forces

Location:	5:6	11 NF	15:16	20 SF	25:26
x: (ft)	12.5	26	37.5	49	62.5
Ac: (in. ²)	450	450	450	450	450
S. top: (in. ³)	2512	2512	2512	2512	2512
S. bot.:	1757	1757	1757	1757	1757
(Ap) ext (in. ²)	2.04	1.53	1.53	1.53	2.04
(Ap) int	.68	.68	.68	.68	.68
(Ap)	2.72	2.21	2.21	2.21	2.72
(e) ext (in.)	6.01	-1.4	6.04	-1.4	6.01
Corrected (e) ext	5.76	-1.4	5.79	-1.4	5.76
(e) int	-5.35	-5.35	-5.35	-5.35	-5.35
(e) eff	2.983	-2.62	2.362	-2.62	2.983
(A) = $(\frac{1}{A_c} + (\frac{e}{S}))$.0039	.0033	.0036	.0033	.0039
Dead Load Moments (M_d)					
Analysis Moments	96.19	-66.1	71.14	-31.5	115.9
Measured Moments (from reaction data)	102.6	-60	99.51	19	137.9
1.3* Analysis Moments	125.1	-85.9	92.48	-41.0	150.6
1.3* Measured Moments	133.4	-78	129.4	24.7	179.3
Decompression Load Moments (M_d)					
Load Case	PDNd	PUNd	PDCd	PUSd	PDSd
Analysis Moments	91.5		90.2		129
Measured Moments	92	-190	90	-230	130
(B) = $\frac{(M_{d1}+M_d)}{S}$					
Analysis	1.282	-1.32	1.102	-1.29	1.672
Data	1.329	-1.28	1.294	-0.981	1.830
Tendon Force and Stresses					
$T_{pd} = \frac{(B)}{(A)}$					
Analysis	327.0	403.8	308.9	396.7	426.7
Data	339.1	392.3	362.9	300.5	466.8
$f_{pd} = \frac{T_{pd}}{A_p}$ (ksi)					
Analysis	120.2	182.7	139.8	179.5	156.9
Data	124.7	177.5	164.2	136.0	171.6
f _{pd} -f _{pe} (ksi)	2.4	1	2	1	2.4
f _{pe} (ksi)					
Analysis	117.8	181.7	137.8	178.5	154.4
Data	122.3	176.5	162.2	135.0	169.2
AVG =	120.0	179.1	150.0	156.7	161.8
f _{pe} Tendon Strain Data Average Stress (ksi)	143.6	140.1	147.1	155.3	157.1

high loads were applied, and the exact magnitude of the moments was not as easily determined.

7.2.3 Service Load Tendon Stresses. A calculation procedure was presented in Chapter 1 for determining the service load tendon stresses. To calculate the tendon stress range the Curvature-Eccentricity diagram, $(M/E_c I_c) * e$, is plotted for all locations along the tendon. The elongation of a tendon between two anchored points is the area under the Curvature-Eccentricity diagram between the anchorages. The tendon strain is calculated by dividing the calculated elongations by the tendon length between the two anchorages.

The question arises as to what effective length should be used for calculating the service load tendon stresses. If no slip occurs at the deviators then the free length over which the tendon elongates is limited to the length between adjacent deviators. If no friction exists between the tendon and the deviator then the tendon can slide freely, and the elongations are averaged over the entire tendon length between the anchorages. From the test results the tendons did not begin slipping until load levels well above the service load condition. This was true for all load cycles including those in which the tendon had slipped during previous load cycles. The free length of tendon should therefore be taken as the length between adjacent deviators for calculation of the service load response. This is a conservative approach since this is the shortest free length that the tendon can have, and will lead to the largest service-load stress range.

The service load tendon stresses for the three tendons in the north span are calculated for the model bridge structure by integrating the Curvature-Eccentricity diagram between adjacent deviators. Since each tendon has a different profile and deviation locations, the service load stresses must be calculated separately for each tendon. The service-load tendon stress ranges are shown in Fig. 7.8 for each of the tendons of the north span. The measured stress ranges are also shown for comparison, and they agree closely with the calculated stresses at the support region, and were slightly less than calculated for all midspan locations.

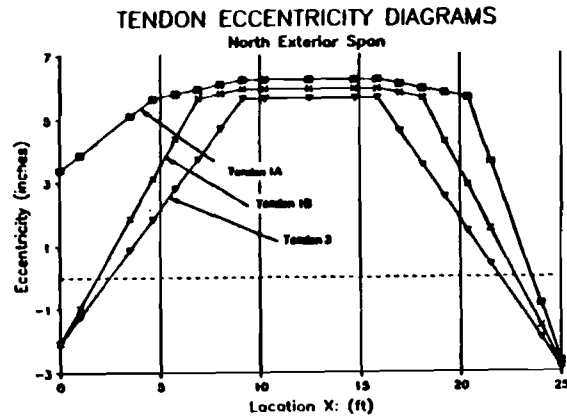
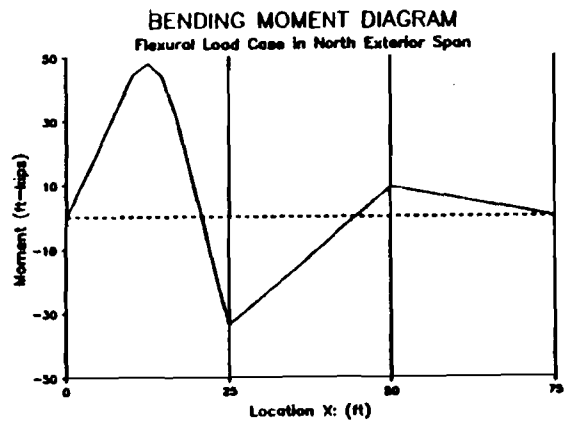
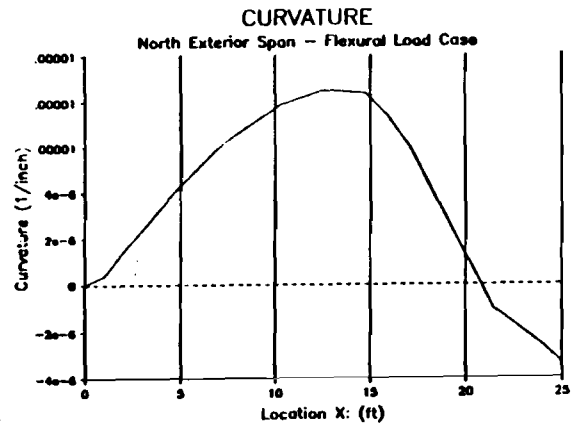
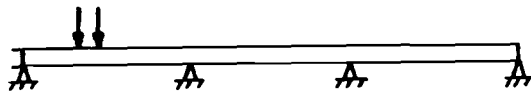


Figure 7.8 Service Load Tendon Stresses

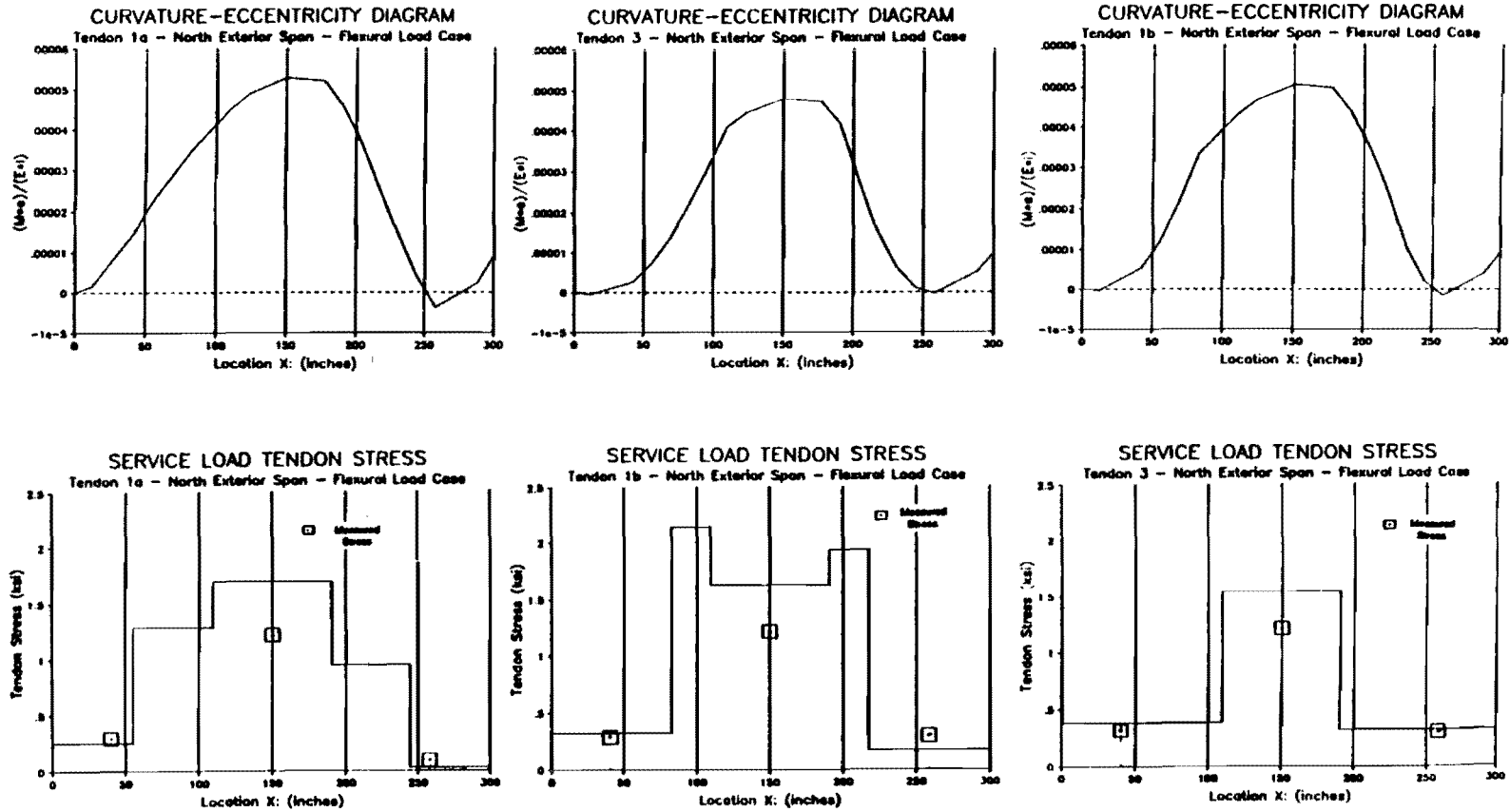


Figure 7.8 Service Load Tendon Stresses - continued

7.3 Effect of Epoxy on Model Behavior

7.3.1 Effect of Epoxy on Construction. The epoxy application process during erection of the center and south spans revealed several practical considerations concerning the handling of epoxy joining material. The epoxy should be delivered in clearly labeled, premeasured quantities of each component so they can be mixed directly without site measurement of quantities. This will ensure that the proper mix proportions are used and a minimum of material is lost in the mixing process. The epoxy supplier should also provide information regarding the necessary storage conditions and mixing techniques. In addition, the contractor should be experienced with epoxy and be able to recognize substandard materials.

A common argument for the use of epoxy in segmental construction is that it provides lubrication during closing of the match-cast faces. With the small segments of the model structure, lubrication did not appear to be necessary in the dry-jointed span of the structure. The matching faces were moistened with a cloth during closing. Lubrication during closing may be a more severe problem for full-size segments, however.

Finally, the epoxy application process must be planned carefully to ensure that all necessary tasks are completed within the usable life of the epoxy. The epoxy pot-life serves as a maximum time limit for completion of: epoxy measuring and mixing, application of the epoxy to both surfaces of a match-cast joint, joint closure, temporary post-tensioning, and cleaning of the epoxy from tendon ducts and equipment. Time studies were conducted to estimate the necessary manpower and the proper staging of the various tasks. The procedure was also practiced and timed during closing of the dry-jointed north span.

7.3.2 Effect on Service Load Behavior. A primary purpose for using epoxy at segment joints is to provide reserve capacity against joint opening for overload conditions. The cracking load and decompression loads for the two epoxied spans of the model structure are compared in Table 7.5. In each case cracking occurred through the concrete adjacent to a midspan match-cast joint at approximately twice the applied load required to decompress the flexural tension fiber and cause the cracked epoxy joint to begin to open. If zero tension is used as the limit for service

Table 7.5 Cracking and Decompression Loads

Cracking Loads in Epoxy Jointed Spans		
	Center Span	South Span
Cracking Load	DL+5.2 * (LL+I)	DL+5.4 * (LL+I)
Decompression Load	DL+2.4 * (LL+I)	DL+2.6 * (LL+I)
$\frac{\text{Cracking} - \text{DL}}{\text{Decompression} - \text{DL}}$	2.2	2.1

behavior, then the epoxy joints provided a potential factor of safety against joint opening of approximately 2.

In setting design criteria, however, it should be realized that the true factor of safety against cracking might be less than this because of traffic overloads, calculation inaccuracies, actual insitu epoxy behavior, and fatigue behavior of the concrete/epoxy joint. It would therefore be prudent to specify a small residual compressive stress in the extreme tension fiber for epoxy-jointed segments without bonded reinforcement crossing the joint. In dry joints without bonded reinforcement crossing the joint the beneficial tensile capacity offered by the epoxy is not present, so higher design residual compressive stresses are recommended.

7.3.3 Effect on Factored Load Behavior. In the epoxy-jointed south span the factored design load was less than was required to crack the span. The governing design criterion for the tendons of the model structure was the service load concrete-stress condition. Prestress was provided to induce a residual compressive stress in the extreme fiber where tensile stresses are caused by applied loads, as described in Section 2.1.3. The calculated extreme-fiber stresses for the dead load and service load conditions at the start of testing are plotted with respect to location along the structure in Fig. 5.10. The minimum residual compressive stresses under service load conditions were slightly greater than the PTI proposed limits for dry or epoxy joints without bonded reinforcement (see Table 2.2). In meeting the stress condition for design, significantly more prestress was provided than was required for ultimate strength. This was possibly aggravated in the model structure since the ratio of eccentricity to the distance from the neutral axis to the tension fiber (e/Y_b) was

less than the corresponding prototype value, thus reducing tendon efficiency with respect to stresses.

With the large reserve in ultimate strength, it would appear that smaller design stresses could be specified. This however would have a direct impact on the cracking load, thus reducing the factor of safety against cracking.

7.3.4 Effect on Flexural Strength. The primary influence of epoxy joints on the ultimate flexural behavior of the system was to concentrate the midspan rotations required for increased tendon stresses at a single joint. In the dry-jointed span, several midspan joints opened causing the rotations to be distributed over several joints. In the epoxy-jointed span, a single joint/crack opened causing the large rotations to be concentrated at a single location. If the ultimate strength is limited by the maximum rotation that can occur at a concrete-hinge, then the dry-jointed span may be able to withstand larger cumulative midspan rotations than the epoxy-jointed span. This may lead to a slightly higher ultimate flexural strength for spans with dry joints.

7.3.5 Effect on Shear Strength. As previously discussed in Section 7.1.4, the shear behavior at an opening joint was a function of the amount of shear crossing the joint, and was not noticeably affected by the epoxy. Under high shear the concentrated rotations required for increased tendon stresses occurred at an inclined crack with the match-cast joint region remaining in firm contact to transfer the shears. This behavior was similar for both exterior spans and has been subsequently investigated and confirmed by Ramirez (26).

One possible advantage of epoxy joints is that it provides a more direct flow of forces through the joint region. The shear transfer at the match-cast joint has the additional component of adhesion between the two matched faces. This component is in addition to the friction and shear key strength associated with dry joints.

7.3.6 Effect on Ductility. The epoxy did not provide any noticeable increase in ductility, and in some respects may cause some slight reduction. As was discussed earlier in Section 7.3.4, the epoxy tended to concentrate the hinge rotations at a single joint. This caused a severe strain gradient in the segments adjacent to the opening joint, and the ultimate capacity is limited by the maximum crushing

strain in these segments. If the hinge rotations are distributed to several joints, as for dry joints, larger total rotations may be possible with the same limiting strain gradient. The larger rotations would lead to larger deflections and more warning of impending failure.

Another reason that epoxy may reduce ductility was discussed earlier in Section 7.1.5. The epoxy prolongs elastic behavior until the tensile stress exceeds the modulus of rupture of the concrete or the tensile capacity of the epoxy joint. If the load that causes cracking is larger than the flexural strength of the system, then failure will occur suddenly with no warning. This form of brittle behavior requires direct treatment during the design process. If epoxy is used at segment joints, and the moment capacity is less than the cracking load, then additional factor of safety on the required capacity should be provided.

7.4 Flexural Strength Model

A structural member resists applied bending moments by an internal force couple between a compressive force, C , and a tension force, T , separated by a known lever arm, Z_p , as shown in Fig.7.9. For horizontal equilibrium of a beam member, the magnitude of C and T must be the same. Therefore, to predict the flexural capacity of a beam it is necessary to estimate either the maximum resultant concrete compressive force or the maximum tendon force and the distance between these two equal and opposite forces.

In a bonded-tendon girder the tendon strains are assumed to be compatible with the adjacent concrete, and as a result the tendon undergoes large strains. If the girder is detailed so that the tendons yield prior to failure, by specifying a maximum reinforcement ratio for example, then the simplest method for determining the ultimate flexural strength is by predicting the stress in the tendon when the ultimate strength is reached. This is the approach that is commonly taken for bonded-tendon girders.

In an unbonded-tendon girder, the tendon strains are not compatible with the adjacent concrete, and are instead averaged over the entire length of the tendon. In this case it is difficult to predict the tendon stress that corresponds with ultimate flexural strength. The tendon strains are a function of many different variables, all of

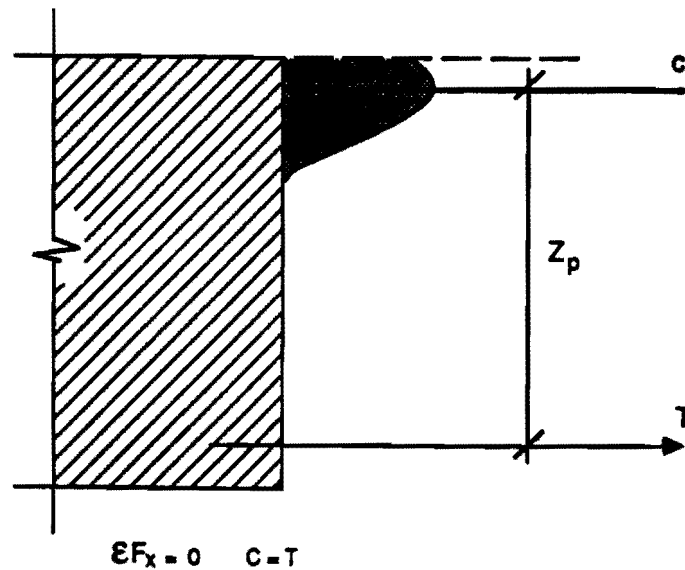


Figure 7.9 Flexural Model

which are difficult to predict and control during construction. The flexural behavior of unbonded systems is limited by the rotation capacity of the concrete at a plastic hinge. The tendon stress corresponding with ultimate flexural strength is therefore determined from the effective prestress in the tendons before applying load plus the change in tendon stress that occurs as the plastic hinges deform (open).

7.4.1 Observations from Load Tests. As loads are increased beyond service levels, the tendon stresses exhibit several stages of behavior, as shown in Fig. 7.10a. The concrete stress profile at the critical opening joint is shown in Fig. 7.10b for important stages of tendon stress development. Initially, before the joints begin to open, the tendon-stress increases are linearly related to the applied load. The tendon stresses remain linear until the neutral axis at the opening joint reaches the level of the tendon, Point B, at an applied load that is slightly greater than the decompression load, P_d . Beyond this load, the tendon stresses increase slowly at first as the increased moments are resisted primarily by an increased internal-force lever arm. When the resultant concrete compressive stresses are concentrated in the top flange of the section, Point C, then additional moments must be resisted by increased tendon forces. To develop the required tensile forces with

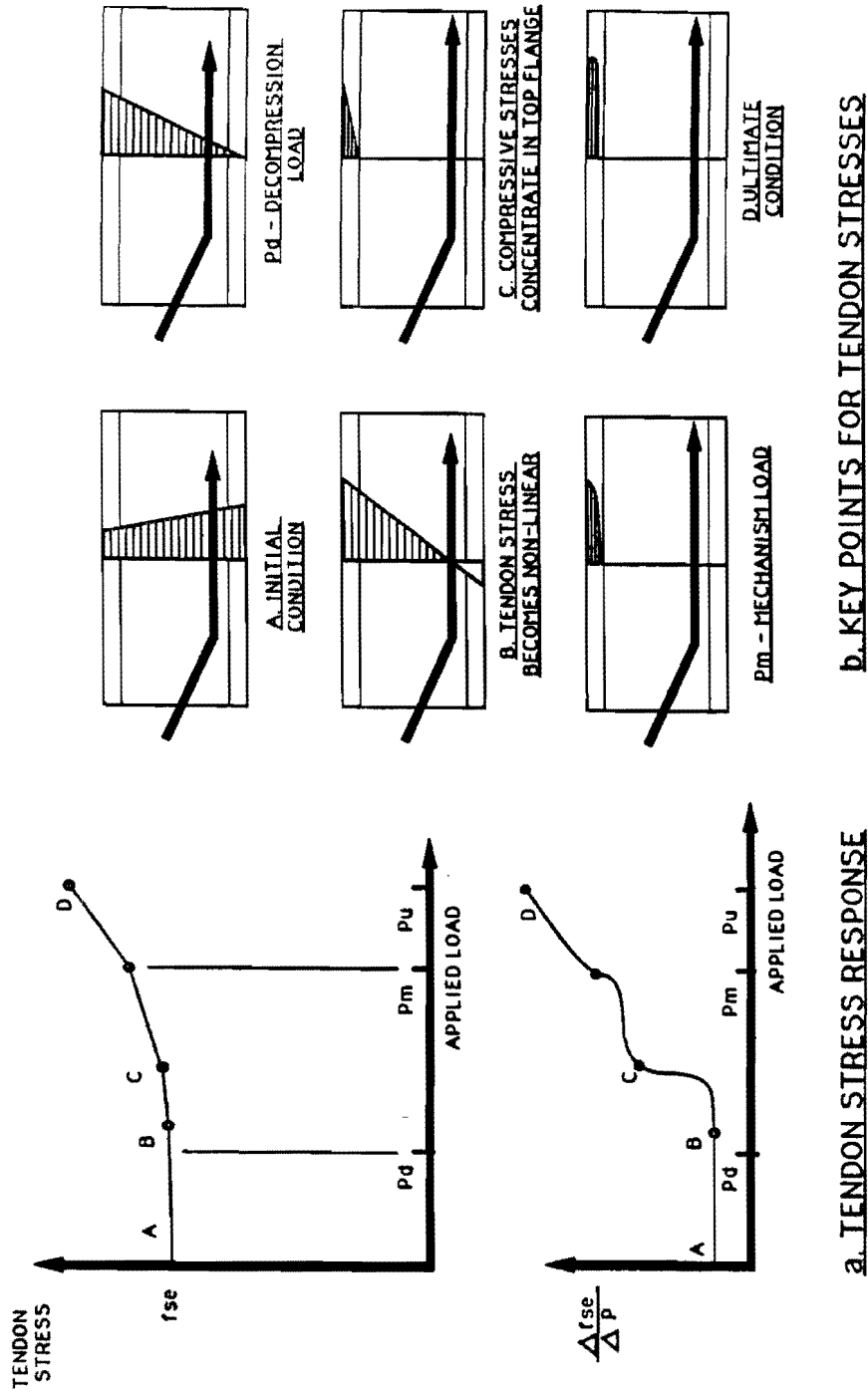


Figure 7.10 Tendon Stress Response to Applied Load

external tendons, large rotations must occur at opening joints resulting in increased deflections and joint openings.

The applied-load stresses for a typical tendon during the flexural strength load cycle for the north span are shown in Fig. 7.11. Tendon strain measurements were made at the exterior and interior ends of the span, joints (1,2) and (9,10) respectively, at midspan, and at joint (5,6). The midspan tendon stresses remained linear with applied load up to approximately $1.8(LL+I)$ when the concrete section had decompressed to the level of the external tendons. This load is slightly higher than the measured decompression load of $1.4(LL+I)$. The tendon stresses increased slowly at first until the midspan joints opened at $3.0(LL+I)$. At this load level the resultant compressive stress had concentrated in the top flange, and additional moments were resisted by a direct increase in tendon stress. Subsequently, as the support joint opened at approximately $4.8(LL+I)$, midspan moments increased and the rate of tendon stress development ($\Delta f_s/\Delta P$) also increased.

7.4.2 Factors Affecting the Unbonded Tendon Stress at Nominal Flexural Capacity

7.4.2.1 Effective Prestress Force. The effective stress in the prestressed reinforcement after allowance for all prestress losses, f_{pe} , is the most important parameter affecting the tendon stress at nominal strength. If friction losses are higher than expected during stressing, or the long-term relaxation and creep losses are higher than expected during the service life, then there is a direct reduction in the ultimate flexural strength. This dependency is clearly illustrated by comparing the ultimate flexural behavior of the two exterior spans of the model structure, as shown in Fig. 7.12. The load-deflection response of the two spans was virtually identical, except the south span response was offset by the difference between the decompression loads. As illustrated in Table 7.4, the effective prestress was higher in the south exterior span than in the north exterior span causing the decompression load to be lower for the north span. The difference in the decompression loads is approximately equal to the difference in the ultimate capacities. The effective prestress force, therefore, acts as a starting point from which the tendon stresses increase under applied loads.

CHANGE IN TENDON STRESS vs APPLIED LOAD

Flexural Strength Tests of North Span – Tendon 1b – Ultimate Cycle

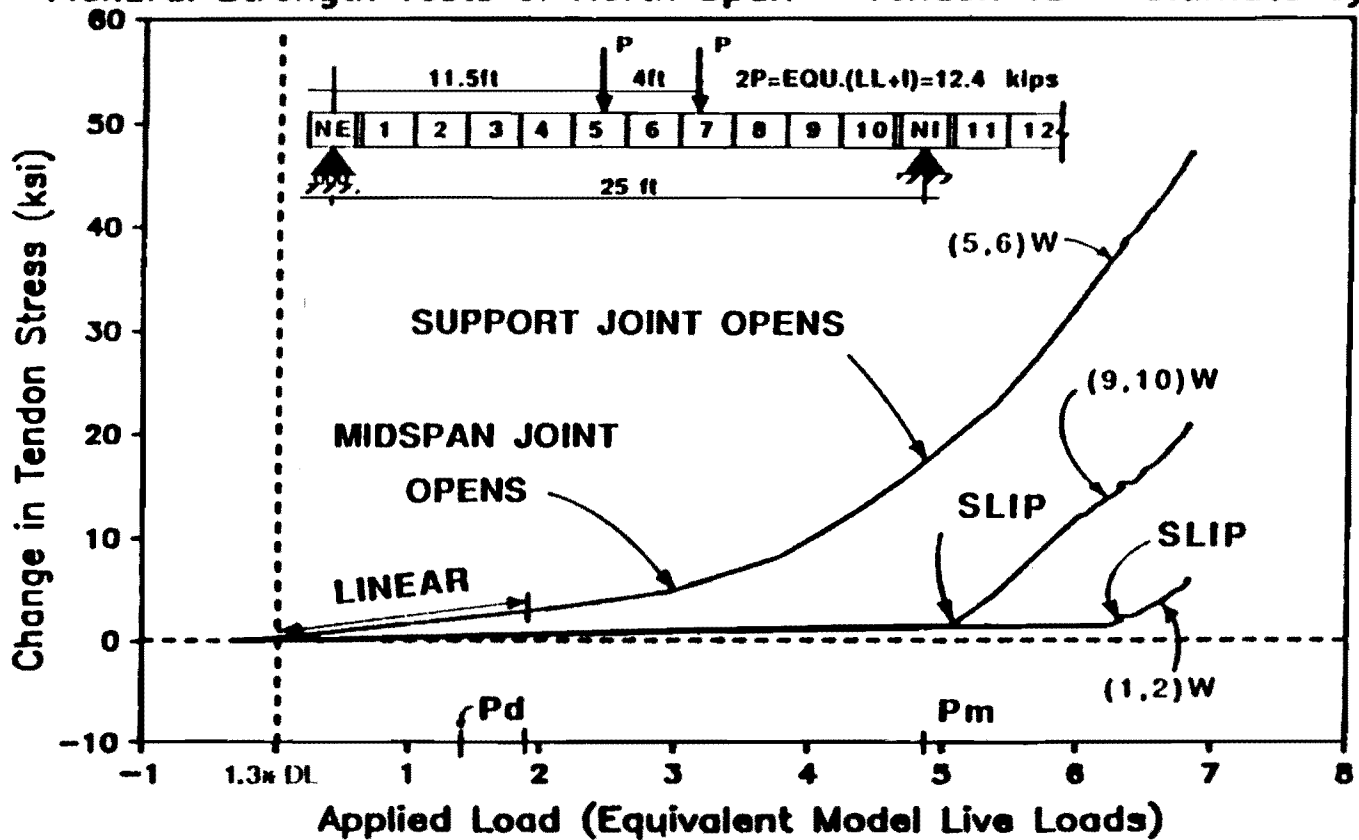


Figure 7.11 Typical Tendon Stress Response

Side Span Flexural Strength Tests

Applied Ram Force vs Midspan Deflection

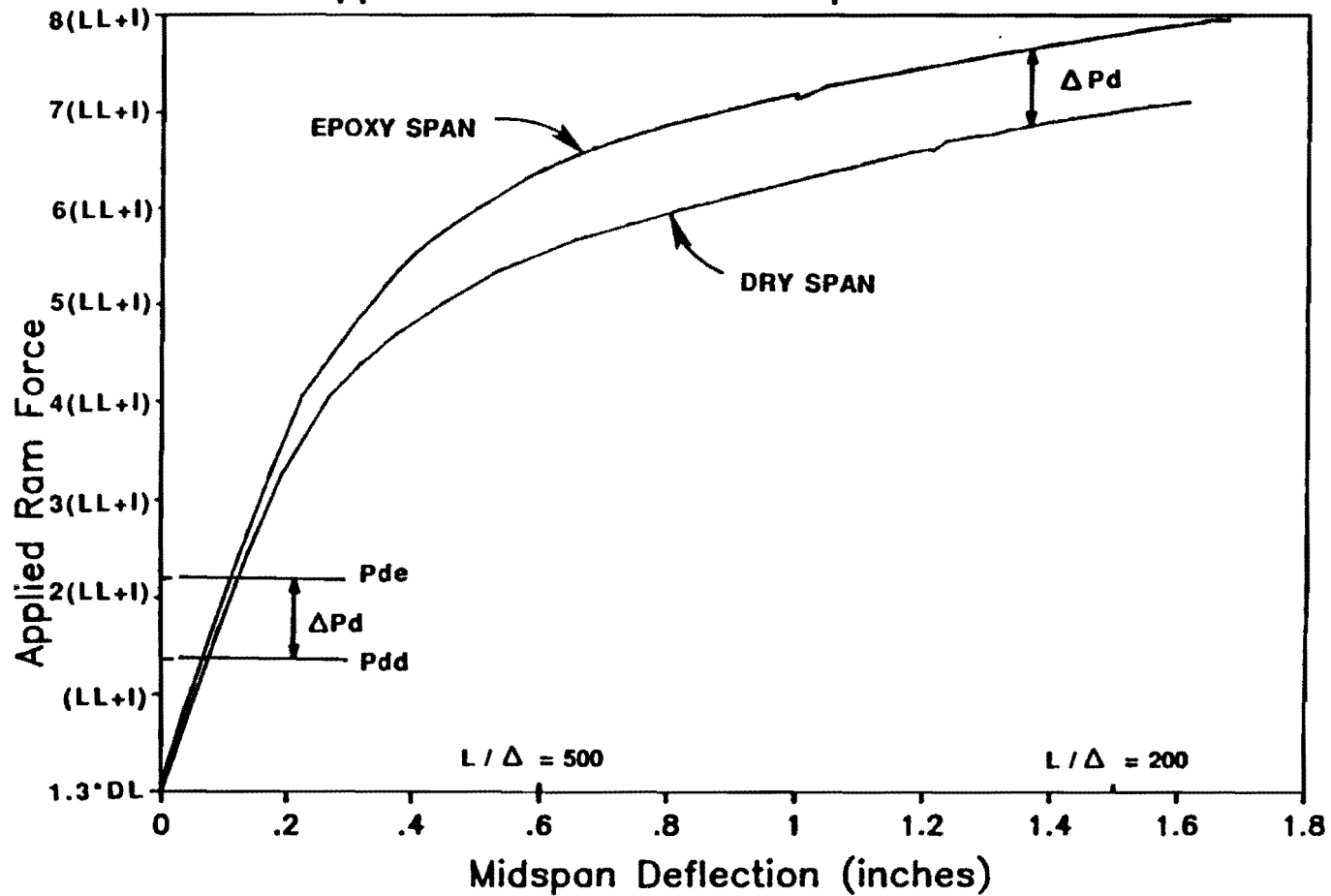


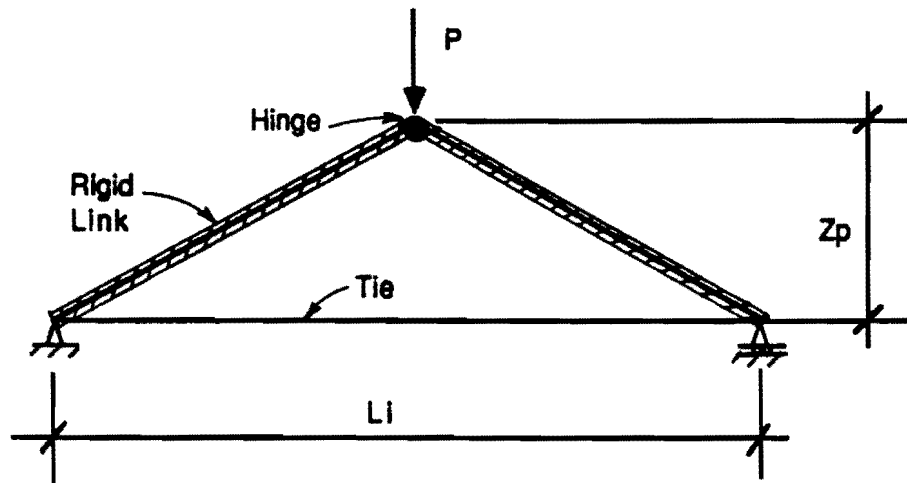
Figure 7.12 Comparison of Ultimate Flexural Behavior of Exterior Spans

7.4.2.2 Ratio of Prestress Depth to Tendon Free Length. The ratio of the plastic depth of the prestress to the free length of the tendon segment (Z_p/L_i) is the most important factor affecting the increase in tendon stress above the effective prestress level. The elongations that occur at a plastic hinge are a direct function of the plastic depth, Z_p . Tendon strain is calculated from the tendon elongations divided by the free length of the tendon segment, L_i .

A simple truss model was presented by Mojtahedi and Gamble (27) to illustrate this effect on the development of tendon stress. The model, shown in Fig. 7.13a consists of two rigid links connected by a hinge and tied at the base by a flexible tie. A vertical deflection is induced on the hinge which results in elongation of the flexible tie. For a constant induced deflection the aspect ratio of the truss was varied. The resultant stress response, (Fig. 7.13b) illustrates the relationship between Z_p/L_i and the change in tendon stress. A large value of Z_p/L_i indicates a deep beam in which large tendon elongations are averaged over a short length, thus leading to large tendon-stress increases. A small value of Z_p/L_i indicates a slender girder in which small elongations are averaged over a long length, thus leading to small increases in tendon stress.

7.4.2.3 Neutral Axis Depth. It has been shown that the length of the plastic hinge region is a function of the depth to the neutral axis (28). A longer hinge length will allow larger hinge rotations, and therefore, larger tendon elongations. The neutral axis depth at ultimate is a function of several factors, including the amount of prestressed and nonprestressed reinforcement crossing the joint, the ultimate tendon stress, the concrete strength, and the shape of the concrete compression zone. Generally, larger reinforcement percentages and lower concrete strengths will lead to larger neutral axis depths and larger ultimate tendon elongations at ultimate.

7.4.2.4 Rotation Capacity at Precast Joints. In Section 1.2.2.2.1 the ultimate rotation capacity and the ultimate tendon elongations were shown to be dependant on the limiting strains in the concrete compression zone, and in the passive segment reinforcement on the tension side of the girder. Increases in either of these limiting strains will cause a direct increase in the hinge rotation at ultimate.



a. Simple Truss Model

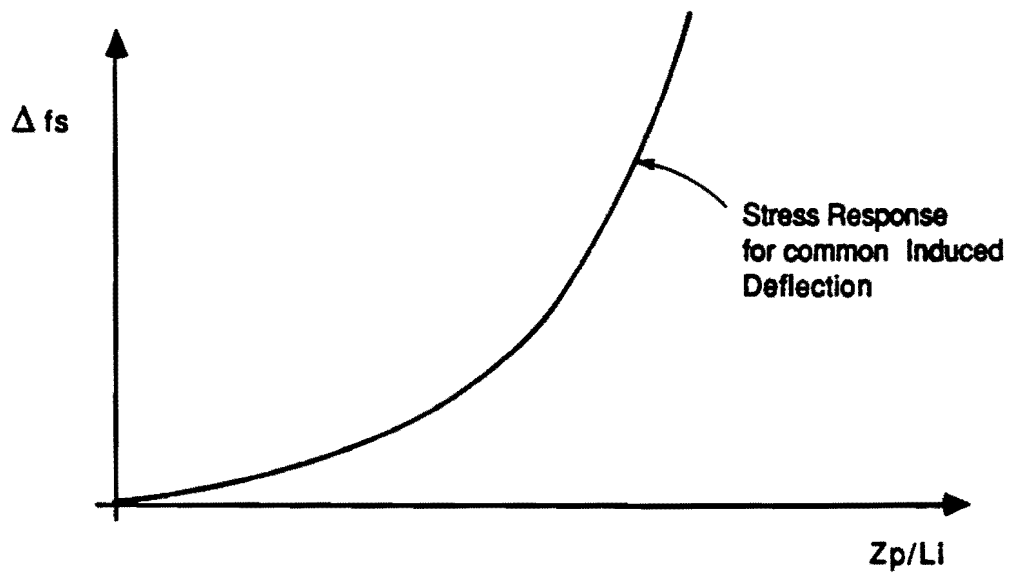
b. Change in Tendon Stress vs Z_p/L_i

Figure 7.13 Tendon Profile Slenderness Ratio

Confinement of the compression zone - It is well documented that the ultimate concrete strain is dependant on the degree of confinement of the concrete compression zone (29, 30). The most direct method of increasing the concrete strain capacity is by providing reinforcement to confine the compression zone. This indicates that proper anchorage of the web reinforcement up to the extreme surface of the compression flange could possibly increase the rotation capacity at a flexural hinge.

Segment reinforcement - The ultimate rotation capacity at an opening joint was also believed to be a function of the passive segment reinforcement on the tension side of the girder. In order to develop the required strains, tension reinforcement must be properly anchored as close to the joint as possible. This requirement is especially critical at the tension flange-web interface. Segments should be detailed with well anchored reinforcement at each web-flange junction. In addition, observations made during testing indicate that well anchored and well distributed longitudinal web reinforcement may increase the ultimate rotation capacity by distributing distortions to several opening cracks.

7.4.2.5 Tendon Slip at Deviators. Substantial tendon slip was noticed in all tendons at all deviator locations for ultimate load levels. The tendon slip behavior can be illustrated by examining Fig. 7.11 which shows the change in stress in tendon 1b during the flexural strength test of the north span. The tendon began to slip from the interior end towards the midspan region at an applied load of $5.0(LL+I)$. Slip also occurred from the exterior end at approximately $6.2(LL+I)$. The tendon slipped through the deviator when the change in tendon force exceeded the maximum friction capacity.

When the tendon began to slip it did not suddenly slip and release stress in the midspan region. Instead, initial tendon slip was followed by continual slip as load was increased. For ultimate load levels the tendon was elongating over its entire length.

The maximum midspan stress that was achieved in the model tendons was affected by the load level at which slip began. If tendon slip began at a low load level then the ultimate midspan tendon stress was low. Conversely, if slip did not

occur until higher load levels then the ultimate midspan tendon stress was increased. Therefore, before prototype extrapolation can be made, additional information is required to determine the force transfer mechanism at deviators and the level of force at which tendons begin to slip at deviators.

7.4.3 Prediction Equations for Tendon Stress in Unbonded Tendons Corresponding to Nominal Capacity. Several methods are currently available to predict the stress in unbonded tendons at flexural strength. Each of the available methods calculates the ultimate tendon stress as the sum of the effective prestress and an increment occurring under applied load. Each of the methods is summarized below, and predicted and measured ultimate stresses are compared.

7.4.3.1 ACI. The current ACI Building Code equations (17) for ultimate tendon stress in unbonded beams (Fig. 7.14a) was originally proposed by Mattock et al (31) to provide a reasonable lower bound to the available test data for simply supported, unbonded post-tensioned beams having reinforcement ratios permissible under the ACI code. It was later noticed by Gamble and Mojtahedi (27) that slender girders developed unbonded tendon stresses at a much reduced rate which lead to the second ACI equation for slender beams with span-to-depth ratios greater than 35.

7.4.3.2 AASHTO. The ACI provisions described above were based on test data for 25 to 30-foot single and double-span girders. For large bridge structures it was not known whether the same level of stress increase could be attained. AASHTO therefore limited the stress increase to 15 ksi for bridge structures, as shown in Fig. 7.14b.

7.4.3.3 Tam and Pannell. The Tam and Pannell method was presented in Section 1.2.2.2.1 and was based on the elongations that occur at a plastic hinge. The length of the plastic hinge was experimentally related to the depth of the neutral axis. The ultimate curvature was calculated from the concrete crushing strain and the depth to the neutral axis. The ultimate elongation in the tendon at the plastic hinge was the product of the ultimate curvature, the length of the plastic hinge, and the plastic depth of the tendon. The increase in tendon stress at the plastic hinge is therefore calculated as shown in Fig. 7.14c.

Span/Depth ≤ 35

$$\left\{ \begin{array}{l} f_{ps} = f_{pe} + 10000 + \frac{f'_c}{100 f_p} \\ = f_{pe} + 60000 \\ = f_{py} \end{array} \right\} \quad \text{use lesser of}$$

Span/Depth > 35

$$\left\{ \begin{array}{l} f_{ps} = f_{pe} + 10000 + \frac{f'_c}{300 f_p} \\ = f_{pe} + 30000 \\ = f_{py} \end{array} \right\} \quad \text{use lesser of}$$

a. ACI Method

$$f_{ps} = f_{pe} + 15000$$

b. AASHTO Method

$$f_{ps} = f_{pe} + \left[\Psi \epsilon_{cu} E_p \left(\frac{d_p - c_y}{l_i} \right) \right]$$

Assume $\Psi = 10.5$ (determined experimentally)

c. Tam and Pannell Method

Figure 7.14 Methods for Calculating f_{ps}

$$f_{ps} = f_{pe} + 725 \left(\frac{d_p - c_y}{l_e} \right)$$

c_y = neutral axis depth assuming the tendons have yielded

l_e = length of tendon between anchors divided by the number of plastic hinges required to develop a failure mechanism in the span under consideration.

d. CSA Method

$$f_{ps} = \frac{f_{sc} + \phi_m Z_p Z_s E_p}{l_i}$$

$$\phi_m = \frac{\epsilon_{cm} + \epsilon_{sm}}{d_s}$$

ϵ_{cm} = limiting compressive strain in concrete

= 0.002 for design

= 0.003 for ultimate

ϵ_{sm} = limiting tensile strain in passive segment reinforcement

= 0.010 for design

= 0.020 for ultimate with proper anchorage

e. Virlogeux Method

Figure 7.14 Methods for Calculating f_{ps} - continued

In the equation for ultimate tendon stress, shown in Fig. 7.14c the solution is iterative because the depth of the neutral axis at ultimate, c_u , is a function of the ultimate tendon stress, f_{ps} .

7.4.3.4 Canadian Standards Association (CSA). The iterative solution of Tam and Pannel can be simplified by replacing the neutral axis depth at ultimate, c_u , with the neutral axis depth when the tendon yields, c_y . Since unbonded tendons generally remain within the elastic range, the value of c_y will always be slightly larger than the true neutral axis depth, c_u . This will lead to a conservative estimate of the maximum increase in tendon force.

This approach was adopted by the Canadian Standards Association CAN3-A23.3-M84 (32) for calculating the ultimate tendon stress in unbonded tendons (Fig. 7.14d). After making the appropriate simplifications to the Tam and Pannel formula, the result yields an equation very similar to the CSA code equation.

There appears to be a small conceptual error in the CSA equation for the reasons described in Chapter 1 for multiple hinge structures. The value of l_e in the CSA equation is defined as "the length of the tendon between anchors divided by the number of plastic hinges required to develop a failure mechanism". This means that for an interior-span mechanism in which three hinges must form, the effective length is divided by three, or the elongations are multiplied by three. Because support hinges rotate only half of the midspan-hinge rotation, the elongations should only be multiplied by two. In addition, it must be checked whether the mechanism hinges all involved the same tendons. A correction to the CSA code equation is presented in Section 7.4.4.

7.4.3.5 Virlogeux. Virlogeux's method was presented in Section 1.2.2.2.1 and was based on the elongations that occur at a plastic hinge. The ultimate rotation capacity was determined from limiting strains in the concrete and the steel, and the length of the plastic hinge. The maximum elongation in the tendon at a plastic hinge was the product of the rotation capacity and the plastic lever arm of the unbonded tendon. The change in tendon stress above the effective prestress force is therefore calculated as shown in Fig. 7.14e. Virlogeux recommended limiting strains in the concrete and passive segment reinforcement corresponding to both the design and ultimate conditions.

7.4.3.6 Comparison of Prediction Equations with Test Data. The increase in midspan tendon stresses corresponding with flexural strength ranged from 36 to 60 ksi in the midspan region and from 15 to 27 ksi at the critical support joint. Stress increases were generally larger for the shear test than for the flexural test. In Table 7.6 the measured tendon stress increases are compared with the calculated stress increases determined using the procedures described above. In general, the methods tend to underestimate the midspan tendon stress increases and overestimate the support tendon stress increases. This appears to indicate that the global behavior was governed primarily by the midspan strength with the support region not developing full capacity. This is consistent with the mechanism behavior in which the midspan region undergoes approximately twice the concentrated rotations induced at the support regions. It is important to note that if the total calculated tendon stress ($f_{pe} + \Delta f_p$) is compared with the total measured tendon stress, then the predicted-to-measured percentages will be substantially smaller than the percentages shown in Table 7.6.

The following specific observations can be concluded about each of the methods presented:

ACI Method - The ACI formula accurately predicted the measured tendon stress response in the midspan regions with predicted-to-measured ratios between 80 and 113 percent. This result is reasonable if it is remembered that the tests used to develop the ACI formula were conducted on specimens with short span lengths approximately equal to that used in the model bridge.

The average measured tendon stress increase at the critical support joint was overestimated by the ACI formula with predicted-to-measured ratios ranging between 127 and 172 percent. At these locations the effective depths of external tendons are reduced because of the drape from the support. An increased ratio of tendon depth to tendon free length leads to reduced stress development under applied loads.

AASHTO Method - The AASHTO formula predicted much lower tendon stress increases than measured in the midspan regions but implicitly assumes much longer spans. In the support regions the AASHTO formula

Table 7.6 Comparison Between Measured and Calculated Tendon Stress Response

Location	Measured Stress Change (ksi)				Calculated Stress Change												Proposed (ksi) %					
					ACI (ksi) %		AASHTO (ksi) %		Tam/Pannell (ksi) %		CSA (ksi) %		CSA - Corr. (ksi) %		Virlogeux-D (ksi) %				Virlogeux-U (ksi) %			
	1a	1b	3	Wt. Avg.																		
Midspan Region - Exterior Spans																						
North Span External Tendons:	1a	1b	3	Wt. Avg.																		
Stress (ksi) Flexural Test	36	48	33	40.5	39	96%	25	37%	33	81%	52	128%	26	64%	13	32%	24	59%	32	79%		
Shear Test	42	59	41	48.9		80%		31%		67%		106%		53%		27%		49%		65%		
South Span External Tendons	4a	4b	5	Wt. Avg.																		
Stress (ksi) Flexural Test	38	41	57	42.4	48	113%	15	135%	33	78%	53	125%	27	64%	13	31%	25	59%	34	80%		
Shear Test	50	57	60	54.6		88%		27%		60%		97%		49%		24%		46%		62%		
Support Regions - Interior																						
Face of Interior Support																						
North Span External Tendons	2	3	5	Wt. Avg.																		
Stress (ksi) Flexural Test	15	21	12	15.7	27	172%	15	96%	26	166%	39	249%	20	128%	10	64%	20	128%	25	159%		
Shear Test	20	27	15	20.4		132%		73%		127%		191%		98%		49%		98%		122%		
Internal Tendons	iT	iT	iT		27		15		12		19		10		5		9		12			
Stress (ksi)	(Not Measured)																					
South Span External Tendons	2	3	5	Wt. Avg.																		
Stress (ksi) Flexural Test	18	18	16	17.6	28	159%	15	85%	26	148%	39	222%	20	114%	10	57%	20	114%	25	142%		
Shear Test	22	23	21	22.0		127%		68%		118%		177%		91%		45%		91%		114%		
Internal Tendons	iT	iT	iT		28		15		12		19		10		5		9		12			
Stress (ksi)	(Not Measured)																					

predicted the ultimate stress increases relatively closely which would perhaps indicate a reduced level of safety in the negative moment regions.

Tam and Pannell Method - The Tam and Pannell iterative solution tended to slightly underestimate the maximum stress increases at midspan with the ratio of predicted-to-measured ranging between 60 and 81 percent. This conservatism is probably caused by the fact that the tendons do not begin to slip until considerable load has been applied. The effective length of the tendon can therefore be considered to be less than the length between anchorages, thus leading to increased stress.

The Tam and Pannell method tended to overestimate the tendon stress increases at the support with predicted-to-measured ratios ranging between 118 and 166 percent.

CSA Method - The CSA method generally overestimated the midspan tendon stress increases with predicted-to-measured ratios ranging between 97 and 128 percent. The larger predicted stresses are caused by the conceptual problem described earlier. The two hinges that form to cause a mechanism intersect different sets of tendons. The elongations occurring at each hinge are therefore independent and should not be added as is inherent in the CSA determination of effective tendon length. If the true tendon length is used the CSA-Corrected Method underestimates the tendon stress increases with predicted-to-measured ratios ranging between 49 and 64 percent. This conservatism is again caused by the delayed slip in the tendons as described for the Tam and Pannell method above.

Virlogeux Method - Virlogeux recommended two sets of assumptions for calculating the tendon stress increases for unbonded tendons. The first assumption was intended for design and assumed conservative values for the limiting strains in the concrete and steel. The design assumptions underestimated the tendon stress increases with predicted-to-measured ratios ranging between 24 and 32 percent at midspan and 45 and 64 percent at the support region. In the ultimate case, the limiting concrete and segment reinforcement strains were estimated using less conservative assumptions. In the ultimate case the predicted stress increases were less conservative at

midspan with predicted-to-measured ratios ranging between 46 and 59 percent. At the support the ultimate limiting-strain assumptions predicted the tendon stress increases fairly accurately with predicted-to-measured ratios ranging between 91 and 128 percent.

The Virlogeux method offers a convenient method by which local effects can be incorporated in the design. A series of tests could be run with varying degrees of confinement in the compression zone, and anchorage of the passive tension reinforcement in the segment. A series of design guidelines could then be developed in which limiting strains are prescribed depending on the level of confinement and anchorage.

7.4.4 Recommendation for Calculation of Flexural Strength. In light of the above discussion, a method similar to the CSA method is recommended for determining the stress increase in unbonded tendons at ultimate. It provides a convenient design method that incorporates most of the important factors described in Section 7.4.2. The effect of bonded reinforcement in the compression and tension zones can also be incorporated in the calculation of the neutral axis depth at ultimate.

Figure 7.15 summarizes the recommended design procedure. The equation is derived in the same way as the Tam and Pannell method with the neutral axis depth at ultimate, c_u , replaced by the neutral axis depth assuming yielding in the tension reinforcement, c_y . The neutral axis depth, c_y , can be calculated with only unbonded tendons crossing the critical joint, as shown in Fig. 7.16a, or with bonded compression and tension reinforcement as shown in Fig. 7.16b.

The free length of the unbonded tendon, l_e , should be estimated from the length between anchorage locations and the number of hinges crossed by the tendon under question. Since support hinges undergo approximately half the concentrated rotation as the midspan hinges, elongations occurring at a support hinge will be approximately half the elongations occurring at midspan. The effective length of tendon should therefore be calculated as

$$l_e = \frac{l_i}{1 + .5N_s}$$

$$f_{ps} = f_{pe} + \psi E_p \epsilon_{cu} \left(\frac{d_p - c_u}{l_e} \right) \text{ (ksi)}$$

$$\psi = 10.5 \text{ (determined experimentally by Tam and Pannell)}$$

$$E_p = 28. \times 10^3 \text{ ksi (AASHTO)}$$

$$\epsilon_{cu} = 0.003 \text{ (ACI)}$$

$$l_e = \left(\frac{l_i}{1 + \frac{N_s}{2}} \right)$$

l_i = length of tendon between anchorages

N_s = number of support hinges crossed by the tendon (draped tendons only)

Assume $c_u = c_y$

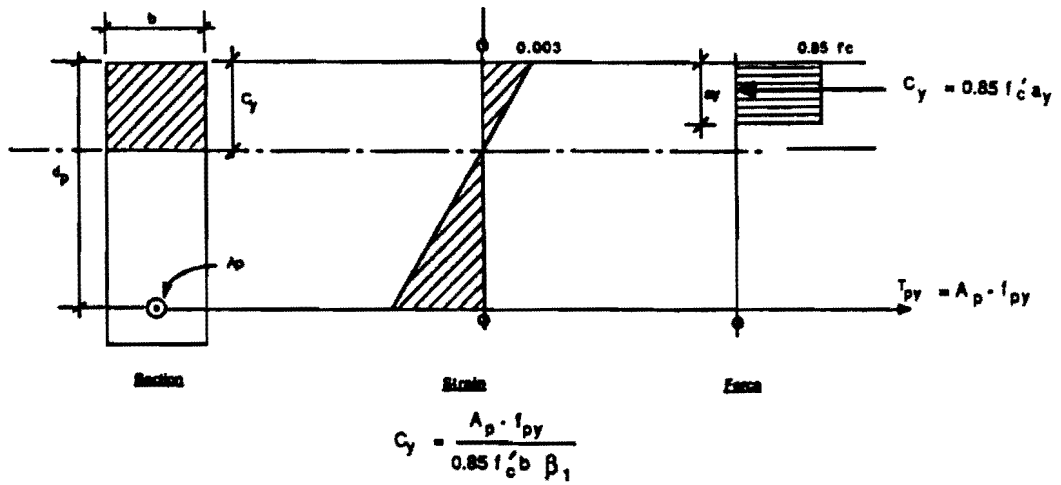
$$\therefore f_{ps} = f_{pe} + 10.5 \times 28 \times 10^3 \times .003 \left(\frac{d_p - c_y}{l_e} \right)$$

$$f_{ps} = f_{pe} + 882 \left(\frac{d_p - c_y}{l_e} \right)$$

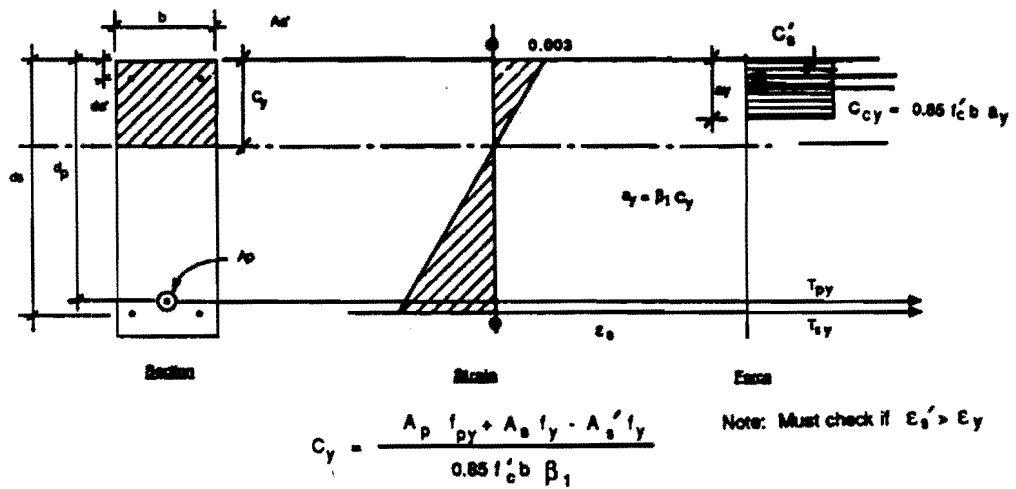
\therefore Recommended Design Equation

$$f_{ps} = f_{pe} + 900 \left(\frac{d_p - c_y}{l_e} \right)$$

Figure 7.15 Recommended Design Equation



(a) Unbonded tendons only



(b) With bonded reinforcement

Figure 7.16 Neutral Axis Depth, c_y

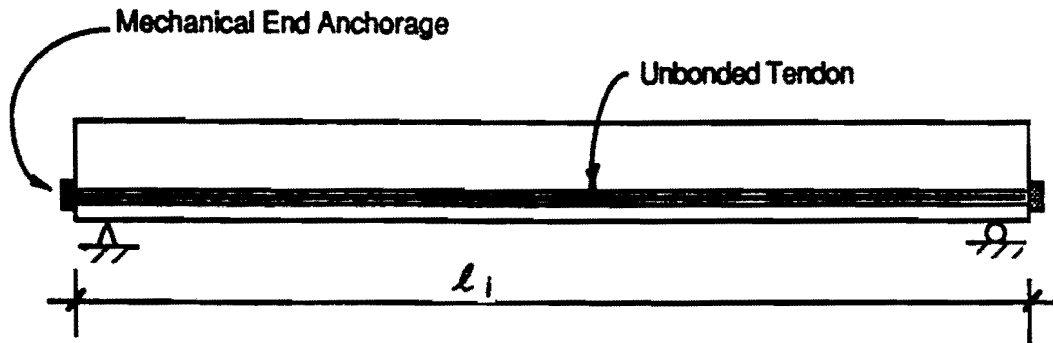
with ℓ_i equal to the length between anchorage locations and N_s equal to the number of support hinges crossed by the tendon. Note that this equation is true only for draped tendons in which the tendon is on the tension (opening) side at each hinge location. The length between anchorage locations, ℓ_i , may refer to the length between mechanical end anchorages as shown in Fig. 7.17a or the free unbonded length between regions in which the tendon is bonded and fully developed, as shown in Fig. 7.17b.

The calculated tendon stress increases using the proposed design procedure are also tabulated in Table 7.6. The proposed method generally underestimated the midspan tendon stress increases with predicted-to-measured ratios ranging between 62 and 80 percent. The conservatism is probably caused by the delayed slip in the tendons leading to a higher measured stress increase in the model structure.

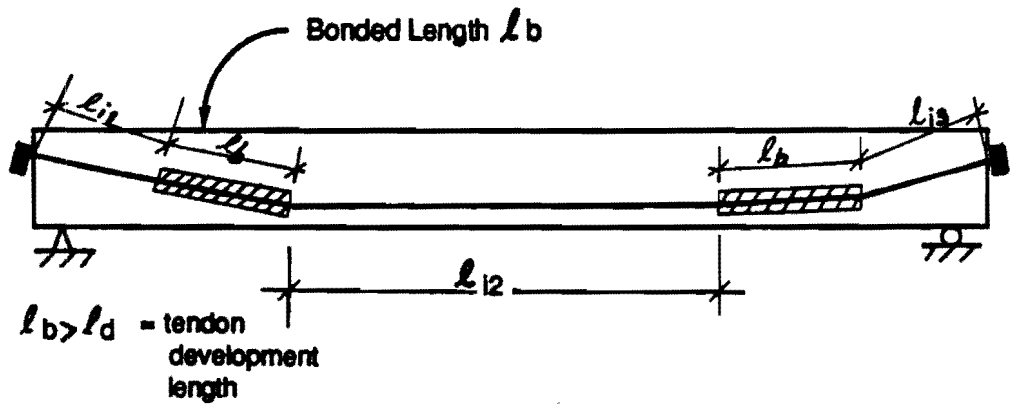
7.5 Load Rating Existing Structures

The AASHTO Manual for Maintenance Inspection of Bridges (33) requires that all bridges be inspected at regular intervals at a frequency not exceeding two years. For each inspection it is necessary to rate the structure at two load levels. The first level, called the Operating Load Rating, is the maximum permissible load level to which the structure can be subjected. This represents the factored ultimate strength of the structure, and load levels higher than the Operating Load will result in permanent deformation or damage. The second level, called the Inventory Load Rating, is the load level which can be safely applied to the structure for an indefinite period of time. This represents the service strength of the structure, and load levels higher than the Inventory Load will result in gradual deterioration of the load carrying capacity.

This need to rate existing bridges requires accurate methods for predicting the ultimate and service capacities of existing structures. For most structures these capacities can be accurately calculated from the section properties, either from the as-built drawings or from field measurements. For an unbonded prestressed system however the ultimate and service level behaviors are dependant on the effective prestress in the tendons. An accurate knowledge of existing tendon stress is therefore required to determine both ultimate strength and the limits to service level behavior.



a. Between Mechanical End Anchorages



b. Between Bonded Regions

Figure 7.17 Free Tendon Length

Overestimating the insitu tendon stresses will lead to a direct overestimation of structural strength.

Two general methods are therefore available to rate an existing unbonded structure. By the first method the engineer must make a conservative estimate of the insitu tendon stresses. The insitu tendon stress must be calculated assuming artificially high stressing friction and long term losses. The rating engineer must be sure that the calculated tendon stress is an extreme lower bound to the true insitu stress.

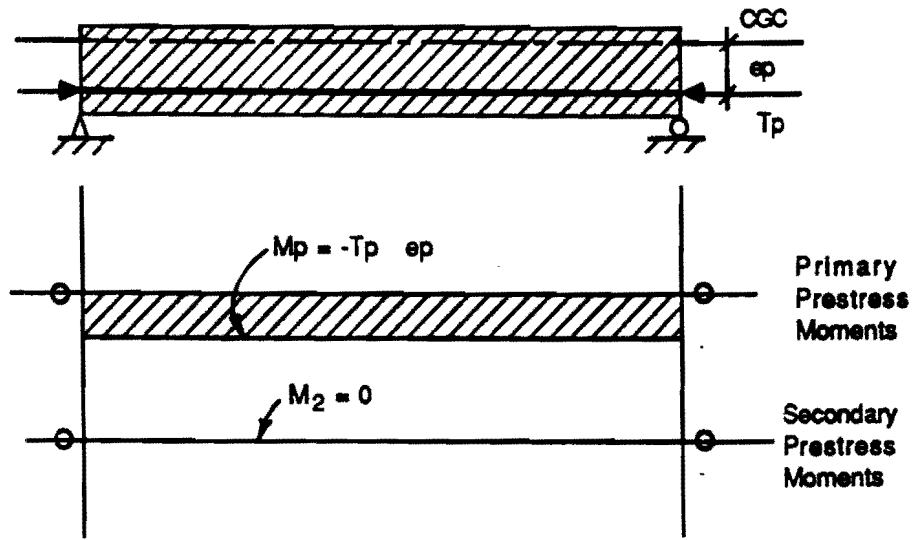
The second method for rating an existing structure is by load testing. The structure must be loaded and monitored in an attempt to determine the load that causes decompression at the extreme tension fiber. From this load an estimate of the effective prestress can be made.

7.6 Secondary Prestress Forces at Ultimate Load Levels

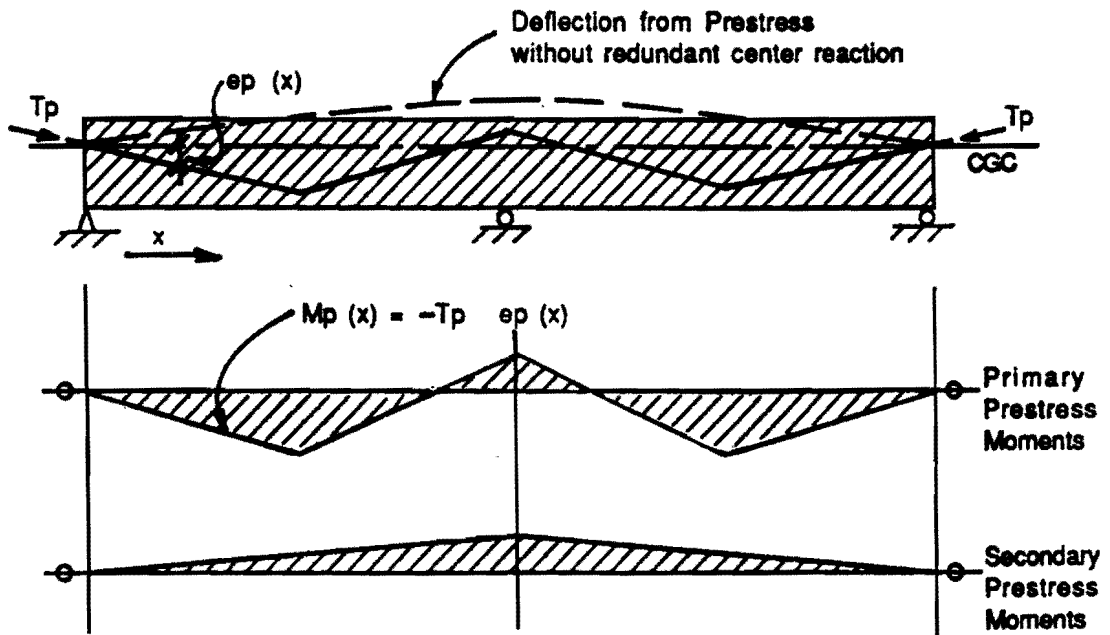
7.6.1 Background Information. Secondary prestress forces are caused by stressing a restrained structure. When prestress is applied to a structure, the structure will develop stresses to equilibrate the forces. The stresses cause strains that result in deflections in the structure. If these deflections are restrained in any way then the restraining forces will cause additional stresses to occur in the beam. These additional stresses are commonly known as the secondary prestress forces.

If prestress is applied to a statically determinate structure, as shown in Fig. 7.18a, the structure is free to deflect and the prestress forces are self-equilibrating. The prestress causes local changes in cross-sectional stresses but does not alter the global equilibrium of forces. The structure remains statically determinate externally but is determinate internally only if magnitude and location of the prestress force are exactly known. The local changes in cross-sectional stress are called the primary prestress forces and are calculated directly from the effect of the eccentric prestress at a section.

If prestress is applied to a statically indeterminate structure, as shown in Fig. 7.18b it is not free to deflect since restraint is provided by the redundant reaction. Global equilibrium is altered by the restraining reactions, called the secondary



a. Statically Determinate Structure



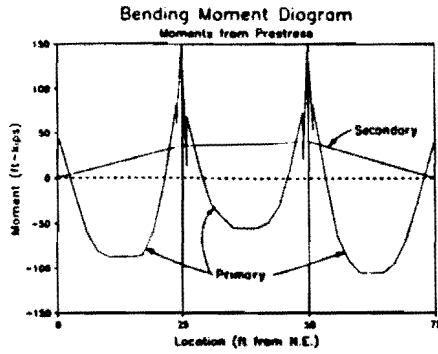
b. Statically Indeterminate Structure

Figure 7.18 Primary and Secondary Prestress Forces

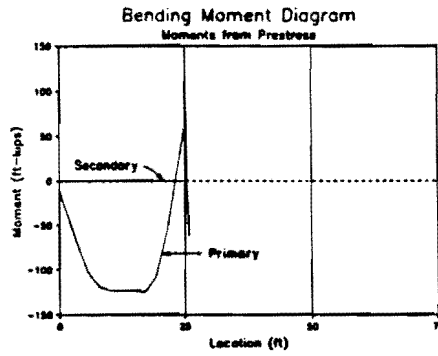
prestress reactions, which causes a redistribution of forces. In this case the structure is statically indeterminate with respect to both global and local forces. Global force distribution must consider both the girder stiffness and the secondary prestress forces. The sectional stress distribution caused by the prestress at a particular location must consider the primary prestress forces as above plus the additional stresses caused by the secondary prestress forces.

7.6.2 Secondary Prestress Forces from Construction. The secondary prestress forces are dependant on the method and order of construction. Secondary forces develop during construction from the restraining forces that exist when a tendon is stressed. The restraining forces are therefore a function of the structural configuration at the time of stressing. This phenomenon can be illustrated by considering the primary and secondary prestress forces for two similar three-span beams. The first beam was stressed in its final three-span configuration, and the prestress forces are shown in Fig. 7.19a. Because tendons are symmetrical with respect to the center of the structure, the secondary prestress forces are also symmetrical. For the second beam, the structure was constructed in a sequential span-by-span manner by starting at one end-span and proceeding towards the other end. The prestress forces at the end of each stage of construction are shown in Fig. 7.19b. Since the one-span configuration is statically determinate, the prestress causes only primary prestress forces. In the two-span configuration the structure is restrained by one redundant reaction, and the secondary prestress forces develop as shown. When the tendons of the third span are stressed, the structure is restrained by two redundant reactions and the secondary prestress forces develop as shown. The final distribution of secondary forces is calculated from the addition of the secondary forces that occur during each stage of construction. Note that the final secondary prestress forces are not symmetrical with respect to the center of the girder, even though the tendon profiles are.

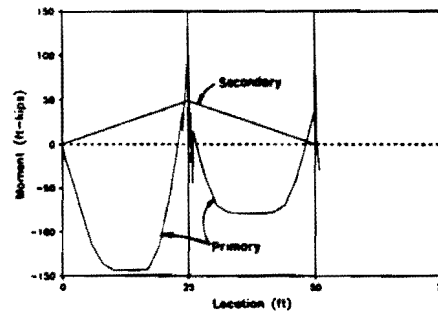
Attempts have been made in prototype construction to reduce the secondary prestress forces by using staged casting and stressing procedures. If rotations are allowed to occur at the ends of the span at the time the tendons are stressed, then the restraining forces and secondary prestress forces will be small or nonexistent. The staged casting procedure, shown in Fig. 7.20, has been used to reduce the secondary prestress forces in prototype span-by-span construction. The first span



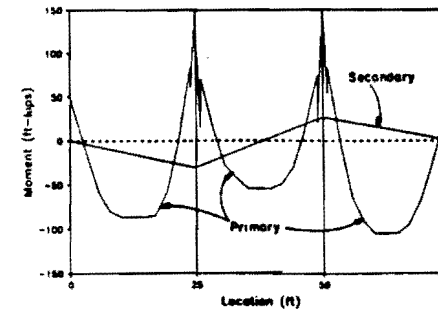
a. Stressed in Three-Span Configuration



One-Span Configuration



Two-Span Configuration



Three-Span Configuration

b. Structural Constructed Span-by-Span

Figure 7.19 Secondary Prestress Forces from the Construction Method

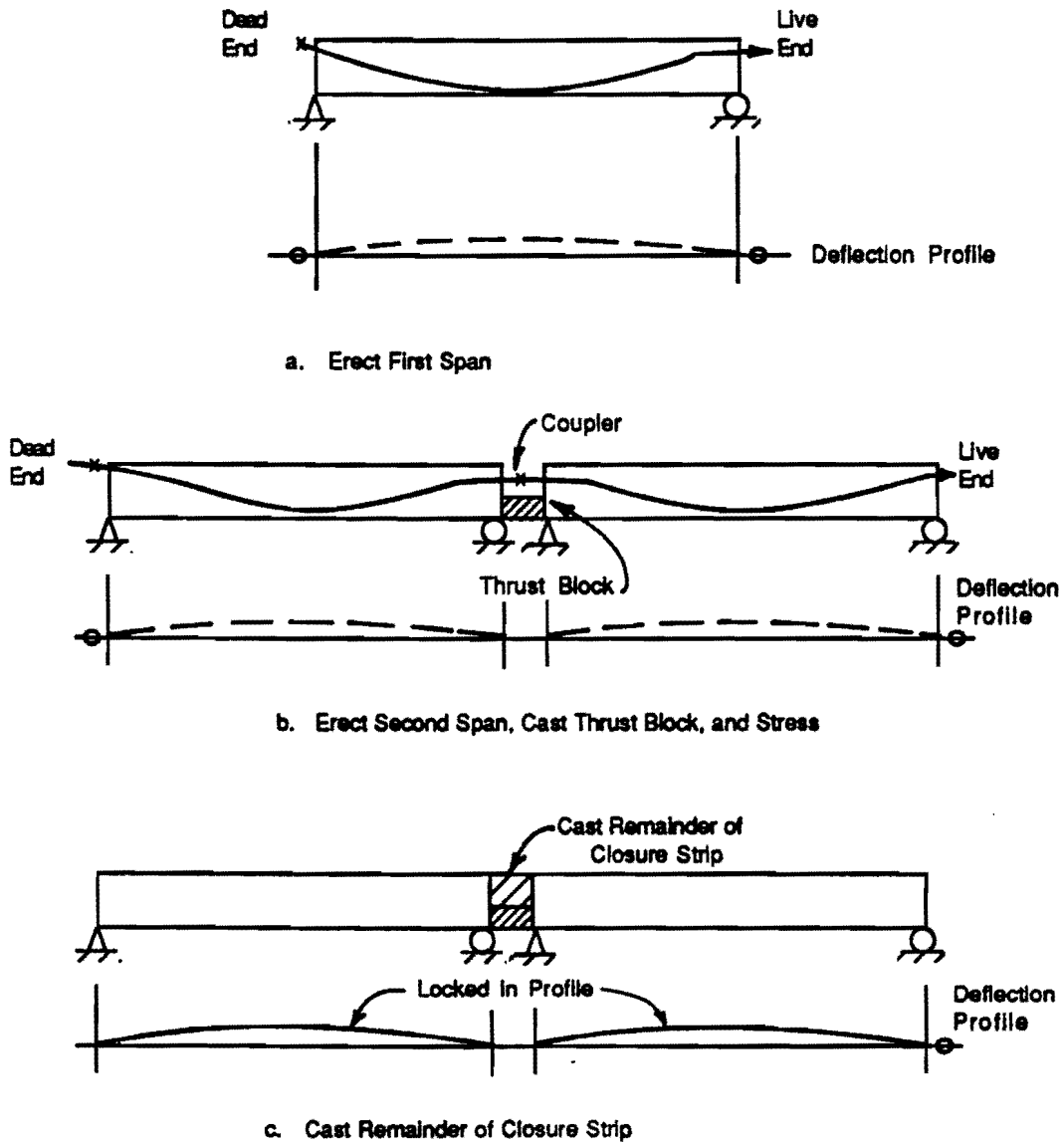


Figure 7.20 Staged Construction to Relieve Secondary Forces

is erected normally with the tendons causing only primary prestress forces. The second span is then erected and the closure strip is cast only at the level of the bottom flange. The tendons are then coupled to the ends of the first-span tendons (Fig. 7.20b) and then stressed. The thrust from the prestress forces is carried by the continuous bottom flange. Since only the bottom flange is in contact at the time of stressing, the ends of the second span are relatively free to rotate, and the resulting secondary prestress forces are small or nonexistent. The closure strip is then completed and the next span is erected in a similar manner.

This staged method of casting and stressing to reduce secondary forces has several critical problem areas, however, that must be carefully addressed during design. At the time of stressing, the bottom flange is the only concrete present for transferring the large prestress forces between spans. This causes relatively higher stresses to occur in the bottom flange which remain during the life of the structure. In addition to the high stress, the concrete must also undergo local deformations to allow the ends of the beam to rotate and relieve the secondary prestress forces. The high stresses combined with the induced rotations may cause distress in this concrete. Crushing of this concrete before the remainder of the closure strip is cast will cause a serious safety problem.

A final concern with this construction procedure is the effect of the tendon coupler at the location of maximum negative moment. The top part of the closure strip is cast after stressing the primary tendons, so the compressive stress in this region is minimal. Under applied loads the closure strip will crack allowing moisture to penetrate into the coupler region. In addition, the stress range in the coupler may be large at this cracked section. This indicates that a serious fatigue problem in the coupled tendon, which may be aggravated by moisture infiltration, could possibly develop.

7.6.3 Redistribution of Secondary Prestress Forces. Because the external tendons are bonded to the concrete section only at discrete locations along the span, large concentrated rotations must occur at opening joints to develop the large tendon elongations required for increased tendon stresses. These rotations allow the internal forces to redistribute to stiffer uncracked regions. This is apparent from the reaction and joint moment data for the flexural test of the north span, shown in Fig. 7.21. As the midspan joints begin to open at the decompression load, the resultant loss in

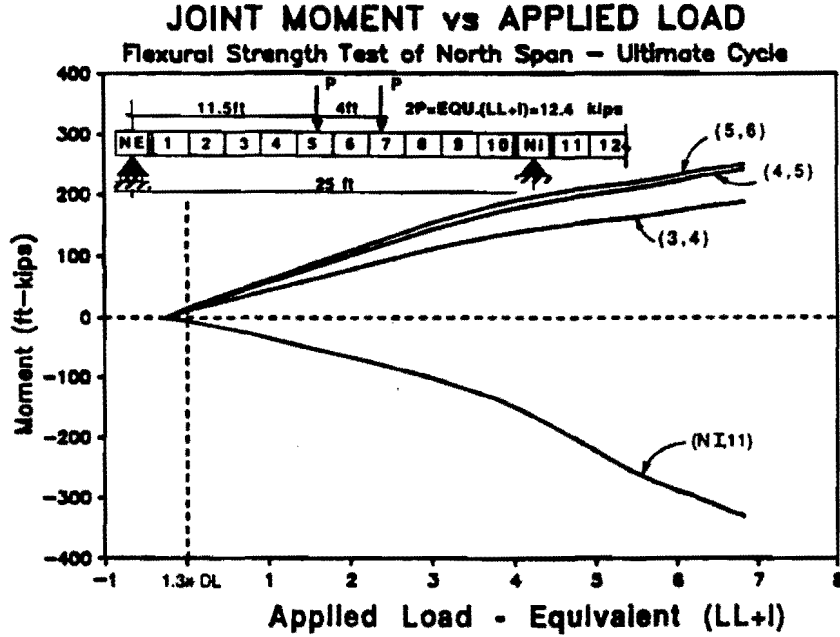
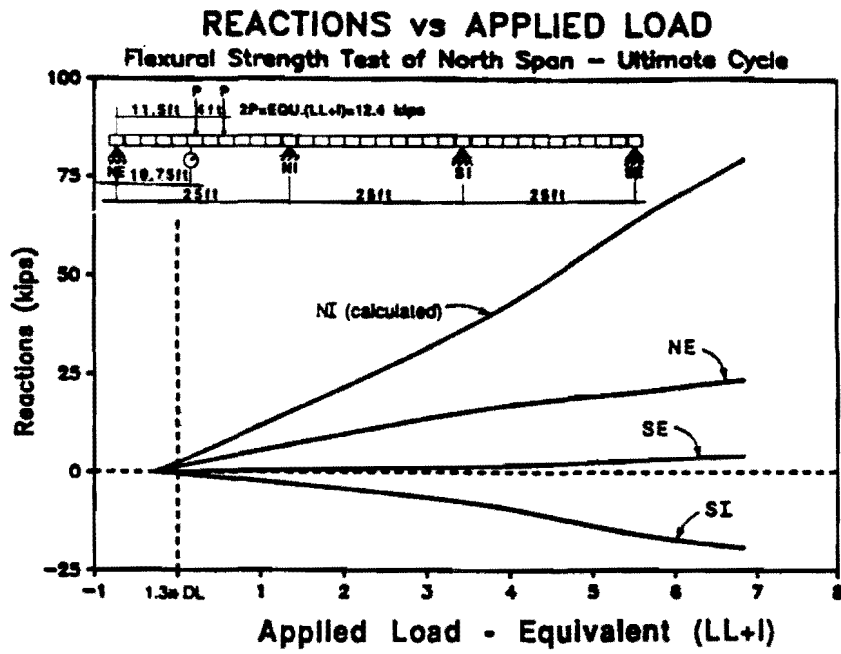


Figure 7.21 Reactions and Joint Moments

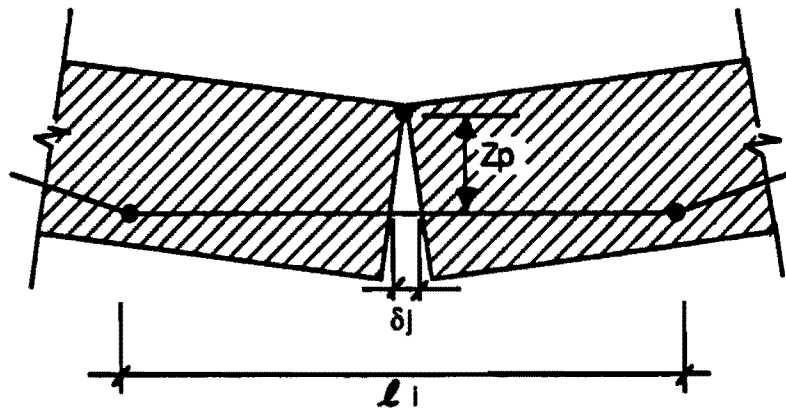
stiffness causes a larger portion of the additional load to be carried at the interior support. As loading is further increased, the support joint opens causing a reduction in stiffness at the support. The internal forces then redistribute back towards the midspan region with the distribution of internal forces at ultimate being controlled by the relative stiffness of the support and midspan regions.

The distribution of applied loads becomes dependant on the relative rotational stiffness at the support and at midspan. As ultimate loads are approached the plastic hinges can be idealized by a rotational spring with a moment-rotation stiffness as described in Fig. 7.22. The idealized spring has a non-zero stiffness which is dependant on the effective depth of the prestress and the free length of the tendon. This behavior is quite different from the behavior of a plastic hinge that forms because of yielding of a bar, as is common in bonded construction.

From the equation for the rotational spring constant several observations can be made. First, the values of E_p and A_p are constant and known. The value of Z_p is smallest at the decompression load, and increases as the compressive forces concentrate in the top flange. After the hinge has fully developed, the value of Z_p remains approximately constant throughout the range of hinge behavior. Near ultimate loads, the rotational spring stiffness is almost entirely dependant on the free length of the tendon.

For low load levels before the tendon slips at the deviators, the length of the tendon segment is equal to the length between adjacent deviators. As load is increase the tendons begin to slip at the deviators, and the length of the tendon segment becomes larger, and the resultant rotational joint stiffness decreases. For ultimate load levels the tendon slip advances until the length of the tendon segment approaches the total length between end anchorages. This was evident during the test with tendons slipping at all locations as load approached the ultimate level.

The rotational joint stiffness, therefore, behaves as shown in Fig. 7.23. For load levels below the decompression load the joint remains in contact with no local joint rotation. This is analogous to having an infinite rotational spring stiffness. After the joint decompresses, the rotational joint stiffness decreases until the compressive forces are concentrated in the top flange at M_o . For moments larger than M_o , the rotational joint stiffness remains approximately constant. At some moment,



$$K_{\Theta} = \frac{\Delta M}{\Delta \Theta}$$

$$\begin{aligned} \Delta M &= Z_p \cdot \Delta T = Z_p \cdot (\Delta \sigma_p \cdot A_p) \\ &= Z_p \cdot \left[\left(\frac{\delta_j}{l_j} \cdot E_p \right) \cdot A_p \right] \end{aligned}$$

$$\Delta \Theta = \frac{\sigma_j}{z_p} \quad \text{or} \quad \sigma_j = Z_p \cdot \Delta \Theta$$

$$\therefore \Delta M = Z_p \times \left[\left(\frac{Z_p \cdot \Delta \Theta \cdot E_p}{l_i} \right) \cdot A_p \right]$$

$$\text{or} \quad \frac{\Delta M}{\Delta \Theta} = K_{\Theta} = \frac{Z_p^2 E_p A_p}{l_i}$$

Figure 7.22 Rotational Stiffness at an Opening Joint

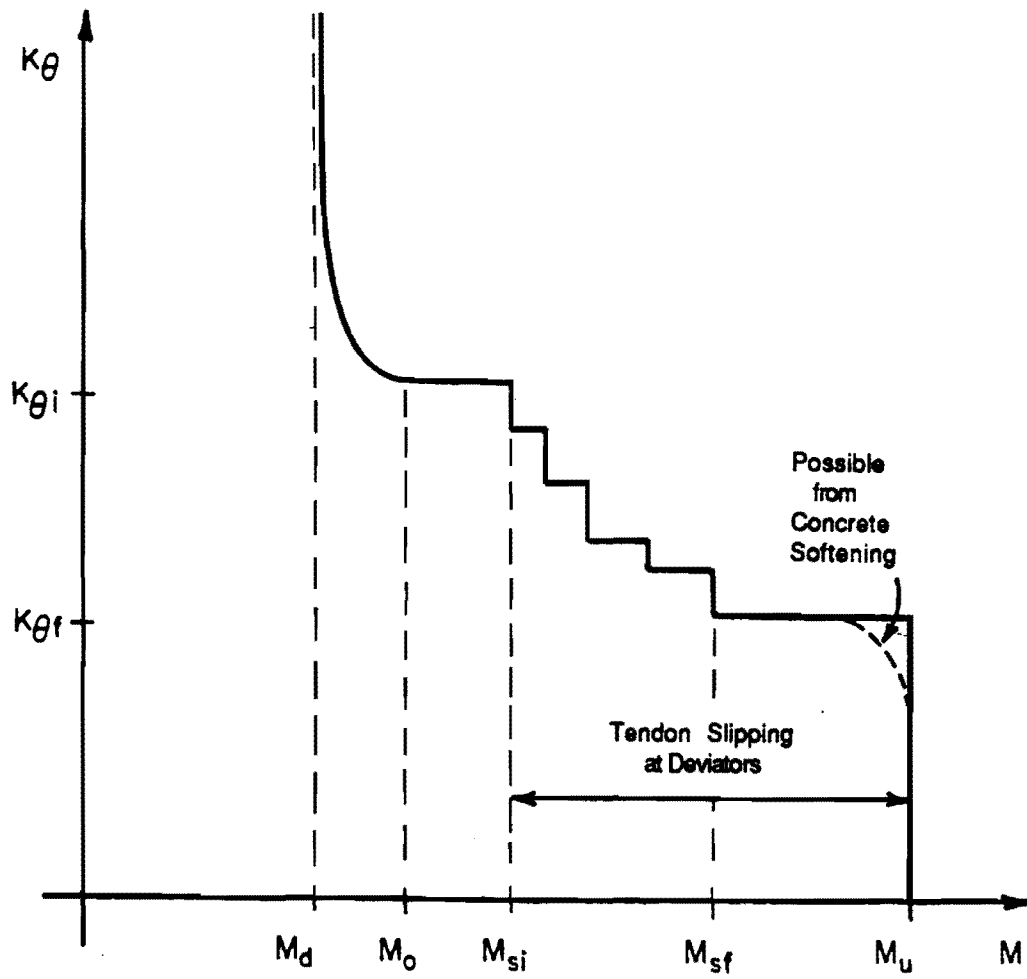


Figure 7.23 Rotational Joint Stiffness vs. Moment

$M_{s,i}$, the tendon begins to slip and the stiffness begins to decrease, with a stiffness reduction occurring each time the tendon slips. Finally at some moment, $M_{s,f}$, the tendon is slipping at all locations and the length of the tendon segment is the length between end anchorages. For moments above $M_{s,f}$ the rotational joint stiffness remains approximately constant with small decreases occurring due to softening in the concrete compression zone.

Figure 7.24 shows the relationship between the applied load and the bending moments at the midspan and support hinges for the flexural strength tests of the two exterior spans. Three separate expressions for bending moment are presented for each hinging joint. The first case, designated as "E", shows the theoretical response of the structure assuming elastic behavior and no secondary prestress moments. The second case, designated as "E+P2" shows the theoretical response of the structure assuming elastic behavior including the effects of the initial secondary prestress moments. The final case shows the measured response of the structure during the test.

As was described above for Fig. 7.21, the measured TEST response starts at the initial secondary moment and follows the E+P2 case. When the midspan joint begins to open, the load is redistributed to the stiffer support region. When the support joint begins to open, the internal forces are redistributed back towards the midspan region with the distribution of internal forces at ultimate controlled by the relative rotational stiffness at the support and midspan hinges.

Once the mechanism is fully developed and the ultimate load is approached, it appears that the Load - Moment response again becomes linear. The slopes of the resultant lines are dependant on the relative rotational stiffness of the midspan and support hinges. It also appears from the data that the moment response is asymptotic to a line which passes through a point defined by zero moment and the applied load at the start of the test (initial load was required to simulate the factored dead load condition as described in Section 6.2.3). This behavior is clearly visible in the south-span test data, although the north span data is inconclusive. This would appear to indicate that the internal force distribution at ultimate is dependant entirely on the rotational stiffness at the mechanism hinges, and is independant of initial conditions such as the secondary prestress forces.

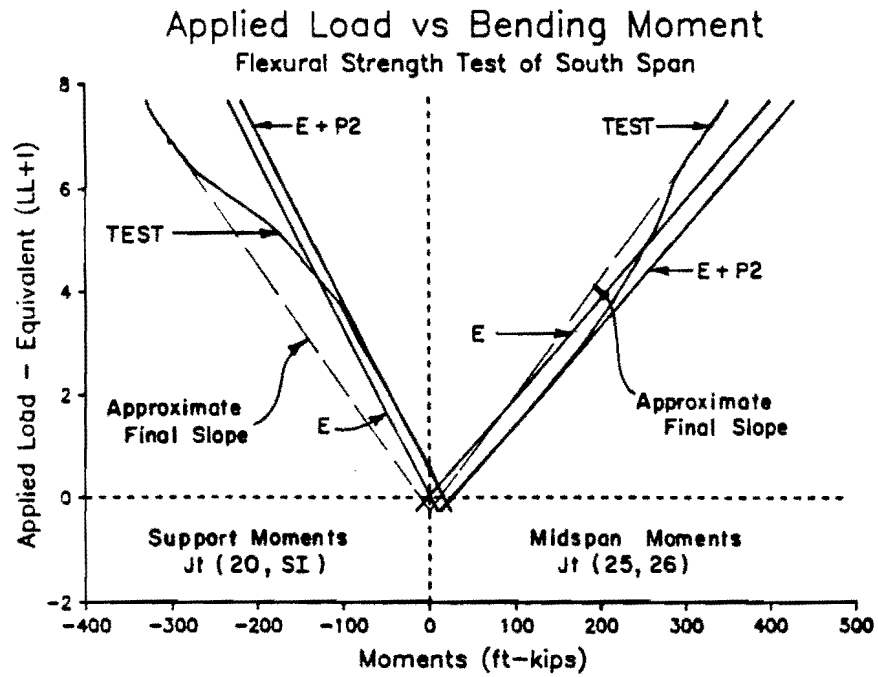
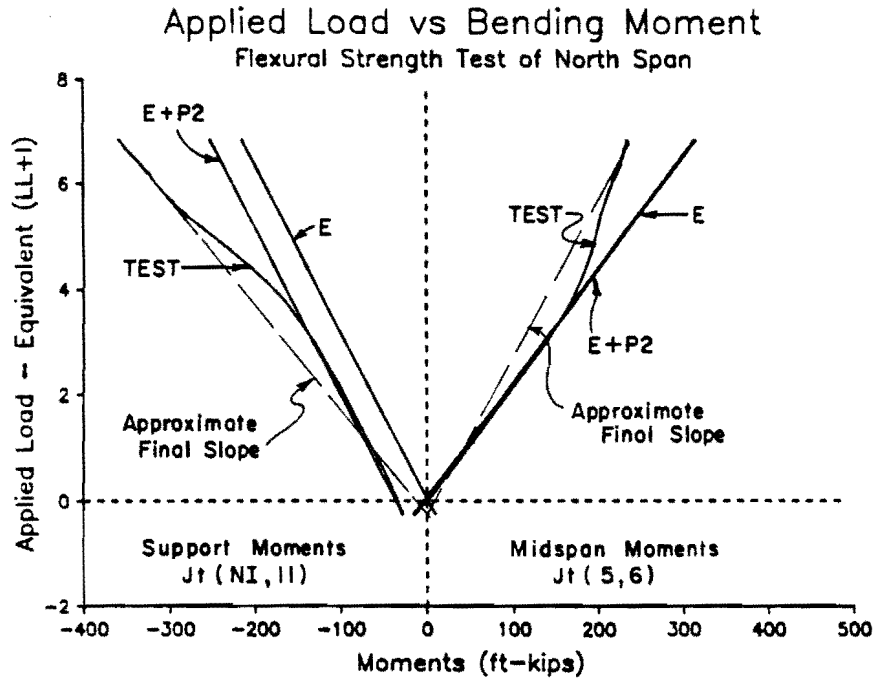


Figure 7.24 Applied Load vs. Bending Moment

The redistribution of internal forces, caused by "hinging" at the critical joint locations, causes redistribution of the secondary prestress forces near ultimate load levels. As described above, the secondary prestress forces are caused by geometric constraints on the entire structure when the tendons are initially stressed. To develop the required tensile forces with external tendons, large rotations must occur at the segment joints. As joints "hinge" and a mechanism forms, the forces from the initial geometric constraints dissipate. If the segments are detailed to allow large rotations to occur at the segment joints, then the geometric constraints will no longer be valid. Therefore, the geometric constraints and the corresponding secondary prestress forces affect the service load behavior, while the conditions at ultimate load approach plastic mechanism behavior with small, non-zero rotational stiffnesses at flexural hinges.

This page replaces an intentionally blank page in the original.

-- CTR Library Digitization Team

8. CONCLUSIONS AND RECOMMENDATIONS

An experimental investigation was conducted to examine the service and ultimate load behavior of segmentally precast box-girder bridges with external post-tensioning tendons. A primary interest of this study was to examine the effect of joint type (dry versus epoxied joints) on the stiffness, strength, and ductility of the structure. A three-span reduced-scale segmental box-girder bridge model was constructed, then tested in three stages corresponding to service loads, factored design loads, and ultimate loads. Flexural behavior was examined first, then shear tests were conducted on the partially damaged structure. Test results and observations were presented in previous chapters.

The conclusions presented in this chapter are based on the tests of the model structure and hence their applicability may be limited to similar precast segmental bridges with external tendons, similar tendon anchorage, deviation, and segment joinery details. In this research program a realistic reduced-scale model of an externally post-tensioned box-girder bridge was constructed and tested. Results of the tests indicate that both dry and epoxy-jointed systems behave in a ductile manner with considerable reserve capacity beyond service and factored design load conditions. The joints remained closed and the structure uncracked for loads as high as the factored design load. For higher load levels the structure displayed considerable visible distortion before reaching ultimate strength.

In this chapter, observations and recommendations are summarized from all aspects of the research program. Important information concerning the fabrication and erection processes are presented to assist designers in constructing better structures. Behavior, design recommendations, and conclusions are then summarized from the test data and observations. Finally, additional research needs in areas related to externally post-tensioned bridge structures are presented.

8.1 Fabrication Conclusions and Recommendations

The following conclusions were drawn from experience gained during fabrication of the model bridge components:

1. Precasting match-cast box-girder bridge segments is a highly complex operation requiring thorough planning before production casting begins. The following is a partial list of important items to be considered before beginning precast operations of match-cast segments: concrete mix-design, concrete properties, concrete and cement supplier, aggregate availability and consistency, concrete batching, concrete approval methods, concrete placement and consolidation, concrete finishing, concrete curing and testing, form preparation, form operation, form stripping, debonding agent, geometric control of match-cast segments, quality control procedures, post-tensioning hardware support and preparation, post-tensioning hardware reinforcement, shear-key details, segment reinforcement,... All of these factors, plus others, will need to be assessed during the precast operation. Initial planning will help eliminate most construction problems (Chapter 2).
2. The post-tensioning anchorage details should be pretested prior to use in the prototype structure. The pretest can be conducted either by proof testing prototype anchorage regions or by load testing a mockup of the anchorage region (Section 7.3.2.2).
3. Unequal web reactions can be expected with segmental systems erected on shoring. Provision should be made in the bearing design and fabrication to equalize web reactions after erection (Section 4.4).

8.2 Erection Process

The following conclusions were drawn from experience gained during the erection of the model bridge structure:

1. The layout of the temporary post-tensioning is controlled by several factors: the workable life of the epoxy joining material, the weight of segments being joined, and the stiffness of the supporting falsework. Each factor must be considered independently, as well as its relationship to the other factors. The temporary post-tensioning equipment and procedure should also be tested before production erection begins (Section 2.4.3).

2. The epoxy should be delivered in clearly labeled, premeasured quantities of each component so they can be mixed directly without site measurement of quantities. The epoxy supplier should also provide information regarding the necessary storage conditions and mixing techniques. The contractor should also have experience with epoxy and be able to recognize substandard materials (Section 2.4.5).
3. The epoxy application process must be planned carefully to ensure that all the necessary tasks are completed within a required time frame. The epoxy pot-life serves as a maximum time limit for completion of: epoxy measuring and mixing, application of the epoxy to both surfaces of a match-cast joint, joint closure, temporary post-tensioning, and cleaning of the epoxy from tendon ducts and equipment. Time studies should be conducted to estimate the necessary manpower and the proper staging of the various tasks (Sections 2.4.3 and 2.4.5).
4. The use of superplasticizers is recommended in the cast-in-place closure strip to ensure proper workability of the concrete. The high surface-to-volume ratio in the closure strips requires that the forms and matching segment faces be moistened to reduce water loss due to absorption. The super-plasticizer is beneficial in providing a concrete with a high workability that is independent of water loss through absorption (Section 2.4.6).
5. Each post-tensioning ram should be operated independently with its own pump and pressure control system. Coupling of post-tensioning rams into parallel systems is not advised (Section 2.4.7).

8.3 Analysis

The following conclusions were drawn from experience gained by applying various analysis methods to the model bridge structure:

1. The model structure was adequately analyzed using a plane-frame elastic analysis to load levels as high as the factored design load (Section 5.3).

2. A plastic mechanism analysis can be used to reveal important information about the behavior of the structure near ultimate loads. Critical mechanism joints can be determined and an estimate of the ultimate flexural strength can be obtained. For the model structure, when the ACI formula for unbonded tendon stress was used in the calculation of hinge capacities, the mechanism analysis yielded calculated strengths less than, and within 15 percent of measured strengths (Section 5.2).
3. To properly predict the insitu condition of the structure it is necessary to analyze each structural configuration that occurs during construction of the structure. Dead loads, prestress forces, and construction or service live loads must be applied to each intermediate structure. The resultant internal forces and deflections from a particular configuration must be superposed with subsequent configurations (Section 5.3).

8.4 Behavior

The following conclusions are drawn from the tests which documented the full range of behavior of a segmental box-girder bridge model with external post-tensioning tendons erected in a span-by-span sequence:

1. The structure remained uncracked for service load conditions with live-load deflections of approximately $L/6000$ for both exterior spans and $L/7500$ for the interior span. The deflection of the dry-jointed exterior span was about 10 percent greater than for the epoxy-jointed exterior span. The reduced stiffness in the dry-jointed span is perhaps caused by differential shrinkage in segments, due to variable thicknesses, which results in less than full contact between match-cast segments. Epoxy effectively filled any space left by differential shrinkage, and restored full contact between segments. Additionally, lower concrete strengths in the north span may have lead to decreased stiffnesses (Section 7.1.1.1).
2. The live-load tendon-stress increases in the midspan region of the loaded span were measured to be less than 2 ksi in all spans. Tendon slip was not noticed during service load cycles (Section 7.1.1.1).

3. The box-girder shape used for the model structure exhibited high torsional stiffness with rotational deformations less than could be accurately measured with the instrumentation (Section 6.6.1.3).
4. The cracking load in the epoxy-jointed span was approximately twice the load required to decompress the flexural tension fiber and begin to open an existing flexural crack or a dry joint. Cracking occurred through concrete adjacent to an epoxied joint (Section 7.3.2).
5. The structure remained uncracked to load levels higher than the factored design load (Section 7.3.3).
6. The structure was quite stiff under the factored design load. While carrying 1.3 DL, the measured factored live load deflections were $L/1764$ for the dry-jointed exterior span and $L/2310$ for the epoxy-jointed exterior span. The approximately 25 percent higher stiffness in the epoxy-jointed span reflects the tensile capacity of the joints and the reduced effective cross-section in the dry-jointed span (Section 7.3.3).
7. The factored-load tendon stress increases in the midspan region of the loaded exterior spans were measured to be less than 5 ksi in both exterior spans. Tendon slip was not noticed for any of the factored load cycles (Sections 6.6.2 and 6.7.2).
8. Failure of the exterior span in flexure (defined as when the tangent stiffness of the load-deflection response was reduced to 4% of the initial elastic stiffness) occurred after development of a failure mechanism involving concentrated rotations in a joint or crack near midspan of the exterior span and subsequent opening at a joint at the interior face of the first interior pier segment (Section 7.1.3).
9. The total moment at midspan of the north span when flexural capacity was reached was approximately 2.5 times the total service-load moment in the north dry span and 3.0 in the epoxied south span. This indicates that the midspan moment has an overall factor of safety above the service load condition of approximately 2.5 in the dry north span and 3.0 in the epoxied south span. The difference in capacity was due to a larger effective prestress in the south span (Section 7.1.5).

10. The maximum applied-load moment at midspan of the north span when flexural capacity was reached was approximately 5.6 times the maximum applied service-load moment in the dry north span and 7.8 in the epoxied south span. This indicates that the midspan moment has an overall safety margin above the service load condition of approximately 5.6 in the dry north span and 7.8 in the epoxied south span. Again, the difference in capacity was caused by a larger effective prestress in the south span (Section 7.1.5).
11. Two important ductility requirements should be considered during design of externally post-tensioned girders.
 - i. Details should be provided to ensure that plastic hinges form in a ductile manner. Bonded reinforcement and multi-hinge mechanisms will lead to more ductile structures.
 - ii. If epoxy is used at segment joints, and the moment capacity is less than the cracking load then an additional factor of safety on the required capacity should be provided (Section 7.1.5).
12. The tendon stress corresponding to nominal flexural strength, f_{ps} , is dependant on many factors. The primary variable affecting f_{ps} is the effective stress in the prestressed reinforcement after allowance for all prestress losses, f_{pe} . Other factors that may influence f_{ps} are: the ratio of section effective depth to unbonded tendon length ((Z_p/l_i)), the depth to the neutral axis (c_u), the amount of prestressed and nonprestressed reinforcement (ρ_p and ρ_s), the concrete strength ($f'c$), the level of confinement in the compression zone, and detailing of the segment reinforcement (Section 7.4.2).
13. The tendon stress corresponding to nominal flexural strength, f_{ps} , is critically dependant on the effective stress in the prestressed reinforcement after allowance for all prestress losses, f_{pe} . To ensure adequate safety, the design should be based on conservative assumptions with respect to losses from friction, creep, and shrinkage (Section 7.4.2.1).
14. The following design method is recommended for design of post-tensioned girders with unbonded external tendons (Section 7.4.4):

$$f_{ps} = f_{pe} + 900 \left(\frac{d_p - c_y}{\ell_e} \right) \quad (\text{ksi})$$

but not to exceed f_{py}

where:

f_{ps} = the tendon stress corresponding to nominal strength (ksi).

f_{pe} = effective stress in the prestressed reinforcement after allowance for all prestress losses (ksi).

d_p = distance from the extreme compression fiber to center of prestressed reinforcement (in.).

c_y = distance from the extreme compression fiber to the neutral axis calculated using factored material strengths and assuming the tension reinforcement, prestressed or mild, has yielded (in.).

ℓ_e = effective length of the tendon for calculation of nominal strength

$$\ell_e = \left(\frac{\ell_i}{1 + \frac{N_s}{2}} \right) \quad (\text{in.})$$

where:

ℓ_i = the length of the tendon between anchorages (in.).

N_s = the number of support hinges crossed by the tendon (draped tendons only).

15. Large concentrated rotations are required at opening joints to cause tendon stresses to increase with the applied load. These rotations allow the internal forces to redistribute to stiffer regions. The secondary prestress forces also redistribute as ultimate load levels are reached (Section 7.6.3).
16. Two general methods are available to rate an existing unbonded structure. With the first method, the engineer must make a conservative assumption of the insitu tendon stresses and be sure that the calculated tendon stress is an extreme lower bound to the true insitu stress. With the second method the structure must be loaded and monitored in an attempt to determine

the load that causes decompression at the extreme tension fiber. From this load an estimate of the effective prestress can be made (Section 7.5).

17. Tendon slip was observed for all tendons at all deviators during the ultimate strength cycles. Tendons also slipped during cracking and joint-opening cycles. When a tendon began to slip, it did not suddenly slip and release stress in the midspan region. Instead, the tendon started to slip and then continued to slip as load was increased. For ultimate load levels the tendons were elongating over their entire unbonded lengths between anchorages (Section 7.4.2.5).
18. The maximum midspan stress that was achieved in the model tendons was affected by the load level at which slip began. If tendon slip began at a low load level, then the ultimate midspan tendon stress was low. Conversely, if slip did not occur until higher load levels, then the ultimate midspan tendon stress was increased (Section 7.4.2.5).
19. The local transfer of forces across opening joints depended on the level of shear being transmitted across the joint. For opening joints with small shear transfer, the joint/crack opened in a flexural mode into the top flange of the structure with the concentrated rotations occurring at the joint. For opening joints with large shear transfer, an inclined crack formed from the load point to the lower corner of the segment adjacent to the joint. The concentrated rotations occurred at the inclined crack (Section 7.1.4).
20. The tests results indicated that there was a measured decompression load of 1.9(LL+I) in the dry-jointed north span. However, the design of this span provided substantial residual compression at service load levels only slightly above the recently recommended PTI-NCHRP-AASHTO recommended levels. In addition, the true factor of safety may be less because of traffic overloads, excessive prestress losses, or calculation inaccuracies. The epoxy joints offered substantial reserve against cracking. The use of epoxy joints is recommended for segmental box girder construction (Sections 5.4, 7.1.4 and 7.3).

8.5 Research Needs

The goal of any research project is to obtain a better understanding of the research subject. Frequently, a better understanding of the subject will lead to an increased awareness of subject areas still requiring investigation. The following is a list of possible research topics which will improve understanding of externally post-tensioned box-girder bridge systems.

1. An important aspect of the behavior of externally post-tensioned systems is the shear behavior at a critical mechanism joint. This subject was partially studied with the scale model bridge project and was also studied independently by Ramirez (26) at the Ferguson Structural Engineering Laboratory of the University of Texas at Austin. Additional research is required to fully document all components of shear strength at an opening joint (Section 7.1.4 and 7.3.5).
2. During stressing of the scale model bridge structure it appeared there was substantial friction loss through the live-end anchor. This was also noticed by Quade (19) in another project at the University of Texas at Austin. Because the ultimate flexural strength of unbonded systems is critically dependant on the insitu tendon stress, research is needed to quantify the friction losses in standard industry anchorage hardware. Friction loss studies should also be conducted for deviator regions and regions of high duct curvature (Section 4.1).
3. The deviators provide the only positive connection between the prestressing tendons and the concrete box-girder. Complete understanding is therefore required for this critically important detail. Components contributing to deviator strength have been investigated by Powell and Beaupre (3). Other areas important to deviator behavior requiring study are (Sections 1.3.3, 7.1.1.4 and 7.4.2.5):
 - fretting fatigue
 - bond mechanism between the deviator and grouted external tendon.
 - possible improved details

4. The finite element program prepared by El-Habr (10) provides an excellent starting point for analyzing externally post-tensioned systems. The following refinements are suggested to make the program easier to use and more applicable to bridge structures (Section 1.3.2.1):
 - include a method for tracing the segmental construction process.
 - include the potential for slip between the tendons and deviators.
 - post-tensioned tendons rather than prestressed tendons.
5. The scale model bridge structure was designed and constructed with many features which could extend the testing program. The following is a list of additional studies that could be conducted on the model:
 - bond external tendons to intermediate diaphragms.
 - bond external tendons to the bottom flange with a secondary cast of concrete.
 - stress and grout internal tendons.
 - conduct direct shear tests.
 - investigate the fatigue behavior of the global system.
 - investigate the seismic behavior of externally post-tensioned structure.
 - investigate redistribution of secondary prestress forces.
 - develop and verify code equations for flexural strength of externally post-tensioned bridge structures.
6. Prototype testing can be used to verify and extrapolate model test data. The following is a list of possible research that could be conducted on prototype structures:
 - apply instrumentation to a prototype structure during construction to monitor true behavior under service loads.
 - apply strain gages to external tendons and monitor friction losses during stressing.
 - monitor long-term serviceability of dry-jointed structures.

REFERENCES

1. Powell, L. C., Breen, J. E., and Kreger, M. E. *State of the Art for Externally Post-Tensioned Bridges with Deviators*, The University of Texas at Austin Center for Transportation Research, Research Report 365-1, June 1988.
2. Carter, Lisa L., "Deviator Behavior in Externally Post-Tensioned Bridges," unpublished M.S. Thesis, The University of Texas at Austin, Aug. 1987.
3. Beaupre, R. J., Powell, L. C., Breen, J. E., and Kreger, M. E., *Deviation Saddle Behavior and Design for Externally Post-Tensioned Bridges*, The University of Texas at Austin Center for Transportation Research, Research Project 365-2, July 1988.
4. Beaupre, Richard J., "Deviation Saddle Behavior and Design for Externally Post-Tensioned Bridges," unpublished M.S. Thesis, The University of Texas at Austin, Aug. 1988.
5. MacGregor, Robert J. G., "Strength and Ductility of Externally Post-Tensioned Segmental Box Girder Bridges", unpublished Ph.D. Dissertation, The University of Texas at Austin, May 1989.
6. Hoang, L. H., and Pasquignon, M., "Essais de Flexion sur des Poutres en Beton Précontraintes par des Cables Extérieurs," Volumes 1 and 2, Contrat SETRA-CEBTP 1985, Dossier de Recherche 91017, Nov. 1985.
7. Ritz, P., "Biegeverhalten von Platten mit Vorspannung ohne Verbund" ("Flexural Behavior of Unbounded Post-Tensioned Slabs"), Dissertation, Institut für Baustatik und Konstruktion, Swiss Federal Institute of Technology at Zurich, Bericht Nr. 80, Birkhauser Verlag Basel und Stuttgart, May 1978.
8. Virlogeux, M., "La Précontrainte Extérieure," *Annales de l'Institut Technique du Bâtiment et des Travaux Publics*, Dec. 1983.
9. Sowlat, K., and Rabbat, B. G., "Testing of Segmental Girders," Final Report to Figg and Muller Engineers, Inc., Project No. 0217, July 1984.
10. El-Habr, Kamal C., "Finite Element Analysis of Externally Prestressed Segmental Construction", unpublished M.S. Thesis, The University of Texas at Austin, May 1988.
11. Muller, J. and Gauthier, Y., "Ultimate Behavior of Precast Sequential Box Girders with External Tendons", *Proceedings of the International Symposium on Externally Post-Tensioned Bridges*, Houston, Texas, October 1988, in press.

12. Podolny, W. and Muller, J., *Construction and Design of Prestressed Concrete Segmental Bridges*, John Wiley and Sons, Inc., 1982.
13. AASHTO, "Standard Specification for Highway Bridges", 13th Edition, American Association of State Highway and Transportation Officials, 1983.
14. Post-Tensioning Institute, "Design and Construction Specifications for Segmental Concrete Bridges," Final Report on NCHRP Project 20-7/32, Feb. 1988.
15. Koseki, Kikuo, "Shear Strength of Joints in Precast Segmental Bridges", unpublished M.S. Thesis, The University of Texas at Austin, May 1981.
16. Stone, W. C. and Breen, J. E., "Design of Post-Tensioned Girder Anchorage Zones", *Journal of the Prestressed Concrete Institute*, Vol. 29, No. 2, March-April 1984, pp. 28-61.
17. *Building Code Requirements for Reinforced Concrete*, (ACI Standard 318-83), Detroit, American Concrete Institute, 1983, pp. 318-82.
18. Yates, "A Study of Fretting Fatigue in Post-Tensioned Concrete Beams", unpublished M.S. Thesis, The University of Texas at Austin, December 1987.
19. Quade, C. E., "Distribution of Post-Tensioning Forces Prior to Grouting Tendons", unpublished M.S. Thesis, The University of Texas at Austin, May 1988.
20. Post-Tensioning Institute, "Design and Construction Specifications for Segmental Concrete Bridges", Unpublished Draft No. 1, NCHRP Project 20-7/32, January 1987.
21. Lin T. Y., and Thornton K., "Secondary Moment and Moment Redistribution in Continuous Prestressed Concrete Beams", *PCI Journal*, Jan- Feb 1972, Vol. 17 No. 1.
22. American Concrete Institute Committee 318, "Building Code Requirements for Reinforced Concrete (ACI 318-83), American Concrete Institute, Detroit, Michigan.
23. Mattock, A. H., Yamazaki, J., and Kattula, B. T., "Comparative Study of Prestressed Concrete Beams, With and Without Bond", *ACI Journal*, Proceedings Vol. 68, No. 2, Feb. 1971, pp. 116-125.
24. Naaman A.E., "Partially Prestressed Concrete: Review and Recommendations", *PCI Journal*, Vol. 30, No. 6, Nov-Dec 1985, pp. 30-71.
25. Wittfoht H., "Outstanding and Innovative Construction Methods in Concrete Structures: Recent and Future Trends", *FIP OC/4*.

26. Ramirez G., "Behavior of Unbonded Post-Tensioning Segmental Beams with Multiple Shear Keys", unpublished M.S. Thesis, The University of Texas at Austin, January 1989.
27. Mojtahedi S. and Gamble W.L., "Ultimate Steel Stresses in Unbonded Prestressed Concrete", Journal of the Structural Division, ASCE, Vol.104, No.ST7, July 1978, pp. 1159-1165.
28. Tam A. and Pannel F.N., "The Ultimate Moment of Resistance of Unbonded Partially Prestressed Reinforced Concrete Beams", Magazine of Concrete Research, Vol.28, No.97, Dec.76, pp. 203-208.
29. Corley W.G., "Rotational Capacity of Reinforced Concrete Beams", Journal of the Structural Division, ASCE, Vol.92, No.ST5, Oct.1966, pp. 121-146.
30. Kaar P.H., Fiorato A.E., Carpenter J.E., Corley W.G., "Limiting Strains of Concrete Confined by Rectangular Hoops", PCA Research and Development Bulletin - RD053.01D, Portland Cement Association, 1978.
31. Mattock A.H., Yamazaki J., and Kattula B.T., "Comparitive Study of Prestressed Concrete Beams With and Without Bond", ACI Journal, No.2, Vol.68, Feb.71, pp. 116-125.
32. Canadian Standards Association Committee A23.3, "Design of Concrete Structures for Buildings CAN3-A23.3-M84", Canadian Standards Association, Ottawa, Ontario, 1984.
33. AASHTO, "Manual for Maintenance Inspection of Bridges", 4th Edition, American Association of State Highway and Transportation Officials, 1983.